Development of Electrocatalysts for the Oxygen Evolution Reaction in Alkaline Water Electrolysis

by
Sophia Mellsop

A Thesis submitted in partial fulfilment of the requirements for the degree of
Doctor of Philosophy in Chemical and Process Engineering
at the
University of Canterbury

April 2016

Contents

Acknowledgements

There are a number of people whose guidance, assistance, and support have helped make this journey possible. I would like to thank the following people:

- My supervisor, Dr. Aaron Marshall, for giving the opportunity to carry out this research, for his guidance and support throughout this work, and for his constant optimism which helped to keep me motivated.
- Dr. Alister Gardiner, and all those at Callaghan Innovation for giving me the opportunity to carry out this work, for their guidance, and and for allowing me to use their testing facilities
- Dr. Bernt Johannessen for his assistance in carrying out X-ray absorption spectroscopy analysis on the XAS beamline at the Australian Synchrotron, Victoria, Australia and the following data analysis.
- Dr. Colin Doyle for his assistance in carrying out XPS measurements at the Research Centre of Surface and Materials Science, University of Auckland.
- Departmental technicians in the Mechanical Workshop (Leigh Richardson, Stephen Hood and Frank Weerts) and Electrical Workshop (Stephen Beuzenberg and Tim Moore) for their technical assistance. Thanks also to Tony Allen for helping with computer issues, Michael Sandridge for his analytical support and Glenn Wilson for purchasing lab supplies
- Mike Flaws from Mechanical Engineering for TEM and SEM training and support, and Tobias Baldhoff for taking SEM images of the iridium electrocatalysts for me.
- My parents, Maryanne and Geoff Mellsop, as well as Anna and Nick Mellsop for their encouragement and support throughout the Ph.D. process.
- Ben Washington-Yule for his general encouragement and support throughout the last years of this Ph.D. and particularity for his grammar editing support.

Funding for this work was provided under MSI Contract C08X1002.

Summary

With the ever depleting oil resources around the world, an alternative transportable and storable fuel is required for the future. Water electrolysis is one method of producing hydrogen (an alternative fuel) that does not require oil and gas. It has the advantage of producing extremely pure hydrogen without directly harming the environment through carbon emissions. This work focuses on improving the efficiency of the water electrolysis process through reducing the oxygen evolution overpotential by utilising electrocatalysis. The electrocatalysts need to exhibit good activity, good electrochemical stability and be economic to produce. The long-term goal is to utilise an electrocatalyst in a zero-gap, alkaline electrolyser developed by Callaghan Innovation.

Based on the literature review, the following electrocatalysts were chosen for further investigation: $La_xSr_{1-x}CoO_3$, $CoFe_2O_4$, Co_3O_4, $NiCo_2O_4$, IrO_2 and NiO_x. Due to differences in preparation procedures and testing conditions, it can be difficult to directly compare performance results from literature. The initial work enables the comparison of these catalysts through using a standard preparation procedure (thermal decomposition) and an identical testing procedure. The majority of the electrochemical studies in this research were performed using a 30 wt.% KOH electrolyte due to its high conductivity, with potentials referenced against Hg/HgO (30 wt.% KOH). The electrocatalyst with the lowest overpotential, and therefore best performance in this study is IrO_2, however due to its cost, Co_3O_4 is also considered as a promising option as it has the second best performance while only having a mid-range surface area when compared to the other electrocatalysts. This indicates high intrinsic activity. Another observation from the preliminary work is that the nickel substrate material itself has better electocatalytic performance than some of the other electrocatalysts tested. Thus, it was decided that methods of obtaining and maintaining good performance with an uncoated nickel electrode be investigated.

To gain a better understanding of the nickel hydroxides which catalyse the oxygen evolution reaction (OER), the complex phase changes which occur on the electrode surface were investigated. It was found that a process in addition to the standard α-$Ni(OH)_2$/γ-NiOOH and β-$Ni(OH)_2$/β-NiOOH reactions occur in the more concentrated KOH electrolyte. It is also confirmed that the initial hydroxide layer formed anodically from metallic nickel is not α-$Ni(OH)_2$, but rather a layer which is more readily reducible. While in situ XAS suggested that γ-NiOOH is not transformed to any further phase up to 0.665 V vs Hg/HgO in 1 M KOH, at higher potentials, after extensive OER (at least 40 hrs) at 50 mA cm^{-2} and in 30 wt.% KOH, an additional phase can be identified by cyclic

voltammetry. During galvanostatic oxygen evolution, the nickel anodes follow an ageing behaviour characterised by a brief activation period, a short period of high activity (i.e., low overpotential) followed by deactivation and eventually stable but poor activity.

After studying the structural changes which occur on the surface of the nickel electrode, as well as the ageing behaviour, methods of rejuvenation of nickel anodes are investigated. The deactivation caused by ageing can be mitigated by temporarily reducing the potential for brief periods. Continuous rejuvenation of nickel anodes is investigated and it is shown that rejuvenation at 0.5 V vs Hg/HgO for 10 min out of every 100 min can prevent ageing of the anode, thus maintaining a low overpotential during galvanostatic oxygen evolution at 50 mA cm^{-2}. It is suggested that the short potentiostatic rejuvenation periods at regular intervals prevents the ratio of Ni(IV) to Ni(III) from increasing, thereby maintaining the intrinsic activity of the material. Additionally it is found that the rejuvenation potential must be above 0.36 V vs Hg/HgO to ensure the rejuvenation is successful in improving performance, i.e., the material must not reduce to Ni(II). It is estimated that by using rejuvenation steps, an energy saving of 8% is possible in an alkaline water electrolyser using nickel anodes.

While the performance decrease of the nickel anodes over time can be reduced by rejuvenation, addition of electrocatalytic coatings are still recommended where the goal is to further improve performance and stability without the need for rejuvenation steps. As cobalt oxide was identified as one of the most promising electrocatalysts earlier, its catalytic performance is further optimised by investigating deposition procedure options. Layers produced by both thermal decomposition and electrochemical deposition had similar electrochemical behaviour, provided that the layers were annealed at temperatures $\geq 350°C$. This thermal treatment was required to mechanically stabilise the electrochemically deposited cobalt oxide layer. Due to this finding, the effect of annealing temperature was investigated for the electrochemically deposited layer, and it was found that the overpotential for oxygen evolution increased with annealing temperature. Using cyclic voltammetry and impedance spectroscopy, it is concluded that the decrease in performance with increasing annealing temperature is largely caused by the corresponding decrease in active surface area. However, for annealing temperatures $\geq 400°C$, additional resistances are introduced which cause lowered performance.

As iridium oxide is identified as another promising but costly electrocatalyst, deposition of thin iridium layers are investigated. Spontaneous deposition onto nickel substrates was investigated as a method of producing these thin electrocatalytic iridium layers. UV/Vis spectroscopy, cyclic voltammetry and other electrochemical methods are used to investigate the deposition process and the activity of the electrocatalytic coating towards the OER. From three solutions ($IrCl_3$ + HCl, H_2IrCl_6 + HCl, and H_2IrCl_6), H_2IrCl_6 is shown to give the most active and stable coating, with deposition times of 45 min at 60°C being enough to increase the activity of the nickel substrate for the OER. While the iridium oxide coatings are highly active at low current densities (less than 45 mA cm^{-2}), coatings with higher surface area would be needed to maintain a high performance at higher current densities.

Finally, some preliminary work was carried out in order to scale up the cobalt oxide coating procedure to a 20 cm x 25 cm nickel foam electrode. Firstly it is shown that electrodeposition can be used to coat a 0.5 cm x 1 cm nickel foam electrode (most previous work had been done on nickel foil) and achieve an overpotential decrease of 150 mV at 50 mA cm^{-2} relative to the uncoated nickel foam. Next a 20 cm x 25 cm cobalt oxide coated electrode was successfully produced via electrodeposition. Testing the performance in one cell of the zero-gap Callaghan Innovation electrolyser shows no increase in performance over the uncoated electrode. However, by testing a cobalt oxide coated electrode in a smaller scale zero-gap cell (nickel foam electrodes 5 cm x 4 cm in size) it is shown that a performance improvement can indeed be achieved in a zero-gap configuration. A number of reasons for the lower than expected performance at full-scale (20 cm x 25 cm) are discussed and recommendations for future work are made.

Chapter 1

Introduction

1.1 Hydrogen, Water Electrolysis and Overpotentials

With the ever depleting oil resources around the world, a new transportable and storable fuel will be required in the future. Prices of energy resources such as oil and gas are increasing as they become more difficult to obtain. There is also a need to reduce the harmful effects these resources have on the environment. Hydrogen is one possible alternative to oil and gas as it is able to act as an energy carrier, emitting almost nothing but water when used as a fuel [1]. A possible hydrogen energy economy is illustrated in Figure 1.1 [2].

Water electrolysis is a method of producing hydrogen that does not require oil and gas. Other methods used to produce hydrogen are reforming of natural gas [3, 4] and gasification of coal and petroleum coke [3, 5, 6]. Water electrolysis has the advantage of producing extremely pure hydrogen [1] without directly harming the environment through carbon emissions. Provided the electricity required is produced from a renewable source, hydrogen is considered sustainable [1].

Fully renewable hydrogen fuel systems are being developed for settlements in remote locations which only utilise solar and wind power. Energy from these renewable systems is produced intermittently and thus must be stored. Hydrogen is one storage option. The hydrogen can then either be used directly for heating or converted back to electricity when required through the use of a fuel cell.

In these systems, water electrolysis is used to convert electricity to hydrogen energy through electrochemically splitting water into hydrogen and oxygen. A water electrolysis cell has the hydrogen evolution reaction (HER) occurring at the cathode and the oxygen evolution reaction (OER) at the anode. An illustration of a basic water electrolysis system is shown in Figure 1.2.

This work focuses on improving the efficiency of the water electrolysis process. This can be done by reducing the overpotential. The overpotential is defined as the additional energy required, above the equilibrium potential, to drive the reaction at a desired rate. There is an HER overpotential and an OER overpotential, and both can be significant in water electrolysis. The overpotentials can be reduced through the use of electrocatalysis. It has been found that the oxygen overpotential is

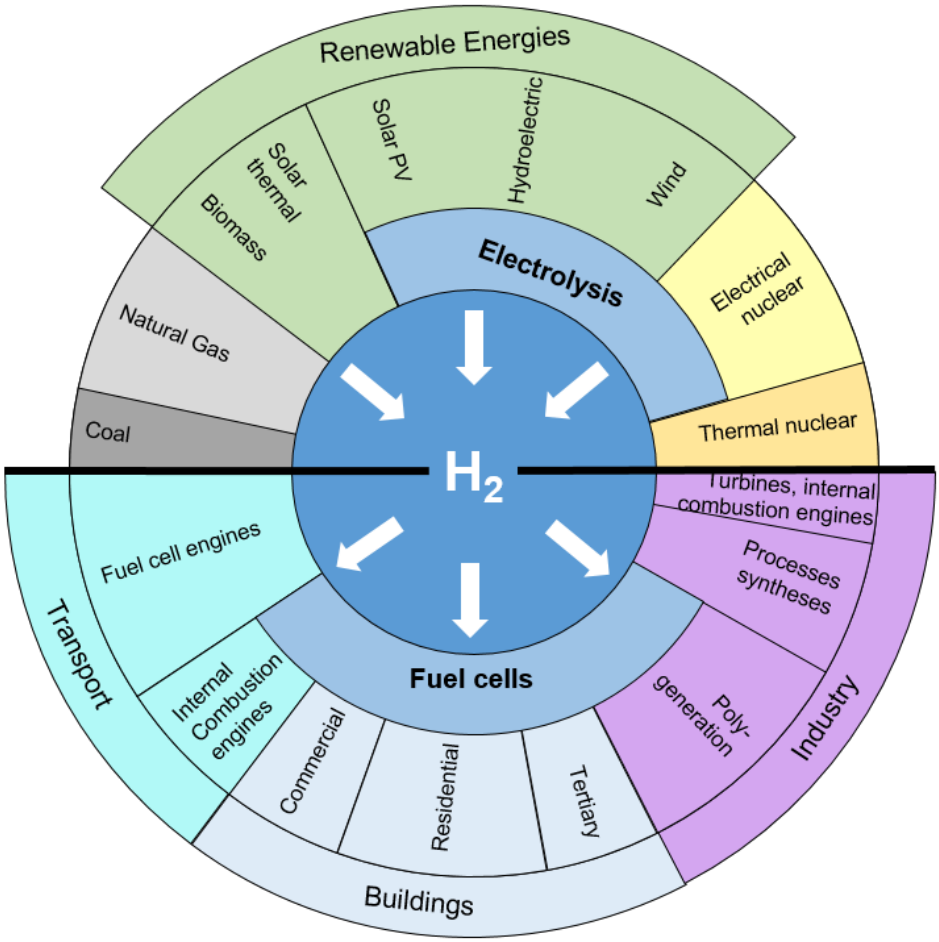

Figure 1.1: Diagram of the hydrogen production and use in a hydrogen economy.

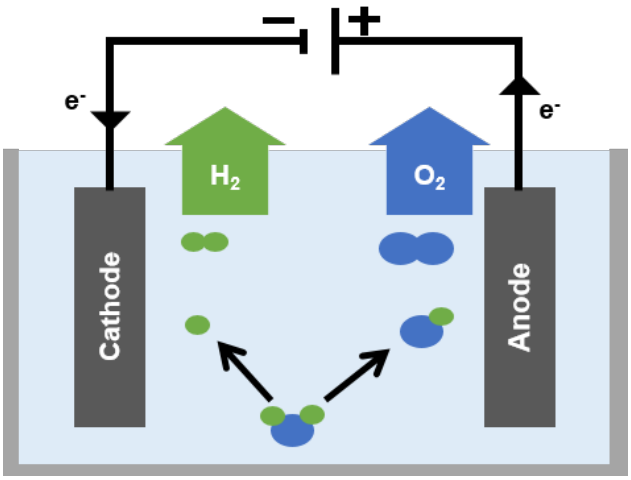

Figure 1.2: Diagram of a simple water electrolysis system.

generally more difficult to reduce than the hydrogen overpotential [1]. The focus of this research is to investigate electrocatalysts to help reduce the oxygen evolution overpotential. The electrocatalysts need to exhibit good activity, good electrochemical stability and be economic to produce.

This work is specifically focussed on producing an electrocatalyst for a zero gap, alkaline electrolyser developed by Callaghan Innovation. This electrolyser utilises electrodes made of a nickel foam material which allows for gas transport and increases surface area. The long-term goal is to produce an optimised electrocatalyst which can be deposited onto a nickel foam electrode and used in the Callaghan Innovation electrolyser. Further information on the Callaghan Innovation electrolyser can be found in Chapter 9.

1.2 Thesis Structure

Over the last thirty years there has been a significant amount of literature investigating a range of electrocatalysts [7] and this thesis begins with a literature review to outline key themes and to identify electrocatalysts for further investigation (Chapter 3). From this review, six electrocatalysts are identified for further investigation, which are analysed in Chapter 4 for their performance, surface area and stability. The most promising electrodes from this screening chapter are Co_3O_4 and IrO_2 and therefore these are investigated further in Chapter 7 and Chapter 8. Only thin coatings are investigated in Chapter 8 due to the cost of IrO_2 electrocatalyst production. Chapters 5 and 6 investigate how the nickel metal performs as an electrocatalyst. This is done to investigate whether the performance could be improved without the additional complexity of adding another another material layer. Co_3O_4 is identified as the most promising material and therefore an investigation into scaling up the production of this catalyst was conducted (Chapter 9).

The majority of this thesis (Chapters 4-9) is written in article format with each data chapter containing its own abstract, introduction, experimental, results and discussion, and conclusions section. Because of this, some details have been unavoidably repeated. Chapters 5, 6, 7, and 8 have been published as journal articles [8, 9, 10, 11] with Sophia Mellsop (author of this thesis) as lead author. There are some minor alterations to the papers upon inclusion in this thesis. It should also be noted that the analysis of the XANES data in Chapter 5 was carried out by Bernt Johannessen (Australian Synchrotron, Victoria, Australia)[9]. In addition to these published papers some of the detail in Chapter 4 has been included in a peer-reviewed paper written for the Chemeca2012 conference [12].

Chapter 2

Background and Theory

2.1 Water electrolysis: The cell and energy

The basic equation for the water electrolysis reaction is:

$$2\,H_2O \longrightarrow 2\,H_2(g) + O_2(g) \tag{2.1.1}$$

Water is very stable and thus the energy requirement for this reaction is high. In an isolated system the energy requirement for the reaction is -1.48 V (based on the enthalpy of reaction) [13] but with absorption of heat from surroundings the potential difference required decreases to -1.23 V (based on the Gibbs energy of reaction) [13].

In industrial water electrolysers the cell potentials are larger, typically 1.8-2.0 V at a current density of 300-1000 A m^{-2} [1]. A large portion of this additional potential energy requirement is due to the overpotentials (already mentioned in Chapter 1). The overpotential can be calculated from the difference between the reversible potential for the OER or HER and the actual measured potential for the OER or HER. Figure 2.1 shows that the reversible oxygen and hydrogen evolution potential depends on the pH of the system.

2.2 Water Electrolysers

The main types of electrolysers found in industry are proton exchange membrane (PEM) electrolysers and alkaline electrolysers [15, 16]. PEM electrolysers use a solid, ion conducting membrane to transfer H^+, rather than using a liquid electrolyte. Alkaline electrolysers have an alkaline electrolyte (usually KOH due to its high conductivity) and use a membrane to separate the oxygen and hydrogen gas. The high capital cost of PEM means that only small units are produced (e.g., if fuelling a small number of hydrogen cars), and alkaline electrolysers are used when larger electrolysers are required [15]. In this work the focus is on alkaline electrolysers.

Alkaline electrolysers can be unipolar or bipolar. Unipolar electrolysers have electrodes connected in parallel while electrodes in bipolar designs are connected in series. Membranes separate

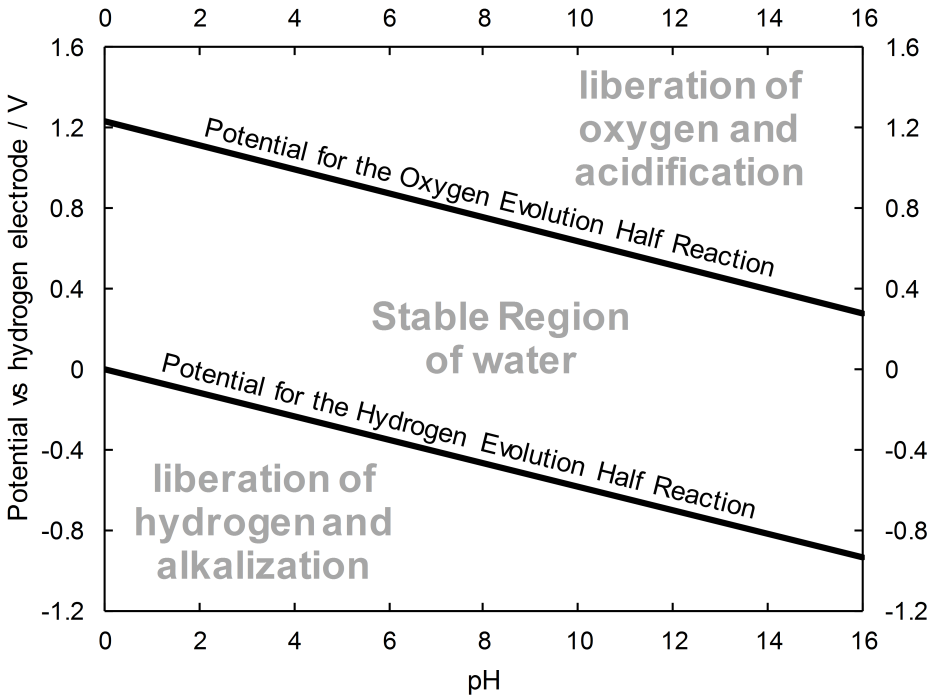

Figure 2.1: Pourbaix diagram for water [14].

the anode and cathode in both designs. The electolyser developed by Callaghan Innovation uses a biopolar design.

The two main costs of running water electrolysers are the capital and electricity costs, with the portion related to electricity cost becoming the larger cost as the size of the electrolyser increases [15]. For this reason it is important that the overpotential is decreased as much as possible to reduce the electricity costs.

2.3 Water Electrolysis and Catalyst Theories

The mechanisms for both the HER and OER have been discussed in literature [1, 2, 17, 18, 19, 20]. In alkaline solution the hydrogen evolution half reaction is:

$$2\,H_2O + 2\,e^- \longrightarrow H_2 + 2\,OH^- \tag{2.3.1}$$

It is widely accepted that the mechanism for the hydrogen evolution reaction in alkaline solution is as described here [17, 18, 1]. The first step is the Volmer step:

$$M + H_2O + e^- \longrightarrow M{-}H_{ads} + OH^- \tag{2.3.2}$$

where M is an adsorption side on the electrode surface. This is followed by a desorption step either by the Tafel reaction (chemical desorption):

$$\mathrm{M{-}H_{ad}} \longrightarrow 2\,\mathrm{M} + \mathrm{H_2} \tag{2.3.3}$$

or the Heyrovský reaction (electrochemical desorption):

$$\mathrm{M{-}H_{ad}} + \mathrm{H_2O} + \mathrm{e^-} \longrightarrow \mathrm{M} + \mathrm{H_2} + \mathrm{OH^-} \tag{2.3.4}$$

In this mechanism the strength of the M-H bond is important in determining the performance of the electrocatalyst. The hydrogen atom must bind strongly to the reaction site, but not too strongly.

The reaction that is focussed on in this work however, is the OER. It is known that the kinetics are slower than the HER and require greater overpotential [13]. The oxygen evolution half reaction in alkaline solution is as follows:

$$2\,\mathrm{OH^-} \longrightarrow \tfrac{1}{2}\,\mathrm{O_2} + \mathrm{H_2O} + 2\,\mathrm{e^-} \tag{2.3.5}$$

The details of the oxygen evolution reaction mechanism are still unclear [2]. There are a number of possible pathways through which the reaction may occur [18]. The most accepted mechanisms involve these three steps [1, 19, 20]:

$$\mathrm{M} + \mathrm{OH^-} \rightleftharpoons \mathrm{M{-}OH_{ads}} + \mathrm{e^-} \tag{2.3.6}$$

$$\mathrm{OH^-} + \mathrm{M{-}OH_{ads}} \rightleftharpoons \mathrm{M{-}O_{ads}} + \mathrm{H_2O} + \mathrm{e^-} \tag{2.3.7}$$

$$2\,\mathrm{M{-}O_{ads}} \rightleftharpoons \mathrm{O_2} + 2\,\mathrm{M} \tag{2.3.8}$$

The activity of a certain electrocatalyst depends on the binding energy of the intermediates to the electrocatalysts. Recent advances in desity functional theory (DFT) calculations have enabled authors to more accurately determine surface binding energies, which can be used as an indicator of activity [21]. This will be discussed further in Chapter 3.

2.4 Electrochemical Properties

A number of properties are important for an electrocatalyst, not just the electrocatalytic activity. Properties that make a good electrocatalyst are listed here [22]:

- high intrinsic electrocatalytic activity
- high surface area
- high electrical conduction

- long-term mechanical and chemical stability
- minimized gas bubble problems
- enhanced selectivity
- availability and low cost

When choosing the best electrocatalyst all of these properties must be considered, not just the intrinsic activity of the catalyst. When analysing the performance of a catalyst it must be noted that both the intrinsic activity and surface area will have an influence on overall performance, as will gas blocking.

The Tafel slope and exchange current are values used to describe the performance of an electrocatalyst (b and i_0 respectively in Figure 2.2). The Tafel slope (b) is simply the slope of the Tafel plot: a plot of overpotential versus the decadic logarithm of current density at steady state. The Tafel slope indicates which reaction step is rate determining [22]. A low Tafel slope is preferable, as this means the overpotential does not increase rapidly with current density. The Tafel slope can be determined for both the OER and the HER. For the OER it typically varies between 40 and 120 mV [22]. This slope is an intensive property and should not depend on the electrode surface area [23], and therefore gives information on intrinsic activity.

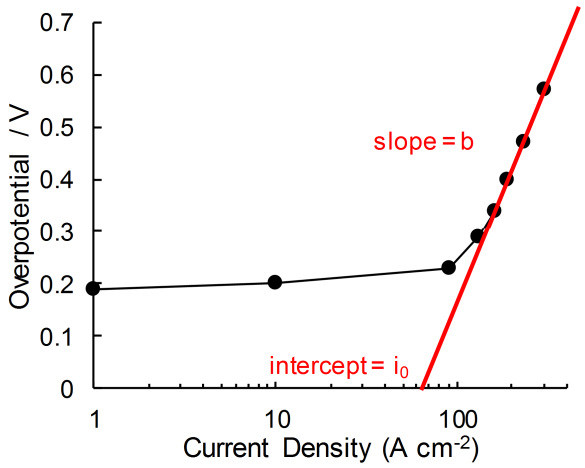

Figure 2.2: Typical Tafel plot for the OER.

The exchange current (i_0), however, is an extensive property and changes with surface area. The exchange current is the x-intercept of the Tafel line in Figure 2.2. A higher exchange current is preferable, as this indicates a lower overpotential. A higher exchange current density may indicate a higher intrinsic activity and/or a higher surface area.

2.5 Reference Electrodes

Understanding reference electrodes is a key requirement for electrochemical studies. A reference electrode is an electrode having a well-known, stable potential. They are commonly used to measure

the potential of a half cell reaction. The normal hydrogen electrode (NHE) consists of a platinum sheet immersed in a 1 M H^+ (aq.) solution in contact with hydrogen gas at a pressure of 1 atm. The standard hydrogen electrode (SHE) is a hypothetical electrode containing 1 M H^+ having unit activity and no ionic interactions [24]. The potential of the standard hydrogen electrode (SHE) is, by definition, 0 V. The half cell reaction occurring which determines the potential of the electrodes is:

$$2\,H^+_{(aq)} + 2\,e^- \longleftrightarrow H_{2(g)} \tag{2.5.1}$$

The hydrogen electrode has certain disadvantages when used experimentally [25] and alternative reference electrodes have been developed. These include the silver-sliver chloride electrode ($Ag/AgCl/Cl^-$), the calomel electrode ($Hg/Hg_2Cl_2/Cl^-$) and the mercury oxide electrode ($Hg/HgO/OH^-$), used often in this work. When saturated KCl solution is used in the calomel electrode it is referred to as the saturated calomel electrode or SCE. The potentials of these electrodes versus the hydrogen electrode at 25°C are shown in Table 2.1. For reference, these electrodes are shown against the Pourbaix diagram for water [14] (Figure 2.3). Note that for the Hg/HgO (KOH) reference electrode it is assumed that the potential is the same as the Hg/HgO (NaOH) electrodes with the same OH^- molality, that is, it is assumed that the potential difference due to activity differences between NaOH and KOH are not significant.

Table 2.1: Reference electrode potentials versus the hydrogen electrode at 25°C.

Electrode	**Solution Concentration**	**Potential (V)**	**Reference**
Silver-silver chloride	Saturated KCl	0.1976	[25]
Calomel electrode	Saturated KCl	0.2415	[25]
Mercury oxide electrode	1 M NaOH	0.1080	[26]
Mercury oxide electrode	30wt.% KOH	0.0233	[26]

2.6 Electrochemical Methods of Analysis

In this thesis a number of electrochemical methods are used to analyse the electrocatalysts produced. These include cyclic voltammetry and electrical impedance spectroscopy (EIS).

2.6.1 Cyclic Voltammetry

Cyclic voltammetry is a popular technique for studying electrochemical systems and is useful for complicated electrode reactions [27]. To carry out this method, the potential is swept over a range, E_0 to E_1, at a certain sweep rate (ν), typically between 10 mV s^{-1}-100 V s^{-1} and then reversed [27] (Figure 2.4). The current response to this potential sweep gives information about charge transfer in the system. Multiple cycles of the potential sweep are often performed.

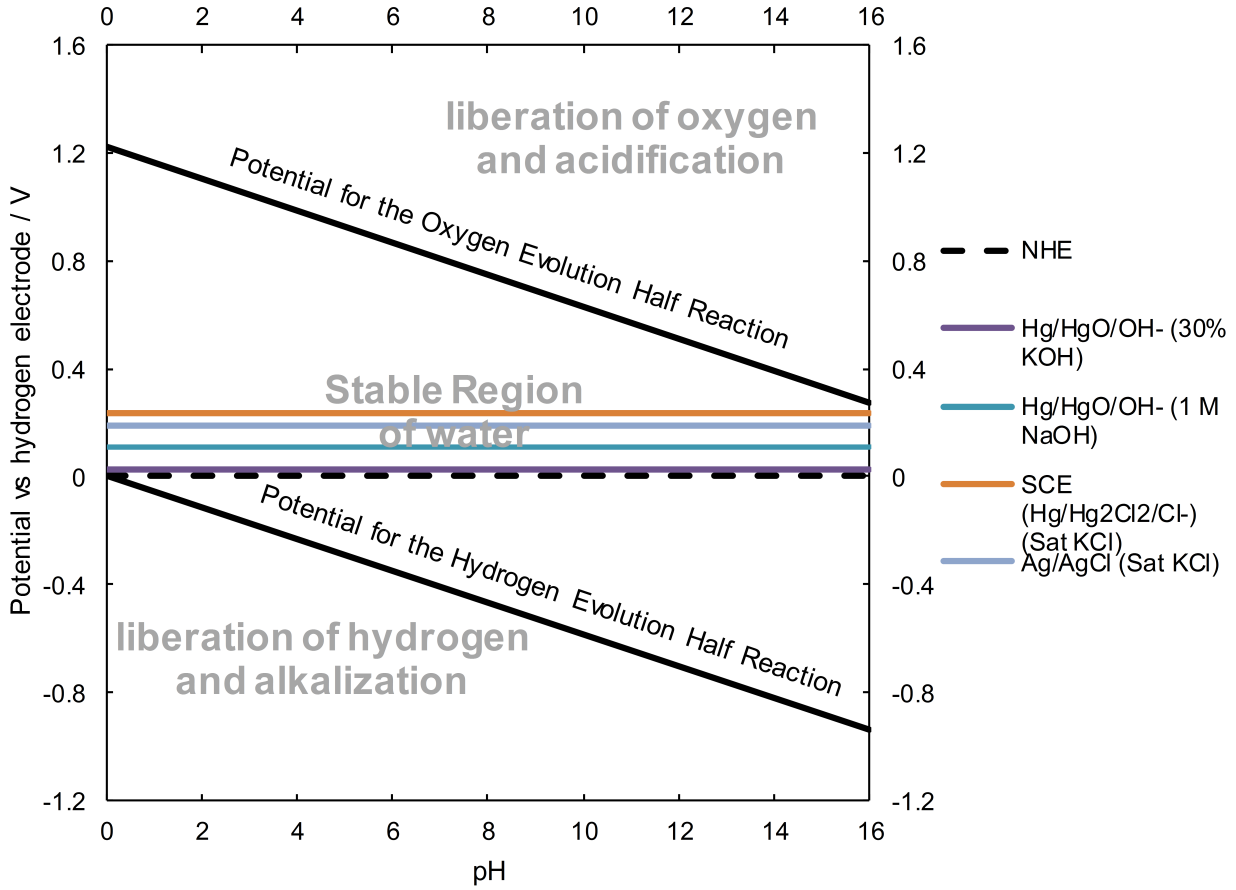

Figure 2.3: Pourbaix diagram for water [14] with reference potentials shown.

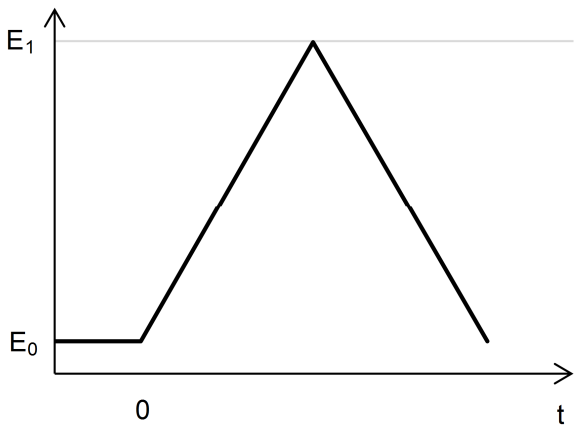

Figure 2.4: Illustration of cyclic voltammetry sweep.

Cyclic voltammograms are a useful tool to provide information about reactions occurring in the potential range through which the scan takes place. If the following reversible oxidation-reduction reaction is occurring:

$$R \rightleftharpoons O + e^- \tag{2.6.1}$$

this can appear in the cyclic voltammogram as a pair of peaks (Figure 2.5). Through referring to Pourbaix diagrams [14] or results from other authors, and taking into account the electrode surface composition, it is possible to determine the reactions occurring at the surface of the electrode. For a number of oxygen evolution electrocatalysts the catalyst forms a higher oxidation state oxide at potentials just prior to oxygen evolution.

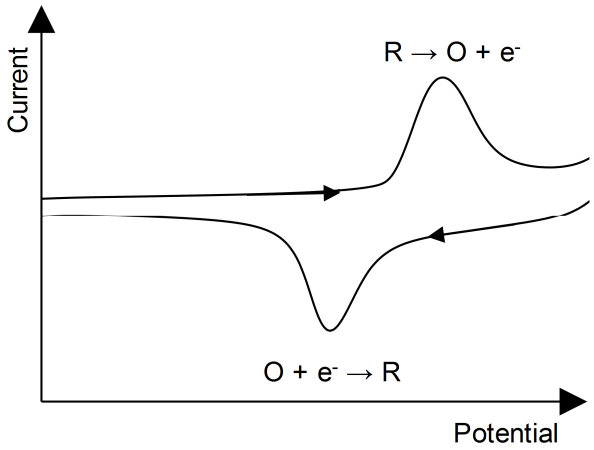

Figure 2.5: Cyclic Voltammogram showing a reversible oxidation-reduction reaction.

Charge transfer during a cyclic voltammogram gives further information about the electrode being studied. Integrating the curve under the redox surface reaction peak gives the charge transferred during the reaction (q^*). This transferred charge is proportional to the number or reaction sites [28], and therefore gives an indication of surface area [29, 30]. It should be noted, however, that q^* often decreases with increasing potential scan rate [31]. This is usually attributed to the porosity of the surface with slower scan rates allowing for the diffusion of ions into pores, cracks and grain boundaries [31]. Some authors attempt to determine the inner and outer charge (q_i^* and q_o^* respectively) by determining q* at a range of sweep rates and then extrapolating to $\nu = 0$ and $\nu = \infty$ [28, 31, 32, 29].

In addition to current due to redox reactions there is also a background capacitive current. Assuming no redox transitions occur at a chosen potential, the measured currents are primarily due to the charging and discharging of the surface double layer [33]. If cyclic voltammograms are performed at a range of sweep rates and in a potential region where no redox transitions take place the double layer capacitance can thus be determined. The gradient of the line of current versus sweep rate gives the differential capacity of the double layer [33, 34, 35] (Figure 2.6). At higher sweep rates the slope may decrease due to the exclusion of surface area in more "difficult to access"

regions [34]. Thus lower sweep rates (less than 100 mV s^{-1}) are recommended for this test. The calculated double layer capacitance is often divided by a reference capacitance for a "flat surface" to obtain a roughness factor [36]. Often a capacitance given by Levine and Smith [37] of 60 μF cm^{-2} is used [38, 39]. However, other values have been used [33, 36, 40] and in order to accurately compare different oxides a reference capacity must be known for the exact oxide being delt with, which is rarely the case [34].

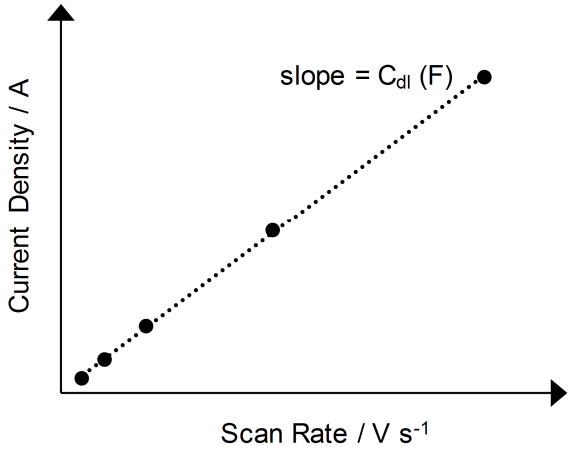

Figure 2.6: Example graph of sweep rate versus current used to find the double layer capacitance, C_{dl}.

2.6.2 Electrochemical Impedance Spectroscopy

Electrochemical impedance spectroscopy is a technique used to analyse electrochemical processes. A small AC signal (frequency typically ranging from 1 mHz to 1 MHz) is imposed over a galvanostatic or potentiostatic signal. The resultant AC component is compared with the original signal and the impedance thus found. Impedance has a magnitude (|Z|) and a phase shift (θ) in degrees and can be plotted on a Bode diagram (Figure 2.7a). Alternatively the magnitude and angle can be converted to a resistance in ohms ("real") and reactance ("imaginary") impedance and plotted on a Nyquist plot (Figure 2.7b).

Impedance results are modelled as an electrical circuit. A pure resistor has no phase shift and the magnitude of the impedance is equal to the resistance. An electrochemical system is more complex than this however, due to the capacitive behaviour of the double layer and surface reactions occurring. The electrical impedance spectroscopy results are modelled using electrical components. One of the most simple impedance models is Randles model [41], shown in Figure 2.8. R_Ω is the ohmic resistance between the working and reference electrode, R_{ct} is the charge transfer resistance at/through the electrode coating, and C is the double layer capacitance.

Many authors modelling the behaviour of oxygen evolution electrocatalysts during oxygen evolution have found that a more complex model is required [20, 42, 43, 44]. The model often includes

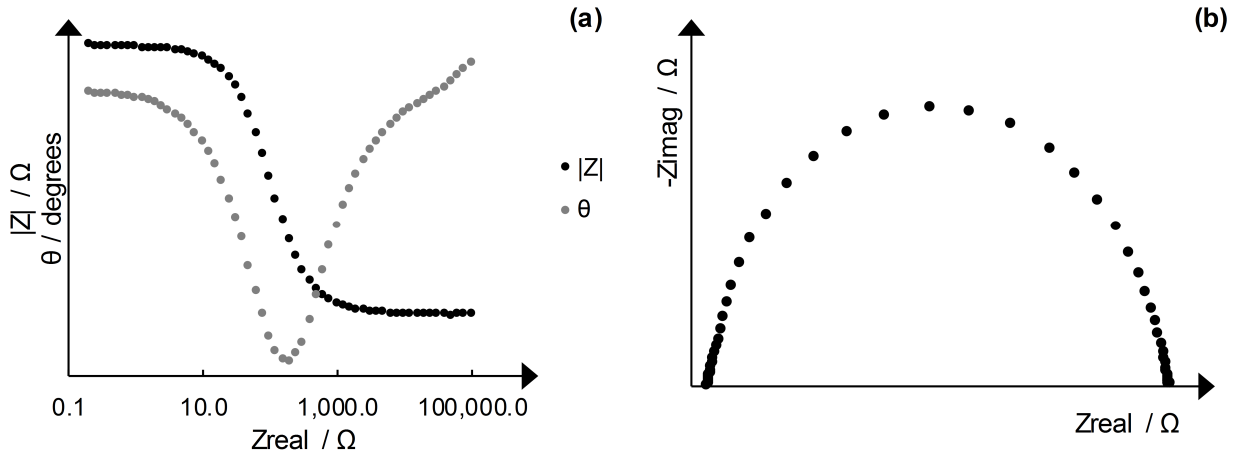

Figure 2.7: Example electrical impedance spectroscopy results represented on a Bode (a) and Nyquist plot (b).

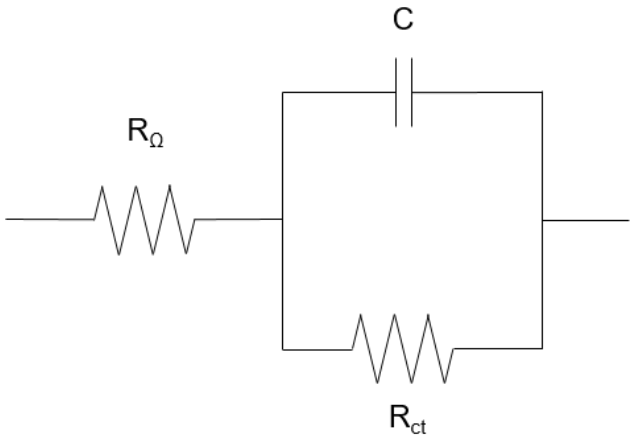

Figure 2.8: Randles model: a simple electrical model for electrochemical systems.

not only the double layer capacitance, but also a capacitance due to the oxide film itself, and additional capacitance related to the oxygen evolution reaction steps [43]. A common theme among many of the models is the capacitive elements are replaced with constant phase elements (CPE) [42, 44, 45]. The impedance for a CPE is calculated:

$$Z = \frac{1}{Y_0(j\omega)^n} \tag{2.6.2}$$

For an ideal capacitor, n is equal to 1 and Y_0 is the capacitance. For CPEs, n is less than 1. CPEs are used in these models because the capacitive-like features in electrochemical systems do not behave as ideal capacitors due to electrode heterogeneities and/or roughness [46].

Chapter 3

Literature Review

3.1 Electrocatalyst Options

3.1.1 Electrocatalyst Performance

A significant amount of work has been carried out on electrocatalysts for the oxygen evolution reaction (OER). This Chapter summarises the performance of a number of the electrocatalysts from literature (Table 3.1). The Tafel slope and the potential at 10 and 100 mA cm^{-2} is summarised in the table, with details of the electrocatalyst preparation method and testing conditions included. Where two Tafel slopes are reported in the table, the first is at low overpotentials, and the second at high overpotentials. Only electrocatalysts tested in alkaline solution have been included in the table.

Different reference electrodes and temperatures are used by different authors, and therefore potential conversions must be made to summarise the data into Table 3.1. The most common reference electrode used in the literature was the saturated calomel electrode (SCE) at 25°C; this reference electrode has therefore been used to report the potentials. The potentials in Table 3.2 were used to convert the potentials, to potentials versus the SCE. Note that for the Hg/HgO (KOH) reference electrodes, it was assumed that the potential was the same as the Hg/HgO (NaOH) electrodes with the same OH^- molality. I.e. it is assumed that the potential difference due to activity differences between NaOH and KOH are not significant.

Table 3.1 shows that many researchers found differing performances for what ostensibly appear to be the same electrocatalysts. Other reviews by Matsumoto and Sato [47] and Trasatti and Lodi [22] also reported large differences in performance for the same electrocatalytic oxide. This makes the intrinsic activity of the electrocatalysts difficult to compare. There are two main causes for the observed differences: the method by which the catalyst is prepared, and the conditions in which the electrocatalyst is tested.

Table 3.1: Electrocatalysts and their activity toward the oxygen evolution reaction. NA indicates that data is not available.

Electrocatalyst	Conditions of testing	Support	Tafel slope (mV)	Potential vs SCE (mV) at 10 mA cm^{-2}	Potential vs SCE (mV) at 100 mA cm^{-2}	Electrocatalyst Preparation Method	Substrate Coating Method	Ref.
Ni	25°C in 1 M NaOH	-	48	590	NA	Polished metal	NA	[48]
Ni	25°C in 1 M NaOH	-	40	590	820	Polished and electrochemically reduced metal	NA	[48]
Ni	25°C in 1 M NaOH	-	40	540	690	Polished and electrochemically oxidised metal	NA	[48]
Ni	25°C in 1 M KOH	-	NA	600	NA	Metal	NA	[49]
Ni	25°C in 5 M KOH	Carbon Steel	39, 114	450	NA	Electrodeposition and annealing	Direct	[50]
Ni (Mesoporous)	80°C in 1 M NaOH	Steel	NA	NA	420	Electrodeposition from solution with Surfactant	Direct	[51]
Ni (Polished)	80°C in 1 M NaOH	-	NA	NA	430	Polished Metal	NA	[51]
$Ni(OH)_2$	80°C in 1 M NaOH	Nickel	NA	NA	370	Electrodeposition	Direct	[51]
Fe	25°C in 1 M NaOH	-	39	360	430	Polished metal	NA	[52]
Fe	25°C in 1 M NaOH	-	39	650	750	Polished and electrochemically reduced metal	NA	[52]
Fe	25°C in 1 M NaOH	-	44	660	760	Polished and electrochemically aged metal	NA	[52]
$Fe(OH)_2$	80°C in 1 M NaOH	Nickel or Steel [unclear]	NA	NA	430	Electrodeposition	Direct	[51]

Table 3.1: Electrocatalysts and their activity toward the oxygen evolution reaction. NA indicates that data is not available.

Electrocatalyst	Conditions of testing	Support	Tafel slope (mV)	Potential vs SCE (mV) at 10 mA cm^{-2}	Potential vs SCE (mV) at 100 mA cm^{-2}	Electrocatalyst Preparation Method	Substrate Coating Method	Ref.
Fe_3O_4	25°C 1 M KOH	Nickel	65-67	NA	640	Precipitation	Slurry coating and annealing	[53]
Stainless Steel (Polished)	80°C in 1 M NaOH	-	NA	NA	430	Polished Metal	NA	[51]
Stainless Steel	1 M KOH	-	NA	500	NA	Metal	NA	[54]
Co	25°C in 1 M NaOH	-	46	570	NA	Polished metal	NA	[20]
Co - aged	25°C in 1 M NaOH	-	61	570	NA	Polished and electrochemically aged metal	NA	[20]
Co - pre-reduced	25°C in 1 M NaOH	-	46	580	690	Polished and electrochemically reduced metal	NA	[20]
Co_3O_4	25°C in 1 M KOH	Nickel	41	550	740	Thermal Decomposition	Electrodeposition	[49]
Co_3O_4	25°C in 3.5 M KOH	Nickel	50, 118	430	NA	Thermal Decomposition	Teflon Bonded	[55]
Co_3O_4	25°C in 3.5 M KOH	Nickel	42, 101	430	NA	Thermal Decomposition	Teflon Bonded	[55]
Co_3O_4	25°C in 30 wt.% KOH	Nickel	50, 153	410	460	Spray Pyrolysis	Direct	[56]
Co_3O_4	25°C in 30 wt.% KOH	Nickel	37, 124	400	440	Spray Pyrolysis	Direct	[56]
Co_3O_4	25°C in 30 wt.% KOH	Nickel	61, 166	420	480	Thermal Decomposition	Direct	[56]
Co_3O_4	Room Temperature in 1 M KOH	Stainless Steel	36	510	1160	Electrodeposition at 50°C	Direct	[57]

Table 3.1: Electrocatalysts and their activity toward the oxygen evolution reaction. NA indicates that data is not available.

Electrocatalyst	Conditions of testing	Support	Tafel slope (mV)	Potential vs SCE (mV) at 10 mA cm^{-2}	Potential vs SCE (mV) at 100 mA cm^{-2}	Electrocatalyst Preparation Method	Substrate Coating Method	Ref.
Co_3O_4	Room Temperature in 1 M KOH	Stainless Steel	49	540	800	Electrodeposition at 130°C	Direct	[57]
$Co(OH)_2$	1 M KOH	Stainless Steel	NA	470	NA	Electrodeposition	Direct	[54]
Co_3O_4	Room Temperature in 1 M KOH	Glass	60	870	NA	Spray Pyrolysis	Direct	[58]
Co_3O_4 nanowire array	25°C in 1 M NaOH	Nickel Foam	74	NA	NA	Nanowire growth method and calcination	Direct	[59]
Co_3O_4	100°C in 10 M KOH	Nickel	60	NA	NA	Thermal Decomposition	Direct	[60]
Co_3O_4	60°C in 15 wt.% NaOH	Nickel	145	760	810	Thermal Decomposition	Direct	[61]
Co_3O_4	60°C in 15 wt.% NaOH	Nickel	189	890	NA	Thermal Decomposition	Teflon Bonded	[61]
IrO_2 (Aged)	25°C in 1 M NaOH	Titanium	40	530	760	Thermal Decomposition	Uncler from paper	[62]
IrO_2	20°C in 1 M NaOH	Titanium	43	NA	NA	Thermal Decomposition	Direct	[63]
RuO_2	20°C in 1 M NaOH	Titanium	42	460	NA	Thermal Decomposition	Direct	[63]
MnO_2	30°C in 1 M KOH	Platinum	110	550	NA	Thermal Decomposition	Uncler from paper	[64]
PbO_2	25°C in 1 M NaOH	Nickel	230	960	NA	Electrolytic deposition	Direct	[65]
Ni + Mo	25°C in 5 M KOH	Carbon Steel	43, 116	370	450	Electrodeposition and annealing	Direct	[50]
Ni + Mo	25°C in 5 M KOH	Carbon Steel	49, 130	350	430	Electrodeposition and annealing and leaching of Si particles out of coating	Direct	[50]

Table 3.1: Electrocatalysts and their activity toward the oxygen evolution reaction. NA indicates that data is not available.

Electrocatalyst	Conditions of testing	Support	Tafel slope (mV)	Potential vs SCE (mV) at 10 mA cm^{-2}	Potential vs SCE (mV) at 100 mA cm^{-2}	Electrocatalyst Preparation Method	Substrate Coating Method	Ref.
Ni-P (4% P)	22°C in 1 M KOH	Carbon Steel	57, 157	610	NA	Electroless Deposition	Direct	[66]
Ni-P (6.9% P)	22°C in 1 M KOH	Carbon Steel	57, 159	610	NA	Electroless Deposition	Direct	[66]
Ni-P (13.8% P)	22°C in 1 M KOH	Carbon Steel	59, 217	670	NA	Electroless Deposition	Direct	[66]
Ni-P (6.9% P) - heat treated	22°C in 1 M KOH	Carbon Steel	50, 130	620	NA	Electroless Deposition	Direct	[66]
Ni-P (13.8% P) - heat treated	22°C in 1 M KOH	Carbon Steel	52, 139	610	NA	Electroless Deposition	Direct	[66]
Ni-P (4% P) - electrochemically treated	22°C in 1 M KOH	Carbon Steel	44, 125	560	NA	Electroless Deposition	Direct	[66]
Ni-P (13.8% P)- electrochemically treated	22°C in 1 M KOH	Carbon Steel	50, 129	570	NA	Electroless Deposition	Direct	[66]
$NiCo_2O_4$	60°C in 15 wt.% NaOH	Nickel	54, 112	410	540	Thermal Decomposition	Direct	[67]
$NiCo_2O_4$	60°C in 15 wt.% NaOH	Nickel	150	490	870	Precipitation and Calcination	Teflon Bonded	[67]
$NiCo_2O_4$	60°C in 15 wt.% NaOH	Nickel	94, 140	360	590	Precipitation and Calcination	Teflon Bonded	[67]
$NiCo_2O_4$	60°C in 15 wt.% NaOH	Nickel	79, 109	NA	NA	Evaporation and Calcination	Teflon Bonded	[67]
$NiCo_2O_4$	60°C in 15 wt.% NaOH	Nickel	134	NA	NA	Freeze Drying and Calcination	Teflon Bonded	[67]
$NiCo_2O_4$ (Core Ring Structure)	25°C in 1 M KOH	Nickel	54	510	620	Precipitation and Calcination	Electrodeposition	[49]

Table 3.1: Electrocatalysts and their activity toward the oxygen evolution reaction. NA indicates that data is not available.

Electrocatalyst	Conditions of testing	Support	Tafel slope (mV)	Potential vs SCE (mV) at 10 mA cm^{-2}	Potential vs SCE (mV) at 100 mA cm^{-2}	Electrocatalyst Preparation Method	Substrate Coating Method	Ref.
$NiCo_2O_4$	25°C in 1 M KOH	Nickel	59	530	650	Thermal Decomposition	Electrodeposition	[49]
$NiCo_2O_4$	80°C in 1 M NaOH	Nickel or Steel [unclear]	NA	NA	380	Thermal Decomposition	Direct	[51]
$Ni/Co(OH)_2$	80°C in 1 M NaOH	Nickel	NA	NA	380	Electrodeposition	Direct	[51]
$Ni_{0.2}Co_{2.8}O_4$	25°C in 3.5 M KOH	Nickel	47, 113	NA	NA	Thermal Decomposition	Teflon Bonded	[55]
$NiCo_2O_4$	25°C in 3.5 M KOH	Nickel	44, 111	470	NA	Thermal Decomposition	Teflon Bonded	[55]
Mixed Co-Ni Oxides (2:1)	25°C in 1 M NaOH	Nickel	35	450	NA	Electrodeposition	Direct	[68]
Mixed Co-Ni Oxides (2:1)	25°C in 1 M NaOH	Iron	42	470	NA	Electrodeposition	Direct	[68]
$NiCo_2O_4$	25°C in 1 M NaOH	Nickel	60	530	NA	Thermal Decomposition	Direct	[68]
$NiCo_2O_4$	25°C in 1 M KOH	Nickel	86	550	710	Precipitation and Annealling	Annealed directly onto substrate	[69]
$NiCo_2O_4$	25°C in 1 M KOH	Nickel	86	540	670	Precipitation and Annealling	Annealed directly onto substrate	[69]
$NiCo_2O_4$	25°C in 1 M KOH	Nickel	86	510	620	Precipitation and Annealling	Annealed directly onto substrate	[69]
$NiCo_2O_4$	25°C in 1 M KOH	Nickel	77	510	640	Precipitation and Annealling	Annealed directly onto substrate	[69]
$NiCo_2O_4$	25°C in 1 M KOH	Nickel	99	570	740	Precipitation and Annealling	Annealed directly onto substrate	[69]
$NiCo_2O_4$	25°C in 1 M KOH	Nickel	NA	NA	610	Precipitation and Annealling	Annealed directly onto substrate	[70]

Table 3.1: Electrocatalysts and their activity toward the oxygen evolution reaction. NA indicates that data is not available.

Electrocatalyst	Conditions of testing	Support	Tafel slope (mV)	Potential vs SCE (mV) at 10 mA cm^{-2}	Potential vs SCE (mV) at 100 mA cm^{-2}	Electrocatalyst Preparation Method	Substrate Coating Method	Ref.
$NiCo_2O_4$	25°C in 1 M KOH	Nickel	NA	500	630	Precipitation and Annealling	Annealed directly onto substrate	[70]
$NiCo_2O_4$	25°C in 1 M KOH	Nickel	NA	600	960	Precipitation and Annealling	Annealed directly onto substrate	[70]
Ni/Co_3O_4 Composite	1 M NaOH	Nickel	75	680	750	Electrolytic deposition with Co_3O_4 particles in solution	Direct	[71]
$Ni_{0.6}Co_{2.4}O_4$ nanowire array	25°C in 1 M NaOH	Nickel Foam	67	NA	NA	Nanowire growth method and calcination	Direct	[59]
$Ni_{1.2}Co_{1.8}O_4$ nanowire array	25°C in 1 M NaOH	Nickel Foam	68	NA	NA	Nanowire growth method and calcination	Direct	[59]
$Ni_{1.5}Co_{1.5}O_4$ nanowire array	25°C in 1 M NaOH	Nickel Foam	66	510	NA	Nanowire growth method and calcination	Direct	[59]
$Ni_{1.8}Co_{1.2}O_4$ nanowire arrat	25°C in 1 M NaOH	Nickel Foam	68	NA	NA	Nanowire growth method and calcination	Direct	[59]
$Ni_{2.4}Co_{0.6}O_4$ nanowire array	25°C in 1 M NaOH	Nickel Foam	65	NA	NA	Nanowire growth method and calcination	Direct	[59]
$NiCo_2O_4$	100°C in 10 M KOH	Nickel	62	NA	NA	Thermal Decomposition	Direct	[60]
Li-Co_3O_4 (3% Li)	Room Temperature in 1 M KOH	Glass	60	830	1110	Spray Pyrolysis	Direct	[58]
Li-Co_3O_4 (7% Li)	Room Temperature in 1 M KOH	Glass	60	810	1070	Spray Pyrolysis	Direct	[58]
Li-Co_3O_4 (10% Li)	Room Temperature in 1 M KOH	Glass	60	780	1040	Spray Pyrolysis	Direct	[58]
Co_3O_4+5%Li	100°C in 10 M KOH	Nickel	58	NA	NA	Thermal Decomposition	Direct	[60]
Li-doped (10at.%) Co_3O_4	60°C in 15 wt.% NaOH	Nickel	84, 117	600	NA	Precipitation of mixed oxalate and calcination	Teflon Bonded	[61]

Table 3.1: Electrocatalysts and their activity toward the oxygen evolution reaction. NA indicates that data is not available.

Electrocatalyst	Conditions of testing	Support	Tafel slope (mV)	Potential vs SCE (mV) at 10 mA cm^{-2}	Potential vs SCE (mV) at 100 mA cm^{-2}	Electrocatalyst Preparation Method	Substrate Coating Method	Ref.
Li-doped (10at.%) Co_3O_4	60°C in 15 wt.% NaOH	Nickel	98, 124	610	690	Precipitation of mixed hydroxide and calcination	Teflon Bonded	[61]
Li-doped (10at.%) Co_3O_4	60°C in 15 wt.% NaOH	Nickel	71, 193	610	NA	Evaporation and thermal decomposition	Teflon Bonded	[61]
Li-doped (10at.%) Co_3O_4	60°C in 15 wt.% NaOH	Nickel	86, 170	740	920	Thermal Decomposition	Direct	[61]
Co_3O_4+5%Fe	100°C in 10 M KOH	Nickel	60	NA	NA	Thermal Decomposition	Direct	[60]
$Ni/Fe(OH)_2$	80°C in 1 M NaOH	Nickel	NA	NA	360	Electrodeposition	Direct	[51]
$NiFe_2O_4$	25°C in 1 M KOH	Nickel	70, 100	560	NA	Precipitation and Calcination	Slurry coating and annealing	[72]
$NiFeVO_4$	25°C in 1 M KOH	Nickel	42, 70	500	560	Precipitation and Calcination	Slurry coating and annealing	[72]
$NiFe_{1.75}V_{0.25}O_4$	25°C in 1 M KOH	Nickel	39, 68	510	580	Precipitation and Calcination	Slurry coating and annealing	[72]
$NiFe_{1.5}V_{0.5}O_4$	25°C in 1 M KOH	Nickel	40, 66	500	560	Precipitation and Calcination	Slurry coating and annealing	[72]
$Fe_{0.25}Co_{0.75}MoO_4$	25°C in 1 M KOH	Nickel	39, 66	460	510	Precipitation and Calcination	Slurry coating and annealing	[73]
$Fe_{0.5}Co_{0.5}MoO_4$	25°C in 1 M KOH	Nickel	42, 76	480	NA	Precipitation and Calcination	Slurry coating and annealing	[73]
$Fe_{0.75}Co_{0.25}MoO_4$	25°C in 1 M KOH	Nickel	40, 83	500	NA	Precipitation and Calcination	Slurry coating and annealing	[73]
$CoFe_2O_4$	Room Temperature in 1 M KOH	Iron	57	680	NA	Ceramic powder method (multiple heat treatment steps at 800/1100°C)	Slurry coating and annealing	[74]

Table 3.1: Electrocatalysts and their activity toward the oxygen evolution reaction. NA indicates that data is not available.

Electrocatalyst	Conditions of testing	Support	Tafel slope (mV)	Potential vs SCE (mV) at 10 mA cm^{-2}	Potential vs SCE (mV) at 100 mA cm^{-2}	Electrocatalyst Preparation Method	Substrate Coating Method	Ref.
$CoFe_2O_4$	Room Temperature 1 M KOH	Iron	57	710	NA	Ceramic powder method: Heat Treatment of oxides at 1100°C	Slurry coating and annealing	[75]
$CoFe_2O_4$	Room Temperature 1 M KOH	Iron	57	710	NA	Ceramic powder method: Heat Treatment of oxides at 1100°C	Slurry coating and annealing	[75]
$CoFe_{1.7}Ni_{0.3}O_4$	Room Temperature 1 M KOH	Iron	63	680	NA	Ceramic powder method: Heat Treatment of oxides at 1100°C	Slurry coating and annealing	[75]
$CoFe_{1.6}Ni_{0.4}O_4$	Room Temperature 1 M KOH	Iron	70	850	NA	Ceramic powder method: Heat Treatment of oxides at 1100°C	Slurry coating and annealing	[75]
$CoFe_{1.7}Ni_{0.3}O_4$	Room Temperature in 1 M KOH	Iron	63	710	NA	Ceramic powder method (multiple heat treatment steps at 800/1100°C)	Slurry coating and annealing	[74]
$CoFe_{1.7}Ni_{0.3}O_4$	Room Temperature 1 M KOH	Iron	63	680	NA	Ceramic powder method: Heat Treatment of oxides at 1100°C	Slurry coating and annealing	[75]
$CoFe_{1.6}Ni_{0.4}O_4$	Room Temperature 1 M KOH	Iron	70	850	NA	Ceramic powder method: Heat Treatment of oxides at 1100°C	Slurry coating and annealing	[75]
$CoFe_{1.6}Mn_{0.4}O_4$	Room Temperature in 1 M KOH	Iron	70	840	NA	Ceramic powder method (multiple heat treatment steps at 800/1100°C)	Slurry coating and annealing	[74]
$Mn_{0.5}Fe_{2.5}O_4$	25°C 1 M KOH	Nickel	61-62	NA	600	Precipitation	Slurry coating and annealing	[53]
$MnFe_2O_4$	25°C 1 M KOH	Nickel	36-42	NA	510	Precipitation	Slurry coating and annealing	[53]

Table 3.1: Electrocatalysts and their activity toward the oxygen evolution reaction. NA indicates that data is not available.

Electrocatalyst	Conditions of testing	Support	Tafel slope (mV)	Potential vs SCE (mV) at 10 mA cm^{-2}	Potential vs SCE (mV) at 100 mA cm^{-2}	Electrocatalyst Preparation Method	Substrate Coating Method	Ref.
$Mn_{1.5}Fe_{1.5}O_4$	25°C 1 M KOH	Nickel	45-47	NA	580	Precipitation	Slurry coating and annealing	[53]
$Ni/Cr(OH)_2$	80°C in 1 M NaOH	Nickel	NA	NA	390	Electrodeposition	Direct	[51]
$Ni/Mn(OH)_2$	80°C in 1 M NaOH	Nickel	NA	NA	400	Electrodeposition	Direct	[51]
$Ni/Cu(OH)_2$	80°C in 1 M NaOH	Nickel	NA	NA	440	Electrodeposition	Direct	[51]
$Li_{0.07}Co_{2.93}O_4$	25°C in 3.5 M KOH	Nickel	34, 65	430	NA	Thermal Decomposition	Teflon Bonded	[55]
$Li_{0.22}Co_{2.78}O_4$	25°C in 3.5 M KOH	Nickel	32, 63	NA	NA	Thermal Decomposition	Teflon Bonded	[55]
$Cu_{0.2}Co_{2.8}O_4$	25°C in 3.5 M KOH	Nickel	46, 149	NA	NA	Thermal Decomposition	Teflon Bonded	[55]
$Cu_{0.5}Co_{2.5}O_4$	25°C in 3.5 M KOH	Nickel	45, 138	NA	NA	Thermal Decomposition	Teflon Bonded	[55]
$Cu_{0.7}Co_{2.3}O_4$	25°C in 3.5 M KOH	Nickel	44, 114	390	NA	Thermal Decomposition	Teflon Bonded	[55]
$Cu_{0.9}Co_{2.1}O_4$	25°C in 3.5 M KOH	Nickel	40, 107	NA	NA	Thermal Decomposition	Teflon Bonded	[55]
$ZnCo_2O_4$	25°C in 1 M KOH	Nickel	70, 130	NA	NA	Electrophoretic deposition (oxide powders in solution) and annealing	Direct	[76]
Pb/Co_3O_4 Composite	1 M NaOH	Nickel	73	640	730	Electrolytic deposition with Co_3O_4 particles in solution	Direct	[71]
$PbO_2 + Co_3O_4$ Composite	25°C in 1 M NaOH	Nickel	105	660	760	Electrolytic deposition with Co_3O_4 particles in solution	Direct	[65]
$PbO_2 + Co_3O_4$ Composite	25°C in 1 M NaOH	Nickel	60	620	680	Electrolytic deposition with Co_3O_4 particles in solution	Direct	[65]

Table 3.1: Electrocatalysts and their activity toward the oxygen evolution reaction. NA indicates that data is not available.

Electrocatalyst	Conditions of testing	Support	Tafel slope (mV)	Potential vs SCE (mV) at 10 mA cm^{-2}	Potential vs SCE (mV) at 100 mA cm^{-2}	Electrocatalyst Preparation Method	Substrate Coating Method	Ref.
PbO_2/Co_3O_4 Composite	1 M NaOH	Nickel	68	560	650	Electrolytic deposition with Co_3O_4 particles in solution	Direct	[71]
PbO_2 + CoO_x Composite	25°C in 1 M NaOH	Nickel	59	620	680	Electrodepostion	Direct	[77]
$Ir_{0.2}Ru_{0.8}O_2$	20°C in 1 M NaOH	Titanium	38	430	NA	Thermal Decomposition	Direct	[63]
$Ir_{0.5}Ru_{0.5}O_2$	20°C in 1 M NaOH	Titanium	37	370	NA	Thermal Decomposition	Direct	[63]
$Ir_{0.8}Ru_{0.2}O_2$	20°C in 1 M NaOH	Titanium	38	420	NA	Thermal Decomposition	Direct	[63]
$La_2NiO_{4+\delta}$	25°C in 1 M KOH	-	77	900	980	Self Combusion and Annealing at temperatures of 100-1430°C	NA	[78]
$LaNiO_3$	100°C in 10 M KOH	Nickel	75	NA	290	Precipitation and Calcination and Pressing into Powder and Heat Treatment	Using an Ag-binder	[60]
$LaNiO_3$	25°C in 1 .2 M KOH	-	41	430	470	Precipitation and Calcination and Pressing into Powder and Heat Treatment	NA	[79]
$LaNiO_3$	100°C in 10 M KOH	Nickel	72, 110	NA	NA	Thermal Decomposition	Direct	[60]
$LaNiO_3$	60°C in 15 wt.% NaOH	Nickel	78, 144	510	670	Thermal Decomposition	Direct	[61]
$LaNiO_3$	25°C in 1 M NaOH	-	43	450	490	Precipitation and heat treatment followed by pressing and sintering	NA	[80]

Table 3.1: Electrocatalysts and their activity toward the oxygen evolution reaction. NA indicates that data is not available.

Electrocatalyst	Conditions of testing	Support	Tafel slope (mV)	Potential vs SCE (mV) at 10 mA cm^{-2}	Potential vs SCE (mV) at 100 mA cm^{-2}	Electrocatalyst Preparation Method	Substrate Coating Method	Ref.
$LaNiO_3$	25°C in 1 M NaOH	-	65, 130	530	660	Heat treatment of binary oxides or carbonates at 1100-1400°C followed by pressing and sintering	NA	[80]
$LaMnO_3$	25°C in 1 M NaOH	-	126	NA	NA	Heat treatment of binary oxides or carbonates at 1100-1400°C followed by pressing and sintering	NA	[80]
$LaCoO_3$	25°C in 1 M NaOH	-	70, 135	650	NA	Heat treatment of binary oxides or carbonates at 1100-1400°C followed by pressing and sintering	NA	[80]
$LaVO_3$	25°C in 1 M NaOH	-	175	NA	NA	Heat treatment of binary oxides or carbonates at 1100-1400°C followed by pressing and sintering	NA	[80]
$SrVO_3$	25°C in 1 M NaOH	-	235	NA	NA	Heat treatment of binary oxides or carbonates at 1100-1400°C followed by pressing and sintering	NA	[80]
$SrCoO_{3-x}$	100°C in 10 M KOH	Nickel	80	NA	270	Thermal Decomposition	Direct	[60]
$La_{0.3}Sr_{0.7}CoO_{3-\delta}$	25°C in 1 M KOH	-	59	590	640	Self Combusion and Annealing at temperatures of 100-1430°C	NA	[78]
$(La_{0.3}Sr_{0.7})_{0.97}CoO_{3-\delta}$	25°C in 1 M KOH	-	58	570	630	Self Combusion and Annealing at temperatures of 100-1430°C	NA	[78]

Table 3.1: Electrocatalysts and their activity toward the oxygen evolution reaction. NA indicates that data is not available.

Electrocatalyst	Conditions of testing	Support	Tafel slope (mV)	Potential vs SCE (mV) at 10 mA cm^{-2}	Potential vs SCE (mV) at 100 mA cm^{-2}	Electrocatalyst Preparation Method	Substrate Coating Method	Ref.
$La_{0.5}Sr_{0.5}CoO_3$	25°C in 30 % KOH	Nickel	55, 88	350	410	Sol Gel Method and Annealing	Slurry coating and annealing	[81]
$La_{0.5}Sr_{0.5}CoO_3$	100°C in 10 M KOH	Nickel	73	NA	NA	Thermal Decomposition	Direct	[60]
$La_{0.5}Sr_{0.5}CoO_{3-\delta}$	25°C in 1 M KOH	-	59	610	670	Self Combusion and Annealing at temperatures of 100-1430°C	NA	[78]
$La_{0.55}Sr_{0.4}CoO_{3-\delta}$	25°C in 1 M KOH	-	57	610	670	Self Combusion and Annealing at temperatures of 100-1430°C	NA	[78]
$La_{0.6}Sr_{0.4}CoO_3$	25°C in 1 M NaOH	-	64, 132	480	620	Heat treatment of binary oxides or carbonates at 1100-1400°C followed by pressing and sintering	NA	[80]
$La_{0.65}Sr_{0.3}CoO_{3-\delta}$	25°C in 1 M KOH	-	57	610	670	Self Combusion and Annealing at temperatures of 100-1430°C	NA	[78]
$La_{0.7}Sr_{0.3}CoO_3$	25°C in 30 % KOH	Nickel	56, 92	340	400	Sol Gel Method and Annealing	Slurry coating and annealing	[81]
$La_{0.7}Sr_{0.3}CoO_{3-\delta}$	25°C in 1 M KOH	-	61	610	670	Self Combusion and Annealing at temperatures of 100-1430°C	NA	[78]
$La_{0.9}Sr_{0.1}CoO_3$	25°C in 1 M NaOH	-	66, 95	590	680	Heat treatment of binary oxides or carbonates at 1100-1400°C followed by pressing and sintering	NA	[80]
$La_{0.7}Sr_{0.3}Co_{0.8}Al_{0.2}O_{3-\delta}$	25°C in 1 M KOH	-	90, 60	570	640	Self Combusion and Annealing at temperatures of 100-1430°C	NA	[78]

Table 3.1: Electrocatalysts and their activity toward the oxygen evolution reaction. NA indicates that data is not available.

Electrocatalyst	Conditions of testing	Support	Tafel slope (mV)	Potential vs SCE (mV) at 10 mA cm^{-2}	Potential vs SCE (mV) at 100 mA cm^{-2}	Electrocatalyst Preparation Method	Substrate Coating Method	Ref.
$La_{0.5}Sr_{0.5}FeO_3$	25°C in 1 M NaOH	-	110	550	660	Heat treatment of binary oxides or carbonates at 1100-1400°C followed by pressing and sintering	NA	[80]
$La_{0.7}Sr_{0.3}FeO_3$	25°C in 1 M NaOH	-	130	660	NA	Heat treatment of binary oxides or carbonates at 1100-1400°C followed by pressing and sintering	NA	[80]
$La_{0.5}Sr_{0.5}MnO_3$	80°C in 1 M KOH	Glassy Carbon	60	NA	NA	Annealing of Oxides at 997°C	Teflon Bonded	[82]
$La_{0.9}Sr_{0.1}MnO_3$	25°C in 1 M NaOH	-	125	NA	NA	Heat treatment of binary oxides or carbonates at 1100-1400°C followed by pressing and sintering	NA	[80]
$La_{0.6}Sr_{0.4}MnO_3$	25°C in 1 M NaOH	-	125	760	NA	Heat treatment of binary oxides or carbonates at 1100-1400°C followed by pressing and sintering	NA	[80]
$La_{0.8}Sr_{0.2}CrO_3$	25°C in 1 M NaOH	-	20	NA	NA	Heat treatment of binary oxides or carbonates at 1100-1400°C followed by pressing and sintering	NA	[80]
$La_{0.5}Ba_{0.5}MnO_3$	80°C in 1 M KOH	Glassy Carbon	34	NA	NA	Annealing of Oxides at 997°C	Teflon Bonded	[82]
$La_{0.5}Ca_{0.5}MnO_3$	80°C in 1 M KOH	Glassy Carbon	30	NA	NA	Annealing of Oxides at 997°C	Teflon Bonded	[82]
$La_{0.997}Ce_{0.003}NiO_3$	100°C in 10 M KOH	Nickel	68	NA	NA	Thermal Decomposition	Direct	[60]

Table 3.1: Electrocatalysts and their activity toward the oxygen evolution reaction. NA indicates that data is not available.

Electrocatalyst	Conditions of testing	Support	Tafel slope (mV)	Potential vs SCE (mV) at 10 mA cm^{-2}	Potential vs SCE (mV) at 100 mA cm^{-2}	Electrocatalyst Preparation Method	Substrate Coating Method	Ref.
$LaNi_{0.2}Co_{0.8}O_3$	100°C in 10 M KOH	Nickel	60	NA	NA	Thermal Decomposition	Direct	[60]
$La_{0.5}Ba_{0.5}CoO_3$	100°C in 10 M KOH	Nickel	75	NA	NA	Thermal Decomposition	Direct	[60]
$La_2Ni_{0.9}Co_{0.1}O_{4+\delta}$	25°C in 1 M KOH	-	80	820	900	Self Combusion and Annealing at temperatures of 100-1430°C	NA	[78]
$La_2Ni_{0.8}Cu_{0.2}O_{4+\delta}$	25°C in 1 M KOH	-	83	890	970	Self Combusion and Annealing at temperatures of 100-1430°C	NA	[78]
$La_{0.9}Ce_{0.1}CoO_3$	25°C in 1 M NaOH	-	62, 130	650	NA	Heat treatment of binary oxides or carbonates at 1100-1400°C followed by pressing and sintering	NA	[80]
$La_{0.9}Th_{0.1}CoO_3$	25°C in 1 M NaOH	-	65, 136	690	NA	Heat treatment of binary oxides or carbonates at 1100-1400°C followed by pressing and sintering	NA	[80]
$La_{0.8}K_{0.2}MnO_3$	25°C in 1 M NaOH	-	125	NA	NA	Heat treatment of binary oxides or carbonates at 1100-1400°C followed by pressing and sintering	NA	[80]
$La_{0.2}Ca_{0.8}MnO_3$	25°C in 1 M NaOH	-	130	720	NA	Heat treatment of binary oxides or carbonates at 1100-1400°C followed by pressing and sintering	NA	[80]

Table 3.1: Electrocatalysts and their activity toward the oxygen evolution reaction. NA indicates that data is not available.

Electrocatalyst	Conditions of testing	Support	Tafel slope (mV)	Potential vs SCE (mV) at 10 mA cm^{-2}	Potential vs SCE (mV) at 100 mA cm^{-2}	Electrocatalyst Preparation Method	Substrate Coating Method	Ref.
$Nd_{0.9}Sr_{0.1}CoO_3$	25°C in 1 M NaOH	-	65, 114	550	670	Heat treatment of binary oxides or carbonates at 1100-1400°C followed by pressing and sintering	NA	[80]
$Gd_{0.9}Sr_{0.1}CoO_3$	25°C in 1 M NaOH	-	70, 140	660	NA	Heat treatment of binary oxides or carbonates at 1100-1400°C followed by pressing and sintering	NA	[80]

Table 3.2: Reference electrode potentials used for conversion of potentials for Table 3.1. Note that m=mol/$kg_{solvent}$ and M=mol/$L_{solution}$.

Electrode	**Temperature**	**Potential (mV)**	**Reference**
NHE	25°C	0	
SCE	25°C	241.5	[25]
SCE	20°C	245.8	[83]
SCE	22°C	244.3	[83]
SCE	60°C	215.4	[83]
Ag/AgCl (Sat KCl)	25°C	197.6	[25]
Hg/HgO (1 M NaOH)	25°C	107.7	[26]
Hg/HgO (1 M NaOH)	80°C	41.6	[26]
Hg/HgO (1 M KOH)	25°C	107.7	[26]
Hg/HgO (1 M KOH)	30°C	102.7	[26]
Hg/HgO (17 wt.%/3.5 M/3.7 m KOH)	25°C	68.5	[26]
H/gHgO (27 wt.%/6.0 M/6.6 m KOH)	25°C	35.2	[26]
Hg/HgO (30 wt.%/6.8 M/7.6 m KOH)	25°C	23.3	[26]
Hg/HgO (41 wt.%/10 M/12.2 m KOH)	30°C	-28.9	[26]

Variation in preparation method cause the electrocatalysts to have different surface areas and sometimes different structures [17, 30, 61, 70, 84] resulting in electrocatalytic performance differences. Often changing the surface finishing on a substrate (e.g., pickling vs sandblasting) causes changes in performance [85]. The Tafel slope is a good property to use for comparison as it is an intensive property [23] and thus, in theory, does not depend on surface area. However, different authors have recorded different values for the Tafel slope too. Additionally it is worth noting, the Tafel slope does not give the absolute activity but instead, the change in activity with current.

In addition to the preparation methods, the conditions in which the electrocatalysts have been tested (e.g. temperature, electrolyte, electrolyte concentration) strongly influence the performance of the electrocatalysts. Some authors have looked at the effect of electrolyte concentration on the electrocatalysts [20, 51, 65, 71] and the performance is clearly seen to improve with increased concentration, which is assumed to be due to the increased conductivity of the electrolyte. Increasing the temperature of the system also improves the electrocatalytic performance [55, 56, 65, 81]. In addition, Lyons et al. [20, 52, 48] has shown that the performance of a catalytic material can change depending on the type of electrochemical pretreatment that has occurred.

In addition to experimental methods, some authors have used theoretical methods in an attempt to determine the electrocatalyst with the best intrinsic activity [21, 86, 87]. These methods are based on the concept that the activity of a certain electrocatalyst depends on the binding energy of the electrocatalysts to the intermediates. This concept was briefly mentioned in Chapter 2. Density functional theory (DFT) calculations allow researchers to accurately determine surface binding energies which can be used as an indicator of activity [21]. This has been used to obtain a volcano curves [21, 86] assuming OER intermediates are HO*, HOO* and O*. Man et al. [21]

found that the there was a constant difference between ΔE_{HOO*} and ΔE_{HO*}, and therefore the energy difference between ΔE_{O*} and ΔE_{HO*} can be used as a key descriptor for the OER activity. Man et al. [21] analysed both perovskites and other oxides separately using this method. For the perovskites, the activity from highest to lowest was listed as: $SrCoO_3$ > $LaNiO_3$ > $SrFeO_3$ > $LaCoO_3$ > $LaFeO_3$ > $LaMnO_3$. For other oxides the order was Co_3O_4 ≈ RuO_2 > PtO_2-rutile phase ≈ RhO_2 > IrO_2 ≈ PtO_2-β-phase($CaCl_2$) ≈ Mn_xO_y ≈ $NiOb_2$ ≈ RuO_2 and IrO_2 anatase phase > PbO_2 >> Ti, Sn, Mo, V Nb, Re oxides. A similar study was also carried out by Rossmeisl [87] focussing only on RuO_2, IrO_2 and TiO_2. The order of activity for these oxides from highest to lowest intrinsic activity was RuO_2 > IrO_2 > TiO_2.

Noble metals such as ruthenium and iridium are commonly used electrocatalysts [1]. They are well known to be good electrocatalysts for the oxygen evolution reaction [22] and have Tafel slopes of 40 - 50 mV in alkaline solutions at room temperature [1, 22, 63, 88]. Anodes based on RuO_2 and IrO_2 are said to have the lowest overpotential at practical current densities [7, 63]. While ruthenium oxide is known to have slightly better activity then iridium oxide (Table 3.1), the ruthenium oxide electrocatalysts are not stable when used in alkaline solutions [22]. There are also some concerns over the stability of IrO_2 in alkaline solutions, but dissolution mainly occurs for electrochemically grown IrO_x, rather than thermally prepared IrO_2 [22]. A drawback of these electrocatalysts is that both ruthenium and iridium are precious metals and are therefore very expensive.

There has been a significant amount of interest in the spinel-type oxides, Co_3O_4 and $NiCo_2O_4$, as seen in Table 3.1. While these catalysts do not have Tafel slopes as low as those of RuO_2 and IrO_2, most of the reported Tafel slopes are in the comparatively low range of 41 - 60 mV. Koza et al. [57] have reported a Tafel slope as low as 36 mV for Co_3O_4. In addition, the overpotentials at 10 mA cm^{-2} are found to be comparatively low. All but four of the potential values of these electrocatalysts (in Table 3.1) are below 600 mV vs SCE, with most being below 500 mV vs SCE. It is also noted that the theoretical study by Man et al. [21] showed Co_3O_4 to have one of the highest intrinsic activities.

In addition to spinel structures, there has been significant interest in catalysts having a perovskite structure [82, 80, 81, 89, 60]. Examples include $LaNiO_3$, $La_xSr_{1-x}CoO_3$ and $La_xK_{1-x}MnO_3$. Of the perovskites summarised in Table 3.1, $LaNiO_3$ and $La_xSr_{1-x}CoO_3$ had the lowest potentials at 10 mA cm^{-2} on average, and $La_xSr_{1-x}CoO_3$ had the lowest average Tafel slope of these two electrocatalysts (60 mV).

In some cases the addition of iron to an electrocatalyst has been shown to improve the activity of an oxygen evolution electrocatalyst [90, 73, 51]. There are a number of iron containing mixed oxides that have been tested for their activity toward the oxygen evolution reaction including $NiFe_2O_4$ [72], $CoFe_{1.6}Mn_{0.4}O_4$ [74], $Fe_{0.25}Co_{0.75}MoO_4$ [74], $CoFe_{1.7}Ni_{0.3}O_4$ [74] and $CoFe_2O_4$ [47, 74]. Of these, $CoFe_2O_4$ has been shown to have a comparatively low Tafel slope of 57 mV.

Another observation from Table 3.1 is that the performance of nickel metal without any coating is not significantly worse that the performance of the electrodes with a catalytic coating. The average Tafel slope at low potentials is 42 mV, which is lower than that for a number of other ma-

terials. Additionally, the average potential at 10 mA cm^{-2} is 545 mV, which is also not significantly different from other electrocatalysts. This indicates that a high surface area nickel oxide or metal may be a good oxygen evolution electrocatalyst.

3.1.2 Stability

The stability of an electrocatalytic material is a key factor in addition to its intrinsic activity and surface area. An electrocatalyst may have a low overpotential when prepared, but over time this potential may increase. There is significantly less work done on investigating the stability of the electrocatalysts compared to the amount of work investigating the initial performance. This is likely due to the time-consuming nature of stability tests.

Some authors however, have investigated the stability of their electrocatalysts [64, 56, 70, 51, 59, 57, 91, 92]. These tests are typically performed for 20-100 h [64, 71, 78, 81, 56] but are sometimes run for a more longer length of time of 10 - 12 days [89, 51, 93]. The tests over a longer time period show no significantly change in the potential/current after the first 100-150 h (or 4-6 days) [89, 51, 93].

Nickel metal is the substrate for most of the electrocatalysts in Table 3.1, and is also used as a substrate in this thesis work. It is therefore important to note that nickel metal without a coating has been shown to be unstable toward the OER [94, 95, 48]. Lu and Srinivasan [94] have found that the OER reaction rate decreases from 68 mA cm^{-2} to 8 mA cm^{-2} over 20 h at 1.8 V versus RHE. This loss in activity is attributed to a structural change occurring during oxygen evolution [94, 95]. This is not a desired effect, and by depositing another electrocatalyst on top of this nickel substrate, it is possible to improve the stability in addition to the activity.

Authors have reported a number of results for stable electrocatalyts (often on Nickel substrates). Chi et al. [70] performed 8 day stability tests on $NiCo_2O_4$ electrocatalysts (nickel substrate) produced by thermal decomposition and electrophoretic deposition. After holding the electrodes at 0.7 V for 8 days, the voltage at 100 mA cm^{-2} changed by no more than 10 mV, indicating good stability. Bockris and Otogawa [91] found that their $La_{0.9}Sr_{0.1}CoO_3$ electrocatalysts prepared by a precipitation and high temperature annealing method had a potential decrease of 90 mV over 40 h at 25 mA cm^{-2}. Koza et al. [57] found that the potential of Co_3O_4 prepared by electrodeposition varied by 25 mV or 130 mV at 100 mA cm^{-2} depending on the preparation temperature (50°C and 103°C respectively). Unfortunately the most stable electrocatalyst had the lowest performance. Changes in the preparation method have been shown to have an effect on stability of the catalysts in other work [67, 70]. While the stability data referred to in this review give some insights into which oxides may be stable, there is not enough data collected at the same potential or current density to confidently compare the stability of different electrocatalyst types.

3.2 Preparation Methods

There are a number of preparation procedures used by different authors to produce electrocatalysts. These methods can be roughly split into two categories. The first category is where the electrocatalyst is first prepared as a powder and then attached to the electrode surface [67, 49, 55, 81, 72, 74]. The second category is where the oxide is prepared directly on the substrate [51, 68, 71, 56, 63]. Typical direct coating methods include electrodeposition methods [51, 68, 57, 71, 96], thermal decomposition [60, 63], spray pyrolysis [56] and nanostructure growth [59].

For the first category of preparation methods, common powder production techniques are: precipitation followed by calcination [67, 72, 73], thermal decomposition [55, 61, 51] and a sol gel method followed by calcination [81]. After preparation of the powders, most authors used either Teflon bonding, or a slurry coating plus annealing method to attach the powders to the substrate. Three common catalyst/Teflon ratios are: 3:1, 3:2, and 6:1 [67, 61, 82]. This Teflon bonding method involves creating a dispersion of the oxide powder and Teflon in water, brushing onto the substrate, drying and then heat treatment [61]. The slurry coating method typically involves making a slurry with the oxide powder and a fluid, coating the substrate, drying, and then heat treatment [73].

In addition to the techniques already mentioned, a number of authors have recently tried "growing" nanostructured electrocatalysts onto substrates to help improve surface area [59, 97]. Qing et al. [97] grew Co_3O_4 in a nanoflower structure onto nickel foam. This was done by placing nickel foam into a solution of cobalt nitrate with the addition of hexadecyl trimethyl ammonium bromide (CTAB), and heating it to temperatures of 150 - 180°C for 24 h followed by a calcination step. Lu et al. [59] grew nanowire structures of $Ni_xCo_{3-x}O_4$ onto nickel foam using a similar method. The nickel substrate was placed in a water/ammonia solution of $Ni(NO_3)_2$, $Co(NO_3)_2$ and NH_4NO_3 and heated to 90°C for 12 h, again with a calcining step at the end.

Two of the more common, simple and direct deposition procedures are thermal decomposition and electrodeposition which are discussed further.

3.2.1 Direct Thermal Decomposition

Direct thermal decomposition is a common method of producing electrocatalysts [56, 55, 63] and has been found to produce electrodes with comparatively good performance [61, 67]. This method has also been found to produce stable electrocatalysts [64, 61]. For direct thermal decomposition, the electrode is coated in a precursor solution and the solvent is allowed to evaporate. Elevated temperatures are then used to decompose the precursor into the catalytic oxide. A number of coating steps are often performed. For example, Laouini et al. [39] prepared their Fe-Co_3O_4 electrocatalyst using thermal decomposition. They used a precursor solution of mixed metal nitrates, and spread it onto the 60°C electrode surface at using a syringe. In between each drop the solvent was allowed to evaporate. The coatings were then annealed at 400°C and the oxide was formed.

As the surface area has a noticeable effect on the catalytic performance, many researchers have investigated ways of increasing surface area to improve performance. Burke et al. [92] deposited

RuO_2 catalysts using a thermal decomposition method and found that as the temperature for thermal decomposition increased, the surface area decreased. This is a typical annealing effect which has also been observed by other authors [36, 30, 98, 69]. This decrease in surface area leads to a corresponding decrease in performance. Carapuca et al. [30] also found that using a more concentrated solution for thermal decomposition produced a higher surface area $NiCo_2O_4$ catalyst. It should be noted that for this study the solution was coated on the substrate by dipping the substrate into precursor solution.

3.2.2 Electrodeposition

Electrodeposition is a common method for preparation of electrocatalysts. In this work, electrodeposition is defined loosely, and involves any process where current is passed through a solution to deposit a coating onto a metal substrate. Cathodic deposition to produce hydroxide coatings is a commonly used method [51, 99]. A number of researchers have used electrodeposition to prepare OER electrocatalysts [100, 44, 96, 101, 57] and electrodeposition is one technique known to produce high surface area materials [102]. Cobalt oxide is an electrocatalyst which is often produced by electrodeposition.

As with all preparation methods, the conditions in which the electrodeposition is carried out can affect the coatings produced. Brownson and Levy-Clement [99, 103] found that when the temperature for electrodeposition was altered (60°C to 95°C), the structure of the deposited $Co(OH)_2$ that was deposited changed. Qui et al. [104] found the potential used during electrodeposition affected the wettability of the coating. They prepared nano-structured cobalt oxide from electrodeposition and found that when prepared at lower potentials a flower-like structure was formed. This structure had a more hydrophobic behaviour than the structure formed at higher potentials. Hydrophilic behaviour is preferred during the OER as this causes a reduction in electrode bubble coverage, increasing the surface area available for reaction.

3.2.3 Electrocatalyst Preparation Method Comparison Studies

Some work has been performed comparing different preparation procedures for the same electrocatalytic oxide [67, 70, 68].

A study performed by Chi et al. [70] compared three preparation procedures for $NiCo_2O_4$ coatings: (1) electrophoretic deposition of oxide powders, (2) a precipitation, thermal decomposition and slurry coating method and (3) an alloy oxidation method. The alloy oxidation method involved cyclic voltammetry electrodeposition followed by oxidation. It was found that both the electrophoretic and thermal decomposition methods produced catalysts with high activity and good stability. The thermal decomposition method produced the electrocatalyst with the highest activity, while the electrophoretic method produced the most stable electrocatalyst.

Castro et al. [68] compared cathodic electrodeposition with direct thermal decomposition for the preparation of Co-Ni oxides. The electrodes prepared by electrodeposition showed better per-

formance despite its lower surface area, indicating a higher intrinsic activity.

Bocca et al. [67] compared five different procedures to produce $NiCo_2O_4$ electrocatalysts. They found that the methods which produced the most active and stable electrocatalysts were coprecipitation of a mixed oxalate or mixed hydroxide followed by Teflon-bonding to the substrate and the thermal decomposition method. The coprecipitation methods had a higher activity at the measured currents but the thermal decomposition method had the lowest Tafel slope indicating higher intrinsic activity.

3.3 Conclusions

Based on this literature review the following electrocatalysts were chosen for further investigation: $La_xSr_{1-x}CoO_3$, $CoFe_2O_4$, Co_3O_4, $NiCo_2O_4$, IrO_2 and NiO_x. This review shows that the surface area is a key factor influencing the performance of an electrocatalyst and must be measured in order to separate its effect from the intrinsic activity of the oxide. In order to accurately compare the performance of electrocatalysts it is important to ensure that the testing conditions are the same.

Chapter 4

Electrocatalyst Screening

Abstract

Through a literature review, six oxides were identified as promising electrocatalysts for the oxygen evolution reaction (OER): $La_xSr_{1-x}CoO_3$, $CoFe_2O_4$, Co_3O_4, $NiCo_2O_4$, IrO_2 and NiO_x. Due to differing preparation procedures and testing conditions, it can be difficult to compare performance results in literature. This study enabled the comparison of these catalysts by utilizing a standard preparation procedure (thermal decomposition) and an identical testing procedure. The electrocatalyst with the lowest overpotential, and therefore best performance, was IrO_2 by a significant amount (potential at least 47 mV lower at 50 mA cm^{-2}). It is, however, a costly electrocatalyst. Therefore, other electrocatalysts must also be considered. Co_3O_4 had the second best performance at current densities above 20 mA cm^{-2} while only having a mid-range surface area when compared to the other electrocatalysts. This indicates a high intrinsic activity. The comparative surface area was estimated for the six electrocatalysts and the order from lowest to highest surface area was: $CoFe_2O_4 < La_{0.7}Sr_{0.3}CoO_3 < Co_3O_4 < NiCo_2O_4 < NiO_x$. The position of IrO_2 was inconclusive. Over an 18 h period the performance of all six electrocatalysts were relatively stable ($\pm$ 3 - 8 mV) with the exception of $La_xSr_{1-x}CoO_3$ and $CoFe_2O_4$ which both showed a performance improvement with time.

4.1 Introduction

In Chapter 3, six oxides were identified as promising electrocatalysts: $La_xSr_{1-x}CoO_3$, $CoFe_2O_4$, Co_3O_4, $NiCo_2O_4$, IrO_2 and NiO_x. Each had been shown to have high activity toward the OER [105, 81, 89, 47, 74, 55, 49, 69, 62, 63, 51]. IrO_2 is well-known to have a low Tafel slope [22, 63], but as iridium is a precious metal, this catalyst is costly to produce. Electrocatalysts with a spinel structure such as $CoFe_2O_4$, Co_3O_4, $NiCo_2O_4$ have also been studied by many authors (Chapter 3) and are considered very promising for the OER [106]. The performance of perovskite stuctures such as have $La_xSr_{1-x}CoO_3$ have been shown to be excellent with the composition $La_{0.7}Sr_{0.3}CoO_3$

found to have the highest activity of all the strontium-doped $LaCoO_3$ electrocatalysts [81].

Comparing the performance of a range of electrocatalysts from literature can be difficult due to different preparation procedures and conditions used for testing, as mentioned in Chapter 3. In this chapter electrocatalysts will be compared using the same testing procedures (electrolyte, electrochemical cell and testing sequence) and the same technique for electrocatalyst preparation. This is intended to enable better comparison between the six electrocatalysts.

Thermal decomposition is chosen to prepare these electrodes as it is a simple method which can be used to prepare each of these oxides [62, 63, 107, 56, 38, 108, 109, 110]. When compared to other methods used to produce spinel materials, thermal decomposition has been found to produce relatively stable and active electrocatalysts [67, 70]

4.2 Experimental

Nickel foil substrates (1 cm^2, Sigma-Aldrich 99.9%, 0.125 mm thick) were cleaned in acetone for 5 min, ultrasonicated in water, etched and then rinsed in deionised water. Etching was carried out in a 1 M HCl solution with 5.25 g L^1 of hydrogen peroxide for 15 min. Contact with the nickel foil was achieved by spot welding a nickel wire of 0.5 mm diameter to one corner of the foil.

The coatings were produced by thermal decomposition following the normal dimensionally stabilised anode (DSA) approach. The etched nickel anodes were placed onto a hot plate at 85°C and sprayed with a precursor solution (Table 4.1), before being transferred to furnace (static air atmosphere) and being preheated to temperature 1 (Table 4.1) for 10 min. This was repeated four to five times until the electrode was coated with 2 - 2.5 mg cm^{-2} of oxide. The final annealing took 3.5 h and was performed at temperature 2 (Table 4.1). Annealing temperatures were chosen to obtain the desired oxide [62, 107, 56, 38, 108, 110, 109]. Two of each electrode were prepared to check for reproducibility. Once annealed, the back of each electrode and the wire was coated with epoxy resin to give an active geometric surface area of 1 cm^2.

Table 4.1: Electrocatalyst preparation precursor solutions and temperatures.

Electrocatalyst	Precursors	Temperature 1 (^{0}C)	Temperature 2 (^{0}C)
IrO_2	$IrCl_3$	450	400
$CoFe_2O_4$	$Co(NO_3)_2$ and $FeCl_3$ (1:2)	450	400
Co_3O_4	$Co(NO_3)_2$	350	300
$NiCo_2O_4$	$Ni(NO_3)_2$ and $Co(NO_3)_2$ (1:2)	350	300
NiO_x	$Ni(NO_3)_2$	400	350
$La_{0.7}Sr_{0.3}CoO_3$	$La(NO_3)_2$, $SrCl_2$ and $Co(NO_3)_2$ (7:3:10)	700	700

Electrochemical measurements were carried out in a 30 wt.% KOH solution (pellet basis, $\geq$ 85 % purity) at room temperature using a Gamry Instruments Reference 3000 potentiostat. The

Teflon electrochemical cell used for testing had a Hg/HgO (30 wt.% KOH) reference electrode, a nickel foam counter electrode and membrane material separating the three compartments (anode, reference electrode, and cathode compartment). The sequence of tests used on the coated anodes was thus:

1. Open circuit potential for 60 s
2. Galvanostatic testing for 5 min at 1, 2, 5, 10 and 20 mA cm^{-2} (IR corrected after testing)
3. Galvanostatic testing for 18 h at 50 mA cm^{-2} (IR corrected after testing)
4. Open circuit potential for 60 s
5. Three cycles of cyclic voltammetry between -0.15 V to 0.63 V at 5, 10, 20, 50 and 100 mV s^{-1}using the current interrupt method for IR compensation
6. Electrochemical impedance spectroscopy at 0 V (5 mV_{rms}) from 0.2 Hz to 100 kHz
7. Linear sweep voltammetry from 0.5 - 0.8 V at 0.2 mV s^{-1} (IR corrected after testing)
8. Electrochemical impedance spectroscopy (5 mV rms) from 0.2 Hz to 100 kHz at 2, 5, 10, 20, 50 and 100 mA cm^{-2}

Unless otherwise stated, all potentials are referenced to the Hg/HgO reference electrode.

In addition to electrochemical measurements, the electrocatalyst morphology was investigated using scanning electron microscopy (SEM), using a JEOL 7000F FE-SEM.

4.3 Results and Discussion

4.3.1 Electrocatalyst Activity

An analysis of the catalytic performance was carried out by observing the slow linear scanning voltmmetry results. These were assumed to give steady state polarisation curves for the electrodes. Potential and current readings were collected from the polarisation curves, as well as Tafel slopes (Table 4.2). Based on the potential at 10 mA cm^{-2}, and the Tafel slopes, IrO_2, Co_3O_4, $CoFe_2O_4$ and $NiCo_2O_4$ are the most promising electrocatalysts. IrO_2 is the most promising of that group, having the lowest potentials within the entire current density range and the lowest Tafel slope. The high cost of the precious metal must be considered however. It is also observed that the performance of $CoFe_2O_4$ (#1) is very promising at low currents. When increasing current density above 10 mA cm^{-2} however, the overpotential increases steeply (Figure 4.1). The duplicate did not produce the same results, indicating difficulty in consistent electrocatalyst manufacture. Co_3O_4 has the lowest potential above 10 mA cm^{-2}, apart from the already mentioned expensive IrO_2.

Table 4.2: Key data from slow linear scanning voltammetry.

Electrocatalysts	Tafel Slope (mV)	Potential (mV) at 10 mA cm^{-2}	Potential (mV) at 50 mA cm^{-2}	Current Density (mA cm^{-2}) at 650 mV
IrO_2	42	596	635	82
Co_3O_4	58	642	683	14
$NiCo_2O_4$	53	658	699	7
$CoFe_2O_4$	42	645	729	12
NiO_x	62	673	730	4
$La_xSr_{1-x}CoO_3$	75	756	>766	3

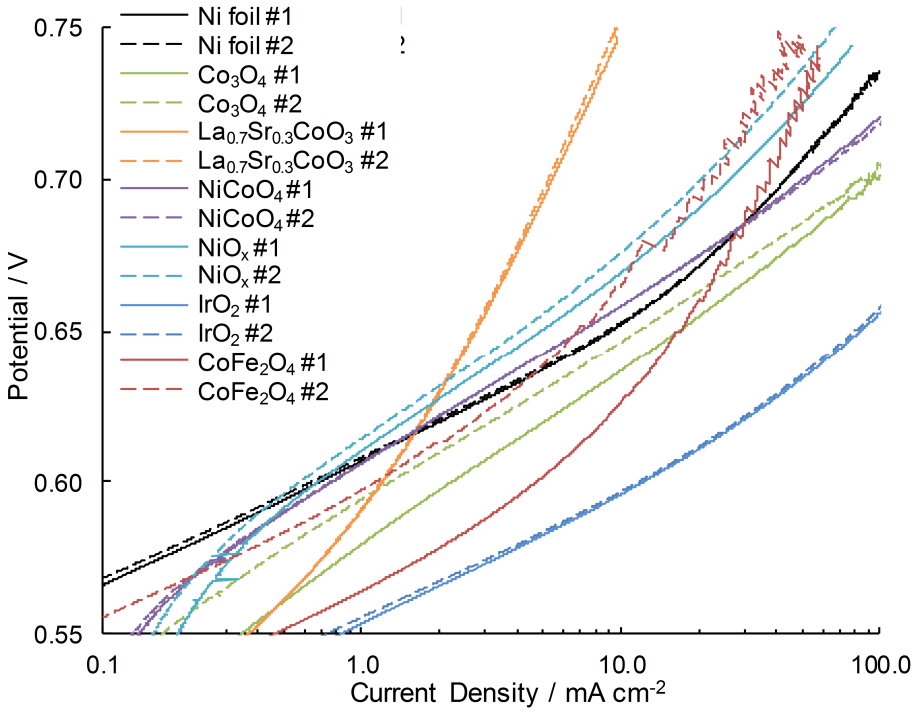

Figure 4.1: Linear Scanning Voltammetry at 0.2 mV s^{-1} for etched nickel foil and the prepared electrocatalysts.

4.3.2 Cyclic Voltammograms

The six electrocatalysts produced were further analysed through observation of the cyclic voltammograms. For comparison purposes, the nickel cyclic voltammogram will be discussed first (Figure 4.2). Peaks are observed at 410 mV in the anodic direction (E_{pa} = 410 mV) and 320 mV in the cathodic direction (E_{pc} = 320 mV) giving an average potential (E_p)[1] of 365 mV. These peaks represent the oxidation/reduction reaction between $Ni(OH)_2$ and NiOOH (Ni(II) to Ni(III)) [48]. Note that nickel cyclic voltammograms will be discussed further in Chapter 5, which will also include a discussion on different forms of NiOOH and $Ni(OH)_2$ (e.g., α and β). Shoulders such as that seen at 370 mV will also be discussed. The nickel cyclic voltammogram is shown for reference in the other six cyclic voltammograms (Figure 4.3).

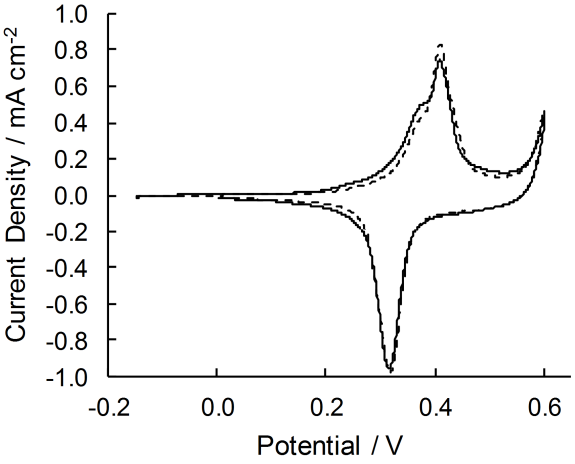

Figure 4.2: Cyclic voltammogram at 20 mV s^{-1} on duplicate etched nickel foil electrodes.

The first electrocatalyst cyclic voltammogram to be discussed is the Co_3O_4 spinel (Figure 4.3(a)). The peaks at 400 mV (E_{pa}) and 320 mV (E_{pc}) are attributed to the Ni(II)/Ni(III) reaction, and are in approximately the same location as the substrate nickel peaks. This indicates that the electrocatalyst is porous, allowing the solution to access the underlying substrate. The peaks at 480 mV (E_{pa}) and 460 mV (E_{pc}) give an E_p of 470 mV, and are attributed to the cobalt Co(III)/Co(IV) reaction [44, 36, 100, 14] for which the surface reaction is $CoOOH/CoO_2$. In addition to the Ni(II)/Ni(III) and Co(III)/Co(IV) peaks, there is also a cathodic peak at -30 mV for which there is no anodic peak. By referring to the Pourbaix diagram [14] it appears that at this potential and high pH, dissolution of Co(III) into $HCoO^{2-}$ is likely to occur. This explains the lack of an anodic peak if the cobalt was lost to solution. The open circuit potential is above this value so there is no concern about dissolution unless the potential is forcibly decreased, as has been done in this cyclic voltammogram. It is also noted that upon increasing the cyclic voltammetry scan rate from 5 mV s^{-1} to 20 mV s^{-1}, there is little to no change in the peak locations for this electrocatalyst.

[1]The average potential (E_p) is defined as the potential halfway between E_{pa} and E_{pc}

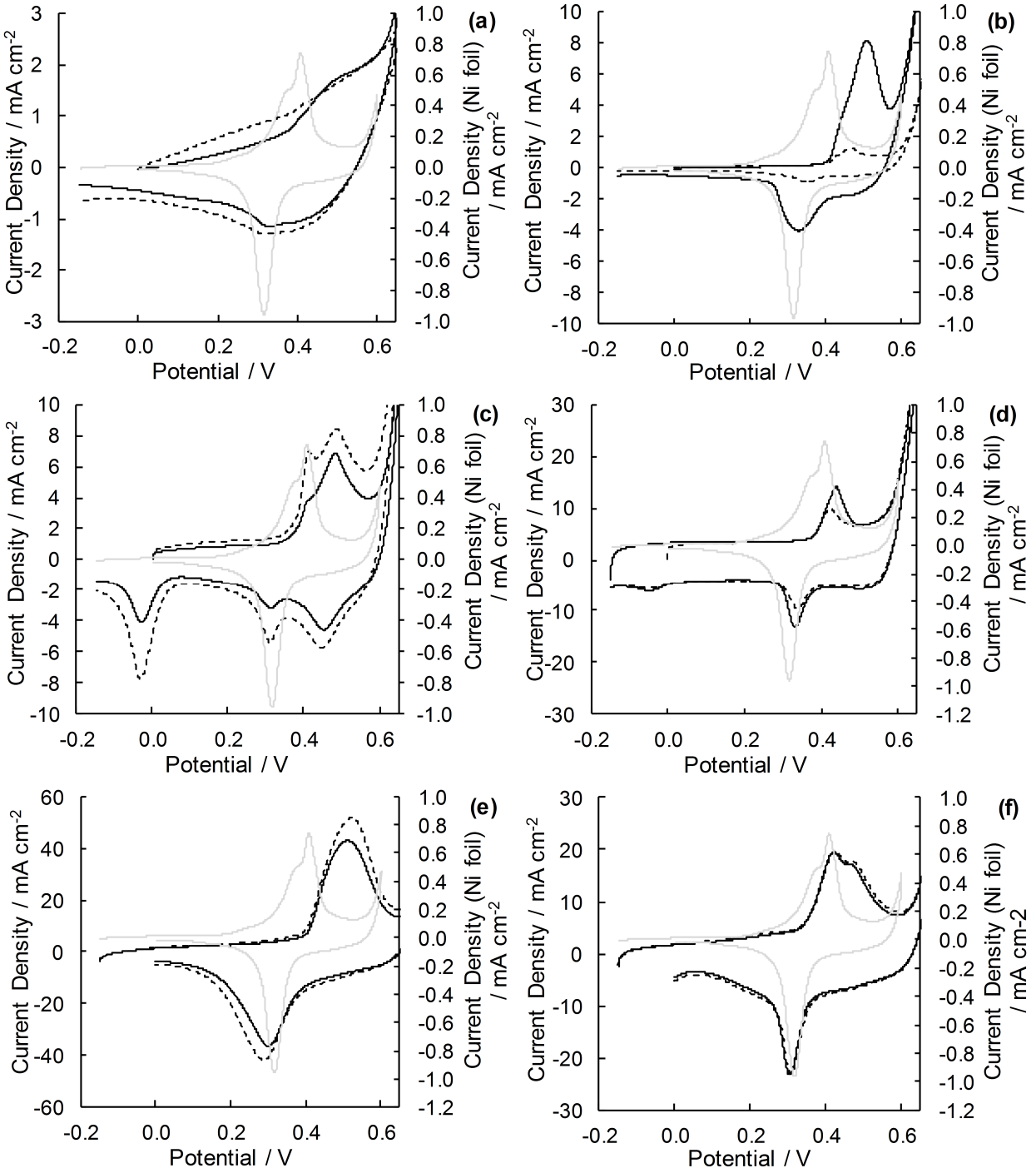

Figure 4.3: Cyclic voltammograms on duplicate electrodes at 20 mV s^1 (3rd cycle) for the Co_3O_4 (a), NiOX (b), $La_{0.7}Sr_{0.3}CoO_3$ (c), $NiCo_2O_4$ (d), IrO_2 (e), and $CoFe_2O_4$ (f) coatings. Note the different scales on the six graphs. The nickel foil cyclic voltammogram is shown in grey to on each graph in grey to show the locations of the nickel oxide peaks.

The cyclic voltammogram for the nickel oxide deposited by thermal decomposition is also investigated (Figure 4.3(b)). Anodic and cathodic peaks are observed at E_{pa} = 510 mV and E_{pc} = 300 mV respectively, giving an E_p of 405 mV. It is noted that there is a shift in peak location with change in cyclic voltammetry scan rate (Figure 4.4), but E_p remains at 405 mV. The peaks are attributed to the Ni(II)/Ni(III) reaction [111, 112, 113, 114]. E_p is slightly higher than that for the etched nickel but as will be discussed later in Chapter 5, there are multiple $Ni(OH)_2$ and NiOOH phases for which the E_p values differ.

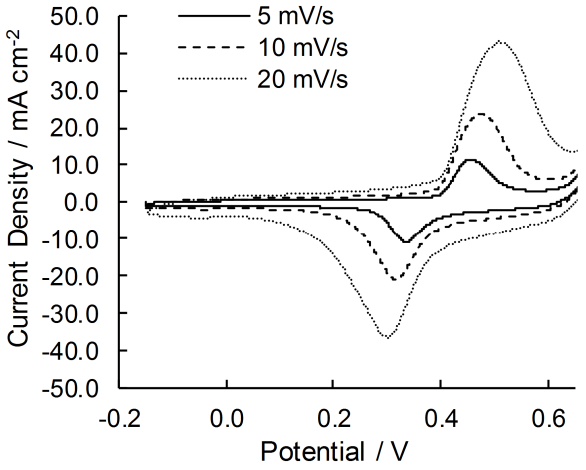

Figure 4.4: Cyclic voltammograms for NiO_x at different scan rates.

The $La_{0.7}Sr_{0.3}CoO_3$ electrocatalyst cyclic voltammogram is now discussed (Figure 4.3(c)). Both Singh et al. [81] and Tiwari et al. [105] have produced $La_xSr_{1-x}CoO_3$ electrodes on a nickel substrate, and both observed one peak in the anodic direction and one in the cathodic direction. Singh et al. [81] observed peaks at approximately 500 mV (E_{pa}) and 310 mV (E_{pc}) vs Hg/HgO (1 M KOH). Tiwari observed peaks at 390 - 420 mV (E_{pa}) and 120 - 240 mV (E_{pc}) vs Hg/HgO (1 M KOH) depending on the preparation procedure and amount of strontium. Both authors attributed the peaks to nickel oxidation and reduction reactions. Typically, strontium doped $LaSrCoO_3$ electrocatalysts on other substrates do not have any peaks in the region investigated here [105], supporting the theory that the peaks seen in the $La_xSr_{1-x}CoO_3$/nickel cyclic voltammograms are related to the nickel oxidation/reduction reaction on the substrate. In this work, the cyclic voltammograms are relatively featureless, although there are some slight shoulders likely attributed to the nickel substrate, but it is difficult to discern their exact potential.

The cyclic voltammogram for the $NiCo_2O_4$ spinel is more complex, having multiple peaks (Figure 4.3(d)). The potential of these peaks changes with voltammetry scan rate (Figure 4.5). At lower scan rates there appears to be only one peak in the anodic direction, i.e., the peaks merge at lower scan rates. Based on the location of these peaks, they are likely related to the Ni(II)/Ni(III) transition. Nkeng et al. [115] came to a similar conclusion for their $NiCo_2O_4$ cyclic voltammograms. It is also possible however, that one of the peaks is related to the oxidation of cobalt, and the potential of this reaction has been influenced by the presence of Ni in the structure.

The small anodic peak at -30 mV is most likely related to the dissolution of Co(III) as seen for the Co_3O_4 electrocatalyst, but again, the open circuit potential is above this potential, and thus is unlikely to cause stability issues.

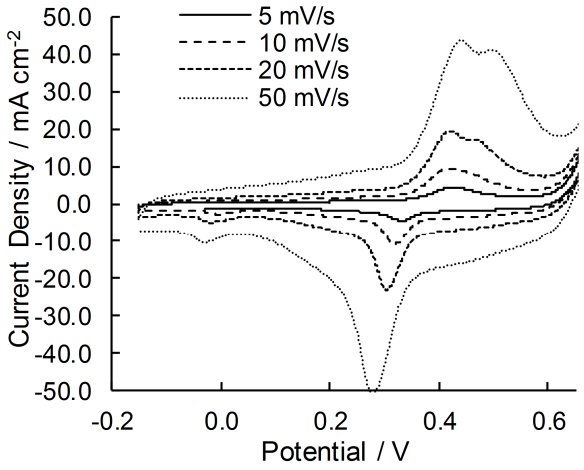

Figure 4.5: Cyclic voltammograms for $NiCo_2O_4$ at different scan rates.

IrO_2 cyclic voltammograms are often broad and featureless [116, 117]. In addition to the broad background current for the IrO_2 voltammogram in this work (Figure 4.3(e)), there are peaks at 420 mV (E_{pa}) and 340 mV (E_{pc}), giving an average potential of 380 mV. There was no significant shift in peak location with cyclic voltammetry scan rate between 5 - 20 mV s^{-1}. These peaks are suggested to be related to the Ni(II)/Ni(III) transition as they are in approximately the right location. The presence of nickel makes sense if the electrocatalyst coating is incomplete/porous, as the electrolyte will reach the substrate.

Finally, the cyclic voltammogram for $CoFe_2O_4$ is observed (Figure 4.3(f) and Figure 4.6). A shoulder at 420 mV in the anodic direction is seen (more visible on electrode number #1 than number 2), in addition to a peak at 460 mV in the anodic direction, and a peak at 350 mV in the cathodic direction. These potentials are based on the 5 mV s^{-1} scan rate. These peaks shift with increasing voltammetry scan rate. The shoulder at 430 mV is likely due to the underlying nickel layer, as it is in a similar position to that seen on the etched nickel. If it is assumed that the peaks at 460 mV and 350 mV come from the same reaction, this gives an E_p of 405 mV. This is not the typical potential for cobalt reactions, and peaks related to a Fe reaction are not typically seen in this potential region [118]. It is suggested that these peaks are due to a cobalt reaction, and the potential is being influenced by the presence of Fe. The large difference in peak height between the two $CoFe_2O_4$ electrodes cannot be easily explained, as both had 2 to 2.5 mg of oxide coating deposited (2.4 mg for #1 and 2.1 mg for #2) and both were heated in the same furnace for the same length of time. It is noted however, that the electrocatalysts with the larger peaks (#1) had a better activity toward the OER (Figure 4.1) as is expected.

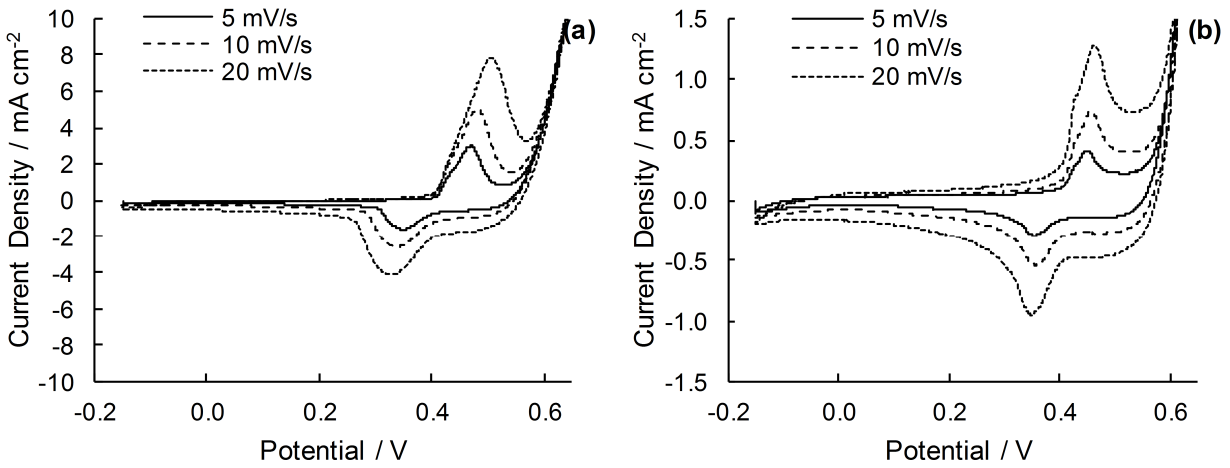

Figure 4.6: Cyclic voltammogram for the #1 $CoFe_2O_4$ electrode (a) and the #2 $CoFe_2O_4$ electrode (b) at different scan rates.

4.3.3 Surface Morphology

The deposition technique and the amount of material deposited can change the surface area of the active material, and therefore change the performance [59]. For this reason, the approximate surface area of each catalyst was investigated to ensure it was taken into account when making a decision on which catalyst to investigate further. No electrochemical method of determining surface area is perfect, particularly when comparing different oxides. Therefore three different methods were used to give an indication of the comparative surface areas of these six electrocatalysts. Note that each method has advantages and disadvantages, and not all methods could be used for all catalysts.

The first method (method 1) uses the surface reaction occurring in the cyclic voltammograms. The charge transferred during this surface reaction is proportional to the surface area of the material involved in the reaction. In this work, the charge transferred in the anodic reaction is calculated for the third cycle of the cyclic voltammogram performed at 5 mV s^1, and is done on both electrodes for each catalyst type (Table 4.3). The slowest rate is chosen to ensure the majority of the surface oxides are involved in the reaction.

This method can only be used where there is a clear and known surface reaction (or reactions) occurring. For the uncoated etched nickel there some confidence the following surface reaction occurs [111, 112, 114, 119]:

$$Ni(OH)_2 + OH^- \longleftrightarrow NiOOH + H_2O + e^- \tag{4.3.1}$$

One electron is being transferred per active nickel on the surface of the catalyst. The same reaction is occurring for NiO_x. The cyclic voltammogram for the Co_3O_4 electrocatalyst has two reactions occurring in the anodic direction: nickel oxidation as shown in Equation 4.3.1 and cobalt oxidation

Table 4.3: Charge transfer and capacitance measurements for the seven electrodes.

Electrocatalyst	Method 1 Charge Transferred in Anodic Surface Reaction (mC)		Method 2 Double Layer Capacitance from Cyclic Voltammetry (mF cm^{-2})		Method 3 Capacitance from EIS modelling (mF cm^{-2})	
	#1	#2	#1	#2	#1	#2
Ni foil	1.9	2.0	1.0	0.7	0.9	0.8
$CoFe_2O_4$	-	-	24	8	8.2	0.8
$La_{0.7}Sr_{0.3}CoO_3$	-	-	31	20	-	-
Co_3O_4	22	18	52	38	72	49
$NiCo_2O_4$	-	-	106	99	130	123
NiO_x	166	147	-	-	188	159
IrO_2	-	-	167	172	233	261

as shown below [100, 57].

$$CoOOH + OH^- \longleftrightarrow CoO_2 + H_2O + e^- \tag{4.3.2}$$

Both nickel and cobalt oxides/hydroxides catalyse the OER and therefore the charge transferred in both reactions is combined. For the other four electrocatalysts ($La_xSr_{1-x}CoO_3$, $CoFe_2O_4$, $NiCo_2O_4$ and IrO_2) there are either no surface reactions or the surface reactions are less clear so the calculations cannot be confidently performed.

The next method used (method 2) also uses the cyclic voltammogram results, but instead of investigating the surface reaction, the double layer capacitance is investigated. The method uses the current at a chosen potential for a range of scan rates and assumes that only double layer charging is taking place at the potential chosen. Under this assumption there should be a linear trend between current and sweep rate, and the slope should give the capacitance of the interface. As double layer capacitance is proportional to surface area [120], this capacitance gives an indication of surface area. The third cycle for each of the cyclic voltammograms was used to calculate the double layer capacitance (Table 4.3). The key to this method is identifying a potential where no surface reactions are taking place. For nickel foil, $CoFe_2O_4$, and $La_{0.7}Sr_{0.3}CoO_3$, 0 mV in the cathodic direction was used (Figure 4.7(a,e, and d)). For $NiCo_2O_4$, 50 mV in the anodic direction was used (Figure 4.7(c)) and for IrO_2 and Co_3O_4, 100 mV in the anodic direction was used (Figure 4.7(f and b)).

The last method (method 3) also gives the double layer capacitance, but at an oxygen evolution potential. This is found using electrical impedance spectroscopy which relies on the use of a suitable equivalent electrical model. Models commonly used for impedance behaviour of oxides for oxygen evolution involve three capacitances (film, double layer and reaction) and four resistances (film,

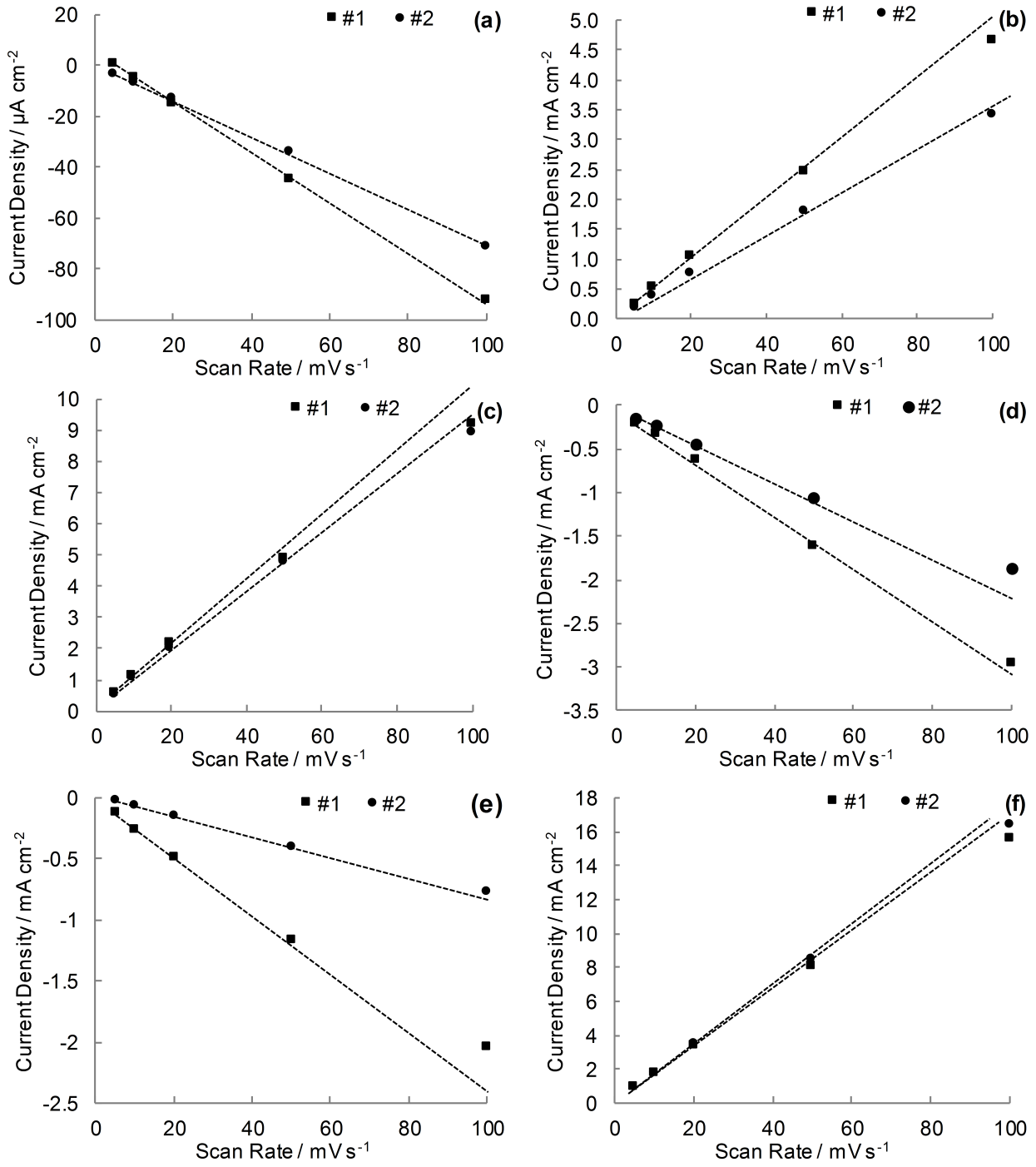

Figure 4.7: Current Density as a function of scan rate for uncoated nickel foil (at 0 mV) (a), Co_3O_4 coated electrode (at 100 mV) (b), $NiCo_2O_4$ coated electrode (at 50 mV) (c), $La_{0.7}Sr_{0.3}CoO_3$ coated electrode (at 0 mV) (d), $CoFe_2O_4$ coated electrode (at 0 mV)(e) and IrO_2 coated electrode (at 100 mV) (f) for use in the calculation of double layer capacitance.

ohmic, and reaction) [100, 43, 121]. The model used here (Figure 4.8(a)) contains R_Ω (the ohmic resistance); Q_{dl} (the double layer charge capacitance); Q_{film} and R_{film} (the film capacitance and the film resistance respectively) and R_{ct}, R_{rds} and Q_{rds} (parameters related to the OER mechanism). After observing the impedance data, R_{film} has been assumed to be much smaller than R_{rds}, as the time constants of the two loops are too similar to model separately without an unacceptable amount of uncertainty [100] (Figure 4.8(b)). The capacitance elements were modelled with a constant phase element (CPE), as has been done by others [19, 43, 46, 122] because the data revealed that the capacitive-like features do not behave as ideal capacitors. CPEs account for heterogeneities and rough surfaces [46].

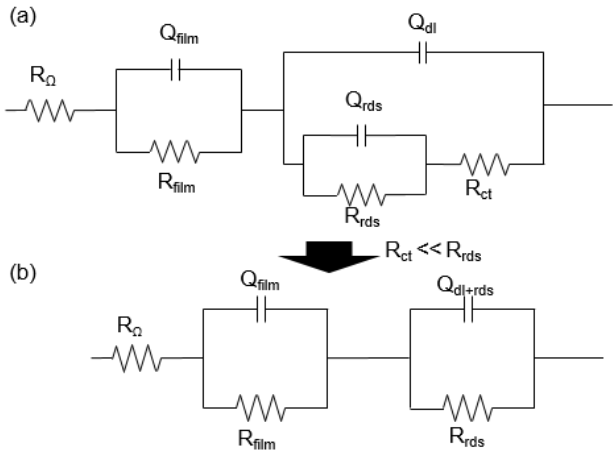

Figure 4.8: Impedance Model with (a) and without (b) R_{ct}.

The data and model curves are shown for each electrode in Figure 4.9. Nickel foil was modelled with R_{film} and Q_{film} set to zero as they are negligible due to the much smaller oxide film, and the data could be modelled with just one capacitive element. The impedance data for the $La_{0.7}Sr_{0.3}CoO_3$ electrocatalyst could not be easily modelled, and thus no capacitance is calculated for this electrocatalyst using this method. When using a CPE as a capacitave element, Y_o and n values are used in the model without a physical meaning. In order to obtain a meaningful capacitance value, Hsu and Mansfeld's relationship was used [123]:

$$C = Y_0(\omega''_m)^{n-1} \tag{4.3.3}$$

where C is capacitance in Farads and ω''_m is the frequency where Z_{imag} is at a maximum. Using this equation a capacitance value for the six catalysts was obtained (Table 4.3). The majority of the capacitance for each electrode is attributed to the the double layer capacitance, but there may also be some contribution from the reaction. This likely explains why the capacitance measured using this method for Co_3O_4 and $NiCo_2O_4$ is slightly higher than the double layer capacitance determined using the cyclic voltammetry method.

All capacitance and charge values recorded for methods 1 through 3 should be approximately

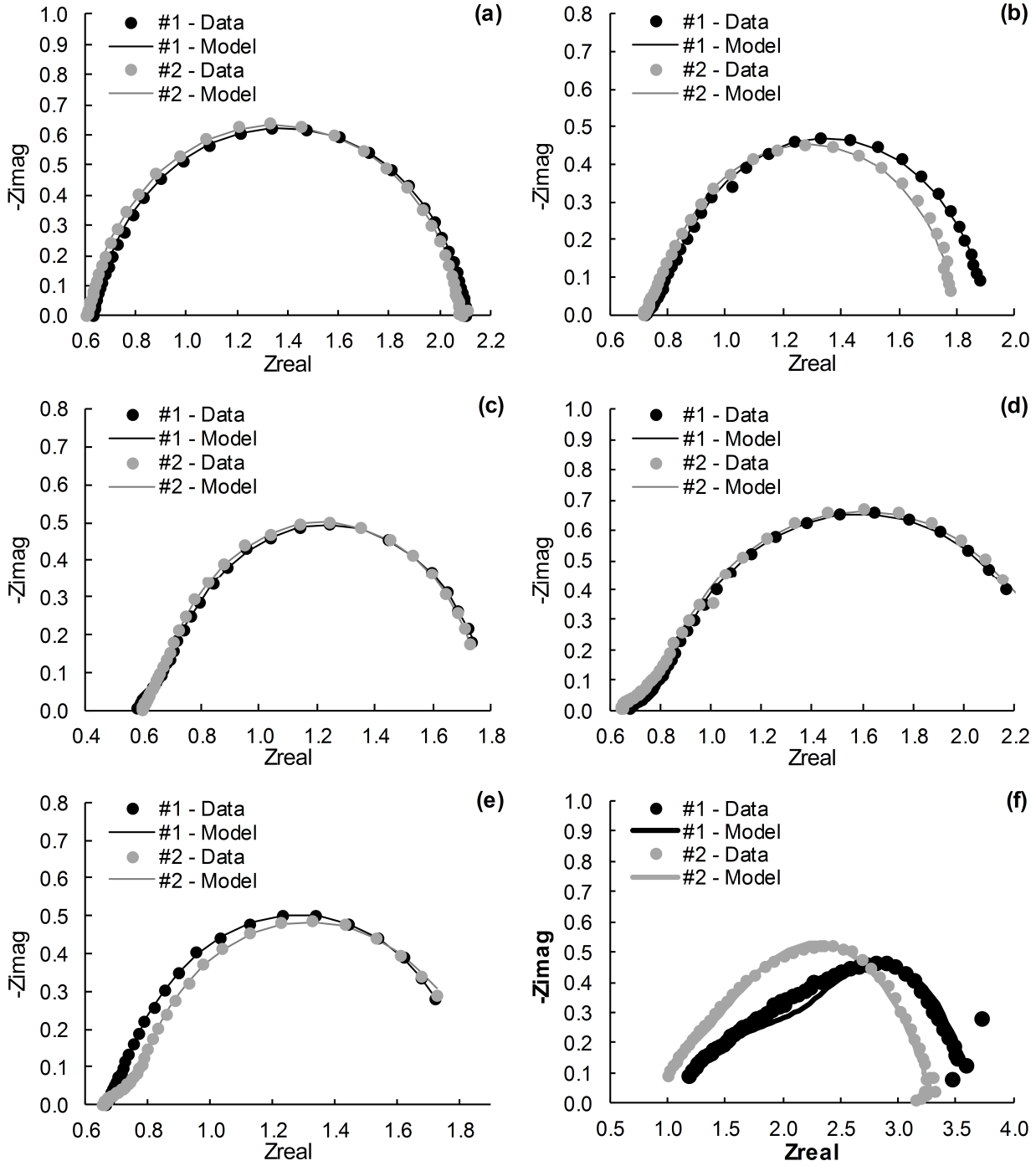

Figure 4.9: Impedance model fit for nickel foil (a) Co_3O_4 (b), $NiCo_2O_4$ (c), NiO_x (d), IrO_2 (e) and $CoFe_2O_4$ (f) electrocatalysts for impedance data collected at 20 mA cm^{-2}.

proportional to surface area. Based on this data the seven electrodes can be ordered from low to high surface area: Ni foil < $CoFe_2O_4$ < $La_{0.7}Sr_{0.3}CoO_3$ < Co_3O_4 < $NiCo_2O_4$ < NiO_x < IrO_2.

To obtain a complete picture of these electrocatalysts, SEM images were taken at 190 - 11,000x (Figure 4.11) and 85,000 - 100,000x magnification (Figure 4.10). The surface of IrO_2 is uniform and compact with "cracks" visible. This is typical of iridium oxide coatings [124]. While the surface of IrO_2 is smooth (with the exceptions of the cracks), the surface of the other catalysts are relatively rough (Figure 4.10). The SEM image of the $NiCo_2O_4$ (Figure 4.11(c)) looks similar to that seen by Gennero de Chialvo and Chialvo [125] for their spinel $NiCo_{3-x}O_4$ coatings. At closer magnification the surface appears very rough, as does NiO_x (Figure 4.10(b and c)). The cobalt oxide has a structure which is noticeably different from the others and appears to be porous in nature (Figure 4.11(d) and 4.10(d)). The surface of $La_{0.7}Sr_{0.3}CoO_3$ and $CoFe_2O_4$ appear more rough than IrO_2, but less so than that of the other three catalysts (Figure 4.10). Based on the SEM images in Figure 4.10, the results in Table 4.3 are logical with the exception of IrO_2, which appears to have a much lower surface area than that indicated by the capacitance values. It is suggested that the capacitance values calculated using methods 2 and 3 include a pseudo-capacitance due to the Ir^{3+}/Ir^{4+} and Ir^{4+}/Ir^{6+} transitions mentioned in other literature [126, 46], and therefore do not correlate to the surface area. Based on this comparison with the SEM images there is confidence in the following order for six electrodes from low to high surface area: Ni foil < $CoFe_2O_4$ < $La_{0.7}Sr_{0.3}CoO_3$ < Co_3O_4 < $NiCo_2O_4$ < NiO_x. However, the location of IrO_2 within this is sequence is inconclusive.

4.3.4 Stability and Activation.

A galvanostatic test at 50 mA cm^{-2} for 18 h was conducted as part of the overall testing procedure. This served two purposes, to pretreat the electrocatalyst and to give an indication of stability. There was no significant increase in potential (more than 20 mV) for any of the seven electrodes, indicating good stability over 18 h (Figure 4.12). For the electrocatalysts chosen for further investigation longer stability tests are recommended.

Multiple electrocatalysts exhibited a decrease in potential with time. This is particularly noticable for $La_{0.7}Sr_{0.3}CoO_3$ and $CoFe_2O_4$ (Figure 4.12(b)) and indicates that activation is required for these electrocatalysts to perform optimally. After 12 - 18 h the potential appears to stabilise at a minimum. The majority of the other testing in this chapter was performed after this stabilisation. The small decrease in potential at approximately 14 - 18 h for NiO_x $NiCo_2O_4$ (Figure 4.12(c and d)) may have been due to changes in room temperature. For this reason electrocatalytic testing in later chapters were carried out in a temperature controlled environment.

4.4 Conclusions

The six electrocatalysts ($La_xSr_{1-x}CoO_3$, $CoFe_2O_4$, Co_3O_4, $NiCo_2O_4$, IrO_2 and NiO_x) were successfully prepared using thermal decomposition and the performance towards the OER compared. The two most high performing electrocatalysts at current densities above 20 mA cm^{-2} were Co_3O_4 and

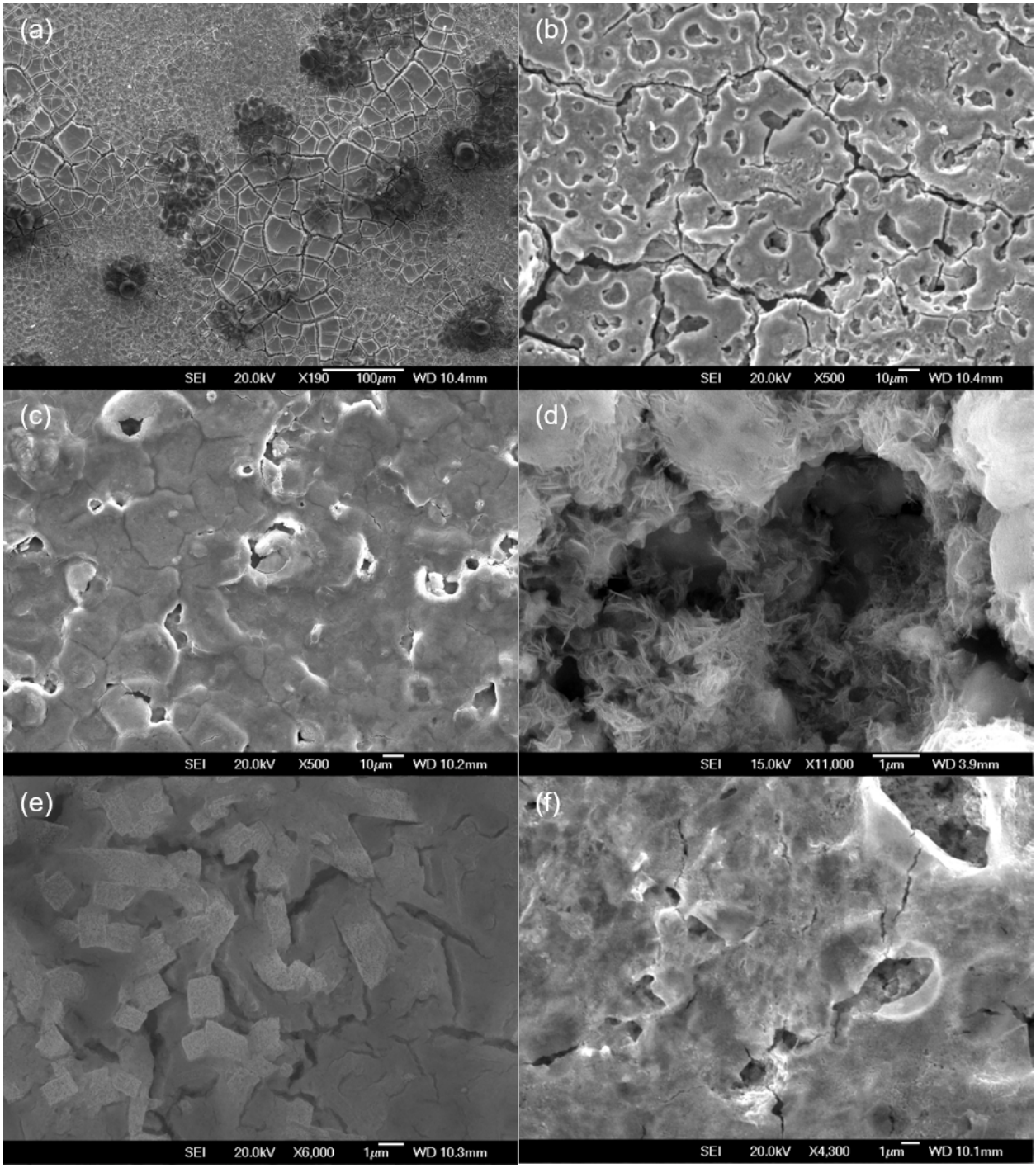

Figure 4.10: SEM images of untested IrO_2 (a), NiO_x (b), $NiCo_2O_4$ (c), Co_3O_4 (d), $CoFe_2O_4$ (e) and $La_{0.7}Sr_{0.3}CoO_3$ (f) electrocatalysts at μm scale.

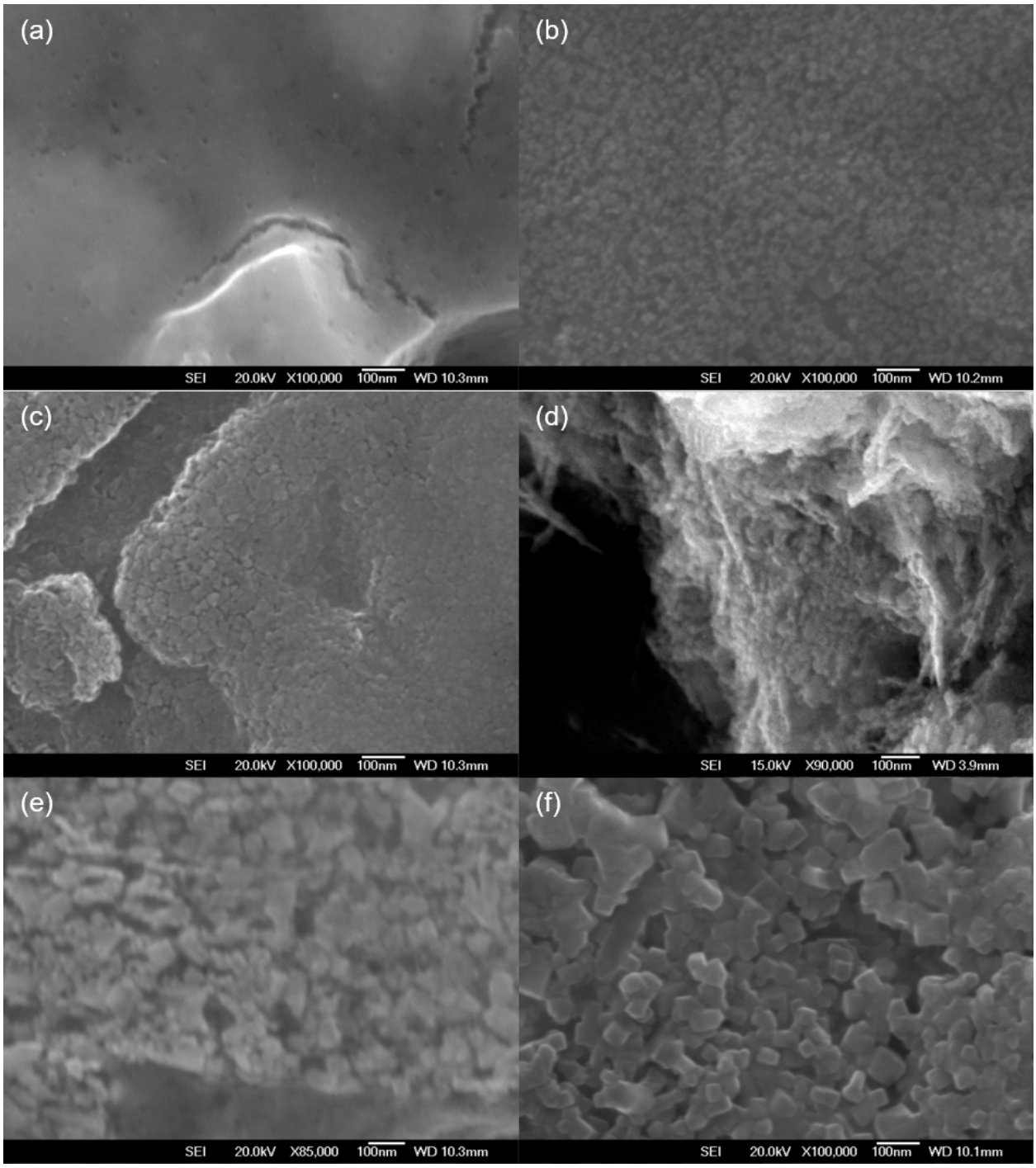

Figure 4.11: SEM images of untested IrO_2 (a), NiO_x (b), $NiCo_2O_4$ (c), Co_3O_4 (d), $CoFe_2O_4$ (e) and $La_{0.7}Sr_{0.3}CoO_3$ (f) electrocatalysts at nm scale.

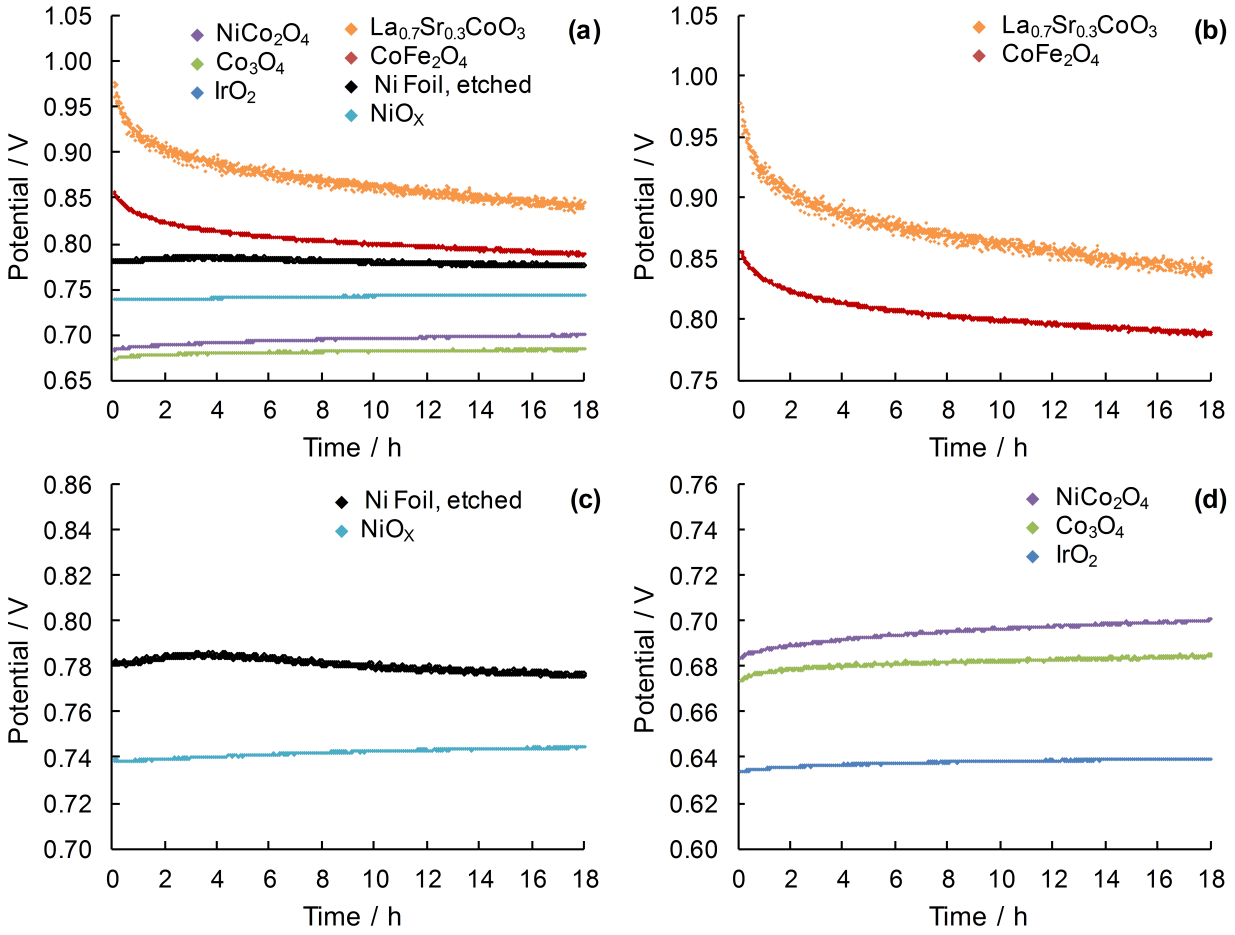

Figure 4.12: Galvanostatic oxygen evolution at 50 mA cm^{-2} for 18 h on $La_{0.7}Sr_{0.3}CoO_3$ (a,b), $CoFe_2O_4$ (a,b), etched nickel foil (a,c), NiO_x (a,c), $NiCo_2O_4$ (a,d), Co_3O_4 (a,d) and IrO_2 (a,d).

IrO_2. IrO_2 had the highest performance but may not be the preferred catalyst due to cost. To gain a better understand of the six electrocatalysts and their intrinsic activity, the comparative surface area was estimated and the electrocatalysts were ordered from lowest to highest: Ni foil $< CoFe_2O_4 < La_{0.7}Sr_{0.3}CoO_3 < Co_3O_4 < NiCo_2O_4 < NiO_x$. This shows that the performance of the Co_3O_4 electrocatalyst was not only due to a high surface area (it had a mid-range surface area), but also a high intrinsic activity. All coatings were found to be relatively stable over an 18 h period, and $La_{0.7}Sr_{0.3}CoO_3$ and $CoFe_2O_4$ required a significant amount of activation before they performed optimally.

Chapter 5

Structure and Transformation of Hydroxide Films on Nickel Anodes

This chapter has been published as:

Mellsop, S., Gardiner, A., Johannessen, B., & Marshall, A. (2015). Structure and transformation of oxy-hydroxide films on Ni anodes below and above the oxygen evolution potential in alkaline electrolytes. Electrochimica Acta, 168, 356364. doi:10.1016/j.electacta.2015.04.020

Abstract

The anodic behaviour of a nickel electrode has been investigated in KOH electrolytes below and above the oxygen evolution potential. As the literature reports a wide range of behaviours, initial repetitive cyclic voltammetry in 1 M KOH was compared to 30 wt% KOH (i.e., that used in alkaline water electrolysers) and it was found that a process in addition to the normal α-$Ni(OH)_2$/γ-NiOOH and β-$Ni(OH)_2$/β-NiOOH occurs in the more concentrated electrolyte. It is also confirmed that the initial hydroxide layer formed anodically from metallic nickel is not α-$Ni(OH)_2$, but a layer which is more readily reducible than α-$Ni(OH)_2$. At higher potentials, while *in situ* XAS suggested that γ-NiOOH is not transformed to any further phase up to 0.665 V vs Hg/HgO in 1 M KOH, after extensive OER (at least 40 hrs) in 30 wt% at 50 mA cm^{-2}, an additional phase can be identified by cyclic voltammetry. Overall, during galvanostatic oxygen evolution, the nickel anodes follow an ageing behaviour characterised by a brief activation period, a short period of high activity (i.e., low overpotential) followed by deactivation and eventually stable but poor activity. While no clear evidence was obtained to identify the most active phase for oxygen evolution, it is likely that this is related to β-NiOOH and confined to the very surface of the electrode.

5.1 Introduction

Nickel is often used as a material for the oxygen evolution reaction (OER) in addition to other electrochemical technologies such as Ni-batteries and sensors [127, 128, 129, 130, 131]. While it is well known that the activity of nickel anodes towards the oxygen evolution reaction can decrease over time [94], and that the preparation procedure has a large influence on activity [113], the mechanisms involved are not fully understood.

There are four nickel oxide phases known to be present near the oxygen evolution reaction potential: α-$Ni(OH)_2$, β-$Ni(OH)_2$, β-NiOOH and γ–NiOOH. These four phases were first described by Bode et al. [132] (Figure 5.1). α-$Ni(OH)_2$ has a hydrated disordered structure [48], and often contains foreign ions [133]. This α-$Ni(OH)_2$ phase does not have a well-defined structure and can vary depending on how the oxidised nickel layer was prepared [133]. Compared with the α-$Ni(OH)_2$ phase, β-$Ni(OH)_2$ is more structured, with more closely packed layers [131]. According to Bode's model, upon oxidation, β-$Ni(OH)_2$ is converted to β-NiOOH, whereas α-$N(OH)_2$ is converted to γ-NiOOH. The γ-NiOOH structure is not well-defined, but is known to contain intercalated alkali metallic cations and water molecules, and results indicate it is at a higher oxidation state than β-NiOOH [48, 134]. It has been proposed that β-NiOOH converts to γ-NiOOH upon further oxidation [114, 135].

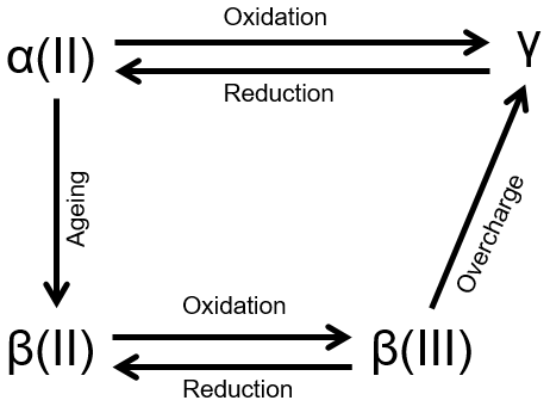

Figure 5.1: Bode diagram of known nickel phases.

Despite the utility of Bode's model, the interconversion between the oxidised nickel phases appears to be more complex than described in the model. For example, Raman spectroscopy indicates that β-NiOOH transforms into an undefined phase (not γ-NiOOH) above 0.52 V vs Hg/HgO in 0.1 M KOH [113], and results obtained by Ohligschlager and Schwitzgebel [135] suggest another intermediate β phase exists (β*) at low alkaline electrolyte concentrations. Furthermore, much of the research has investigated the interconversion of the anodic nickel oxides at lower potentials and lower hydroxide electrolyte concentrations than used in industrial alkaline water electrolysers. Thus in this paper the phase changes are examined over a wide range of potentials, and in both 1 M and 30 wt% (6.8 M) KOH electrolytes, with the intent of relating these results to

the less understood structural changes that occur throughout galvanostatic oxygen evolution.

5.2 Experimental

1 cm^2 nickel foil electrodes (Sigma-Aldrich $\geq$ 99.9%) were cleaned in acetone for 5 min, ultrasonicated in water, etched in 1 M hydrochloric acid solution with 5.25 g L^{-1} of hydrogen peroxide for 15 min, and finally rinsed in deionised water. Contact with the nickel foil was achieved by spot welding a nickel wire (0.5 mm diameter) to a corner of the foil. This wire was insulated from the electrolyte using an inert thermosetting polymer.

A Gamry Instruments Reference 3000 potentiostat was used for electrochemical analysis. Tests were performed in either 1 M or 30 wt% KOH solution (pellet basis, $\geq$ 85 % purity) in a thermostatically controlled PTFE cell at 25°C. Nickel foil (15 cm^2) acted as the counter electrode along with a Hg/HgO (KOH) reference electrode. Cyclic voltammetry was performed at 50 mV s^{-1} from -0.1 V to 0.65 V (unless stated otherwise). Electrochemical impedance spectroscopy (EIS) was performed either at 0 V (to obtain the ohmic resistance between the reference and working electrodes) or 50 mA cm^{-2} (during galvanostatic oxygen evolution) over the frequency range 0.2 - 100,000 Hz at 5 mV rms. Unless stated otherwise the following pretreatment procedure was used: the freshly etched nickel electrodes were subjected to potentiostatic EIS at 0 V, and then the potential held at -100 mV for 2 h. Prior to a galvanostatic ageing test, the electrode also had a cycling pretreatment step at 50 mV s^{-1} for 20 cycles between -0.1 V and 0.65 V.

X-ray photoelectron spectroscopy (XPS) was performed for surface analysis using a Kratos Axis DLD spectrometer with monochromated Al K-α source, and CasaXPS was used to fit peaks to the data. Materials analysed with XPS underwent long-term galvanostatic oxygen evolution measurements for 0 - 100 h at 50 mA cm^{-2}. The samples were removed immediately after galvanostatic-ageing, rinsed in DI water, then isopropanol, and then dried in an oven at 50°C for 10 min.

In situ x-ray absorption spectroscopy (XAS) measurements were performed at the Australian Synchrotron using nickel thin films (approximately 20 nm thick) prepared by thermal evaporation of Ni onto pyrolytic graphite foils. The XAS data was recorded in fluorescence mode using a 100-element Ge fluorescence detector using an electrochemical cell similar to that described by Holstein and Rosenfeld [136], with a Pd counter electrode and AgAgCl reference electrode. The potential of the thin Ni film was controlled with a Digi-Ivy DY2100 potentiostat. A Ni reference foil was measured simultaneously with the fluorescence data, and α-$Ni(OH)_2$ and NiO powders were also used as reference compounds.

5.3 Results and Discussion

5.3.1 Cyclic-Ageing and Phase Changes

Repetitive cyclic voltammetry was used to understand the phase changes occurring on the nickel electrode surface. Much of the recent literature associated with electrochemical oxidation of nickel

used electrolytes of ≤ 1 M OH^-, so in order to allow comparisons between existing literature and the measurements reported here at 30 wt% KOH, cyclic voltammetry was first performed in 1 M KOH (Figure 5.2). Two overlapping peaks are seen on the cathodic sweep at approximately 0.38 V (C1) and 0.35 V (C2), and overlapping peaks are seen in the anodic direction at 0.45 V (A1) and 0.48 V (A2). In existing literature, C1 and A1 are typically associated with the α-γ reaction, and C2 and A2 are associated with the β-β reaction [113, 114]. The β-β reaction occurs at lower potentials in the cathodic direction because the γ-NiOOH phase is more accessible to anions and the β-NiOOH phase is more thermodynamically stable [7]. The individual peaks may be deconvoluted by fitting Gaussian peaks to the voltammetry data (Figure 5.3), in a similar way to that used when interpreting electrochemical behaviour of Ni in QCM studies [135, 137]. It is important to stress that the use of Gaussian peaks is only to illustrate the possible potential and charge associated with the overlapping redox processes, and is not assumed to theoretically described cyclic voltammetry peaks [138]. Despite this, the fits do result in a consistent ageing pattern over all electrodes tested which provides further insights into which processes dominate the voltammetric behaviour over time (Figure 5.4). It is clear that as the cycling proceeds, the A1 peak decreases continuously and is practically gone after approximately 150 cycles (Figure 5.4a). This is consistent with the Bode model, which shows that the α-$Ni(OH)_2$ phase develops into β-$Ni(OH)_2$ upon ageing, and also the findings of others which show the net anodic peak (of the overlapping α-γ and β-β processes) shifts to higher potentials upon cycling [113, 7, 139]. The transition process from α-$Ni(OH)_2$ to β-$Ni(OH)_2$ is described well by Bernard [140], with an initial fast decrease in the quantity of alkali metal ions exchanged during potential cycling due to a decrease in the inter-plane distance, followed by a slow evolution characterised by the coalescence of crystallites leading to the well crystallised β-$Ni(OH)_2$.

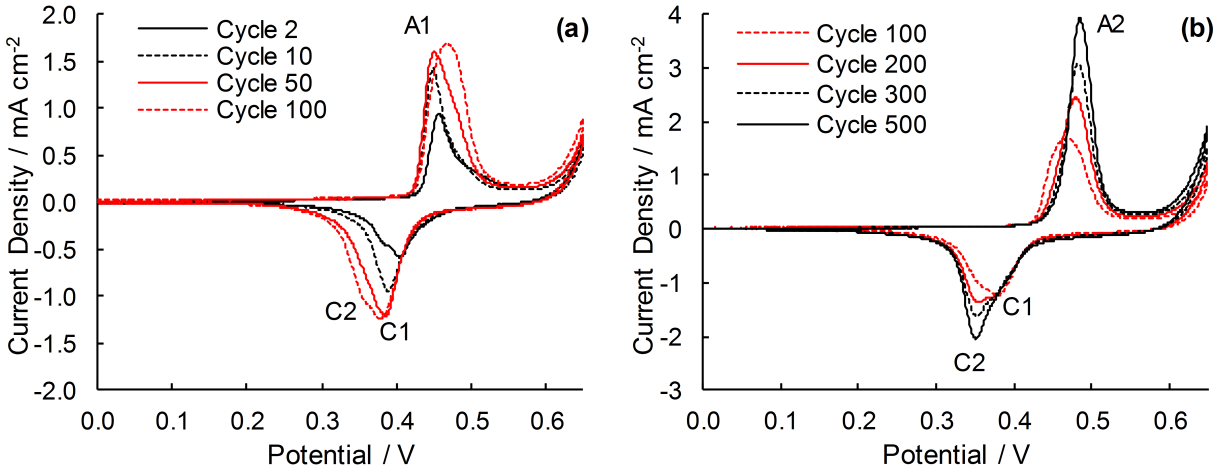

Figure 5.2: Cycles 2-100 (a) and 100-500 (b) of cyclic voltammograms performed at 50 mV cm^{-2} between -0.1 V and 0.65 V in 1 M KOH.

Additional observations are made from fitting Gaussian peaks to the anodic peaks. The charge related to the β-β reaction continues to increase after 150 cycles but at a slower rate, which can

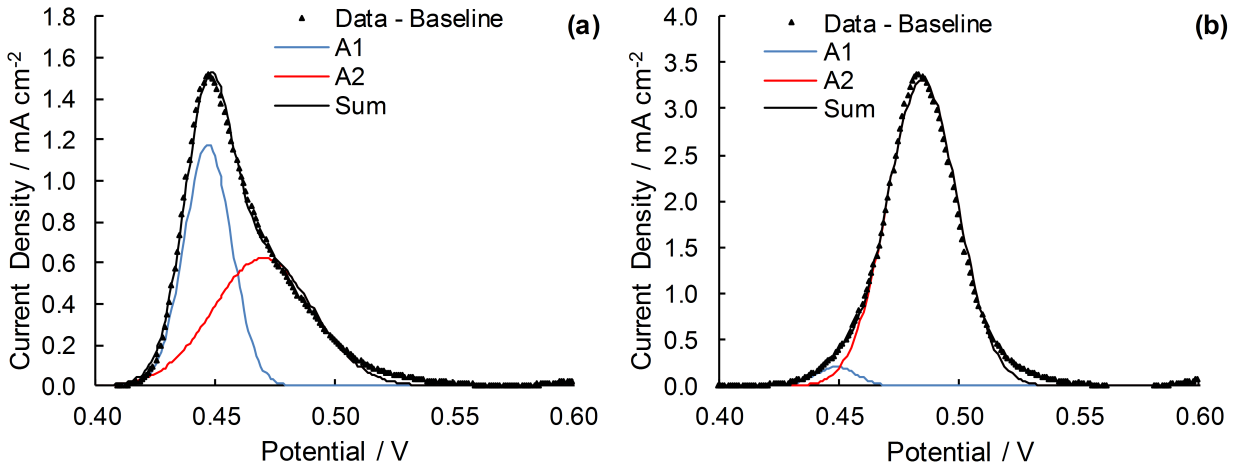

Figure 5.3: Deconvolution of the anodic feature during the cycling of a nickel electrode in 1 M KOH at 50 mV s^{-1} between -0.1 V and 0.65 V. Cycle 20 (a) and cycle 400 (b).

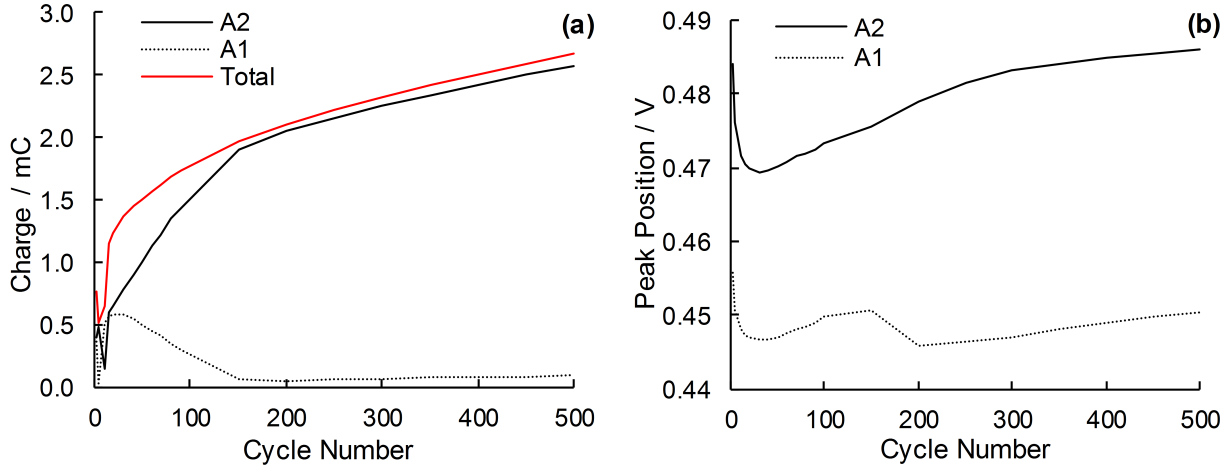

Figure 5.4: Anodic peak charge (a) and peak potential (b) during the repetitive cycling of a nickel electrode in 1 M KOH at 50 mV s^{-1} between -0.1 V and 0.65 V based on Gaussian deconvolution.

be assumed to relate to the growth of the hydroxide layer into the nickel substrate. It is also observed that during the first few cycles, the potentials associated with the two processes decrease considerably (Figure 5.4b), and it is noted that the behaviour of the peak potentials during cycling is very similar to that observed in 1 M NaOH electrolyte [139]. We propose that this change in the peak potentials is related to the restructuring of the anodic layer during the initial oxidation of the nickel hydroxide layer first formed on the nickel substrate (discussed in more detail later in this section).

Three differences in the cyclic voltammograms are observed at the higher concentration of 30 % KOH. Firstly, the peaks have moved to lower potentials as discussed by others [141]. Secondly, the two cathodic peaks which appear in 1 M KOH merge to give a single peak consistent with the observations of Lyons et al. [114] who showed that the potential difference between C1 and C2 decreases as pH increases. Thirdly, there is a change in the anodic peaks which is more difficult to explain. While peaks A1 (0.4 V) and A2 (0.46 V) are again visible, as cycling progresses, A2 increases in size and the first peak, A1, appears to shift to higher potentials by 10 - 20 mV. By fitting Gaussian peaks to this data, it appears that the A1 peak is not a single redox process, but two, A1 and A1' (Figure 5.6). As peak A1 disappears upon cycling, it is likely that this peak is still the α-γ reaction. The fact that the disappearance of this peak is much faster in 30 wt% KOH compared with 1 M KOH (approx 50 cycles compared with 150 cycles in 1 M KOH) is expected as the α-γ to β-β conversion is known to be more rapid in more concentrated solutions [135]. What is not clear however, are the reactions shown by A1' and A2. Barnard and Randell [137, 141] indicate that the peak at 0.46 V (A2 in our work) is due to the β-β reaction, however, this assumption is based on the fact that only one peak is observed below A2 in their work, not two. Here, we observe that as peak A2 stops growing at cycle 200, peak A1' starts to increase (Figure 5.7a), which indicates that these two processes are related.

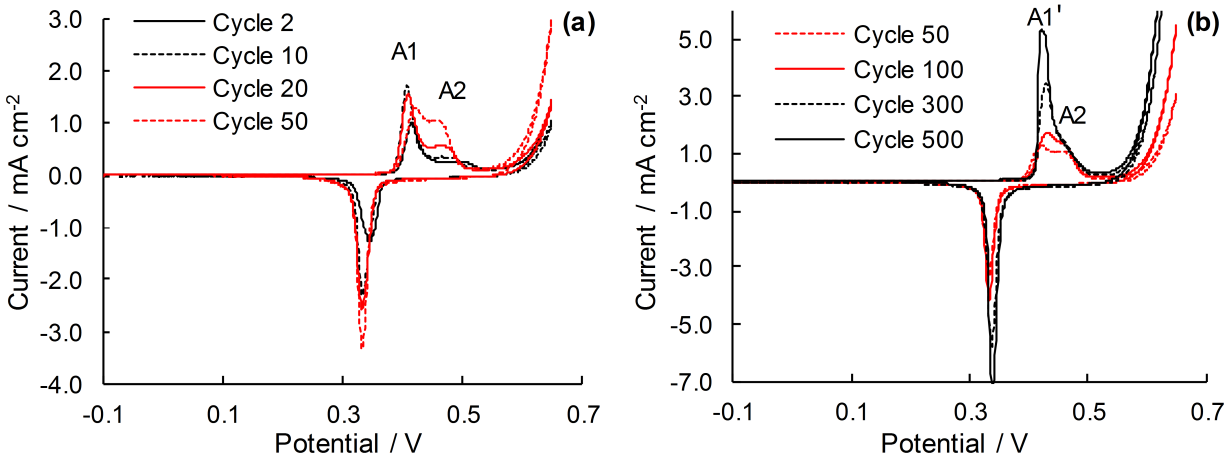

Figure 5.5: Cycles 2-50 (a) and cycles 50-500 (b) of cyclic voltammograms performed in 30 wt% KOH at 50 mV s^{-1} between -0.1 V and 0.65 V.

Phase changes occurring at more cathodic potentials were investigated by cyclic voltammetry (in

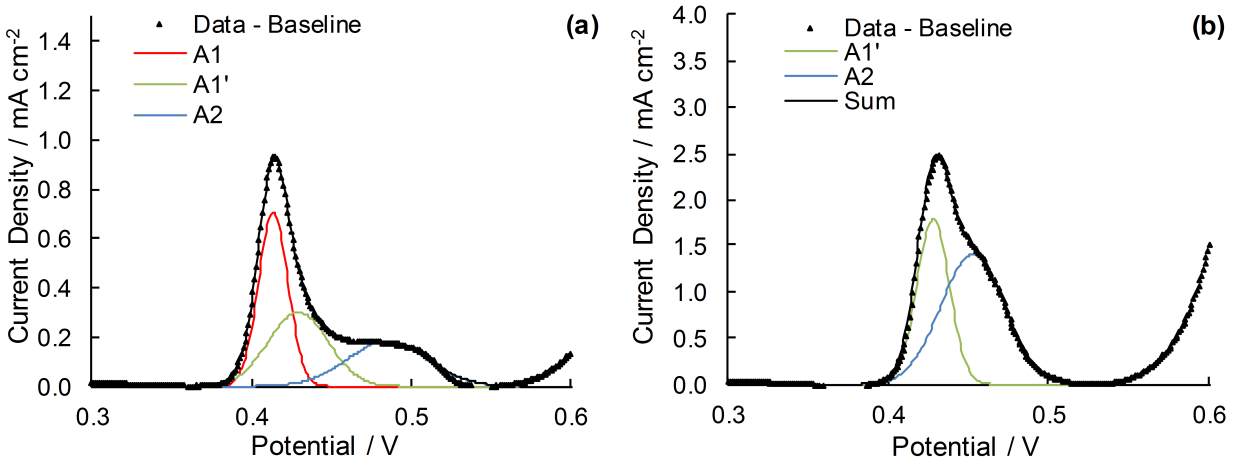

Figure 5.6: Deconvolution of the anodic feature during the cycling of a nickel electrode in 30 wt% KOH at 50 mV s^{-1} between -0.1 V and 0.65 V. Cycle 2 (a) and cycle 200 (b).

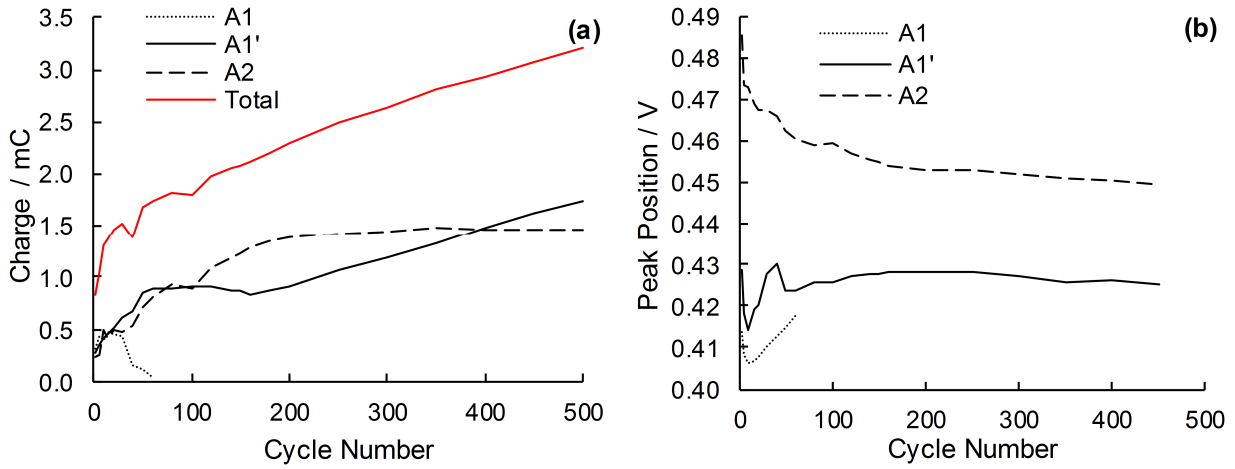

Figure 5.7: Anodic peak charge (a) and peak potential (b) during the repetitive cycling of a nickel electrode in 30 wt% KOH at 50 $mV\ s^{-1}$ between -0.1 V and 0.65 V based on Gaussian deconvolution.

30 wt% KOH) as there has been some seemingly contradictory work in this area [114, 142, 143, 119]. To ensure that any surface oxides were completely reduced back to metallic nickel, the freshly etched electrode was held at -1.1 V for 6000 s prior to recording the cyclic voltammetry from the cathodic limit of -1.1 V to a range of increasing anodic limits (Figure 5.8). Two clear peaks are typically observed, one at approximately -0.5 V on the anodic sweep (A0), and one at approximately -1.0 V on the cathodic sweep (C0), which can be attributed to the Ni-Ni^{2+} reaction [114, 143, 142, 14].

In literature, the A0 peak is often observed by cyclic voltammetry without the corresponding C0 peak. This usually occurs when the potential has been swept up to the oxygen evolution potential and back [114, 142, 119], and suggests that above a certain potential, the nickel oxy-hydroxides convert to a form that is more difficult to reduce back to metallic nickel. Here, good evidence for this is found, with the C0 process clearly being influenced by the upper anodic limit (Figure 5.8). Above an anodic limit of 0.2 - 0.3 V the size of the C0 peak decreases and as the limit reaches 0.5 V the peak is almost indistinguishable from the background. It is also observed that peak A0 reduces in size if the electrode is cycled above an anodic limit of around 0.1 V, and disappears completely if the anodic limit surpasses the potential of the A1 peak (i.e., the $\alpha - \gamma$ transition). Based on this information, it appears that cycling $Ni(OH)_2$ to NiOOH and back causes a change in the $Ni(OH)_2$ structure which makes it difficult to reduce back to metallic nickel. Similarly, Delahaye-Vidal and Figlarz [133] show that significant changes in the structure of the $Ni(OH)_2$ occur in just one sweep above A1, A1' and A2 and back.

Complicating this discussion is the uncertainty in the structure of the nickel oxide which forms during A0, with some literature suggesting NiO and some $Ni(OH)_2$ [114, 142, 143]. The thermodynamics of $Ni(OH)_2$ and NiO formation are essentially the same [143], $E^0 = 0.110$ V for the Ni to $Ni(OH)_2$ reaction and $E^0 = 0.116$ V for the Ni to NiO reaction [14], and thus cannot be used to distinguish between these reactions. Lyons et al. [114] support the theory that Ni(II) initially forms as anhydrous NiO, but as the potential increases it forms a more hydrous $Ni(OH)_2$ phase. XPS work by Alsabet et al. [142] shows that between the $Ni(OH)_2$ and metallic nickel substrate, there is a small NiO layer present. Furthermore, there is disagreement over the initial structure of any $Ni(OH)_2$ formed at these potentials [114, 142, 143]. Alsabet et al. [142] suggest that it is α-$Ni(OH)_2$ which forms initially, but during the first sweep to high potentials (above A1-A2 peaks) and back it is converted to β-$Ni(OH)_2$. Juodkazis et al. [143] however, suggest the reverse: that it is initially β-$Ni(OH)_2$ that is produced, but upon sweeping up into the range of oxygen evolution and back, α-$Ni(OH)_2$ is formed (at approximately 1.2 V vs RHE on the cathodic sweep). Lyons et al. avoid using the strict definitions of α-$Ni(OH)_2$ and β-$Ni(OH)_2$, but they say that a metastable anhydrous film is initially produced and that the film thickening/hydrating reaction is likely to be slow [114, 119]. Burke and Twomey [144] propose that both oxidation and hydrolysis processes operate in the low potential region (between approximately -0.6 V to -0.8 V) and that a species with a formula of $Ni(OH)_{2.4}^{0{\cdot}4-}$ forms. One possible inference is that this is a α-$Ni(OH)_2$-like phase based on the excess OH^- and cations within the structure. However, de Souza et al. [130] used a combination of ellipsometry and cyclic voltammetry to determine that charge transferred during

the A0 peak is more similar to β-Ni(OH)$_2$ than α-Ni(OH)$_2$.

Our measurements support the suggestion by Lyons et al., and Burke and Twomey [114, 119, 144], that slow hydration and slight oxidation occurs above A0 but below A1. Specifically, additional charge transfer is observed between -0.1 V and 0.3 V on newly-formed NiO or Ni(OH)$_2$ compared to an electrode comprising mostly α-Ni(OH)$_2$ (formed by holding a freshly-etched nickel electrode at -0.1 V for 2 h). We observe that the anodic peaks between 0.4 - 0.55 V for the initial NiO or Ni(OH)$_2$ layer is quite different to the typical cyclic voltammogram of α-Ni(OH)$_2$, with A1 (or A1') being small and A2 large (Figure 5.9). The cyclic voltammogram is similar to that seen by Lyons et al. [119] for their un-aged electrode, and it is clear that this initial NiO or Ni(OH)$_2$ layer can be converted to α-Ni(OH)$_2$ by either cycling the potential over the A1/A2-C1/C2 potential window, or by holding the potential for several hours above the A0 peak but below the A1 peak. Voltammetry from both our work and the work of Lyon et al., combined with ellipsometry results from de Souza et al. [130] leads us to believe a compact Ni(II) structure forms initially due to the low change density, and the slightly higher potential of the Ni(OH)$_2$-NiOOH peak (indicating that this initial NiO or Ni(OH)$_2$ layer is more difficult to convert to NiOOH). We do not believe that β-Ni(OH)$_2$ forms initially, as this would not convert back to α-Ni(OH)$_2$. Thus we conclude that the compact Ni(II) layer may have a structure part way between NiO and α-Ni(OH)$_2$ as described by Lyons et al. [114, 119]. For simplicity, in this paper, this phase is referred to as $\alpha(\mathrm{II})_{\mathrm{compact}}$.

To summarise these low potential processes, we suggest that $\alpha(\mathrm{II})_{\mathrm{compact}}$ forms initially from metallic nickel, and this can be converted to α-Ni(OH)$_2$ by either cycling through the γ-NiOOH phase (as per the standard Bode model), or by holding the potential between the A0 and A1 peaks. Once the α-Ni(OH)$_2$ has formed, complete reduction back to metallic nickel is more difficult than from the $\alpha(\mathrm{II})_{\mathrm{compact}}$ phase.

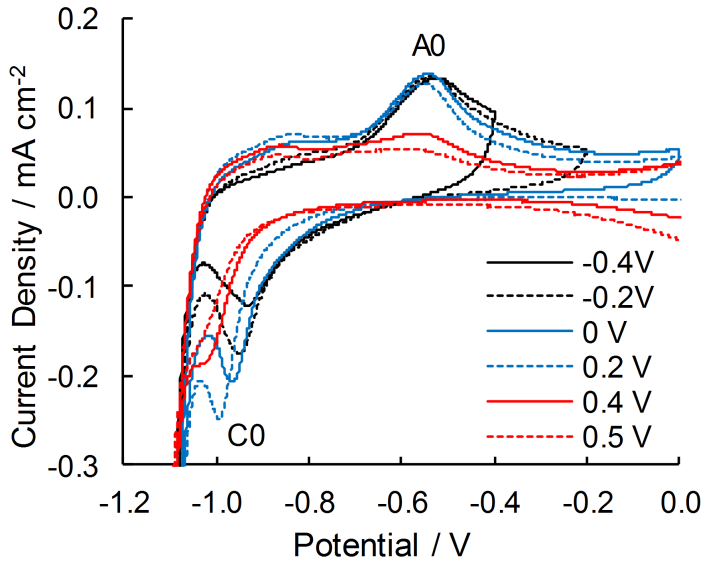

Figure 5.8: Cyclic voltammograms from -1.1 V in 30 wt% KOH at 50 mV s^{-1} with increasing anodic limits. The anodic limits for each curve are given in the legend.

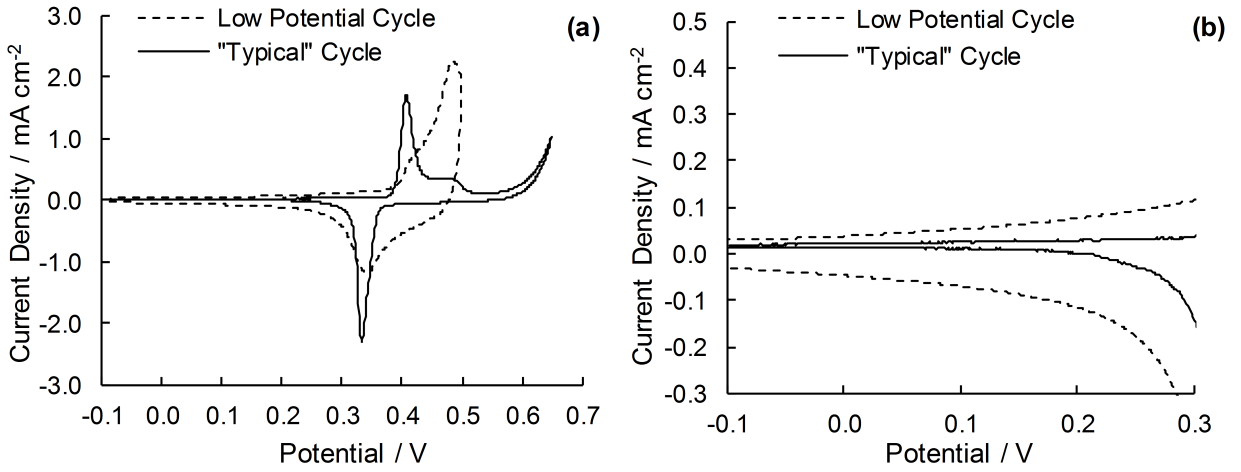

Figure 5.9: Voltammetry of a freshly prepared NiO or $Ni(OH)_2$ layer formed from metallic nickel (after a 6000 s pretreatment at -1.1 V) and α-$Ni(OH)_2$ (after a 2 h pretreatment step at -0.1 V), both at 50 mV s^{-1}. (b) is an enlargement of the -0.1-0.3 V region of (a).

To investigate any phase changes occurring at higher potentials (above those which can be reasonably investigated by cyclic voltammetry) in situ XAS was used on anodes prepared by evaporating a thin Ni film (20 nm) onto a graphite support foil. This ensures that the XAS signal originates predominately from the active Ni oxy-hydroxide layer (estimated to be 10 nm thick).

The structure of the anodic layer produced on the Ni film by oxygen evolution in 1 M KOH electrolyte and then held at 0.34 V vs Hg/HgO has a structure consistent with the α-$Ni(OH)_2$ reference compound (Figure 5.10). Although the XAS of α-$Ni(OH)_2$ and β-$Ni(OH)_2$ are very similar [131, 145], the potentials of the redox peaks measured by cyclic voltammetry for this material are the same as those observed from the α-γ reaction, indicating that the oxy-hydroxide layer formed on the Ni thin film is indeed α-$Ni(OH)_2$. Importantly, neither the XANES (X-ray Absorption Near Edge Structure) or Fourier transformed EXAFS (Extended X-ray Absorption Fine Structure) data show the presence of metallic Ni within the thin Ni film electrodes, indicating the majority of the Ni has been converted to the active α-$Ni(OH)_2$. Interestingly, if the α-$Ni(OH)_2$ film was rinsed in DI water and allowed to dry, the structure of the layer was then consistent with NiO, but rapidly (i.e., within 2-5 min) converted back to α-$Ni(OH)_2$ on immersion in 1 M KOH solution at open circuit potential (approximately 0.3 V). When the potential of the α-$Ni(OH)_2$ layer is increased to 0.54 V vs Hg/HgO, a change in the structure is observed due to the complete transformation of α-$Ni(OH)_2$ to γ-NiOOH with the absorption edge energy increasing (Figure 5.10a), and the first Ni-O shell distance decreasing (Figure 5.10b) in accordance with the observations by others [129, 131, 146, 147, 148].

There have been suggestions that additional phases (other than normal α, γ and β oxide phases) may exist on anodically formed nickel oxide electrodes [113, 135, 140] and that some of these could be present during the oxygen evolution reaction. To investigate this possibility, in situ XAS measurements were conducted under potentiostatic conditions up to 0.665 V vs Hg/HgO. At these high potentials in 1 M KOH, oxygen evolution would mask any current associated with phase

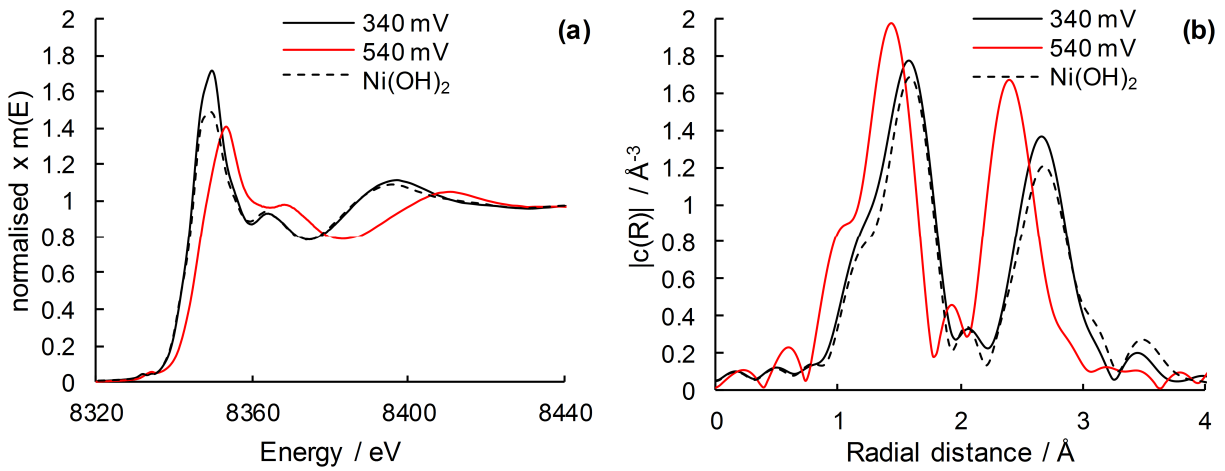

Figure 5.10: (a) XANES and (b) Fourier transform magnitudes of the Ni K-edge EXAFS spectra for a α-Ni(OH)$_2$ reference material, and the thin Ni film electrode at 0.34 and 0.54 V vs Hg/HgO in 1 M KOH.

changes during cyclic voltammetry. In these experiments, no evidence was found to suggest the formation of any additional Ni phases, although it is possible that any new phase transformation requires even higher anodic potentials (the upper potential was largely limited by the gas evolution rate within the in situ XAS cell), or restricted to the surface of the oxide film [94] and not detectable by the XAS analysis used here.

5.3.2 Galvanostatic-Ageing during Oxygen Evolution

During galvanostatic oxygen evolution at 50 mA cm^{-2} in 30 wt% KOH, the nickel anodes follow a complex ageing behaviour (Figure 5.11). To confirm this is a characteristic of nickel anodes initially consisting of α-Ni(OH)$_2$, these long-term galvanostatic measurements were repeated on 20 separate anodes, with a typical ageing curve given in Figure 5.11. Initially the potential decreases for the first 3 h (period I), before stabilising for approximately 7 h (period II). The typical potential observed during period II was 0.74 - 0.78 V and corresponds to the nickel exhibiting its highest activity for oxygen evolution during our long-term measurements. After this period of relatively stable performance, the potential increases linearly with time (period III) before increasing even more rapidly (period IV) and finally stabilising around 1 V vs Hg/HgO (period V). Despite extensive efforts to ensure that the pre-treatment of all electrodes was identical, the potential-time behaviour was never exactly the same, but qualitatively identical for all electrodes (i.e., the same periods were observed for all 20 electrodes). To illustrate this, period V was normally reached at 60 h, but could occur within as little as 40 h or as late as 140 h. As this observed behaviour is likely due to the inter-conversion of the oxidised nickel phases present on the surface of the nickel foil, and because the surface state present during period II is much more active than the others, understanding this behaviour may provide insights into enhancing or stabilising the electrocatalytic activity of nickel for oxygen evolution in concentrated KOH solutions.

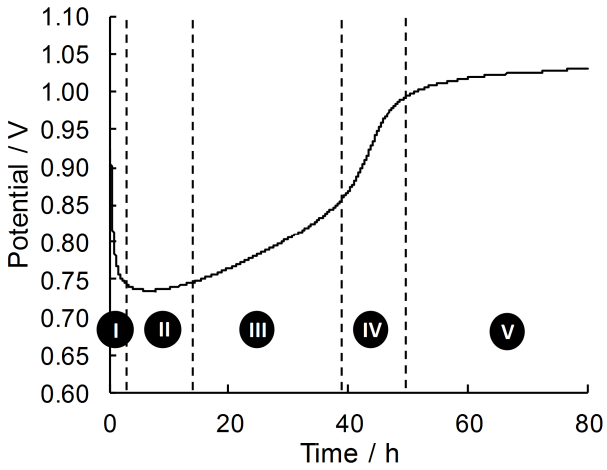

Figure 5.11: Galvanostatic ageing of a nickel electrode (initially in the α-$Ni(OH)_2$-γ-NiOOH form) at 50 mA cm^{-2} for 80 h. The potential has been corrected for the IR drop.

Cyclic voltammetry was used in an attempt to identify the active surface species present on the electrodes in each of the five characteristic periods observed during galvanostatic oxygen evolution. For these measurements, cyclic voltammograms were recorded once the electrode reached each period of interest. Importantly, fresh electrodes were used for every experiment due to the changes in the oxide structure caused by performing these cyclic voltammograms. The initial cyclic voltammogram reveals a single set of oxidation and reduction peaks at 0.39 and 0.32 V respectively, which is assigned to the α-$Ni(OH)_2$ to γ-NiOOH inter-conversion (Figure 5.12). As the potential during oxygen evolution is well above the α-γ transition, it is likely that the oxygen is evolved primarily from a γ-NiOOH surface.

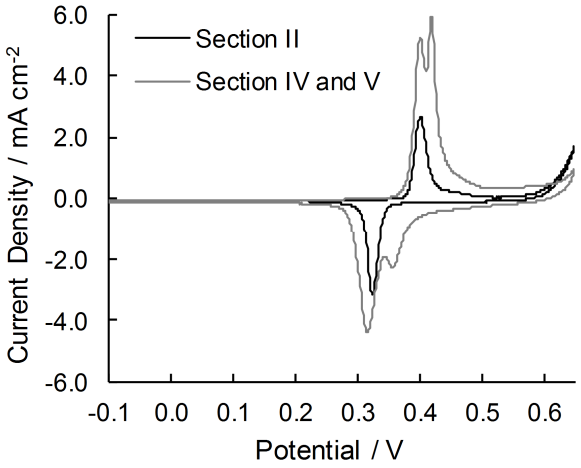

Figure 5.12: Cyclic voltammograms at 50 mV s^{-1} between -0.1 V and 0.65 V in period II and period IV and V of galvanostatic-ageing.

Overall, clear differences in the cyclic voltammograms were not observed until period IV, at which point an additional set of peaks are observed (labelled as A3 at 0.41 V and C3 at 0.36 V)

at slightly higher potentials than the α-γ transitions (Figure 5.12). The most obvious assignment of these additional surface reactions is to the β-$Ni(OH)_2$ to β-NiOOH transition as the anodic peak occurs at more positive potentials to the α-γ peak, however in this case, this is unlikely for the following reasons. Typically the β-NiOOH is referred to the "right kind of oxide" for oxygen evolution [94], and here the A3 and C3 peaks appear when the activity of the electrode becomes very poor (in period IV and V). Furthermore, in strongly alkaline solutions, the reduction peaks normally associated with the β-β transition should occur at a similar, or lower potential than the α-γ reduction peak [114] (Figure 5.5), whereas here C3 occurs at higher potentials than C1. One possibility is that A3 and C3 arise from a solid state reaction involving Ni(IV), which could be formed after prolonged oxidation of the γ-NiOOH surface. Overcharging has been shown to form a structure containing increased amounts of Ni(IV) [149]. Pourbaix diagrams [14] suggest that there should be a Ni(III) to Ni(IV) reaction at approximately 0.2 V above the Ni(II) to Ni(III) reaction. Liu et al. [134] have also observed two distinct cathodic peaks in concentrated KOH electrolytes (7 M) and attributed the higher potential peak (C3) to the reduction of Ni(IV) to Ni(III) in nano-γ-NiOOH, and the lower potential peak to the reduction of Ni(III) in the γ-phase to Ni(II) in α-$Ni(OH)_2$. Two oxygen evolution reaction mechanisms have been discussed in literature, one which suggests Ni(IV) cations are the active centres and one which instead suggests Ni^{3+} are the active centres. As Yeo et al.[113] state, the mechanism based on Ni(III) has the advantage of explaining the loss in activity with time as the phase would deactivate as the surface oxidises to Ni(IV). However it must be noted there was no evidence for a phase transformation during oxygen evolution from our XAS data, but this is likely due to the fact that the anodes could not be aged for a long enough period during the XAS measurements. Additionally, more concentrated KOH solutions may be required to see the phase change.

Significant changes to the cyclic voltammograms occurred during the first few cycles when these voltammograms were measured in periods IV and V, with the position of A3 and C3 decreasing in potential (Figure 5.13). By the fourth cycle there is little potential difference between A1 and A3, indicating the phase involved in the surface reaction represented by A3 and C3 is lost by cycling at these lower potentials. Given that thermodynamics suggests that Ni^{4+} should not be present at these potentials [14] if it is part of the structure in periods IV and V, one would expect this structure to change significantly as the potential is reduced.

While the poorly active Ni oxy-hydroxide phase present in period IV and V is characterised by the additional pair of peaks in the voltammograms, importantly, the most active phase for oxygen evolution (that present in period II, Figure 5.11) shows no obvious differences to the initial cyclic voltammogram response. One possibility is that the active phase responsible for the high OER activity in period II is only present at potentials above 0.6 V (and thus is unobservable by cyclic voltammetry), or is reconverted back to the "normal" Ni oxide surface at the potentials used for the CV measurements (although the in situ XAS measurements were unable to detect such a phase). However, it is most likely that the activity is controlled by a thin surface layer which has a small cyclic voltammogram response relative to the α-γ response and thus is undetectable. This

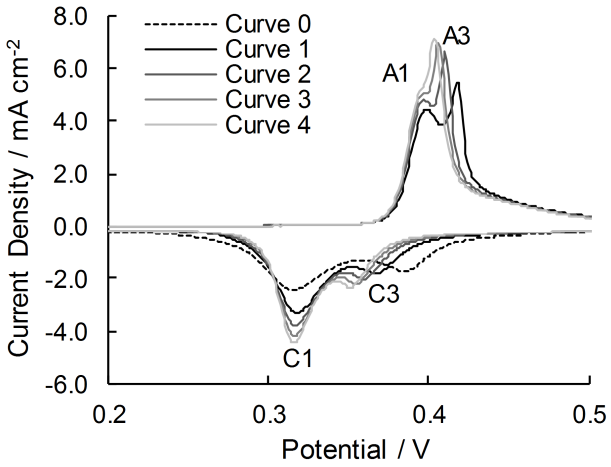

Figure 5.13: First four sweeps of a cyclic voltammogram between -0.1 V and 0.65 V at 50 mV s^{-1} in period V of galvanostatic-ageing. Note that curve 0 is the initial sweep from 0.65 to -0.1 V.

phase could be the β-NiOOH phase or a new phase as discussed by Yeo et al. [113]. To confirm this, an anode with a α/γ layer was subjected to repetitive potential cycling to produce the β/β prior to galvanostatic oxygen evolution. Following this, no significant ageing was observed, and the potential throughout the long term measurement was similar to that in period II for the α/γ anode.

To confirm that the ageing process was characteristic of the oxide phases rather than related to changes in surface area or electrical resistance, electrochemical impedance spectroscopy was performed at different stages throughout galvanostatic-ageing of the α/γ layer (Figure 5.14). A model commonly used for modelling the impedance behaviour of nickel includes three resistances and two capacitances (Figure 5.15a) [48]. In these models R_S is the solution resistance and C_{dl} is the double layer charge capacitance, and R_{ct}, C_{rds} and R_{rds} are parameters relating to the OER mechanism. R_{ct} is the resistance due to interfacial charge transfer [43], and C_{rds} and R_{rds} are kinetic parameters related to the rate determining step [100]. Only one clear loop is seen which means the time constants of the two loops are too similar to be modelled separately. We assume, therefore, that R_{ct} is much smaller than R_{rds} (the same assumption was made by Castro et al. [100]) and thus simplify the model to Model 2 (Figure 5.15b). In this situation C_{dl} and C_{rds} combine to give C_{dl+rds}.

Using Model 2 (Figure 5.15b), it is found that the electrode capacitance increases significantly in the first hour of galvanostatic ageing (Figure 5.16), which is a good indicator that the active surface area is increasing. If the active surface area does increase by this amount, the potential should decrease by approximately 10 - 30 mV (based on a Tafel slope of 40 - 120 mV), but it cannot explain the entire 230 mV overpotential decrease seen during the first 3 h of galvanotstatic ageing i.e., the activation in period I (Figure 5.11) is related to an increase in the specific activity of the anode. After this initial increase in capacitance (and thus surface area), no further changes occur, confirming that the deactivation characterised by periods III-IV (Figure 5.11) is related to a

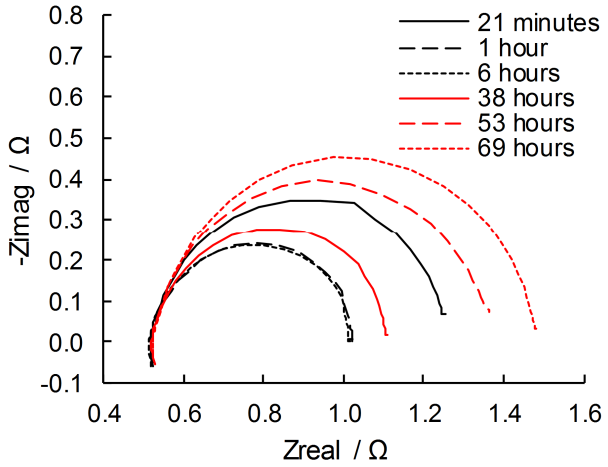

Figure 5.14: Nyquist plot throughout the stages of galvanostatic ageing.

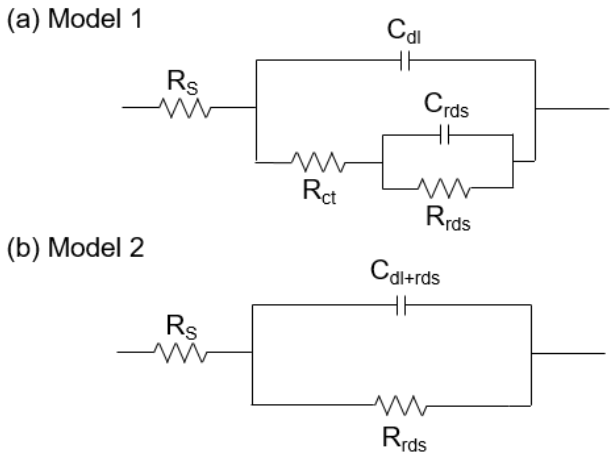

Figure 5.15: EIS models for the nickel electrode during oxygen evolution.

decrease in the specific activity of the anode. Similarly, the electrical resistance of the oxy-hydroxide layer on the nickel substrate does not change throughout the ageing and is thus not a contributor to the ageing process.

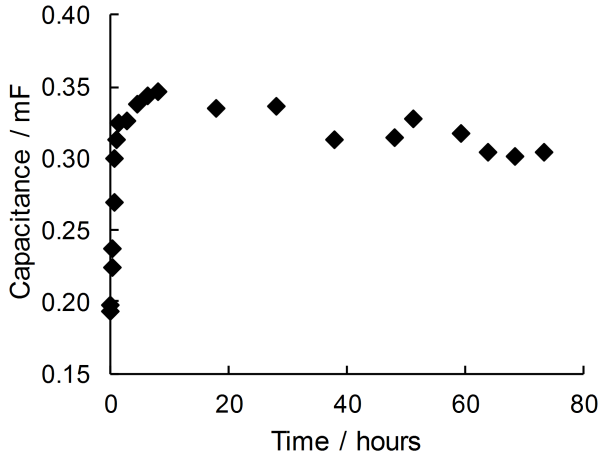

Figure 5.16: Change in C_{rds} throughout galvanostatic-ageing.

XPS was used to further analyse the changes to the nickel surface throughout galvanostatic-ageing (Figure 5.17). While similar XPS spectra is found for all samples galvanostatically-aged for between 6 min and 100 h, the untreated etched nickel sample had an additional peak at 852 eV (and the associated $2\,p_{3/2}$ multiplet splitting peak at 868 eV) from metallic nickel [150]. The sample which had undergone the pre-treatment procedure (potentiostatic EIS at 0 V, -100 mV for 2 h, cycling at 50 mV s^{-1} for 20 cycles) had a significantly smaller nickel peak and a larger peak at 855 eV indicating that the pretreatment procedure was successful in oxidising the surface. The peaks due to metallic nickel cannot be distinguished on samples galvanostatically-aged for 6 min or more. This XPS data suggests that any differences in the surface structure formed during the galvanostatic ageing, are lost under the conditions used for the XPS measurements.

5.3.3 Updated Phase Diagram

Throughout this work it has become clear that there are additional phases to those described by the Bode model in Figure 5.1. As mentioned earlier, we suggest that there is a third Ni(II) phase which forms from metallic nickel at low potentials which we call $\alpha(II)_{compact}$. In addition to this phase, after a long period of oxygen evolution, an additional more highly-charged phase forms (γ_{aged}). We propose an update diagram based on this work (Figure 5.18).

In addition to the phases discussed in this work so far, others have identified phases which may also be present. Ohligschlager [135] shows, using EQCM, that during oxidation there is a third process occurring in addition to the α-γ reaction (shown by a mass gain), and the β-β reaction (shown by a mass loss at higher potentials). The third process occurs at lower potentials than the α-γ reaction. They theorise that this reaction is the oxidation of an inner layer which, with

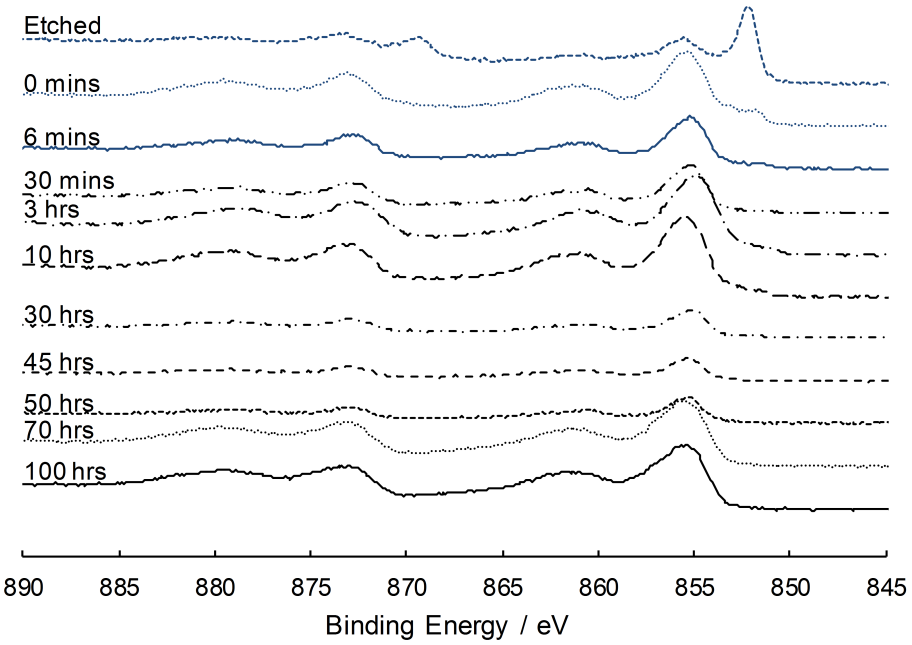

Figure 5.17: XPS data between 840 eV and 900 eV from nickel electrodes galvanostatically-aged for 0-100 h.

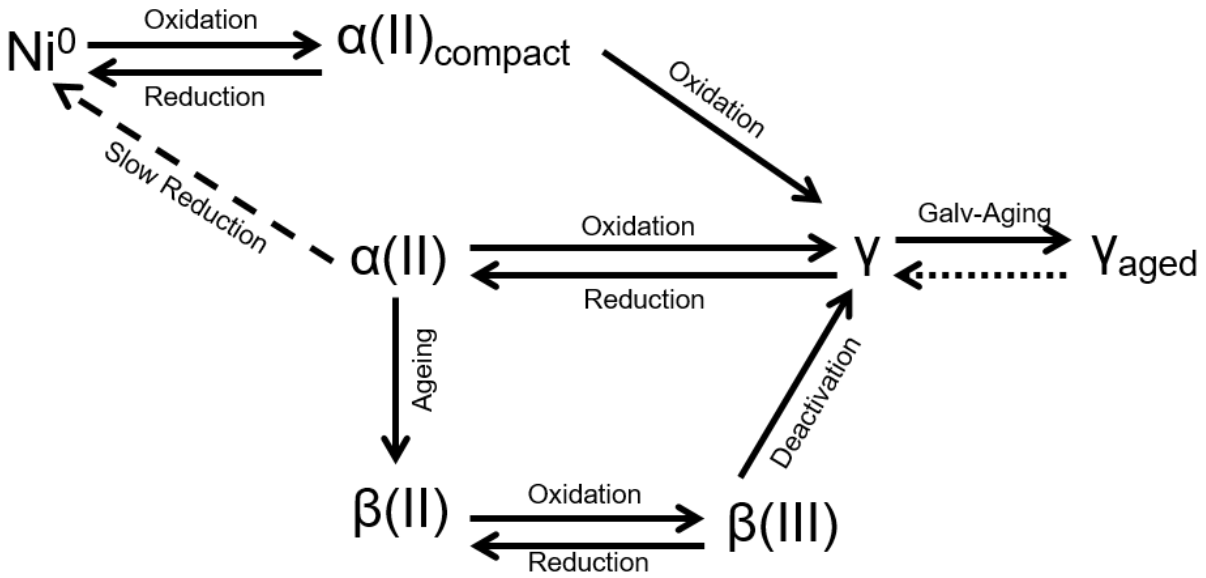

Figure 5.18: Updated model of nickel phases based on this work.

a lack of OH^- ions, oxidises to form a different structure (β*). As we use concentrated KOH and as the nickel oxide layers are unlikely to be as thick as those in Ohligschlarger's work [135] it is unlikely this phase is present in our examples. Another phase is found by Yeo et al. [113] using Raman Spectroscopy at the onset of oxygen evolution, through the transformation of β-NiOOH to a phase which is not equivalent to γ. We will refer to this as $\beta_{\mathrm{O2evolution}}$. Adding these phases to the diagram we obtain Figure 5.19, although it is unlikely that this model is complete and future work will add to it.

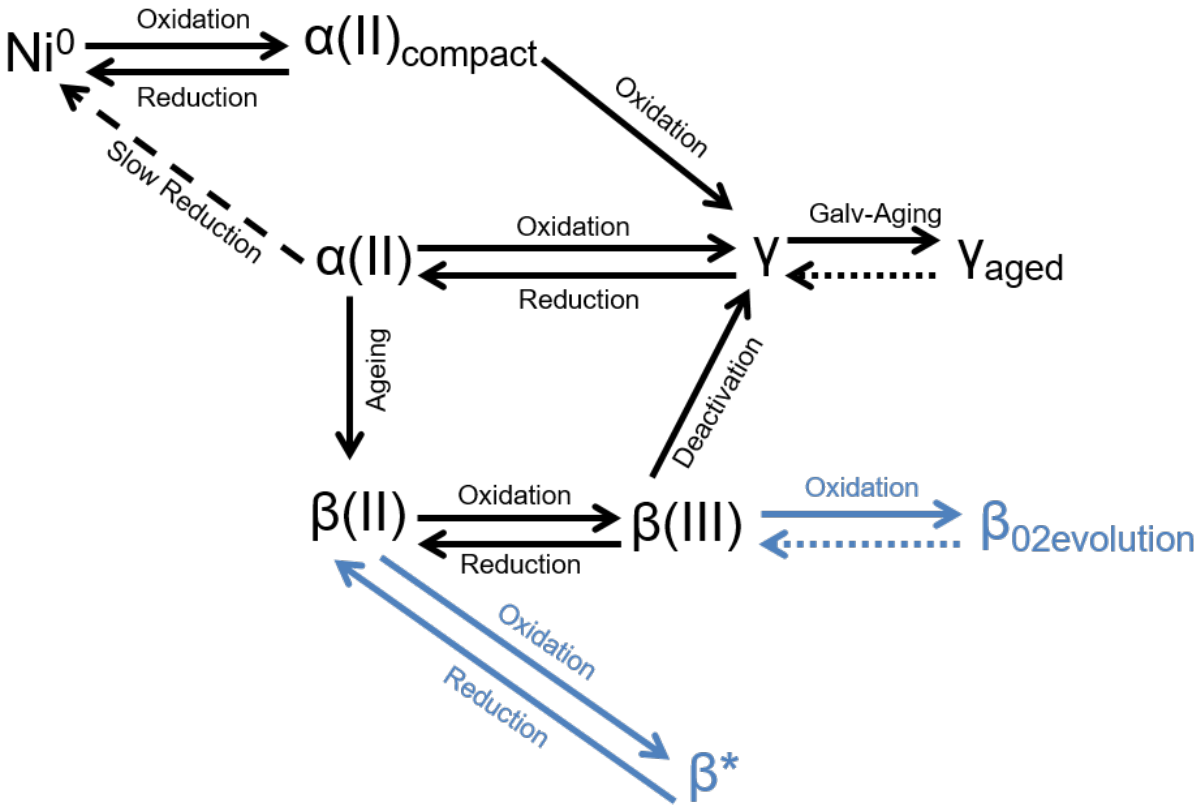

Figure 5.19: Updated model of nickel phases based on this work (black) and that of others (blue).

When referring to these diagrams keep in mind that these phases are not as clear-cut as the diagram suggests. There is often a slow transition from one phase to the next and thus the structure of the nickel oxy-hydroxide phase a point in time may be in fact a transitional phase. Bernard et al. [140] provide a good example, identifying a phase they refer to as badly crystallised β-$Ni(OH)_2$ (β_{bc}) occurring during the transition from α-$Ni(OH)_2$ to β-$Ni(OH)_2$.

5.4 Conclusions

The oxidation reactions on the surface of the nickel electrode in concentrated KOH electrolyte appear to be more complex than the simple α-γ and β-β reactions with cyclic voltammetry results,

indicating there are at least three surface reactions which can occur. In addition to this, there is evidence to suggest that it is neither α-$Ni(OH)_2$ nor β-$Ni(OH)_2$ which is formed from metallic nickel at low potentials, but a third phase which we call $\alpha(II)_{compact}$. At higher potentials, in situ XAS measurements suggest that the γ-NiOOH does not form further phases during oxygen evolution below 0.665 V.

During galvanostatic oxygen evolution, α/γ layers undergo a complex ageing pattern. There is an initial increase in performance (period I) which appears to be at least partially due to an increase in active surface area, followed by a stable potential for approximately 7 h (period II), before the performance begins to decrease (period III), followed by a more rapid performance decrease in period IV at which point a change in the cyclic voltammogram is seen. We suggest that this decrease in performance in period IV is due to the formation of a phase which contains a large amount of Ni^{4+}. The active phase present in period II is still unclear but may be a thin β-NiOOH layer.

Chapter 6

Improvement of Nickel Anode Performance Through Rejuvenation

This chapter has been published as:

Mellsop, S., Gardiner, A., & Marshall, A. (2015). Electrocatalytic oxygen evolution on nickel oxy-hydroxide anodes: Improvement through rejuvenation. Electrochimica Acta, 180, 501506. doi:10.1016/j.electacta.2015.08.061

Abstract

The ageing and rejuvenation behaviour of nickel oxy-hydroxide anodes for alkaline water electrolysis is investigated. The anodically formed oxy-hyroxide material is known to age over time causing a decrease in performance. However, this deactivation can be mitigated by temporarily reducing the potential for brief periods. This work looks at continuous rejuvenation of nickel anodes in 30 wt.% KOH solution and it is shown that rejuvenation at 0.5 V vs Hg/HgO for 10 min every 100 min can prevent ageing of the anode, thus maintaining a low overpotential during galvanostatic oxygen evolution at 50 mA cm^{-2}. It is suggested that the short potentiostatic rejuvenation periods at regular intervals prevents the ratio of Ni(IV) to Ni(III) from increasing, thereby maintaining the intrinsic activity of the material. The rejuvenation potential must be above 0.36 V vs Hg/HgO to ensure it is effective in obtaining good performance (i.e. the material must not reduce to Ni(II)). These findings suggest that electrolysis systems using nickel anodes could benefit from direct coupling to fluctuating power sources such as solar or wind, where the variability in their power output could facilitate the rejuvenation of the nickel anode. We estimate by using rejuvenation steps, an energy saving of 8% is possible in an alkaline water electrolyser using nickel anodes.

6.1 Introduction

Water electolysis has long been investigated as a way of producing very pure hydrogen gas from a renewable energy sources. Much of the research has focussed around developing electrocatalysis to improve the efficiency of electrolysers. Important factors to consider when choosing an electrocatalyst include its stability, performance, and cost. Many researchers have investigated nickel oxides as the electrocatalyst for the anodic oxygen evolution reaction [48, 7, 151, 111, 152, 94, 153], as it is much less costly than options such as iridium or ruthenium oxide and has reasonably good performance, with a potentials of approximately 750 mV vs Hg/HgO at a current density of 50 mA cm^{-2} (Chapter 5), and Tafel slopes as low as 38 mV. However, the performance stability under anodic conditions can be an issue, resulting in the performance of the electrocatalyst decreasing over time [94] (Chapter 5). As the loss in performance of nickel oxide anodes is generally accepted to be related to structural changes in the oxide, much of the research into nickel oxide electrocatalysts has involved investigating the structure of the electrocatalyst [94, 154, 155, 156, 157]. Traditionally four phases are thought to be present as shown in the Bode diagram [132] (Figure 6.1). The true map of phases and their transformations is likely to be more complex based on recent research [135, 113, 114, 119, 144, 130]. For example, Raman spectroscopy suggests that at the onset of oxygen evolution, NiOOH transforms to another phase [113] and similarly our cyclic voltammetry work suggested that after extensive oxygen evolution (at least 40 h at 50 mA cm^{-2}) an additional phase forms (Chapter 5). Many authors have also suggested that over-oxidation causes Ni(IV) to form [94, 158, 159, 134, 160] and XAS work performed by O'Grady shows that an overcharged nickel oxide electrode electrode has a Ni oxidation state of +3.5 clearly indicating the presence of Ni(IV) [149].

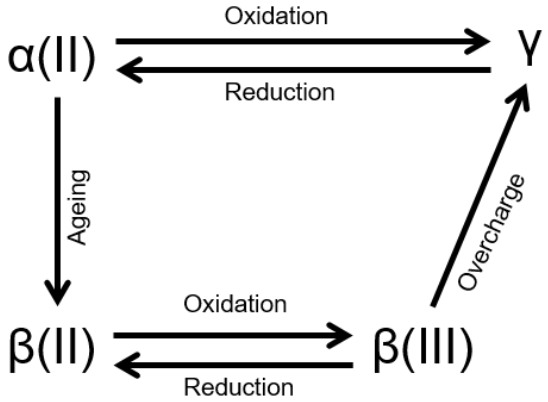

Figure 6.1: Bode diagram of known nickel phases.

Work by Lu and Srinivasan, and Osaka and Yatsuda [94, 153] has shown that the activity of a deactivated nickel oxide anode can be recovered by briefly decreasing the potential of the anode to values where minimal oxygen evolution occurs (1.5 V vs RHE). This rejuvenation can increase the current density by as much as 3-7 times, compared to that just prior to the rejuvenation

process [94]. Lu and Srinivasan [94] also showed that longer rejuvenation times at low potentials, gave larger performance recoveries. One explanation for the ageing or loss in activity (which can be reversed by rejuvenation) is simply that the thickness of the poorly conductive nickel oxide layer increases during the oxygen evolution reaction, thus increasing the ohmic resistance of the electrode. However the work of Lu and Srinivasan appears to rule this out as the main cause, and instead it has been suggested that the activity is improved by a thin layer of more highly active electocatalyst (perhaps *beta*-NiOOH) forming on the surface of the oxide during rejuvenation, and it is this which controls the specific activity, rather than the structure of the bulk oxide [94]. Here the rejuvenation of a nickel oxide electrode is investigated as a way of improving the activity for the oxygen evolution reaction. Specifically, the role of rejuvenation potential, time and frequency is examined, as well as the implications of the ageing and rejuvenation of nickel oxide anodes on the measurement of steady-state polarisation data.

6.2 Experimental

Nickel foil electrodes (Sigma-Aldrich ≥99.9%), with a surface area of 1 cm^{-2}, were cleaned in acetone for 5 min, ultrasonicated in water, etched in 1 M hydrochloric acid solution with 5.25 g L^{-1} of hydrogen peroxide for 15 min, then finally rinsed in deionised water. Contact to the nickel foil was achieved by spot welding a nickel wire (0.5 mm diameter) to a corner of the foil. This wire was insulated from the electrolyte using an inert thermosetting polymer.

A Gamry Instruments Reference 3000 potentiostat was used for electrochemical analysis. The electrochemical tests were performed in 30 wt% KOH solution (pellet basis, ≥ 85 wt% purity) in a thermostatically controlled PTFE cell at 25°C. Nickel foil (30 cm^{-2}) was used as the counter electrode along with a Hg/HgO (KOH) reference electrode. All potentials are referenced to the Hg/HgO (30 wt% KOH). Unless stated otherwise the following pretreatment procedure was used on the nickel electrodes: the freshly etched nickel electrodes were subjected to potentiostatic electrochemical impedance spectroscopy (EIS) at 0 V (to obtain the ohmic resistance between the reference and working electrodes) over the frequency range 0.2 - 100,000 Hz at 5 mV rms before the potential was held at -100 mV for 2 h (to ensure the electrode surface was covered in the α-$Ni(OH)_2$ phase), then cycled at 50 mV $s^{-1}$for 5 to 20 cycles between -0.1 V and 0.65 V.

All rejuvenation measurements involved galvanostatic oxygen evolution at 50 mA cm^{-2} coupled with potentiostatic rejuvenation periods at open circuit potential (OCP), 0.5 V, or 0.2 V. Cyclic voltammetry was performed at the end of all oxygen evolution/rejuvenation measurements at 50 mV s^{-1} from -0.1 V to 0.65 V. Slow linear scanning voltammograms discussed in Section 6.3.2 were performed at a rate of 0.2 mV s^{-1} following the initial electrode pretreatment and 40-80 h of galvanostatic oxygen evolution at 50 mA cm^{-2}. All potential measurements were were corrected for the uncompensated IR drop post measurement using the value determined by EIS.

6.3 Results and Discussion

6.3.1 Galvanostatic Ageing and Rejuvenation

When a nickel electrode is subjected to continuous potential cycling (e.g. cyclic voltammetry), a change in the oxide structure is known to occur [48, 127]. Here the cyclic voltammogram after 200 cycles is noticeably different to that after only 5 cycles (Figure 6.2). It is well known that this cycling causes a transition from the α-$Ni(OH)_2$ / γ-NiOOH solid-state redox couple to the β-$Ni(OH)_2$ / β-NiOOH couple [48, 127]. During cycling, the peak labelled A1, decreases in size while A1' and A2 grow. A2 stops growing at 200 cycles while A1' continues to grow. While it is unclear whether A1' or A2 corresponds to the oxidation of β-$Ni(OH)_2$ to β-NiOOH, galvanostatic oxygen evolution after cycling (data not shown) reveals that at least one of these peaks corresponds to the formation of a more active phase compared to the γ-NiOOH phase (which forms from α-$Ni(OH)_2$, peak A1). This is consistent with the recent work which clearly shows that potential cycling can improve the activity of a nickel oxide electrode towards the oxygen evolution reaction [7].

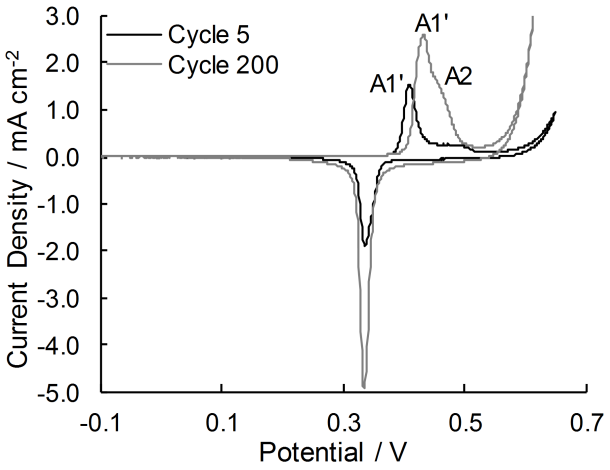

Figure 6.2: Cycle 5 and 200 of cyclic voltammograms performed at 50 mV s^{-1} between -0.1 V and 0.65 V following a pretreatment of potentiostatic EIS at 0 V over the frequency range 0.2 - 100,000 Hz at 5 mV rms and constant potential at -100 mV for 2 h.

For an electrode which has only undergone 5-20 cycles during the initial electrode pretreatment (and thus is only in the α-$Ni(OH)_2$ / γ-NiOOH structure), a very characteristic ageing behaviour is observed during galvanostatic oxygen evolution (Figure 6.3a). The galvanostatic ageing can be split into five periods: an initial decrease in overpotential (period 1), a period of good performance (period 2), a slow increase in overpotential (period 3), a steep increase in overpotential (period 4), and finally a stable high potential (period 5). While it is clear that initially only the α-γ phases are present at the start of galvanostatic ageing, once period 4 is reached, a second pair of peaks appear in the voltammograms (A3 and C3) (Figure 6.3b). By comparing the voltammogram from this galvanostatically aged α-$Ni(OH)_2$ / γ-NiOOH anode with that in Figure 6.2, it is clear that peaks A3 and C3 arise from a different solid-state redox pair to those found after ageing by cyclic

voltammetry. We suggest that peaks A3 and C3 result from the formation of a structure containing Ni(IV).

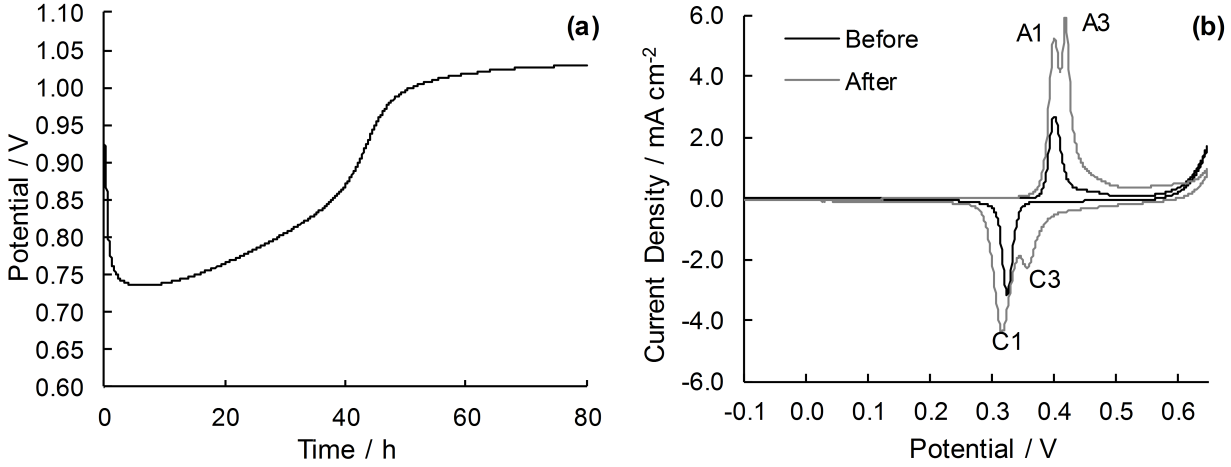

Figure 6.3: Anode potential over 80 h of galvanostatic oxygen evolution at 50 mA cm^{-2} (a) and cyclic voltammograms performed before and after the galvanostatic period (b).

While nickel oxide anodes (initially with the α/γ structure) are slowly deactivated during galvanostatic oxygen evolution, it is observed that the activity can be partially recovered if the potential is temporary decreased to 0.5 V before return back to the galvanostatic oxygen evolution (Figure 6.4). An example of this is given in Figure 6.4, where oxygen evolution at 50 mA cm^{-2} is interrupted after 40 h by a 10 min rejuvenation step at 0.5 V. Just prior the the rejuvenation step, the anode potential is 0.82 V (and increasing), whereas immediately after the rejuvenation step the potential is about 0.8 V (and approximately stable for 5-10 h), i.e. a rejuvenation of 20 mV. This rejuvenation affect is also seen in other work [94, 153] and has been suggested to be related to a rapid change in the surface of the oxide, upon decreasing the potential, to a form which is more intrinsically active toward the oxygen evolution reaction [94]. This active oxide layer is said to have a higher ratio of Ni(III) to Ni(IV) than the layer before rejuvenation, and is consistent with the Pourbaix diagram for nickel [14] which shows that approximately 0.6 V vs Hg/HgO is the transition potential for Ni(III) to Ni(IV).

After the brief period of stable anode potential after the rejuvenation step, the potential increases again and follows the characteristic deactivation or ageing process (in other words, the rejuvenation is only temporary). However, it takes approximately 15 h of galvanostatic oxygen evolution (post rejuvenation) before the anode potential reaches the same value as just prior to rejuvenation, despite the rather brief duration (10 min) of the rejuvenation step. Similar results are described by Lu and Srinivasan [94] but under potentiostatic oxygen evolution conditions.

6.3.2 Periodic or continuous rejuvenation

As brief rejuvenation steps appear to improve the performance for many hours, it was hypothesized that by carrying out the rejuvenation steps periodically throughout oxygen evolution, the slow

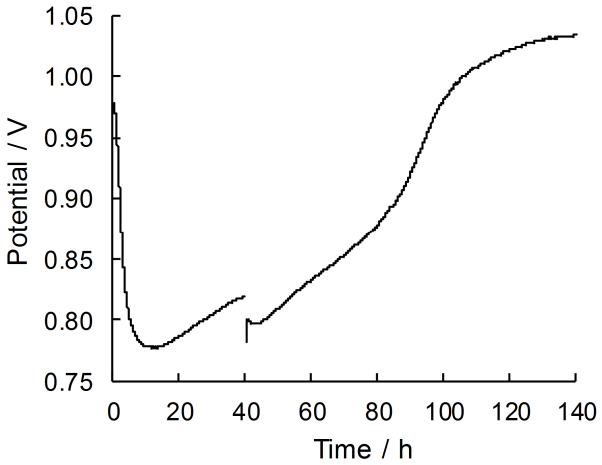

Figure 6.4: Galvanostatic oxygen evolution at 50 mA cm^{-2} with a rejuvenation step at 40 h. The potential was held at 0.5 V for 10 min during the rejuvenation step.

ageing and loss in performance found for nickel oxide anodes may be prevented. Thus continuous rejuvenation was carried out by periodically holding the potential of the anode at 0.5 V for 10 min every 100 min during oxygen evolution at 50 mA cm^{-2} (Figure 6.5a). By rejuvenating the anode periodically, the potential (at 50 mA cm^{-2}) can maintained at low values for at least 120 h (compare Figure 6.3a with Figure 6.5a). We note that the average anode potential over the 120 h is very similar to the minimum potential found during a normal long-term oxygen evolution measurement at 50 mA cm^{-2}. Furthermore, unlike the normal galvanostatic operation, there is very little change in the cyclic voltammograms before and after the 120 h of oxygen evolution under the periodic rejuvenation operation. We therefore conclude that the periodic rejuvenation steps has prevented the slow phase transformation which normally occurs during long-term oxygen evolution. A similar periodic rejuvenation operation was also attempted wherein the rejuvenation step was reduced to 1 min at 0.5 V every 100 min. Under this mode of operation, no significant improvement over the normal galvanostatic operation was observed (i.e. the rejuvenation time was insufficient), and thus further measurements are required to optimise the rejuvenation time.

The effect of rejuvenation potential was also examined by conducting periodic rejuvenation using a lower potential of 0.2 V (Figure 6.6a). This potential was selected to be sufficiently cathodic to ensure that the oxide undergoes the NiOOH to $Ni(OH)_2$ phase change during the rejuvenation step. This clearly gives significantly different results than those seen for a rejuvenation potential of 0.5 V. Overall, the activity is not as good as that achievable when the rejuvenation potential is 0.5 V, nor does the potential reach the same minimum as when no rejuvenation is performed. However, as with the rejuvenation potential of 0.5 V, the severe deactivation (i.e. when the potential slowly increases to approximately 1 - 1.05 V) which normally occurs under galvanostatic operation, is not observed.

Examining the voltammogram measured after the 120 h of periodic rejuvenation, immediately reveals that changes to the oxide structure has occurred over the 120 h of operation (Figure 6.6b).

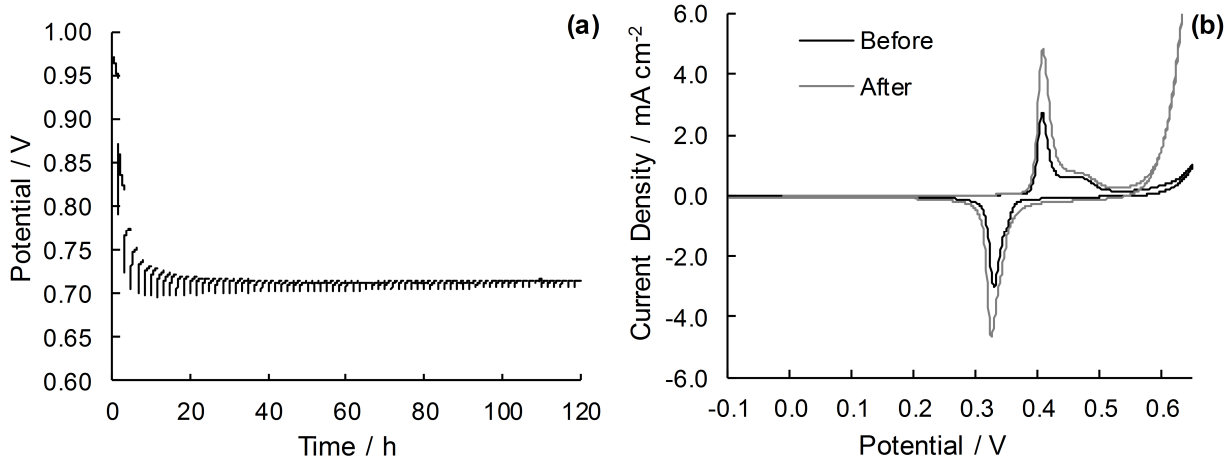

Figure 6.5: Galvanostatic oxygen evolution at 50 mA cm^{-2} with rejuvenation steps down to 0.5 V for 10 min in every 100 min (a) and cyclic voltammograms at 50 mV s^{-1} between -0.1 V and 0.65 V performed before and after oxygen evolution (b).

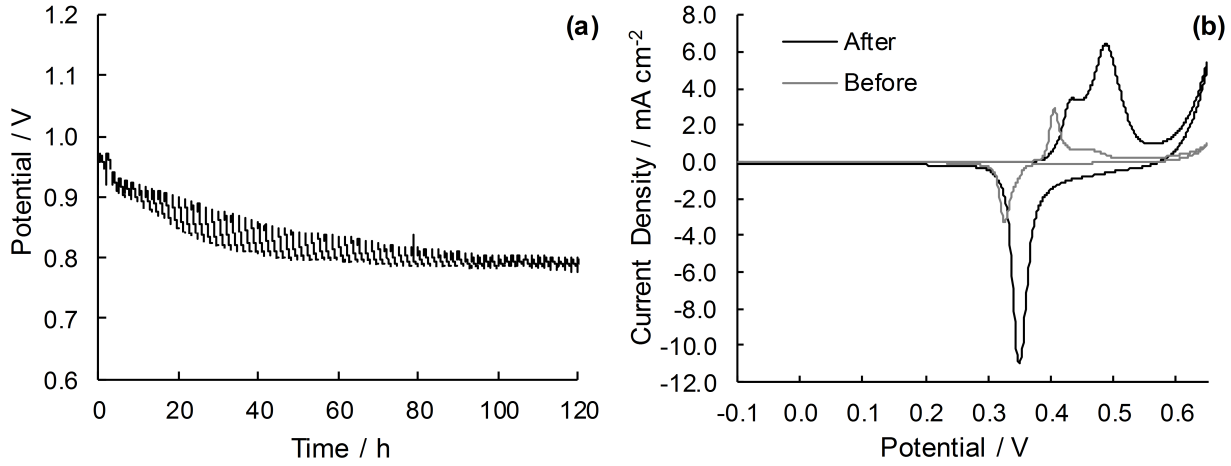

Figure 6.6: Galvanostatic oxygen evolution at 50 mA cm^{-2} with rejuvenation steps down to 0.2 V for 10 min in every 100 min (a) and cyclic voltammograms performed at 50 mV s^{-1} between -0.1 V and 0.65 V before and after oxygen evolution.

A slight anodic shift in the potentials of peaks A1 and C1 have occurred and a large anodic peak at approximately 0.48 V is observed, which we attribute to the process identified by peak A2 in Figure 6.2. As both A1 and C1 have shifted to higher potentials, it is unlikely that this shift is due to the transition of the oxide layer towards the β/β structure as the cathodic peak corresponding to the reduction of β-NiOOH to β-$Ni(OH)_2$ is normally at a more cathodic potential than the γ-NiOOH to α-$Ni(OH)_2$ reaction [155, 114]. One could suggest that these two peaks are equivalent to those labelled as A3 and C3 in Figure 6.3b, but this is also unlikely as A3 and C3 are usually observed along with A1 and C1 [134]. One may also argue that this shift is caused by a shift in the potential of the reference electrode, however this is unlikely due to the regular testing of reference electrodes against stable standards in our laboratory. Despite the uncertainty in the origin of this peak shift, what is more important is the significant growth in peak A2 and the implications that this peak has on the anodes activity towards the oxygen evolution reaction. Given that most authors refer to β-NiOOH as the "right type of oxide" for oxygen evolution [94], the fact that A2 dominates the voltammogram and the performance is relatively poor suggests A2 is not associated with the β-β reaction. However, given the uncertainty in the literature regarding identification of the peaks on a nickel oxide voltammogram, a more accurate statement is possibly that the phase which forms during peak A2 is not active as the phase which forms during peak A1'.

While periodic rejuvenation could enable water electrolysis systems to operate more efficiently, incorporating potentiostatic rejuvenation steps within an electrolyser's control system may add an unacceptable degree of complexity. An alternative and more simple approach would be to use periodic open circuit rejuvenation steps throughout galvanostatic operation. Typically, for this type of anode, the open circuit potential (OCP) is around 0.3-0.5 V (i.e. similar to the potential which does indeed rejuvenate the anode). For this reason the long-term behaviour of the nickel oxide anode was investigated at 50 mA cm^{-2} with periodic rejuvenation steps at OCP for 10 min every 100 min (Figure 6.7a). Given the importance which the rejuvenation potential has on the overall long-term behaviour of the anode, OCP during the 10 min rejuvenation segments was also measured (Figure 6.7a). During the first 10 h the potential at 50 mA cm^{-2} is similar to when a 0.2 V rejuvenation step was used (Figure 6.6), although after this the activity of the anode improves to the point where it is almost equal to that achieved by the electrode operating with the 0.5 V rejuvenation steps (Figure 6.5a). At the point where there is a noticeable improvement in the activity (after approximately 10 h - vertical line on Figure 6.7), the average OCP measured during the open circuit rejuvenation steps increases above 0.36 V. This potential is approximately equal to the potential at which the cathodic reduction peak starts in the cyclic voltammogram (Figure 6.7). From this, it is inferred that in order for rejuvenation to take place, and enable the activity of the anode to remain high, the rejuvenation potential must stay above 0.36 V, i.e. the nickel oxide must not be reduced below Ni(III). The cyclic voltammogram measured after the 120 h is similar to that measured prior to the long-term operation (albeit with slightly larger peaks). This would be expected as the this operation enabled the anode to operate at 50 mA cm^{-2} with similar anode potentials to the electrode with rejuvenation steps controlled at 0.5 V.

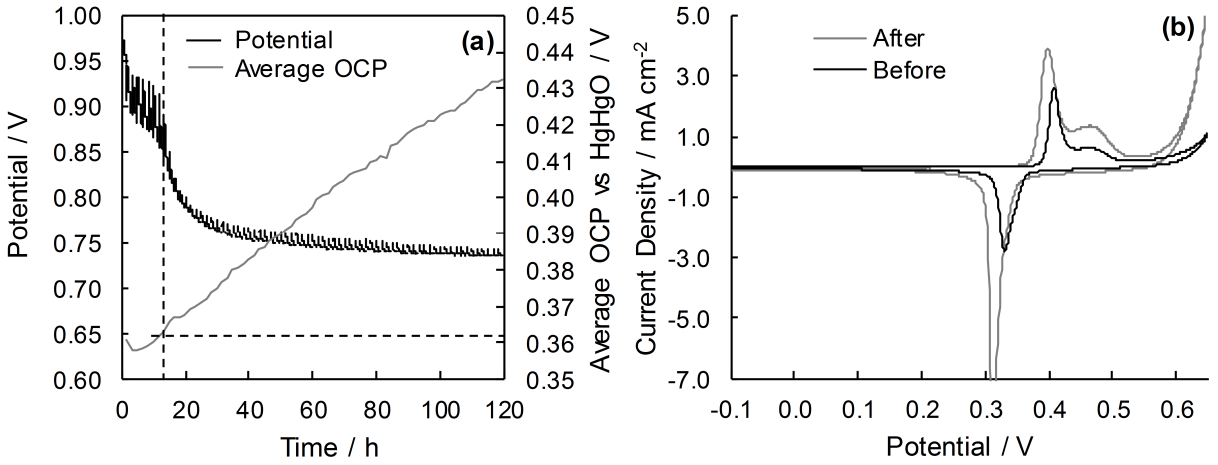

Figure 6.7: Galvanostatic oxygen evolution at 50 mA cm^{-2} with rejuvenation steps at open circuit potential for 10 min in every 100 min (a) and cyclic voltammograms at 50 mV s^{-1} between -0.1 V and 0.65 V performed before and after oxygen evolution at 50 mV s^{-1} between -0.1 V and 0.65 V (b). The dashed lines in (a) indicate the time at which the OCP during the rejuvenation step exceeds 0.36 V.

While the successful rejuvenation appears to require brief periods at potentials between 0.36-0.5 V, the mechanism is not completely clear. Lu and Srinivasan suggest that it is the reduction of Ni(IV) (formed during oxygen evolution) to Ni(III) which is responsible for the rejuvenation [94], however our attempts to measure the charge or current associated with this hypothesised reduction process were unsuccessful due to the presence of anodic oxygen evolution which occurs above approximately 0.3 V. In situ x-ray absorption spectroscopy was also unsuccessful in identifying any oxide structures containing Ni(IV) during oxygen evolution up to 0.665 V (Chapter 5). Although it is important to note that these in situ measurements were performed on Ni anodes which had not undergone extensive galvanostatic ageing immediately prior to testing. Thus it is likely that the concentration of any Ni(IV) species(which may be responsible for the deactivation) present in the oxide film will very low and undetectable by these XAS measure-ments. However others have measured XAS spectra consistent with the Ni oxide films containing Ni(IV) species after extensive anodic polarisation [149].

6.3.3 Linear Scanning Voltammetry and Polarisation Curves

The characteristic ageing of a nickel oxide anode (initially with the α-γ oxide structure) clearly complicates the measurement of a steady-state polarisation curve. To illustrate this, polarisation curves were measured after 40 and 80 h of galvanostatic oxygen evolution at 50 mA cm^{-2} (Figure 6.8), and as expected the activity of the anode which had undergone oxygen evolution for only 40 h was more active than that after 80 h of oxygen evolution. What is more problematic for the accurate determination of the electrodes activity, is that the potential at 50 mA cm^{-2} just prior to the measurement of these polarisation curves was considerable different to that measured during

the polarisation curve (Figure 6.8). This is easily explained by the rejuvenation effect (e.g. Figure 6.4), as the polarisation curve was obtained by stepping the potential from that at 50 mA cm^{-2} (0.86 V after 40 h or 1.07 V after 80 h) to 0.5 V before increasing the potential at 0.2 mV s^{-1}. It is also observed that the polarisation curve for the anode after 40 h of OER, has significant hysteresis between the forward and reverse sweep directions.

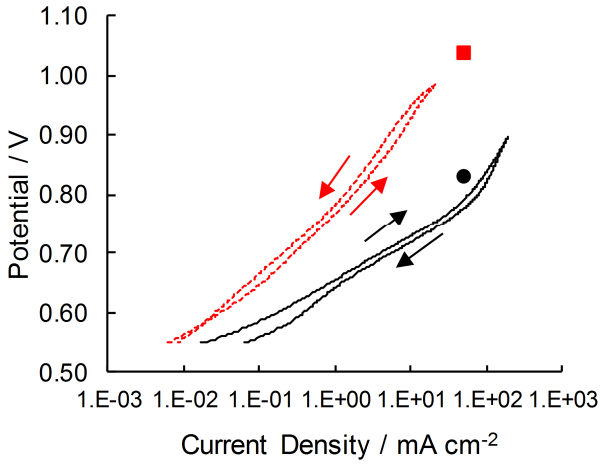

Figure 6.8: Slow linear scanning voltammetry from 0.55 V to 1.0 V and back after galvanostatic OER at 50 mA cm^{-2} for 40 (dashed line) or 80 h (solid line). The arrows indicate the direction of the potential sweep used to measure the polarisation data. The solid data points (circle - 40 hrs, square - 80 hrs) give the potential at 50 mA cm^{-2} measured during the galvanostatic OER prior to these polarisation measurements.

To better understand the hysteresis between the forward and reverse sweeps, three sweeps were performed in succession (reverse, forward, reverse) immediately after galvanostatic OER at 50 mA cm^{-2} for 45 h (Figure 6.9). The use of a reverse sweep from the OER potential at 50 mA cm^{-2} ensures that the rejuvenation effect cannot affect the shape of the polarisation curve until the potential reaches a sufficiently low potential (e.g. 0.5 V). The first reverse sweep starts at approx 0.82 V (close to 50 mA cm^{-2}) and has a steeper slope than the subsequent two curves. On the following forward sweep the slope has decreased and the performance has improved i.e., during the small amount of time at low potentials (e.g. 0.5 V) the material has rejuvenated and the performance improved. During the second reverse sweep (Reverse 2) the performance decreases again but not enough for the potential to follow the same path as that seen for "Reverse 1", suggesting that the rejuvenation process is noticeably faster than the ageing process - consistent with our findings that short rejuvenation steps can result in long periods of rejuvenated performance (Section 6.3.2).

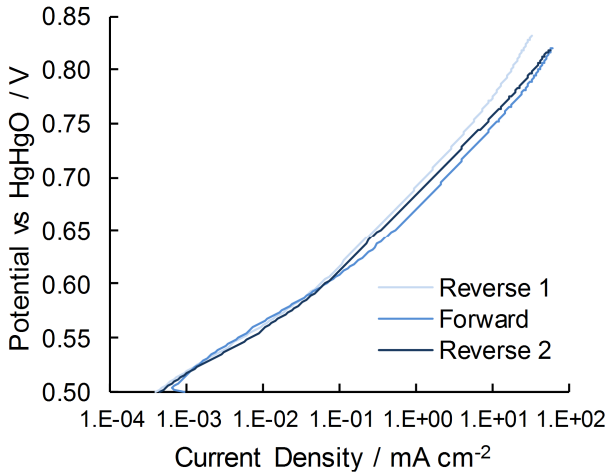

Figure 6.9: Slow linear scanning voltammetry between 0.5 V and 0.85 V (reverse, forward, reverse) after galvanostatic OER at 50 mA cm^{-2} for 45 h.

6.4 Implications of rejuvenation in water electrolysis systems

The potentials shown in the Figures 6.3 and 6.5 were used to calculate the approximate energy requirements for a simple cell with electrodes 500 cm^2 in size. A constant potential for the hydrogen evolution reaction of -1.17 V vs Hg/HgO [161] and a negligible ohmic loss were assumed. For 80 h of hydrogen production at 50 mA cm^{-2} a cell with no rejuvenation requires 4.1 kWh while a cell with rejuvenation requires only 3.8 kWh. That is a saving of 8%. We do note that due to the rejuvenation time it takes longer to complete the 80 h of hydrogen evolution at 50 mA. Because of this a system such as this would work well with solar and wind power as they have inherent variability in their power output. Further studies would need to be performed to investigate whether the natural variation would be enough to rejuvenate the anode.

The potentials shown in the Figures 6.3 and 6.5 were used to calculate the approximate energy requirements for a simple single cell electrolysis cell. A constant potential for the hydrogen evolution reaction of -1.17 V vs Hg/HgO [161] at 50 mA cm^2 and a negligible ohmic loss were assumed. We have also assumed that the rejuvenation steps will have little influence on the stability and performance of the cathodic hydrogen evolution reaction, as the cathode is unlikely change from its metallic state during the brief rejuvenation steps. For the case of no rejuvenation, we have used an anode potential of 0.890 V vs Hg/HgO (the average potential from Figure 6.3), although we note that for long term operation the likely anode potential will be even higher at around 1.0 V vs Hg/HgO. For an anode operating with rejuvenation, the average measured anode potential at 50 mA cm^2 only 0.723 V vs Hg/HgO (Figure 6.5a). Thus under these conditions, the estimated cell potential for a galvanostatic electrolyser would be 0.890+1.17=2.060 V, whereas the electrolyser with rejuvenation would only require approximately 0.723+1.17=1.893 V. Thus at 50 mA cm^2, to supply the charge required to generate 1 kg H_2 gas (9.5722×10^7 C) a galvanostatic electrolyser would require a total of 55 kWh (4.92 kWh per normal m^3 H_2) while a cell with rejuvenation requires

only 50 kWh (4.52 kWh per normal m^3 H_2). This equates to an energy saving of approximately 8%. We do note that due to the minimal electrolysis during the rejuvenation periods, either larger electrodes or longer times would be required to produce a given quantity of H_2, but complete analysis of the economic aspects of these two operation modes is beyond the scope of this paper.

6.5 Conclusions

Electrocatalytic nickel oxide anodes slowly age during the oxygen evolution reaction in alkaline electrolytes. When the performance starts to decrease significantly, a clear change in the anodes cyclic voltammetry response is observed, indicating a change in the anodes surface chemistry. This ageing can be prevented through a rejuvenation process.

Holding the potential at 0.5 V vs Hg/HgO for 10 min every 100 min of galvanostatic oxygen evolution has been shown to rejuvenate the material and prevent the decrease in performance due to anode ageing. It is thought that this rejuvenation prevents an increase in the ratio of Ni(IV) to Ni(III). We have also shown that the rejuvenation potential can be lower than 0.5 V but it must not allow the surface to reduce to Ni(II) (i.e. the rejuvenation potential must be above 0.36 V). Through rejuvenating the nickel anode material at regular intervals, hydrogen can be produced with 8% less energy compared to an electrolyser running under continuous galvanostatic operation.

Chapter 7

Cobalt Electrocatalytic Coatings: The Effects of Preparation Procedure and Preparation Temperature

This chapter has been published as:

Mellsop, S., Gardiner, A., & Marshall, A. (2014). Electrocatalytic Oxygen Evolution on Electrochemically Deposited Cobalt Oxide Films: Comparison with Thermally Deposited Films and Effect of Thermal Treatment. Electrocatalysis, 5(4), 445455. doi:10.1007/s12678-014-0212-3

Abstract

Electrocatalytic cobalt oxide layers have been prepared on nickel substrates using thermal decomposition and electrochemical deposition methods. Importantly, it was confirmed that the electrochemical deposition method could be applied to nickel foam substrates for use in zero-gap alkaline water electrolysis cells. The oxide layers produced were then investigated for their activity towards the oxygen evolution reaction in 30 wt% KOH solution and found to be superior compared with the uncoated nickel substrate. Layers produced by both methods had similar electrochemical behaviour, provided that the layers were annealed at temperatures $\geq 350°C$. This thermal treatment was required to mechanically stabilise the electrochemically deposited cobalt oxide layer. Due to this finding, the effect of annealing temperature was investigated for the electrochemically deposited layer, and it was found that the overpotential for oxygen evolution increased with annealing temperature. Using cyclic voltammetry and impedance spectroscopy, it is concluded that the decrease in performance with increasing annealing temperature is largely caused by the corresponding decrease in active surface area. However, for annealing temperatures $\geq 400°C$, additional resistances are introduced that cause lowered performance. The impedance data suggest that these additional resistances are caused by either a decrease in the conductivity of the cobalt oxide layer itself, or the formation of a passivating-like nickel oxide layer between the active cobalt oxide and the nickel

substrate, or both. The resistances' dependance on potential suggests that they originate from a semi-conducting material and these additional resistances ultimately give rise to non-linear Tafel behaviour.

7.1 Introduction

In order to increase the efficiency of a water electrolysis cell, electrocatalysts are used to decrease the overpotential of the oxygen and hydrogen evolution reactions. These electrocatalysts must exhibit good electrochemical stability and have high activity for the reaction, while being inexpensive and easy to manipulate [3]. In general it is found that the oxygen overpotential is more difficult to reduce than the hydrogen overpotential [1].

The performance of an electrocatalyst is largely defined by the intrinsic activity and the active surface area of the material. Because the Tafel slope is an intensive property, it is a useful measure to compare the intrinsic activity of materials [23]. While noble metals such as ruthenium, rhodium and iridium are highly active for oxygen evolution (with low Tafel slopes of 40-50 mV [88, 63, 22, 1]) the cost of these materials suggests other materials are preferable. Cobalt oxides are one such alternative [17, 162, 54, 163, 56], with some studies showing Tafel slopes between 40 mV and 50 mV are possible [49, 57, 55, 22].

In addition to selecting materials with high intrinsic activity, maximising the active surface area of the electrocatalyst is also advantageous. Recently, cobalt oxides have been used as supercapacitors [164] due to their ability to create high surface area structures, further suggesting cobalt oxides could be a promising OER electrocatalyst.

There are multiple methods of preparing cobalt oxides, including electrodeposition [54, 100], thermal decomposition [36, 42] and sol-gel processes [165], with the preparation method potentially having a large effect on its performance [67, 70, 23]. Thermal decomposition is known to produce electrodes with good stability [70, 39] and high performance in comparison to other methods [67, 70] while having the advantage that it is relatively simple compared to other methods. Electrodeposition can produce electrocatalysts with high surface area [102], can be used to coat more complex surfaces (such as nickel foam) and the thickness of the coating can be easily controlled by manipulating the current or charge applied to the electrodes. As achieving high surface area is an important goal, many researchers have investigated techniques of increasing the surface area to improve electrocatalytic performance by changing the preparation method [70], altering the annealing conditions [36, 166, 42], coating process [56], and precursor solvents [167].

In this work the electrocatalytic behaviour of cobalt oxide coated nickel substrates towards the oxygen evolution reaction in alkaline solution is examined. As the preparation method appears to influence the electrocatalytic behaviour, we compare electrocatalysts prepared by electrodeposition and thermal decomposition. Lastly, the effect of the electrodeposited layer's annealing temperature on the activity, surface area and stability was examined.

7.2 Experimental

Two methods of electrocatalyst preparation were examined: electrodeposition and thermal decomposition. In both cases a 1 cm^2 nickel foil substrate (Sigma-Aldrich $\geq$ 99.9%, 0.125 mm thick) was used. The foils were cleaned in acetone for 5 min, ultrasonicated in water, etched and then rinsed in deionised water. Etching was carried out in a 1 M hydrochloric acid solution with 5.25 g L^{-1} of hydrogen peroxide for 15 min. Contact with the nickel foil was achieved by spot welding a nickel wire (0.5 mm diameter) to one corner of the foil.

The cobalt oxide coatings produced via thermal decomposition followed the normal dimensionally stabilised anode approach. The etched nickel anodes were placed onto a hot plate at 85°C and sprayed with the precursor solution (0.1 M $Co(NO_3)_2$, Sigma-Aldrich $\geq$ 98%) in an 80% isopropanol solution, before being transferred to a pre-heated (250°C or 350°C, static air atmosphere) furnace for 10 min. This was repeated four or five times until the electrode was coated with 2-2.5 mg cm^{-2} of cobalt oxide, before a final annealing at 250°C or 350°C for 2 h.

In addition, oxide layers were prepared by electrodeposition, following a method similar to that described by Brownson and Levy-Clement [103]. $Co(OH)_2$ was galvanostatically deposited onto the etched nickel foil from a 0.005 M $Co(NO_3)_2$, 0.1 M KNO_2 solution at -0.5 mA cm^{-2} for 4000 s in a three electrode glass cell. Nickel foam was used as a counter electrode, and a saturated calomel electrode (SCE) used as the reference electrode. Argon was bubbled through this solution to minimise the influence of dissolved oxygen. After electrodeposition, the electrodes were rinsed in isopropanol for 5 min and dried at 80°C for 30 min, before being annealed at temperatures beween 200°C and 500°C for 2 h. The annealing procedure was required to ensure sufficient mechanical stability of the cobalt oxide coating produced by this method.

All electrochemical measurements were performed in a 30 wt% KOH solution (pellet basis, $\geq$ 85 wt% purity) at room temperature using a Gamry Instruments Reference 3000 potentiostat. Nickel foam was used as a counter electrode together with a Hg/HgO (30 wt% KOH) reference electrode. The hydrogen evolution potential is approximately -930 mV vs Hg/HgO [26] and therefore the equilibrium potential for the OER is 300 mV vs Hg/HgO. The coated electrodes were investigated by cyclic voltammetry from -100 mV to 650 mV; electrochemical impedance spectroscopy (EIS) at DC currents of 5-100 mA cm^{-2} using a 5 mV rms AC amplitude over the frequency range 0.2 Hz - 100 kHz; and examined for their oxygen evolution performance using both galvanostatic measurements at 50 mA cm^{-2} for 6 h and a slow potential scan between 550 mV and 750 mV at 0.2 mV s^{-1}. The ohmic resistance between the working and reference electrodes was determined by EIS measurements and compensated for in the steady state polarisation curves (post-measurement) and CV measurements (positive feedback).

An electrocatalytic coating was also prepared on nickel foam (INCOFOAM^{TM}) for the purposes of longer stability tests, and to confirm the compatibility of the electrode coating method with nickel foam substrates. For this electrode, the etching time was decreased to 5 min and the electrodeposition time was increased from 4000 s to 8000 s due to the additional surface area of

the foam.

7.3 Results and Discussion

7.3.1 Thermal Decomposition vs Electrodeposition

As previous work has indicated that electrocatalytic behaviour can be influenced by preparation method [67, 70], in these experiments we directly compare cobalt oxide coatings prepared by electrodeposition and thermal decomposition. Cyclic voltammetry reveals that the coatings with an annealing temperature of 350°C (prepared by both electrodeposition and thermal decomposition) have similar surface properties to a pair of redox peaks around 480 mV vs Hg/HgO (Figure 7.1). The potential of these peaks is similar to that found by Boggio et al. [36], and corresponds to the following Co(III)/Co(IV) surface reaction [36, 100, 57, 44]:

$$CoOOH + OH^- \rightleftharpoons CoO_2 + H_2O + e^- \tag{7.3.1}$$

where CoOOH is the surface structure of Co_3O_4 when in contact with the alkaline solution at open circuit potentials [36].

In our work, both the coating produced by thermal decomposition at 350°C, and the two produced by electrodeposition have a broad cathodic peak at approximately 350 mV which is not believed to arise from the Co(III)/Co(IV) redox process. Other authors have also seen additional peaks; Castro et al. [100] suggested that these are due to $Ni_xCo_{3-x}O_4$; Singh et al. [56] indicated that their additional peaks are due to the oxidation of the underlying nickel substrate. Another option is that the extra peaks are caused by non-stoichiometric cobalt oxide. According to the Pourbaix diagram for cobalt, CoO oxidises to Co_3O_4 at around -140 mV to 50 mV vs Hg/HgO, which is significantly less than the potentials seen here so it seems unlikely that the anodic peak around 350 mV is due to CoO oxidation. Instead, we attribute the peak to the nickel substrate, as its potential is similar to that observed in our measurements with uncoated nickel in 30 wt% KOH solution. These peaks also increase, rather than decrease, in size after electrolysis for 6 h, supporting our hypothesis that they are due to nickel, as it is known that the peak currents from nickel can increase with electrolysis time [114].

Unlike the electrodeposition samples, which appear similar after annealing at 250°C or 350°C, the thermal decomposition layers at 250°C are significantly different to those annealed at 350°C (Figure 7.1). A temperature of 250°C may be insufficient to completely oxidise the Co^{2+} to Co^{3+} from $Co(NO_3)_2$, resulting in a non-stoichiometric coating, or a coating which is not completely covering the nickel, allowing the KOH solution to reach a larger portion of the nickel layer underneath. Because the electrodeposition process produces a cobalt hydroxide layer prior to annealing, it is likely that the Co_3O_4 phase can be more readily produced at 250°C. Brownson and Levy-Clement [103] showed that similar electrodeposited films undergo complete oxidation or dehydration (as evidenced by TGA) by 250°C. For thermal decomposition, Boggio et al. [36] suggests that 230°C

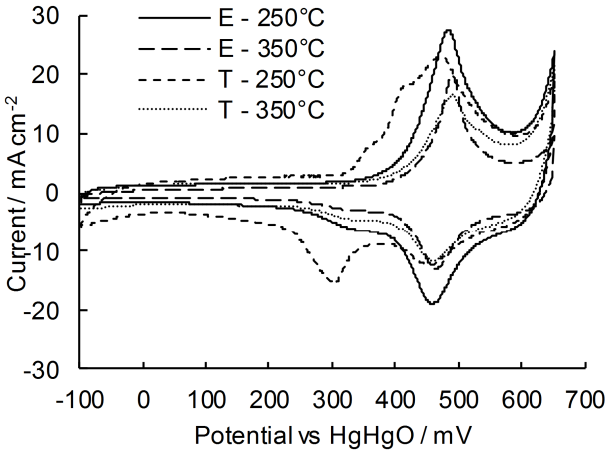

Figure 7.1: Cyclic voltammograms at 50 mV s^{-1} comparing electrodes produced by electrodeposition and thermal decomposition with two annealing temperatures. Cyclic voltammograms were measured after 6 h of electrolysis at 50 mA cm^{-2}. T = Thermal Decomposition, E = Electrodeposition.

is required to form Co_3O_4 electrodes from $Co(NO_3)_2$, while TGA analysis reported elsewhere [167] indicates a temperature of 265°C is required. Although this temperature can be as low as 150°C for long decomposition times (48 h) [167]. Garavaglia [167] also found that when cobalt oxide is deposited in layers, rather than prepared as a powder, a higher temperature is required before stoichiometric Co_3O_4 is obtained. Based on this prior literature, it seems likely that under our preparation conditions, complete conversion of the nitrate precursor to stoichiometric Co_3O_4 does not occur after 2 h at 250°C using the thermal decomposition process.

In order to assess the stability of the oxides, cyclic voltammetry was performed before and after 6 h of oxygen evolution at 50 mA cm^{-2}. Little change in the voltammograms is observed before and after electrolysis, indicating that these electrodes have good stability over this time frame.

Polarisation curves during oxygen evolution indicate that of the four electrodes examined, the electrodeposited electrocatalyst annealed at 250°C has the best performance (Figure 7.2, Table 7.1), despite having a lower catalyst loading than both the thermal decomposition electrocatalysts. The electrodeposited sample with the higher annealing temperature of 350°C has noticeably lower performance than that prepared at 250°C, while there is little difference between the activities of the two electrodes prepared by thermal decomposition. Importantly, all four electrodes have similar, and relatively low Tafel slopes of 45±2 mV (Table 7.1), indicating that they probably follow the same reaction mechanism for the OER. While it is difficult to compare the performance of these catalysts with uncoated nickel due to its well-known ageing process [85, 95, 143], we normally observe that the minimum potential for OER on un-coated nickel electrodes at 50 mA cm^{-2} is approximately 725 mV, 33-50 mV higher than the cobalt oxide coated electrodes.

To confirm the cobalt oxide electrocatalyst can be deposited onto nickel foam (the intended substrate for use in a zero gap electrolysis cell [168]), an electrode was prepared by electrodeposition

Table 7.1: Potential, current and Tafel slope measurements for cobalt oxide catalysts deposited onto nickel foil. The oxide loading on the substrates are also given. T = Thermal decomposition, E = Electrodeposition.

Deposition Method	Annealing Temperature /°C	Loading /mg cm^{-2}	Potential at 50 mA cm^{-2} /mV	Current density at 600 mV /mA cm^{-2}	Tafel Slope /mV
E	250	1.1	675	1.3	46.8
E	350	1.0	692	0.4	43.0
T	250	1.4	681	0.9	46.3
T	350	1.8	678	1.0	45.8

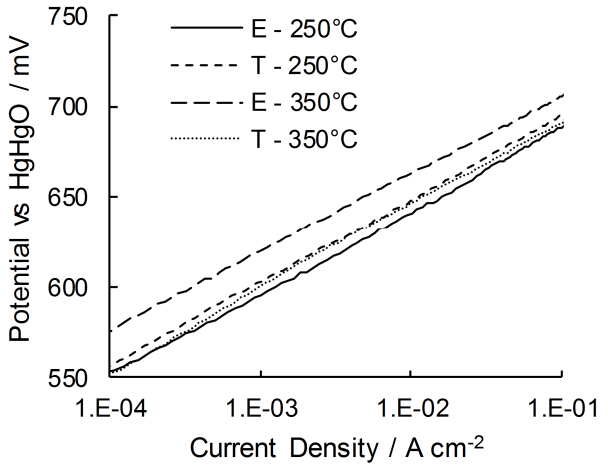

Figure 7.2: Tafel plot of electrodeposited and thermally deposited electrocatalysts at two annealing temperatures. T = Thermal decomposition, E = Electrodeposition.

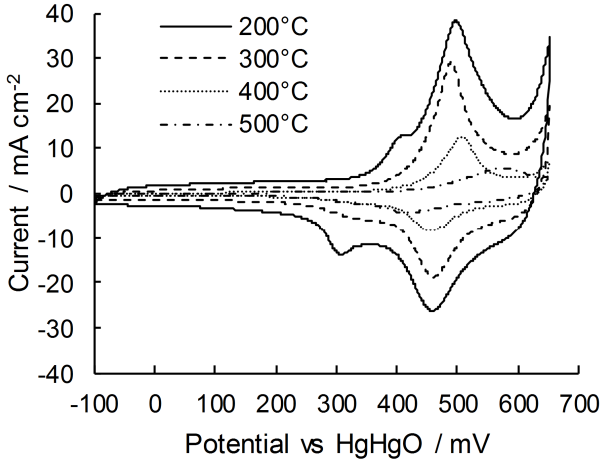

Figure 7.3: Cyclic voltammograms (at 50 mV s^{-1}) of electrodeposited coatings annealed at four temperatures. Cyclic voltammograms were measured after a 6 h of electrolysis at 50 mA cm^{-2}.

followed by annealing. Over a 72 h electrolysis test at 50 mA cm^{-2}, this coated foam electrode exhibited a smaller overpotential than uncoated nickel foam (a difference of 36 mV at 72 h), and better stability, with a performance decrease of ∼0.2 mV hr^{-1} for the cobalt oxide coated material and ∼0.6 mV hr^{-1} for the uncoated material.

7.3.2 Effect of temperature on electrodeposited catalyst

While there has been a significant amount of investigation into the effect of heat treatment on cobalt oxide produced by thermal decomposition [169, 36, 166], to date we know of no reports investigating the effect of annealing temperature when layers are produced by electrodeposition. As the electrodeposition method can be more easily used for complex geometries such as nickel foam, we have conducted these investigations in this work [170].

The cyclic voltammograms (Figure 7.3) show that for the electrocatalysts annealed between 200°C and 500°C, there is a clear set of peaks at approximately 480 mV vs Hg/HgO, corresponding to the reaction given by Equation 7.3.1. At 500°C, the forward peak has moved to a higher potential (and the reverse peak to a lower potential), which is likely due to an additional ohmic resistance within the oxide as observed by impedance spectroscopy discussed in Section 7.3.3.

For the electrocatalyst annealed at 200°C, there is a second peak on the forward scan at approximately 350 mV vs Hg/HgO, likely originating from the nickel substrate as discussed in Section 7.3.1. Generally it is observed that the electrocatalytic coatings treated at 200°C (or lower) are mechanically unstable, indicating that temperatures greater than 200°C are needed to produce mechanically stable layers. This may also explain why the nickel substrate contributes to the CV response: parts of the substrate are not fully coated due to insufficient adhesion of the coating. The nickel peak can also be seen on the back sweep for the sample annealed at 300°C, but is not seen at the higher temperatures, most likely due to further crystallization preventing the electrolyte from accessing the substrate through pores once treated at higher temperatures.

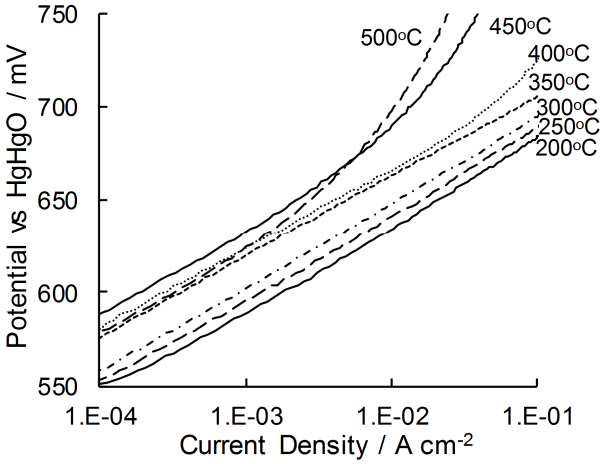

Figure 7.4: Tafel plots of electrocatalysts prepared by electrodeposition with a range of annealing temperatures.

The steady state polarization curves (Figure 7.4) show that at low currents the Tafel slope is similar for all annealing temperatures (45 ± 3 mV), and is similar to those reported in literature [17, 47, 56]. At annealing temperatures of 400°C and above, there is a clear change in Tafel slope at higher currents which, is often attributed to a change in mechanism [22]. However, for these catalysts, the change in slope may be due to an additional ohmic resistance within the electrode after treatment at higher temperatures. While there is a clear trend showing performance decreases with higher annealing temperature (Figure 7.4), all electrodes exhibit lower overpotentials than uncoated nickel.

One explanation of the decrease in performance with annealing temperature is that the electrochemically active surface area of the electrodes decreases due to sintering or crystallisataion of the oxide coating. To evaluate this possibility, capacitance measurements using cyclic voltammetry and EIS have been used to compare the relative active areas of the electrodes as a function of annealing temperature (Figure 7.6). The capacitance can be evaluated by measuring the double layer charging current as a function of sweep rate during cyclic voltammetry [120]. It can be difficult to find a potential on the cyclic voltammogram for which there is no surface reaction occurring. Another problem with this method is that it gives information about the surface area at a lower potential, rather than at an OER potential, where the cobalt oxide has a different surface structure. The capacitance can also be determined by fitting a model to the impedance measurements (such as those in Figure 7.5). The advantage of this method is that the capacitance during the OER can be found, unlike the double layer capacitance method. While the two methods give differing capacitance values, they both reveal that capacitance decreases with increasing annealing temperature (Figure 7.6), consistent with what many find for similar oxide electrode coatings [36, 69, 98] and the results from the two methods are highly correlated (Figure 7.6 insert). One possible reason for the higher capacitance values obtained through impedance modelling is the addition of pseudo capacitance due to a proton exchange reaction between the oxide matrix and the electrolyte, as de-

scribed by Ardizzone et al. [29] and Lyons and Brandon [43]. Taking the double layer capacitance to be 60 μF cm^{-2} [37] gives a roughness factor of 960 cm$^2_{\text{true}}$ cm^{-2} (for the sample with the highest surface area) and thus a specific surface area of 140 m^2 g^{-1}. This is equivalent to 82 F g^{-1}, which is realistic given that cobalt oxide based super-capacitors can achieve capacitance values of greater than 800 F g^{-1}. Upon removing the influence of the surface area by normalising the current by the roughness factor, we find the decrease in with annealing temperature is predominately due to the loss of surface area with no evidence to suggest a change in intrinsic activity.

7.3.3 Impedance Analysis

In order to gain further insight into the electrode changes caused by the annealing conditions, EIS during oxygen evolution was performed. For samples annealed at low temperatures (200°C - 350°C), the Nyquist plot shows one main loop with an indication of a smaller loop at higher frequencies (Figure 7.7a). As the annealing temperature increases to 400°C, this smaller loop increases in size and becomes more visible, and the high frequency real axis intercept appears to shift to higher Z_{real} values (Figure 7.7b). We propose that this shift is due in part to the increasing importance of a third component which appears as a clear high frequency loop for electrodes annealed at 450-500°C (Figure 7.7c). While a shift in the high frequency impedance could be attributed to changes in the uncompensated electrolyte resistance (R_S, such significant changes in R_S are unlikely due to our cell design and electrode placement. Rather, we propose that the additional resistance originates from within the electrode itself, due to either a passive layer on the substrate, or changes to the conductivity of the cobalt oxide layer. When modelling the data we have chosen to set R_S to 0.4560 Ω cm^2 as this was a typical figure observed for electrodes annealed at lower temperatures.

To interpret the EIS data, it is common to use equivalent circuit based modelling. Similar to others [44, 43, 46, 122], constant phase elements (CPEs) are used in our models, as the data reveals that the capacitive-like features do not behave as ideal capacitors. Normally CPEs are used to account for heterogeneities and rough surfaces [46]. In this paper we use the notation RQ to refer to resistors in parallel with CPEs within the equivalent circuit.

For most of the cobalt oxide electrodes in literature, the impedance data shows one main loop (due to the double layer and OER reaction) in the Nyquist plot, and therefore some choose to model the data using an equivalent circuit similar to Randles (for example Castro et al. [100]). In this work, additional circuit elements are required to adequately describe our impedance data. Lyons et al. [20] use a model similar to that shown in Figure 7.5a, where there is an additional RQ element to more accurately describe the kinetic behaviour. Authors have also seen additional loops for cobalt oxide catalysts when deposited onto iron or titanium supports [100, 44, 122]. Additional loops seen in impedance data for oxygen evolution catalysts are often related to a passivating-like oxide layer on the underlying metal substrate [100] or on the electrocatalytic oxide film itself [43].

Two models, each with a high and low temperature form, have been considered for this system (Figure 7.5). Both of these models are based on a baseline model (Figure 7.5b) which is commonly used for oxygen evolution catalysts [100, 121, 43]. The baseline model is used as the high tem-

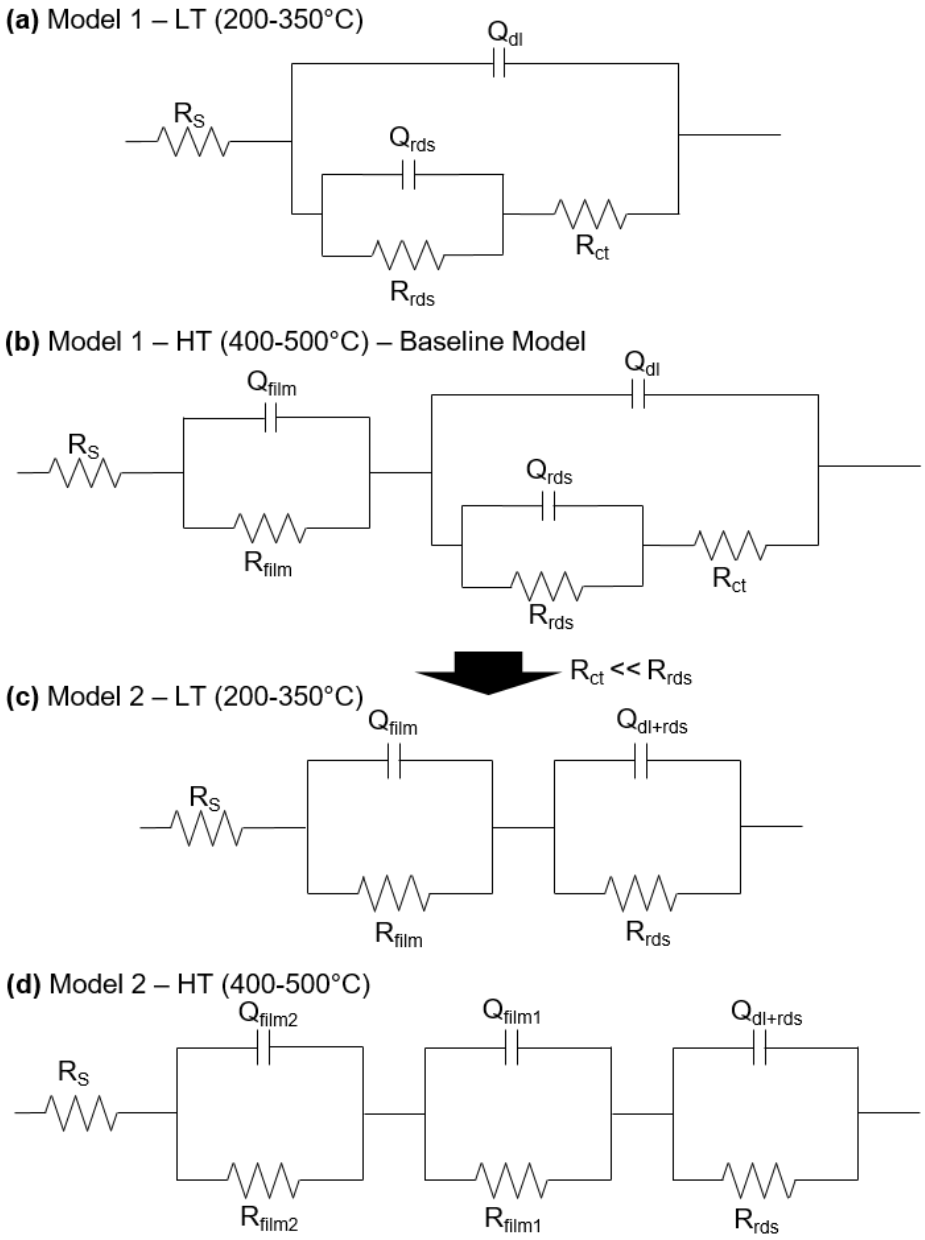

Figure 7.5: Electrical circuit models for use in interpretation of EIS analysis.

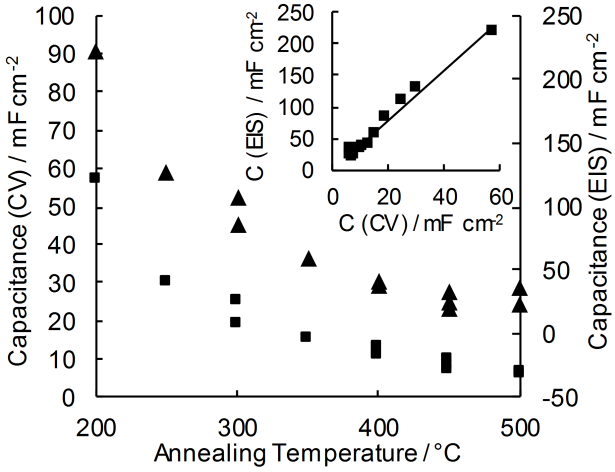

Figure 7.6: The capacitance calculated from the cyclic voltammograms (■) and impedance measurements (C_{dl+rds}) (▲) as a function of annealing temperature. The insert compares the two methods for obtaining capacitance.

perature version of Model 1 (Model 1 HT). Model 1 LT is commonly used for oxygen evolution electrocatalysts, including cobalt oxide [100, 20, 122] which is usually annealed below 400°C. In these models R_S is the solution resistance and Q_{dl} is the double layer charge capacitance. Q_{film} and R_{film} represent the film capacitance and the film resistance respectively, and could be related to the cobalt oxide film or a nickel oxide film. R_{ct}, Q_{rds} and R_{rds} are parameters related to the OER mechanism. R_{ct} is the resistance due to interfacial charge transfer [43], and Q_{rds} and R_{rds} are kinetic parameters related to the rate determining step [100]. Palmas et al. [122], relate Q_{rds} and R_{rds} to the transition of Co(III) to Co(IV) while Lyons et al. [20] relate them to the relaxation of charge of the absorbed intermediate.

The second model is also based off the baseline model for oxygen evolution electrocatalysts (Figure 7.5b) by assuming that R_{ct} is much smaller than R_{rds} and therefore the time constants of the two loops are too similar to model separately without a large amount of uncertainty [100]. Under this assumption, the baseline model (Figure 7.5b) is simplified to Model 2 LT (Figure 7.5c) and Q_{dl} and Q_{rds} combine to give Q_{dl+rds}. In this modified model, R_{film} is significant at lower temperatures, whereas the high frequency feature at low temperatures is assumed to relate to the OER reaction in Model 1. In Model 2 an extra RQ element is added at 400°C and above to account for the additional loop seen in the impedance data. Thus there are two film RQ elements in Model 2 HT, one related to a nickel oxide layer and the other to the cobalt oxide film. Laouini et al. [44] analysed the impedance for cobalt oxide deposited on stainless steel at a temperature of 400°C and used a model with three RQ loops in series to analyse the data, similar to the model being used here at high temperatures.

Either of the two models may correctly describe the behaviour of the electrode, as both fit the data well and have similar goodness of fit parameters. As pointed out by Harrington and van den Driessche [171], often many models can be made to fit the same set of data. As both models appear

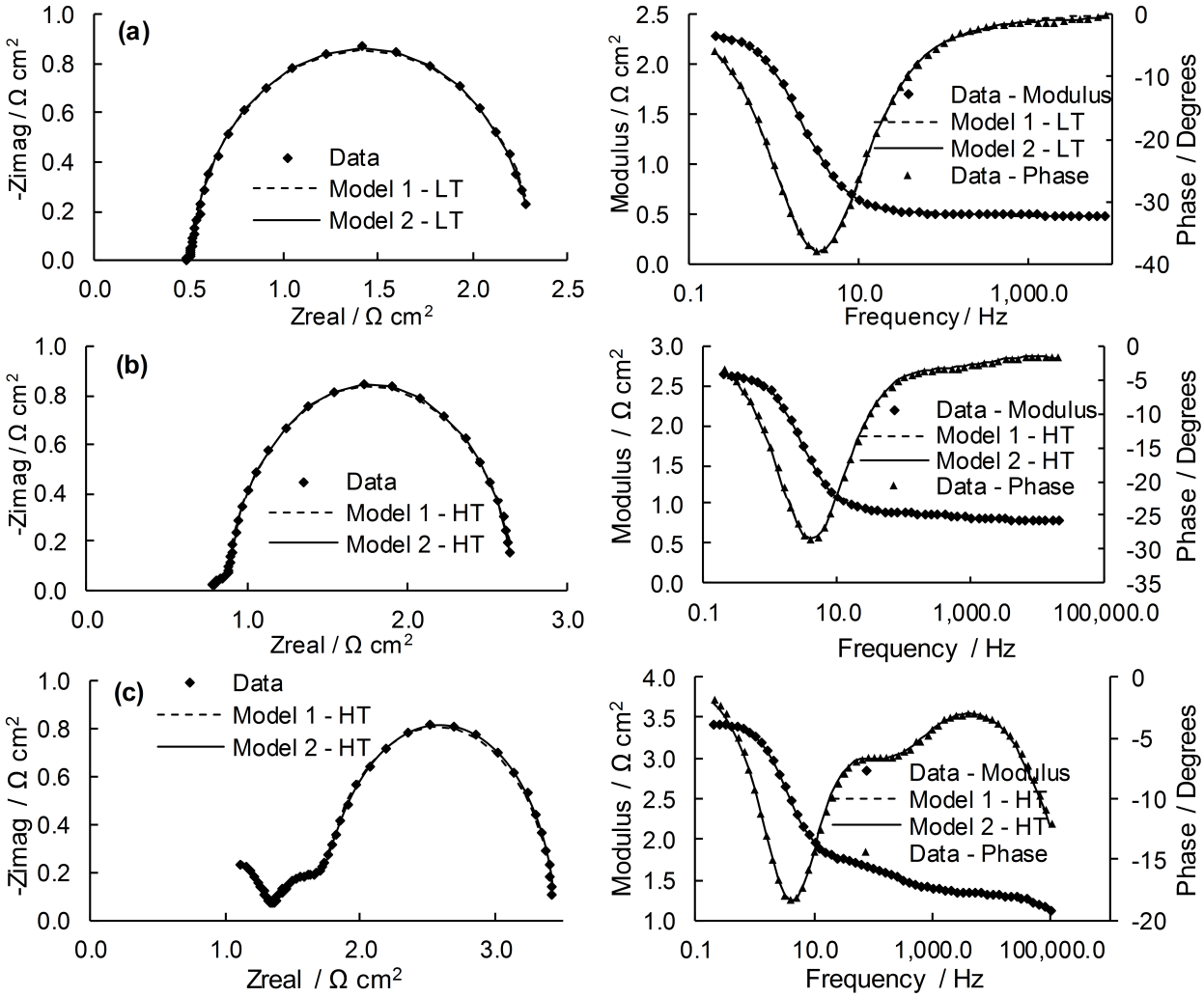

Figure 7.7: Nyquist and Bode plots for an electrodeposited coatings annealed at (a) 350°C, (b) 400°C, (c) 450°C.

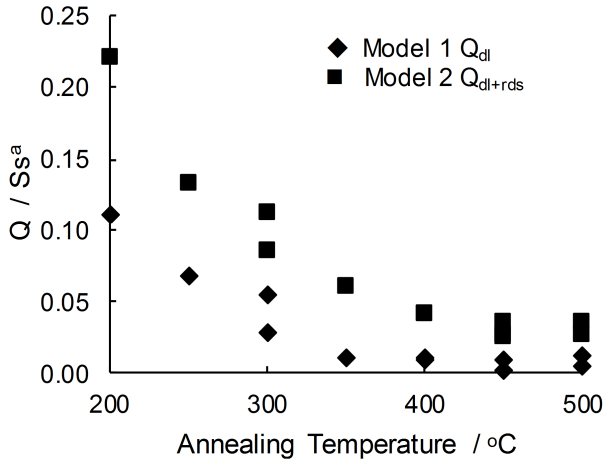

Figure 7.8: Change in Q_{dl} and Q_{dl+rds} with temperature at 10 mA cm^{-2}.

to fit the data equally well, we have chosen to extract the various parameters from both models in order to gain insights into possible physical explanations for the observed changes in the impedance data.

Q_{dl} from Model 1 and Q_{dl+rds} from Model 2 both decrease with temperature in a similar way (Figure 7.8), and are consistent with double layer capacitance measured by cyclic voltammetry, with the most likely explanation simply related to a loss in active surface area through sintering and crystallisation.

Both Model 1 and Model 2 suggest an increase in film resistance with temperature, with this increase more apparent at annealing temperatures greater than or equal to 400°C (Figure 7.9c and 7.9d). Three possible causes for an increased film resistance are: increased cobalt film resistance with annealing temperature; increased resistance between the cobalt and nickel layer; increased nickel oxide film resistance due to a thicker passive nickel oxide layer between the cobalt oxide and nickel metal. Veena Kumari et al. [172] investigated the oxidation mechanism of nickel and found that at temperatures of 400°C and 500°C, the diffusion of nickel cations into the metal oxide surface increases, leading to the formation of a three-dimensional NiO layer. Whereas at temperatures below 400°C, the nickel atoms only oxidise where they have easy access to the atmosphere. These observations suggest that in our work, nickel passivation only becomes significant above 400°C, as this is where an increase in the film resistance parameter is seen. We have also performed impedance measurements on nickel foil electrodes, both fresh and annealed, which show that an additional loop forms in the impedance data when annealed (not shown). It seems unlikely that the increases in R_{film}, R_{film2} and R_{film2} are related to electrochemical surface reactions, as these resistances are not proportional to the active surface areas calculated from capacitance measurements (Figure 7.6).

Applying Model 1 to the data suggests that R_{ct} increases with temperature, particularly above annealing temperatures of 400°C. While this could be explained in part by the observed decrease in surface area with increasing temperature, the relative change in surface area is insufficient to account for all of the increase in R_{ct}. This implies that the intrinsic activity of the cobalt oxide

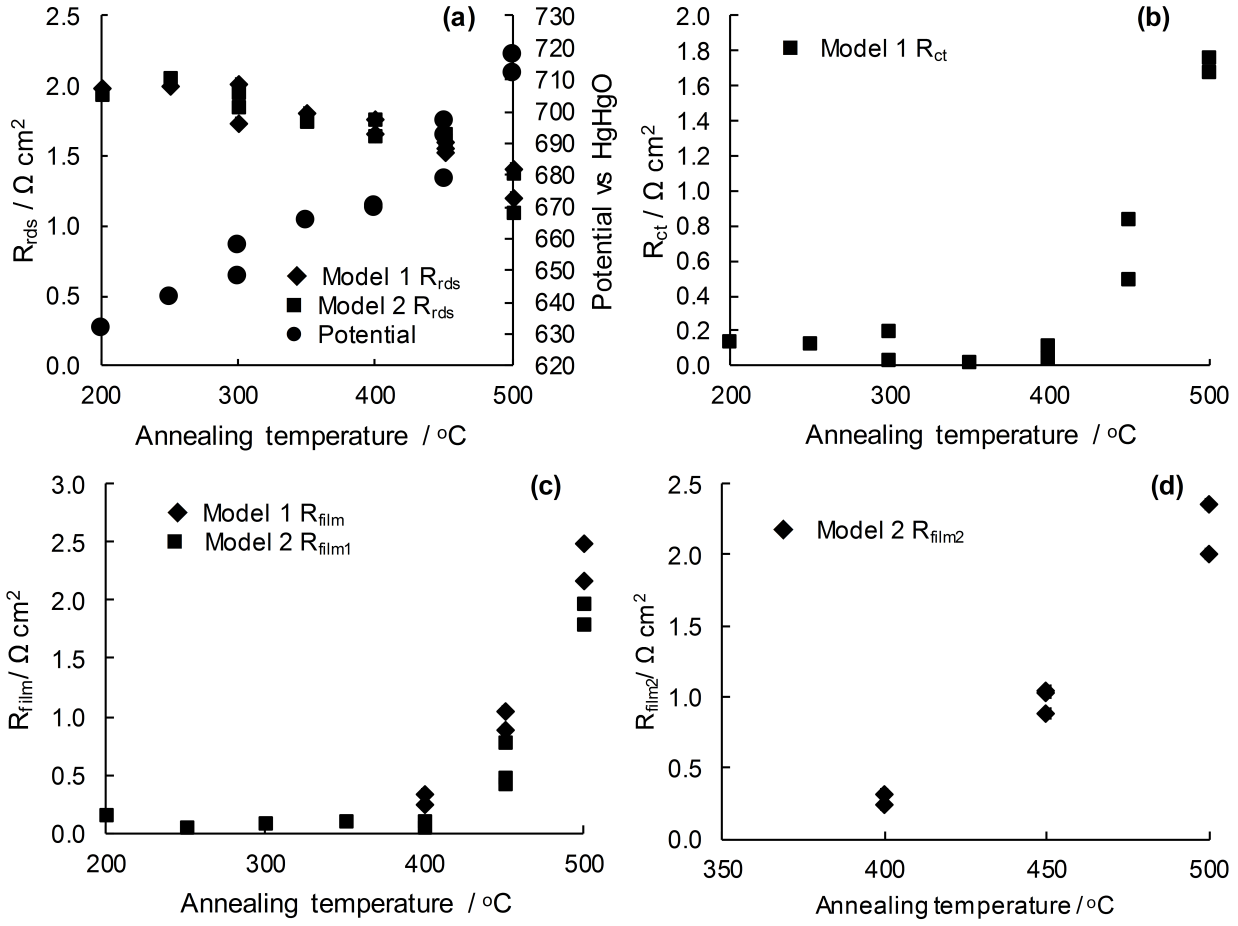

Figure 7.9: Change in R_{rds} (a), R_{ct} (b), R_{film} and R_{film1} (c) and in R_{film2} (d) with annealing temperature at 10 mA cm^{-2}.

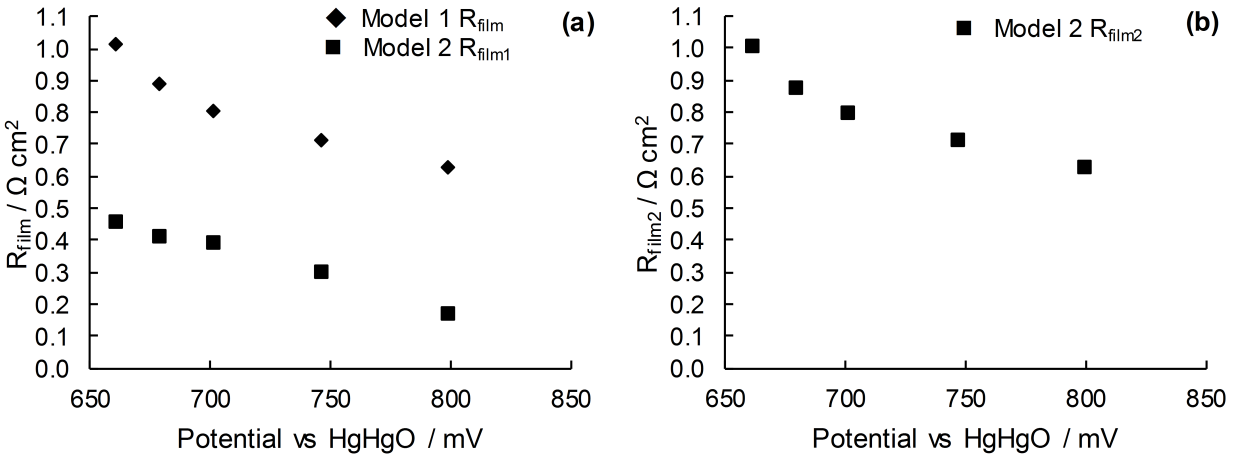

Figure 7.10: Change in R_{film} and R_{film1} (a) and R_{film2} (b) with potential for the coatings annealed at 450°C.

coating decreases with increasing annealing temperature. While this is possible given the likelihood that initial cobalt hydroxide coating crystallises to Co_3O_4 at higher temperatures, others suggest that CoOOH and Co_3O_4 have similar intrinsic activities for the OER [173].

Using the information extracted from the various EIS models, we have attempted to gain an insight into the underlying cause behind the apparent increase in Tafel slope at high currents for the electrodes annealed at high temperature. Many attribute an increase in Tafel slope at high current densities (like that seen in Figure 7.4) to a change in the reaction mechanism or rate determing step [22]. However, the change in Tafel slope seen in our data at high temperatures can be explained by an additional film resistance. As both nickel oxide and cobalt oxide are known to be semiconductors, their resistances (in our case R_{film}, R_{film1} and R_{film2}) change with potential. This is observed in our impedance data recorded over a range of potentials for electrodes annealed at 450°C (Figure 7.10). If we take Model 2 to be correct, it is not the activity of the catalyst itself which is causing the apparent increase in Tafel slope at higher potentials, but the additional uncompensated resistances R_{film1} and R_{film2}. Compensating for these resistances results in the steady-state polarisation curve showing a single Tafel slope over the entire current range (Figure 7.11). This means that rather than the reaction mechanism changing, there are simply additional ohmic resistances (other than R_S) causing the potential to increase. Taking Model 1 to be correct (and compensating for R_{film}) has a similar effect, although there is still some evidence to suggest a change in Tafel slope at currents above 0.01 A cm^{-2}. It is important to realise that film resistances are functions of potential, and using a resistance measured at low potentials over the entire polarisation curve range results in significant overcompensation.

Our results suggest that the annealing temperature of electrochemically deposited cobalt oxide films should be kept as low as possible to both maximise surface area (Fig 7.6) and minimise the impact of resistance increases originating from the film itself (Fig 7.9c and 7.9d). However, as these coatings required some annealing to mechanically stabilise the layer, there may be some long

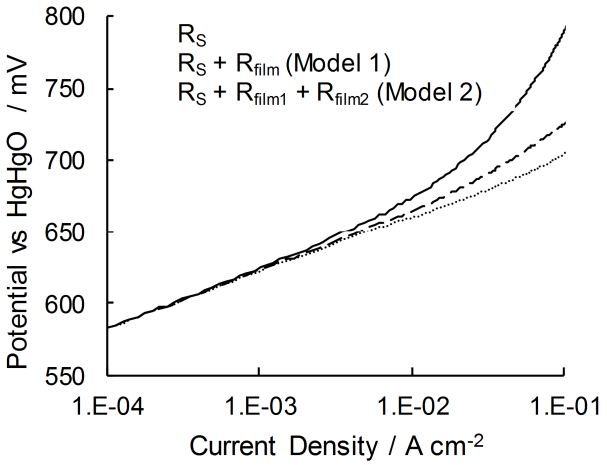

Figure 7.11: Solution resistance and film resistance corrected Tafel Plot for cobalt oxide coated electrodes annealed at 450°C using three different ohmic compensation values.

term stability improvements when the layer is annealed at higher temperatures. Annealing these layers under inert atmospheres may therefore be useful, as this will reduce the likelihood of forming a poorly conductive nickel oxide layer, and thus could also provide evidence that the additional resistance we find in this work do indeed arise from a nickel oxide layer between the active cobalt oxide layer and the nickel substrate.

7.4 Conclusions

The electrochemical behaviour of cobalt oxide layers prepared by thermal decomposition and electrochemical deposition are very similar, provided that the oxide layers have been annealed at a temperature of least 350°C. These electrocatalytic coatings are more active for the oxygen evolution reaction in 30 wt% KOH solution than the uncoated nickel substrate. Measurements on a nickel foam substrate coated with cobalt oxide by electrochemical deposition also showed that these coatings are more stable than the uncoated nickel foam over 70 h at 50 mA cm^{-2}. The annealing temperature of the electrochemically deposited cobalt oxide strongly influences the performance of this coating. Higher annealing temperatures decrease the active surface area of the coating as well as introducing additional resistances to the electrode due to a decrease in conductivity of the cobalt oxide layer and/or the formation of a nickel oxide layer between the coating and the nickel substrate. These additional resistances can account for non-linear Tafel behaviour without the normal change in rate limiting step or reaction mechanism explanation. Overall, this work confirms that cobalt oxide coatings on nickel substrates are promising electrodes for alkaline water electrolysis anodes.

Chapter 8

Thin Iridium Electrocatalytic Coatings Produced by Spontaneous Deposition

This chapter has been published as:

Mellsop, S., Gardiner, A., & Marshall, A. (2016). Spontaneous Deposition of Iridium onto Nickel Substrates for the Oxygen Evolution Reaction. Electrocatalysis, [In Press]. doi:10.1007/s12678-016-0299-9

Abstract

Spontaneous deposition of iridium onto nickel substrates is investigated as a method to produce electrocatalytic layers for the oxygen evolution reaction in 30 wt.% KOH solution. UV/Vis spectroscopy, cyclic voltammetry and other electrochemical methods are used to investigate the deposition process and the activity of the electrocatalytic coating towards the oxygen evolution reaction. From three solutions ($IrCl_3$ + HCl, H_2IrCl_6 + HCl, and H_2IrCl_6), H_2IrCl_6 is shown to give the most active and stable coating, with deposition times of 45 min at 60°C being enough to increase the activity of the nickel substrate for the oxygen evolution reaction. While the iridium oxide coatings were highly active at low current densities (less than 45 mA cm^{-2}), coatings with higher surface area are recommended for higher current densities in order to provide performance greater than the cobalt oxide electrocatalysts prepared and discussed in Chapter 7. It is proposed that iridium deposition can occur via the reduction of the iridium precursor coupled to nickel oxidation, as well as the hydrolysis and localised precipitation of the iridium precursor due to the increase in surface pH during nickel dissolution.

8.1 Introduction

To improve the energy efficiency of water electrolysers, electrocatalysts are used to decrease the overpotentials of the oxygen and hydrogen evolution reactions. These electrocatalysts must have high electrocatalyic activity, high active surface areas and be stable for long periods, while being inexpensive and easy to manipulate [3, 174]. Iridium oxide is highly active toward the oxygen evolution reaction (OER) with Tafel slopes as low at 40 mV and overpotentials as low as 83 mV at 10 mA cm^{-2} [63, 62, 175]. Iridium oxide is also shown to have the highest performance of those investigated in Chapter 4. However as iridium is an expensive metal, thin coatings of iridium (or iridium oxide) on inert substrates are normally used as the active electrodes.

Spontaneous deposition is one approach whereby noble metals can be coated onto nickel substrates [176, 177, 161, 178, 179]. The noble metal precursor is reduced onto the surface of the nickel substrate through the oxidation of Ni to Ni^{2+} [176, 177]. This approach has been used to produce Ir-Ni and Ru-Ni electrodes for the hydrogen evolution reaction (HER) [176, 177, 161, 179], and RuO_2-Ni anodes for the OER [176]. Ir-Ni cathodes for the HER have also been successfully produced via electrodeposition of iridium onto nickel [180]. However, despite the well-known activity of iridium oxide for the OER, spontaneous deposition has not yet been investigated as a method to produce OER electrocatalysts. Importantly, $IrNiO_x$ core-shell nanoparticles were recently shown to be more active and more stable for the OER than IrO_x supported on either carbon or doped-SnO_2 [181], and have been suggested to have higher intrinsic activity for the OER compared to pure iridium electrocatalysts [182]. Similarly, others have shown that IrO_2/Ni anodes prepared by electrochemical deposition are more active than pure nickel substrates for the OER [124]. Here, spontaneous deposition of iridium onto nickel foil is investigated as a simple method to produce active iridium layers for the OER in concentrated KOH electrolytes. Specifically, the effect of the iridium precursor and deposition time on the activity of these electrodes is reported.

8.2 Experimental

Nickel foil substrates (1 cm^2, Sigma-Aldrich $\geq$ 99.9%) were cleaned in acetone for 5 min, ultrasonicated in soapy water, etched in 1 M HCl solution with 5.25 g L^{-1} of hydrogen peroxide for 15 min, and finally rinsed in deionised water (18.2MΩ). Contact with the nickel foil was achieved by spot welding a 0.5 mm diameter nickel wire to the foil. The iridium deposition process was performed immediately after substrate preparation to reduce the effects of self-passivation of the freshly etchede Ni foil.

Spontaneous deposition was performed at 60°C for 30 - 120 min in one of three solutions: 0.001 M H_2IrCl_6 and 0.1 M HCl (solution A), 0.001 M H_2IrCl_6 (solution B) or 0.001 M $IrCl_3$ and 0.1 M HCl (solution C). Note that the iridium concentration used here is 10 times less than that used in most other reports [179, 161], to minimise cost. The deposition solution was deaerated with a 40 cm^3 min^{-1} of argon both during deposition and for at least 10 min prior to deposition

[177, 161, 180, 179]. The coated electrodes were dried at 60°C for 1 h after which there was an optional annealing step (300°C for 2 h). The wire providing the electrical connection to the electrode was coated in a thermosetting polymer prior to testing.

Electrochemical testing was performed in a thermostatically controlled (25°C) PTFE cell with 30 wt.% KOH electrolyte (pellet basis, $\geq$ 85 wt% purity), a nickel foil (30 cm^{-2}) counter electrode and a HgHgO (30 wt.% KOH) reference electrode. All potentials in this work are given relative to the HgHgO (30 wt.% KOH) reference electrode unless otherwise stated. Measurements were performed using a Gamry Instruments Reference 3000 potentiostat. For each electrode the following testing procedure was cused: OCP for 5 min, cyclic voltammetry, galvanostatic oxygen evolution at 10 mA cm^{-2} then 50 mA cm^{-2}, impedance spectroscopy and linear sweep voltammetry. The cyclic voltammetry was carried out between -0.1 V and 0.65 V and positive feedback IR drop compensation was used. Prior to galvanostatic oxygen evolution 20 cyclic voltammetry cycles at 50 mV s^{-1} were performed, and after oxygen evolution 3 cycles at 50, 10, 20, 100 and 200 mV s^{-1} were performed. The galvanostatic oxygen evolution was performed for 5 min at 10 mA cm^{-2} followed by 6 h at 50 mA cm^{-2} with IR drop compensation carried out post-measurement. Impedance spectroscopy was performed at 10 mA between 0.2 Hz and 100 kHz and the linear sweep voltammetry was performed at 0.2 mV s^{-1} between 0.55 and 1 V with IR composition also carried out post-measurement. In addition to electrochemical measurements, the electrocatalyst morphology and surface chemical composition was investigated using scanning electron microsroscopy (SEM) and energy-dispersive X-ray spectroscopy (EDS) using a JEOL 7000F FE-SEM.

UV/Vis spectroscopy was performed on the precursor solutions using a Shimadzu multispec 1500 UV/Vis spectrometer in a quartz crystal curvette over 200 - 800 nm. To confirm that changes in the precursor solution were due to the deposition process itself and not just ageing of the precursor solutions [179], the absorbance of unused solutions was also measured in parallel with the solutions used in the deposition process.

8.3 Results and Discussion

8.3.1 Influence of the Iridium Precursor Solution

While both $IrCl_3$ and H_2IrCl_6 solutions have been used for spontaneous deposition of iridium in previous literature [161, 179], no direct comparison between these precursors has been reported. Thus this study began by investigating the influence of the iridium precursor. In some cases, HCl has been added to the precursor solution [177, 179]. The three solutions chosen for comparison were: 0.001 M H_2IrCl_6 with 0.1 M HCl (solution A), 0.001 M H_2IrCl_6 (solution B) and 0.001 M $IrCl_3$ with 0.1 M HCl (solution C).

Absorption spectra were recorded for the three solutions prior to use (Figure 8.1a), with the H_2IrCl_6 containing solutions (solutions A and B) exhibiting peaks (415, 432 and 488 nm) characteristic of the $[IrCl_6]^{2-}$ complex [183, 184, 117, 185, 186]. The UV/Vis spectra of solution A and B also have a small peak at 360 nm which is most likely from $[IrCl_6]^{3-}$, which also has a peak at 415 nm

[183]. While we cannot quantify the concentration of $[IrCl_6]^{3-}$ present in this solution (as the molar absorptivity of $[IrCl_6]^{3-}$ is about 30 x less than $[IrCl_6]^{2-}$) it is likely that solutions A and B contain more than trace amounts of $[IrCl_6]^{3-}$. In addition to the peaks attributed to $[IrCl_6]^{2-}$ and $[IrCl_6]^{3-}$, peaks are also observed at 305 and 580 nm. These peaks are also seen in the $[IrCl_6]^{2-}$ reported previously [183, 184], and others have suggested that these peaks at originate from $[Ir(OH)_6]^{2-}$ and Ir-O-Ir linkages, respectively [187]. For solution C (prepared from $IrCl_3$), clear peaks at 327 and 390 nm and a small peak at 550 nm were observed. As expected, the overall absorbance of this solution was much lower than the solutions prepared from H_2IrCl_6 [188, 186]. In this case, the peak at 390 nm is assigned to $Ir(H_2O)_3Cl_3$ [184] and the peak at 327 nm to the hydrolysis product $[Ir(OH)_6]^{3-}$ [189]. Interestingly, others have suggested that ageing the precursor solution prior to use can greatly improve the deposition process [177, 179, 190], therefore it is worthwhile to note that the aged $IrCl_3$ solution reported elsewhere [179] has a spectrum which suggests that aged $IrCl_3$ solutions contained a mixture of $[IrCl_6]^{2-}$, $[IrCl_6]^{3-}$ and $[Ir(OH)_6]^{2-}$.

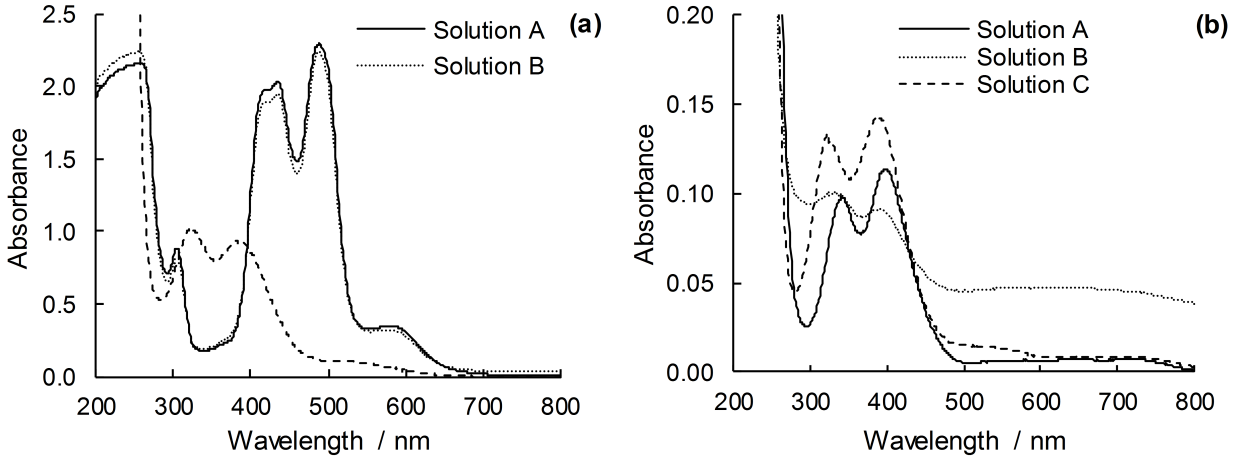

Figure 8.1: UV visible spectra for solution before (a) and after deposition (c). Note that in (a) the absorbance of solution C is multiplied by 10.

After a 2 h deposition, significant changes to the solutions initially containing H_2IrCl_6 were observed, with the complete loss of the $[IrCl_6]^{2-}$ peaks and the development of a spectra similar to the initial $IrCl_3$ (Figure 8.1b). As the absorbance of solution B after deposition is significantly lower (relative to the background absorbance between 550 and 800 nm) than both other precursor solutions, it is concluded that more iridium is deposited onto the nickel substrate from solution B. For solutions A and B, the loss of $[IrCl_6]^{2-}$ supports the general proposal that the deposition process involves the reduction of $[IrCl_6]^{2-}$ to iridium:

$$[IrCl_6]^{2-} + 2\,Ni \rightleftharpoons Ir + 2\,Ni^{2+} + 6\,Cl^- \tag{8.3.1}$$

which is spontaneous under standard conditions according to calculations from the standard reduction potentials. The development of peaks at 330 - 340 nm and 390 - 400 nm suggests the formation of either $[IrCl_6]^{3-}$ (peaks at 360 and 410 nm [183]), $[Ir(OH)_6]^{3-}$ (320 nm [189]) or Ni^{2+}

(394 nm [191]) via:

$$2\,[IrCl_6]^{2-} + Ni \rightleftharpoons 2\,[IrCl_6]^{3-} + Ni^{2+} \tag{8.3.2}$$

$$2\,[IrCl_6]^{2-} + 12\,H_2O + Ni \rightleftharpoons [Ir(OH)_6]^{3-} + Ni^{2+} + 12\,HCl \tag{8.3.3}$$

$$2\,[IrCl_6]^{3-} + 6\,H_2O \rightleftharpoons [Ir(OH)_6]^{3-} + 6\,HCl \tag{8.3.4}$$

It is also possible that the formation of metallic iridium occurs from the reduction of the $[Ir(OH)_6]^{3-}$ complex rather than directly from $[IrCl_6]^{2-}$ as follows:

$$[IrCl_6]^{3-} + 3\,Ni \rightleftharpoons 2\,Ir + 3\,Ni^{2+} + 12\,Cl^- \tag{8.3.5}$$

The presence of Ni^{2+}, which absorbs at 394 nm, is difficult to confirm by UV/Vis spectroscopy as its absorbance is at similar wavelengths to the various Ir species which are also present in the solution. Bianchi et al. have identified Ni^{2+} by forming the Ni-dimethylglyoxime complex [177] when depositing Ru onto Ni substrates, and as thermodynamics suggests that Ni oxidation will occur in the presence of either $[IrCl_6]^{2-}$ or $[IrCl_6]^{3-}$ it is very likely that the solutions will contain Ni^{2+} after deposition. While very little difference in the UV/Vis spectra before and after deposition was observed for solution C, the increase in absorbance, particularly the peak at 390 nm relative to the peak at 327 nm, is most likely due to the presence of Ni^{2+} and suggests that some iridium deposition has also occurred in this solution.

It was observed that the background absorption for solution b (e.g., that between 550 and 800 nm) increased considerably during the deposition process, most likely due to the formation of IrO_x nanoparticles within the solution. These which exhibit a broad absorption peak around 570 - 580 nm [187, 189, 192]. In some cases, a faint blue precipitate was observed in the solution after deposition which is likely to be IrO_2. This blue precipitate was not observed in solution A and B, which suggests that this may occur due to the localised pH changes near the nickel substrate due to proton consumption in this corrosion reaction

$$2\,H^+ + Ni \rightleftharpoons H_2 + Ni^{2+} \tag{8.3.6}$$

As solution B does not contain HCl like solutions A and C do, this proton consumption is able to increase the pH near the Ni surface, which would hydrolyse the $[IrCl_6]^{2-}$ or $[IrCl_6]^{3-}$ leading to IrO_2 formation [187, 189, 192] and possibly IrO_2 deposition directly onto the nickel substrate through a surface-assisted nucleation process. This mechanism of oxide layer formation is similar to cathodic deposition of oxides such as CoO_x described in Chapter 7, which uses cathodic hydrogen evolution to increase the pH at the surface of the cathode to initiate localised hydroxide nucleation. To confirm that the hydrogen evolution reaction occurs in parallel with the Ir deposition process, the potential of the Ni substrate was measured and found to be around -0.22 to -0.2 V vs Ag/AgCl (i.e., close to the hydrogen evolution potential). This supports our proposed mechanism of iridium oxide

deposition via a localised pH increase brough about by the hydrogen evolution reaction, and the measured potential is consistent with the reported by Duca et al. [179] where solution C was used. While this potential value and the observation of a blue IrO_2 precipitate are consistent with this proposed mechanism, the measured potential still allows direct deposition of metallic iridium to occur via reactions 8.3.1 or 8.3.5 and may be occurring in parallel with localised IrO_2 precipitation.

To confirm that the deposition procedure did indeed modify the surface of the nickel substrates, cyclic voltammetry was performed before and after galvanostatic OER (Figure 8.2). For an uncoated nickel substrate, a set of peaks corresponding to the α-$Ni(OH)_2$/γ-NiOOH transition are located at 0.41 V (anodic) and 0.33 V (cathodic) along with a smaller anodic peak at 0.47 V, corresponding to another $Ni(OH)_2$/NiOOH transition of a different phase (discussed further in Chapter 5). These nickel redox peaks are seen on all of the iridium modified electrodes. This indicates that if any Ir or IrO_2 layer had formed on these electrodes, it must be porous enough to allow electrolyte penetration into the substrate. This is consistent with other investigations where the nickel redox behaviour is observed by cyclic voltammetry after iridium deposition [161, 124]. Based on the Pourbaix Diagram for iridium [14] we would expect to see peaks at approximately 0.06 V vs HgHgO (30 wt.% KOH) (0.08 V vs SHE). Alternatively, for anodically formed IrO_x films, anodic solid-state redox peaks corresponding to the Ir^{3+}/Ir^{4+} and Ir^{4+}/Ir^{5+} transitions are expected to range from -0.25 to -0.12 V and from -0.06 to 0.12 V vs HgHgO (30 wt.% KOH) respectively [193, 194, 195, 196]. The corresponding cathodic solid-state redox potentials for the Ir^{3+}/Ir^{4+} and Ir^{4+}/Ir^{5+} transitions are expected to range from -0.38 to -0.19 V and from -0.22 to 0.04 V vs HgHgO (30 wt.% KOH) respectively. Calculation of these potentials for this high pH electrolyte assumed a potential drop of 0.093 V per pH unit which was based on the potential shift of the Ir^{3+}/Ir^{4+} reaction from pH 1 to 10.9 seen in the work of Chen et al. [193].

In addition to the $Ni(OH)_2$/NiOOH transition peaks, the other similarity observed between the three electrodes prepared from different solutions were anodic and cathodic peaks at 0.28 and 0.15 V respectively (Figure 8.3). These peaks are less clear on the solution B cyclic voltammogram due to the background current, but are still present. They are likely due to the Ir^{4+}/Ir^{5+} transitions. The potentials do not match perfectly with those in literature, but this may be due to imperfect assumptions around the potential shift with pH. An additional set of peaks at 0.36 V (anodic) and 0.3 V (cathodic) not seen on the nickel substrate were also found on the electrode prepared from solution B. While the redox behaviour of nickel can undergo significant changes during both cyclic voltammetry and OER (Chapter 5), such peaks are not normally seen on pure nickel electrodes, suggesting that the iridium has indeed modified the nickel surface. One possibility is that the iridium has been incorporated into the nickel oxyhydroxide film which is present on nickel substrates in KOH electrolyte, thereby altering the redox behaviour of the $Ni(OH)_2$/NiOOH redox couple. It seems unlikely that this peak pair comes from the Ir^{4+}/Ir^{5+} transition, because this transition is likely occurring at the 0.36 V (anodic) and 0.3 V (cathodic) peaks. It is noted that the background charging current is significantly larger on the electrode prepared by solution B, which is typical of electrodes with iridium oxide coatings (Chapter 4). It is also found that the onset potential for

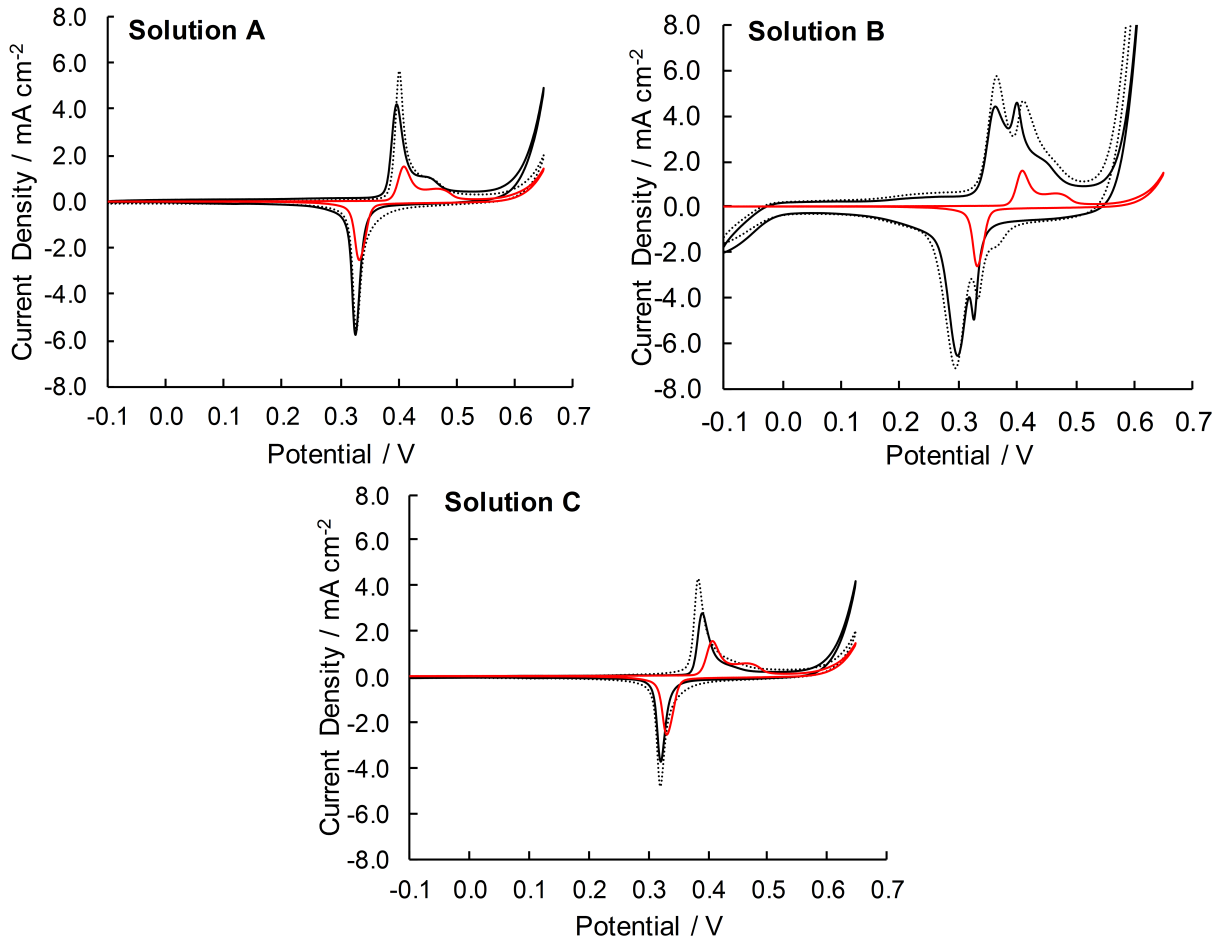

Figure 8.2: Cyclic voltammograms before (solid lined) and after (dashed line) 6 h of OER at 50 mA cm^{-2} on iridium coated nickel electrodes prepared from solutions A, B and C. For comparison, a typical voltammogram measured at an uncoated nickel substrate is also provided (red line).

the OER (defined as the potential at 1 mA cm^{-2}) for coatings produced from solution B decreases following iridium deposition (0.64 $\longrightarrow$ 0.5 V, Figure 8.2) which is not surprising given that iridium is considerably more active than nickel for the OER. These findings lead to the conclusion that a stable iridium or IrO_2 porous layer was successfully deposited onto the nickel substrate when using solution B.

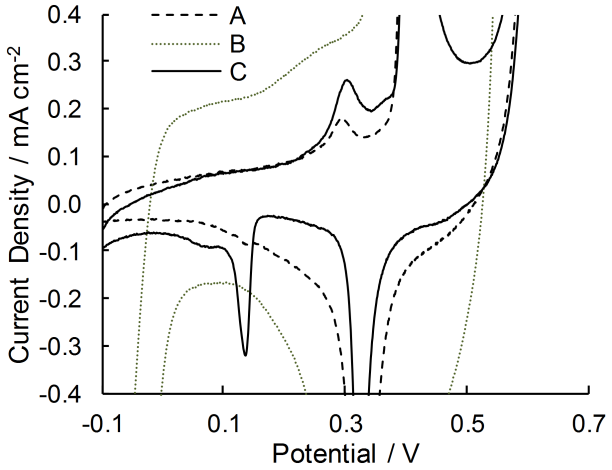

Figure 8.3: Initial cyclic voltammograms of the iridium coated nickel electrode prepared from solutions A, B and C.

The voltammograms recorded at the electrodes prepared from solutions A and C are noticeably different to that prepared from solution B, and are more similar to the nickel voltammogram (Figure 8.2). While the double layer charging current on these electrodes is larger relative to the uncoated nickel substrate, this current (measured at 0.1 V) is only about 25% of the current measured at the electrode produced from solution B, suggesting less iridium has been deposited. It is also possible that this increase in double layer charging is only due to roughening of the nickel substrate caused by nickel dissolution. However, for the electrodes produced from solutions A and C, the additional redox peaks at 0.28 V (anodic) and 0.15 V (cathodic) were observed in the cyclic voltammetry measurements conducted immediately after iridium deposition indicating the presence of iridium. (Figure 8.3). It was found, however, that the size of these peaks decreases during the initial cyclic voltammograms and are completely absent from the electrodes after 6 h of OER at 50 mA cm^{-2}. This indicates that the surface species which give these voltammetric peaks (possibly the Ir^{4+}/Ir^{5+} transition) are not stable during cyclic voltammetry or OER. Furthermore the voltammograms measured just prior to the galvanostatic OER measurements have a higher onset potential for the OER than those measured after 6 h of OER (Figure 8.2).

In order to confirm the presence and stability of the the iridium coating, SEM and EDS analysis was performed on the anodes after the initial cyclic voltammetry measurements and 6 h of OER at 50 mA cm^{-2}. As expected the uncoated etched nickel substrate showed a rough surface, with the crystalline structure of the nickel clearly visible (Figure 8.4a). Following the deposition from solution B, a very thin film is observed to coat the nickel substrate (Figure 8.4b), with EDS analysis

confirming that this layer is iridium. In some images, pores were visible through to the nickel substrate (confirmed by EDS mapping) which accounts for the presence of the nickel redox peaks on the cyclic voltammograms. For the electrodes produced from solutions A and C, no evidence for any iridium deposits could be found by EDS mapping, confirming the suggestion that if these solutions did produce any iridium deposits, they were unstable during the cyclic voltammetry and 6 h of oxygen evolution at 50 mA cm^{-2}. In previous work, both solutions B and C have successfully been used to produce stable coatings for the hydrogen evolution reaction [161, 179]. However, in this investigation, solution C failed to produce a stable layer. The most likely explanation is related to differences in the iridium species present in the precursor solutions due to precursor ageing [177]. In the investigation by Duca et al., their $IrCl_3$ solution was aged prior to deposition and importantly the UV/Vis spectra of their precursor solution [179] is markedly different to that found in this work, with their aged $IrCl_3$ solution more similar to the fresh H_2IrCl_6 solution. Thus, it seems likely the iridium species in the solution used by Duca et al. [179] are actually quite different to those in our solution C, despite the fact that both solutions were prepared from $IrCl_3$ and HCl. It was also reported that the deposition of iridium from the aged solution C was very sensitive to the pre-treatment and etching of the nickel substrate [179] (the pre-treatment of nickel in [179] involved boiling the nickel in 20% HCl), and thus, it may also be possible that both solutions A and C failed to produce a stable layer due to the pretreatment of the nickel in this work (although the SEM analysis does show that the nickel was well-etched prior to deposition).

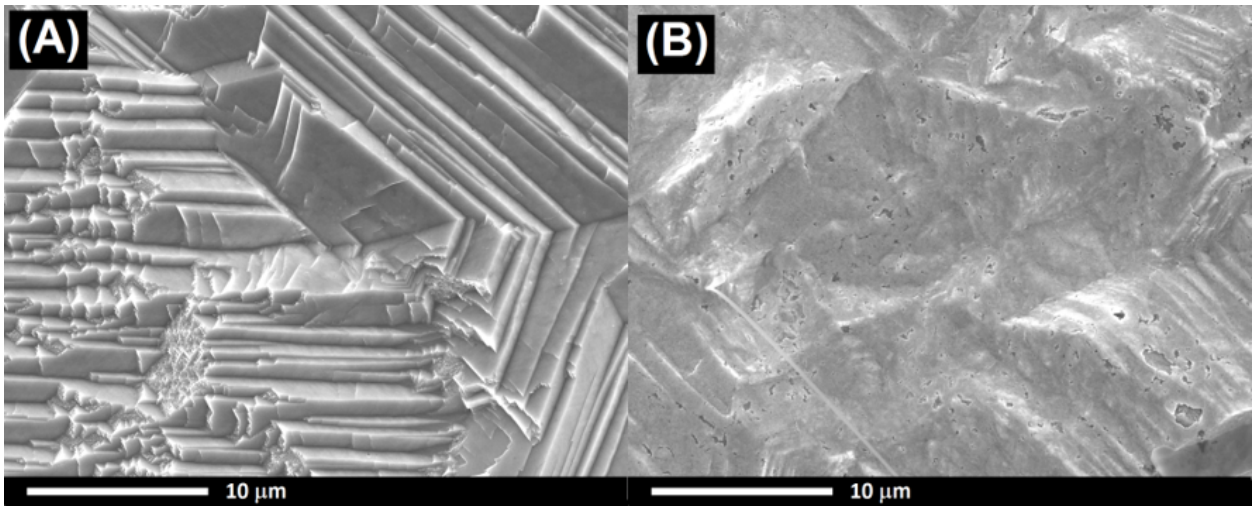

Figure 8.4: SEM micrographs of an uncoated nickel substrate (a) and a nickel substrate coated by iridium using solution B (b).

The performances using all three coating solutions are compared for their electrocatalytic activity against the nickel substrate and electrodeposited cobalt oxide coated electrodes annealed at 300°C (Figure 8.5). Preparation of the cobalt oxide coated electrodes is described in Chapter 7. As discussed elsewhere [7] and in earlier chapters, the activity of nickel for the OER is strongly dependent on its pre-treatment, and can change dramatically when subjected to cyclic voltammetry prior

to measuring the polarisation cure or prolonged OER. It has also been shown that the apparent electrocatalytic activity of nickel for the OER depends on the scan direction used to measure the pseudo-steady-state polarisation curves and periodic interruptions to galvanostatic OER (Chapter 6). This makes direct comparison to an uncoated nickel substrate quite difficult. Therefore, in Figure 8.5, instead of a polarisation curve for the nickel substrate, the lowest potential during the 6 h OER pretreatment at 50 mA cm^{-2} is shown. It is immediately clear that the coating produced by solution B has significantly better performance than that produced by solution A and C. This is expected based on our previous findings indicating coatings produced by solution A and B are unstable and knowing that this data in Figure 8.5 was collected after 6 h of OER at 50 mA cm^{-2}. The performance of the solution B iridium coated electrode was also significantly better than the cobalt oxide coated electrodes at low overpotentials. It is noted however, that as the current density increases there is a step increase in the Tafel slope of the iridium coated electrode, and at the higher current densities the cobalt oxide coated electrode is the better option.

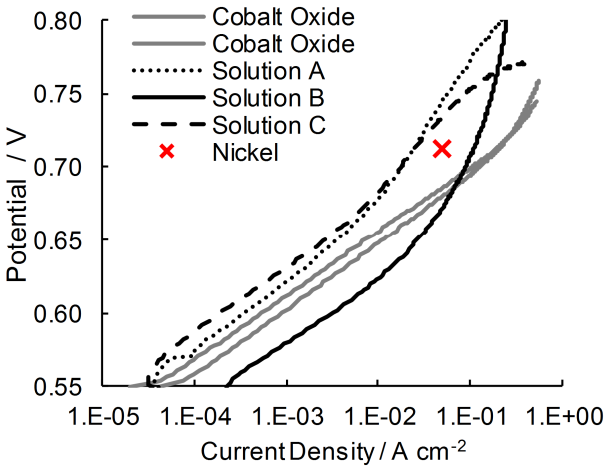

Figure 8.5: Comparison of the electrocatalytic performance of an iridium coated nickel electrodes and cobalt oxide coated nickel electrodes in 30 wt.% KOH. The polarisation curves were meaasured at 0.2 mV s⁻1 after 6 h of galvanostatic OER. The minimum potential during a 6 h pretreatment of nickel at 50 mA cm−2 is also shown.

8.3.2 Deposition Time

To establish the optimal deposition time to produce an active iridum coating from solution B, the deposition time was varied to between 30 and 120 min. Within 30 min, the UV/Vis absorbance peaks associated with the $[IrCl_6]^{2-}$ complex (432 and 488 nm) decreased by approximately 1 order of magnitude suggesting that the initial reaction of $[IrCl_6]^{2-}$ is rapid. For deposition times of 30 - 60 min, $[Ir(OH)_6]^{2-}$ which was present in the fresh H_2IrCl_6 solution (peak at 305 nm) was still observed. However after 60 min this peak is lost suggesting, that it undergoes further reactions such as reduction to $[Ir(OH)_6]^{3-}$ (peak at 327 nm) or hydrolysis/oxidation to IrO_x nanoparticles (Figure 8.6). It is also noted that for the samples at 30 and 45 min, a peak at 345 nm is found which

is suggested to be a combination of the $[Ir(OH)_6]^{3-}$ and $[IrCl_6]^{3-}$ absorption peaks located at 330 and 360 nm respectively (Figure 8.6). It seems reasonable that both $[Ir(OH)_6]^{3-}$ and $[IrCl_6]^{3-}$ will be seen at short deposition times as these are probably intermediates formed from the reduction of the initial iridium species in precursor solution. Again, it is likely that the peaks located at 394 nm after 60 min are from Ni^{2+}, but it is not possible to confirm that it is present at shorter times due to the overlapping absorbance peaks from iridium species. As both hydrolysis and reduction products from $[IrCl_6]^{2-}$ are observed, we propose that the deposition process involves both the reduction of $[IrCl_6]^{2-}$ coupled with Ni oxidation, and the hydrolysis of Ir species due to localised pH changes, although further work is required to gain a complete understanding of the process.

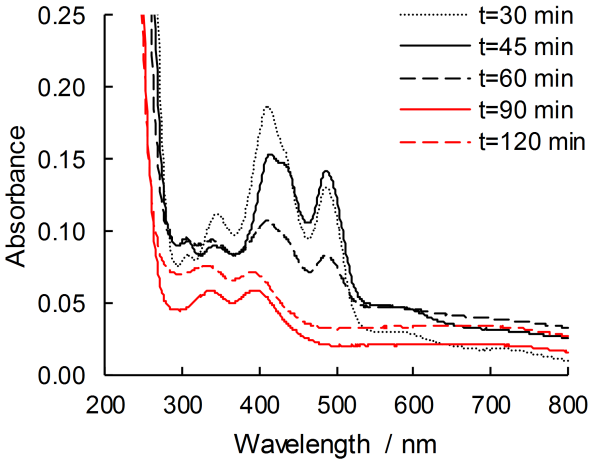

Figure 8.6: UV visible spectra of solution B (0.001 M H_2IrCl_6) as a function of the deposition time.

For deposition times greater than 30 min, cyclic voltammetry shows that electrodes exhibited both the $Ni(OH)_2$/NiOOH behaviour along with the additional redox peaks at 0.35 (anodic) and 0.3 V (cathodic) as discussed previously (Figure 8.7a). The cathodic feature at -0.05 V and the broad redox peak couple at 0.26 (anodic) and 0.18 V (cathodic shoulder) increases with deposition time (Figure 8.7b) as does the charging current density (Figure 8.7c), suggesting that longer deposition times lead to thicker iridium deposits. It is worth noting that the increased quantity of iridium in the layer does not decrease the current from the $Ni(OH)_2$/NiOOH transition, which shows that thicker iridium layers do not alter the accessibility of the electrolyte to the nickel substrate. The lack of features corresponding to an iridium layer at the 30 min deposition time suggests that this time is too short to form a stable and electroactive iridium layer, most likely because the initial intermediates (e.g. $[Ir(OH)_6]^{3-}$ and $[IrCl_6]^{3-}$) have not had sufficient time to react further to form the iridium layer.

It is again clear that iridium deposition (for times greater than 30 min) improves the activity towards the OER compared to the cobalt oxide electrocatalyst in the lower current density range. However, despite the cyclic voltammetry suggesting that increasing the deposition time increases the quantity of iridium deposited on the nickel substrate, almost no difference in the electrocatalytic activity is found for deposition times of 45 - 120 min, suggesting that the activity is improved by

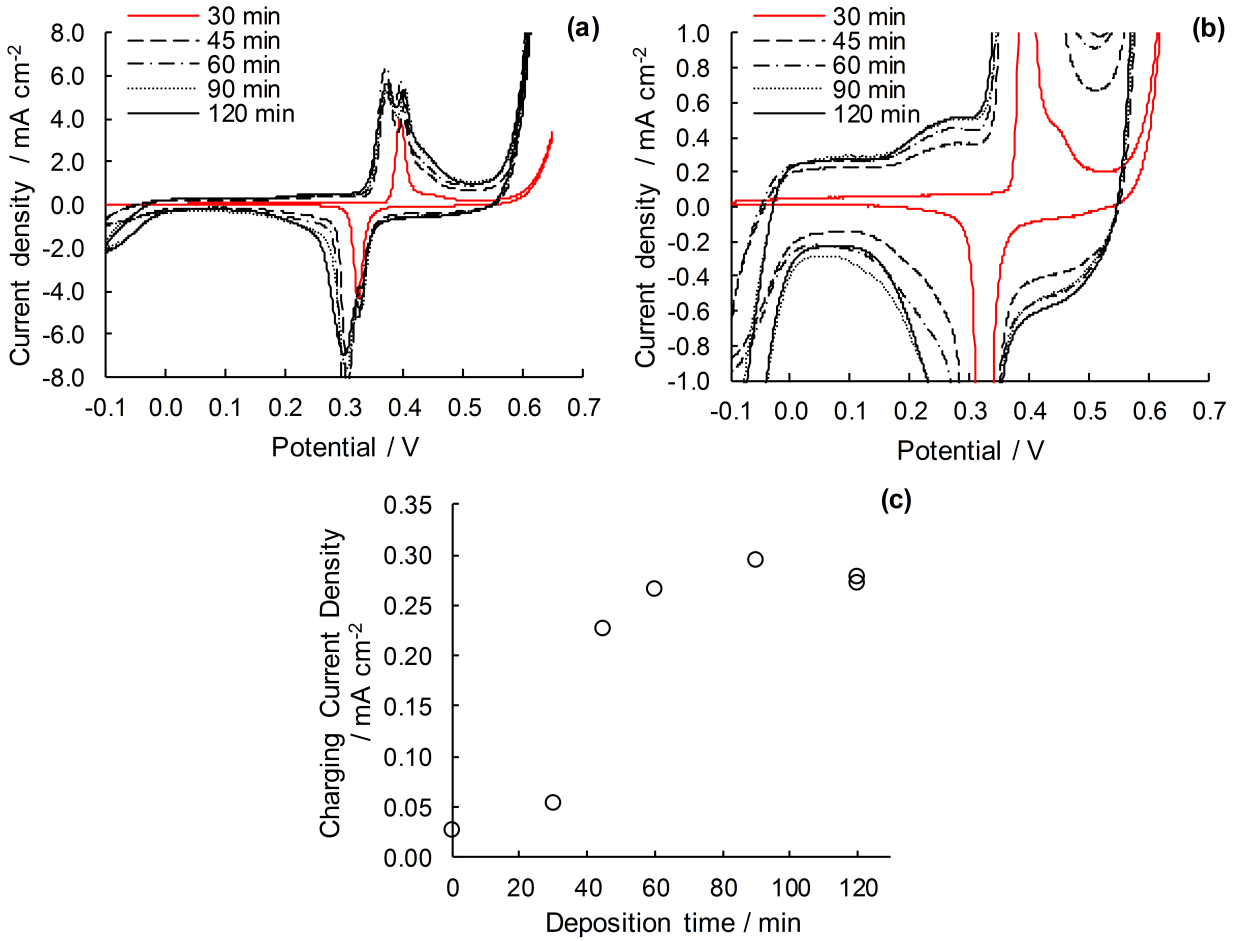

Figure 8.7: Cyclic voltammograms(a and b) at 50 mV s^{-1} on electrodes with coatings deposited for 30-120 min and charging current density at 0.1 V vs deposition time (c).

a small quantity of iridium. This is somewhat expected given that the OER is an electrocatalytic reaction which only occurs on the outer surface of the active iridium layer and suggests that increasing the iridium deposition time increases the thickness of the iridium layer rather than generating more electrocatalytic surface area for the OER. Of course, the voltammetry did show an increase in the quantity of electrochemically active iridium. However it is well-known that unlike the OER, the solid-state redox transition in noble metal oxide films is not restricted to the outermost surface of the oxide layer [29]. As with the cyclic voltammetry results, it is suggested that a deposition time of 30 min is insufficient to produce an active iridium layer on the nickel substrate, with this electrode exhibiting significantly poorer activity than the other electrodes. As briefly mentioned previously, at approximately 50 mA cm^{-2} the Tafel slope of all the iridium modified electrodes increases from 40 mV to values greater than 120 mV. This suggests that the mechanism or rate limiting step for the OER changes at this current density. One possibility is that at these high current densities the active iridium sites become saturated with a reaction intermediate and thus a limiting current is approached. For example if the combination of adsorbed O to form molecular oxygen is rate limiting, and the surface coverage of O on the iridium sites $\longrightarrow$ 1, the Tafel slope will approach infinity [197]. To increase the current density further, the nickel must then begin to act as an electrocatalyst and the potential increases more rapidly with current density. This explanation is similar to that proposed by Duca et al. [179] when describing the kinetics of the hydrogen evolution reaction on iridium coated nickel prepared by spontaneous deposition.

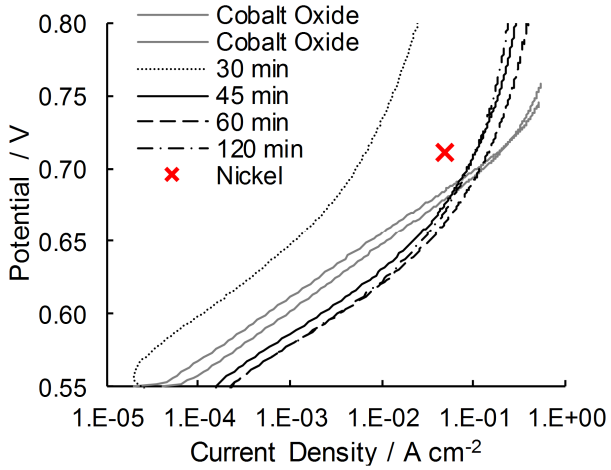

Figure 8.8: Linear sweep voltammetry performed at 0.2 mV s^{-1} for cobalt oxide electrodes annealed at 300°C and iridium coated nickel electrodes prepared through deposition for 30 min to 2 h. The minimum potential during a 6 h pretreatment of nickel at 50 mA cm^{-2} is also shown.

8.4 Conclusions

Spontaneous deposition can be used as a method for the production of thin iridium layers on nickel substrates for the electrocatalytic oxygen evolution reaction. The optimum solution for spontaneous

deposition was found to be a dilute H_2IrCl_6 solution, which is believed to form the active layer on nickel through both reduction and hydrolysis/localised precipitation. Cyclic voltammetry revealed evidence of the active iridium coating and also confirmed that this layer is porous enough to allow electrolyte penetration to the underlying nickel substrate. At 60°C, a deposition time of only 45 min is required to increase the activity of a nickel substrate toward the OER in 30 wt.% KOH. When operating at low currents densities (below 45 mA cm^{-2}) this method of producing an iridium catalyst is very effective in increasing performance of the OER. For higher current densities however, a higher surface area iridium coating is recommended.

Chapter 9

Preliminary Scale-Up of the Cobalt Oxide Electrocatalyst

Abstract

This chapter describes the preliminary work to scale up the cobalt oxide coating procedure to a 20 cm x 25 cm nickel foam electrode. Firstly it is shown that electrodeposition can be used to coat a 0.5 cm x 1 cm nickel foam electrode (the majority of previous work had been carried out on nickel foil) and achieve an overpotential decrease of 150 mV at 50 mA cm^{-2} relative to the uncoated nickel foam. Next a 20 cm x 25 cm cobalt oxide coated electrode was successfully produced via electrodeposition. Upon testing the performance in one cell of the zero gap Callaghan Innovation electrolyser, no increase in performance is seen compared to the uncoated electrode. However, upon testing a cobalt oxide coated electrode in a smaller scale, zero gap cell (nickel foam electrodes 5 cm x 4 cm in size) a performance improvement is achieved. Multiple reasons for the disappointing full-scale performance (20 cm x 25 cm) are discussed, and recommendations for future work made.

9.1 Introduction

The majority of this thesis has focussed on the development of electrocatalysts to decrease the overpotential for the oxygen evolution reaction (OER). It has been shown in Chapter 7 that Co_3O_4 is a promising electrocatalyst for this reaction. Both electrodeposition (with a heat treatment) and thermal decomposition methods have been shown to produce Co_3O_4 coatings which improve activity when deposited on a nickel foil substrate. In Chapter 7 it is suggested that an electrodeposition method may be better for a nickel foam substrate as it is more likely to allow for deposition within the porous structure of the foam.

In addition to the overpotentials of the anode and cathode (η_a and η_c), there are additional resistances which also increase the absolute cell potential (Equation 9.1.1). These resistances are discussed in work by Douglas et al. [198] and Zeng and Zhang [1]. These overpotentials (η_a

and η_c) include the resistances to the reaction (R_a and R_c) as well as the resistances created due to hydrogen and oxygen gas blocking the surface of the electrode ($R_{b,O2}$ and $R_{b,H2}$). Transport resistances include the resistance to ion transport through the solution (R_{ions}) and through the membrane (R_m). There are also electrical resistances associated with the electrode materials and cell hardware (R_1 and R_1'). R_{ions}, R_m and R_1 and R_1' sum together to give the overall ohmic resistance (R_Ω).

$$E_{cell} = \Delta E_e + |\eta_a| + |\eta_c| + IR_\Omega \tag{9.1.1}$$

where ΔE_e is the equilibrium cell voltage and η_a and η_c are the anode and cathode overpotentials, respectively.

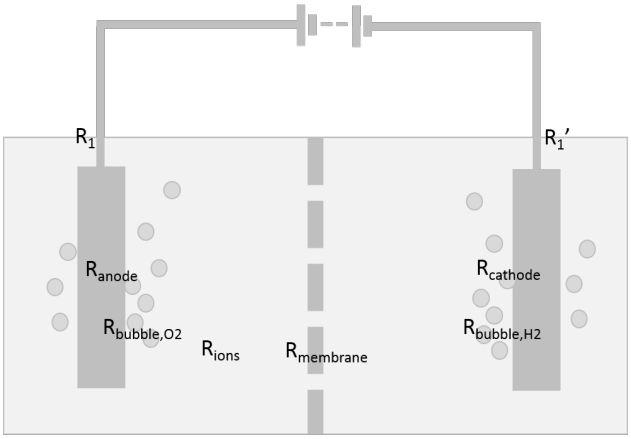

Figure 9.1: Resistances in a water electrolysis cell.

R_{ions} is a key resistance which researchers have reduced through utilising a zero-gap cell configuration. A zero-gap cell configuration is one in which there is no gap between the electrodes, only the membrane material. The anode and cathode must be porous and permeable to liquid electrolyte so that the it can reach between the electrodes [18] and the H_2 and O_2 bubbles can escape. Ideally, a zero-gap configuration should exclude bubbles from the intra-electrode space [18]. The full-scale cell designed by Callaghan Innovation uses a zero-gap system to reduce R_{ions}.

This chapter looks at using the cobalt electrocatalyst on porous electrodes and scaling this up for use in Callaghan Innovation's zero-gap electrolyser. It is important to note that this is preliminary research and further work is required for optimization.

9.2 Experimental

Initial work was focussed on depositing a cobalt electrocatalyst onto a foam substrate, which has been briefly discussed in Chapter 7. The electrodeposition method was then scaled up from deposition on a 0.5 cm x 1 cm electrode to a 25 cm x 20 cm electrode. Further testing was also carried out in a cell designed for 5 cm x 4 cm electrodes. Current densities were calculated as though the electrodes were flat, using the area of both sides. Therefore, for an electrode 0.5 cm

x 1 cm in size an area of 1 cm^2 was used to calculate the current density. This is done to allow for comparison with earlier chapters where the surface area of both sides of the nickel foil was considered.

9.2.1 Foil to Foam

Nickel foam electrodes (INCOFOAM^{TM}, image in Figure 9.2) of size 0.5 cm x 1 cm were cleaned in acetone for 5 min, ultrasonicated in water, etched and then rinsed in deionised water prior to electrodeposition. Etching was carried out in 1 M HCl with 5.25 g L^{-1} of hydrogen peroxide for 5 min during which time the solution was mixed to increase mass transport. The electrode was coated using an electrodeposition procedure performed at -0.5 mA (total current) for 8000 s in a 0.005 M $Co(NO_3)_2$ and 0.1 M KNO_3 solution. The deposition solution was deaerated prior to, and during deposition using argon gas. The solution was also mixed to improve mass transport. After coating the electrode was rinsed in isopropanol for 5 min, and dried at 80°C, prior to heat treating at 250°C for 2 h.

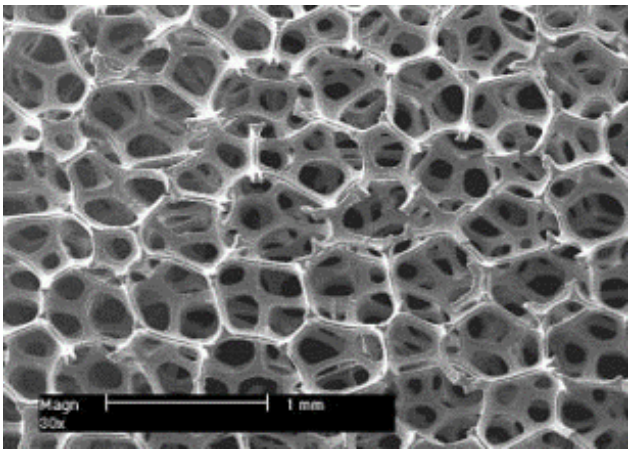

Figure 9.2: Image of an nickel foam substrate.

Electrochemical measurements were performed in a 30 wt% KOH solution (pellet basis, $\geq$ 85 wt% purity) at 25°C using a Gamry Instruments Reference 3000 potentiostat. Nickel foil (30 cm^2) was used as a counter electrode together with a Hg/HgO (30 wt% KOH) reference electrode.

9.2.2 Full-Scale Electrodes

Callaghan Innovation have designed a zero-gap stacked cell electrolyser using 20 cm x 25 cm nickel foam electrodes. Again the electrodes were cleaned in acetone for 5 min, ultrasonicated in water, etched and rinsed in deionised water prior to electrodeposition. Etching was carried out in 1 M HCl with 5.25 g L^{-1} of hydrogen peroxide for 10 min during which time the solution was agitated. After this pretreatment the electrode was dried at 50°C.

Electrodeposition was carried out at -250 mA (total current) for 8000 s in a 15 L vessel. The solution was 0.005 M $Co(NO_3)_2$ and 0.1 M KNO_3, as for the 0.5x1 cm electrode. Argon was bubbled through the solution before and during deposition via a glass frit sparger. The solution was also agitated with an impellar to increase mass transport of the cobalt ions in the solution. The counter electrode was a 20x25 cm nickel foam electrode and a saturated calomel electrode (SCE) was used as the reference electrode. After deposition the coated electrode was rinsed in isopropanol for 5 min and dried at 50°C. Annealing was performed at 300°C for 2 h.

Testing was performed in one cell of the Callaghan Innovation zero gap electrolyser. The cell was modified to include two Hg/HgO reference electrodes as per the diagram in Figure 9.3. The two reference electrodes were placed close to the back of each electrode. KOH resistant acrylic plates are used in the Callaghan Innovation electrolyser to hold the electrodes in place and transfer oxygen and hydrogen gas out of the cell (Figure 9.4). Stainless steel contacts are used as an electrical connection to the electrodes. Electrochemical testing was performed at 33°C in a 30 wt% KOH electrolyte (pellet basis, $\geq$ 85 wt% purity).

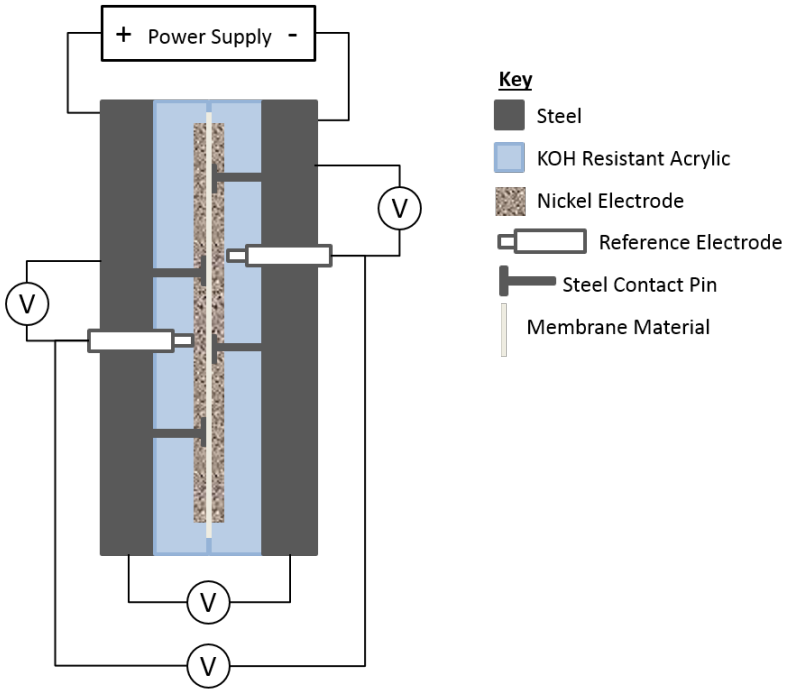

Figure 9.3: Electrochemical cell for the large scale electrode testing.

9.2.3 Mid-Sized Electrochemical Cell

In order to allow for testing in a zero-gap cell at a smaller scale, a cell was designed for electrodes 5 cm x 4 cm in size which could easily be altered to give a zero-gap configuration by removing the middle compartment (Figure 9.5). When in zero-gap configuration, a membrane is placed between the two compartments, and the electrodes are held against the membrane on either side

Figure 9.4: Photograph of a KOH resistant acrylic plate used in the electrochemical cell and a nickel foam electrode.

using inserts placed behind the anode and cathode. When in gap configuration, there are two membranes on either side of the inserted compartment and this middle compartment can house a reference electrode. The electrodes in the anode and cathode compartments are held against their respective membrane.

A 5x4 cm nickel foam electrode was coated using the thermal decomposition method and tested in the mid-sized cell. The electrode was first cleaned and etched using the same method as for the 0.5 cm x 1 cm electrode. The front and back of each electrode was sprayed with 0.48 M $Co(NO_3)_2$ solution (80 vol.% isopropanol). The electrode was placed into an oven at 250°C for 10 min. This coating and annealing process was repeated until a total of approximately 60 mg was deposited. The electrode was then baked in a furnace for 3 h at 300°C. Electrochemical measurements were performed in a 30 wt% KOH solution (pellet basis, $\geq$ 85 wt% purity) at 25°C using a Gamry Instruments Reference 3000 potentiostat.

9.3 Results and Discussion

9.3.1 Foil to Foam

Before scaling up the coating procedure for the 20 cm x 25 cm foam electrode, it was important to show that electrodeposition could be used to deposit a coating onto nickel foam as well as nickel

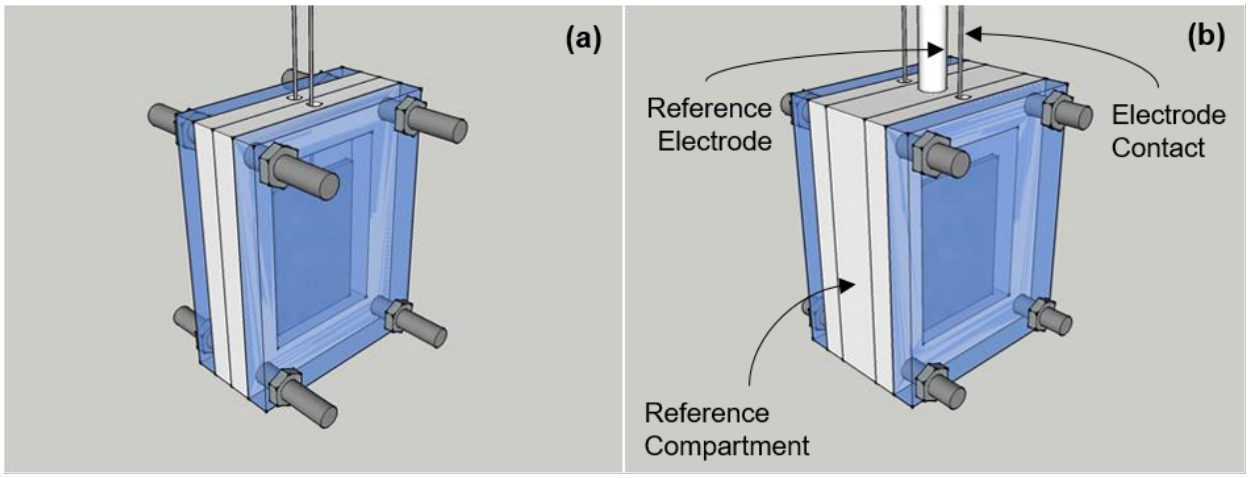

Figure 9.5: Mid-sized electrochemical cell in both zero gap (a) and gap (b) configuration.

foil. Deposition onto nickel foam was mentioned briefly in Chapter 7 but here this is looked into in more detail.

Preparation of the substrate, nickel foam in this case, through cleaning and etching is an important step in the deposition process. Unlike the nickel foil used in previous chapters, the nickel foam substrate is composed of wires linked together which are approximately 50-70 μm in diameter. The effect of etching on the foam was investigated and it was found that etching for the full 15 min, as used for the foil substrates, caused these wires to break (Figure 9.6). This can cause a loss in electrode surface area. For this reason a shorter etching time was used for the preparation of nickel foam electrode substrates.

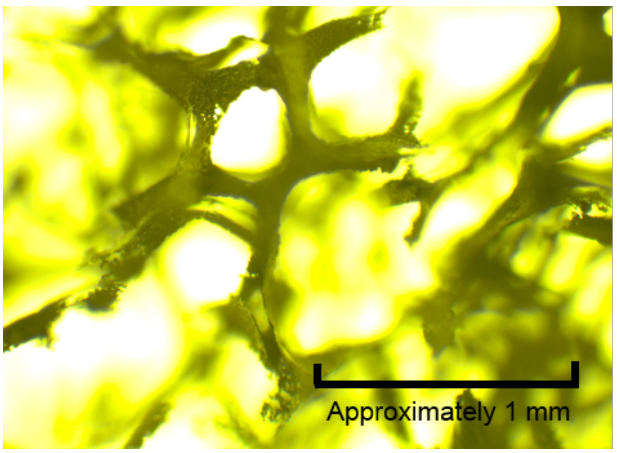

Figure 9.6: Optical microscope image of an overetched nickel foam substrate.

The electrochemical deposition process for $Co(OH)_2$ is described in detail by Brownson and Levy-Clement [103]. The potential applied to the substrate causes a localised pH increase at the electrode, in turn causing the formation of the $Co(OH)_2$ on the surface of the electrode. The nickel foam electrode is porous in nature, as compared to nickel foil, and the solution has a low

concentration of Co^{2+}. It was assumed that more time is required for mass transport of the cobalt through the solution onto the nickel surface, as there is a large surface area and a small volume of solution within the structure. Due to this, and the surface area increase from foil to foam, the time for deposition was increased to 8000 s (from 4000 s on nickel foil).

Before scaling up the electrocatalytic coating process, the performance of the cobalt oxide coated foam and the uncoated foam was compared at small-scale (Figure 9.7). It is clear that the cobalt oxide coated electrode provides a significant improvement with more than 150 mV improvement in activity over a 30 min galvanostatic test at 50 mA cm^{-2}. It must be taken into account that the nickel performance can increase over the first 3 - 6 h (so this potential difference may decrease), as seen in Chapter 5, but eventually the uncoated nickel electrode will deactivate to potentials higher than the starting potential. After observing this initial significant performance improvement it was decided that it was worthwhile scaling up the coating for the Callaghan Innovation electrolyser.

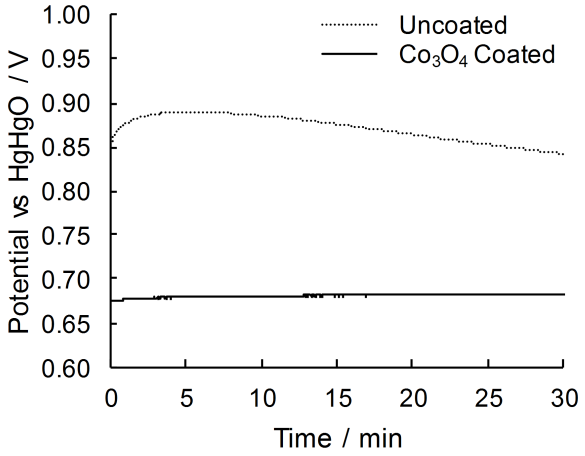

Figure 9.7: Performance comparison of an unetched nickel foam anode and a cobalt oxide coated nickel foam anode during galvanostatic water electrolysis at 50 mA cm^{-2} for 30 min.

9.3.2 Full-Scale Electrodes

After confirming the activity at small-scale, full-scale electrodes were then investigated. The electrolysis cell used for testing these large scale electrodes is shown in Figure 9.3. For increased capacity, a number of these cells are stacked together (Figure 9.8), however in this stacked cell electrolyser the reference electrodes are unable to be used. The full-scale cell, both in testing and stacked cell format, has a zero-gap configuration which minimises the solution resistance to ion transfer (R_{ions}).

A cobalt oxide coated foam electrode was prepared for testing at full-scale and it was clear from a visual observation that a cobalt oxide coating had successfully formed on the surface of the 20 cm x 25 cm foam electrode (as the electrode had turned black). It is noted that a number of changes made in order to scale up the deposition process, likely influenced the electrocatalytic coating. For example, a smaller volume of etching solution was used per unit area than in the

Figure 9.8: Stacked full-scale cell.

small-scale electrode preparation. This was done in order to minimise the total amount of acid required. During etching of the full-scale electrode it was found that the solution turned green, possibly indicating that the solution was saturated with nickel ions and that the etching rate had slowed. Additionally, an impeller spinning at 1000 rpm was used to increase mass transfer of the cobalt ions during the electrodeposition process (at small-scale a magnetic stirrer had been used for this purpose). It was found that the cobalt hydroxide coating was uneven and that the area of the electrode at the same height as this impeller had less coating than in other areas. This indicated that impeller mixing had influenced the deposition, perhaps disturbing the localised pH required for deposition. Both the effect of etching solution volume to surface area, and the mixing influence on electrodeposition need to be investigated further in order to minimise any negative influence on coating preparation and therefore electrolysis performance.

The performance of the full-scale electrode was tested by measuring the cell and reference potential at a range of currents from 100 A to 1 A in steps of 1-10 A. The addition of the catalyst did not show an improvement at large scale, and in fact the performance decreased slightly (Figure 9.9). This was not expected, as all previous tests at smaller scale had shown a performance improvement with the addition of the electrodeposited cobalt catalyst. There are multiple explanations possible. It appeared from visual observation, that the the amount of coating on the anode had decreased during testing, which could indicate that the coating is not as mechanically stable in this cell as in small-scale. This may be due to the limited space available for gas to escape, leading to gas bubble erosion of the coating. A second possibility is over-etching causing the surface area available

for reaction to decrease. This is supported by multiple wire"crumbs" appearing to have become detached from the electrode, and were observed at the bottom of the cell after dismantling. A third possibility relates to the wetting of the electrode. The uncoated nickel anode had been used previously and is therefore likely to have spent an increased amount of time in solution and thus the electrode may have "wetted" more effectively. The cobalt oxide coated electrode did not receive the same treatment, and may have had air bubbles trapped within the electrode from the set up procedure decreasing the surface area accessible to the electrode. Also the potential readings and the anode/cathode potential split are investigated in an attempt to help explain the poor results.

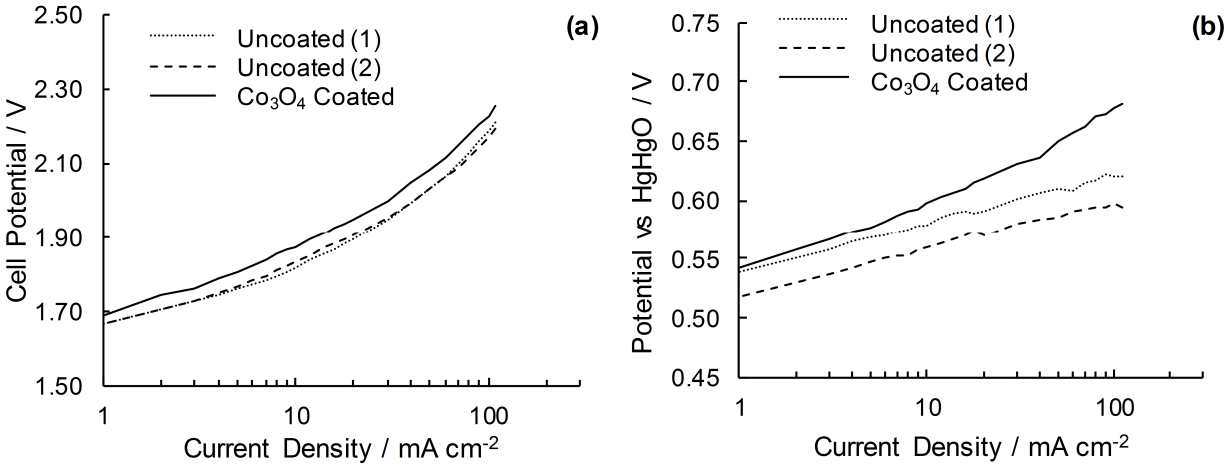

Figure 9.9: Current density stepping down from 110 mA cm^{-2} to 1 mA cm^{-2} (10 mA cm^{-2} step intervals from 110 mA cm^{-2} to 10 mA cm^{-2}, 2 mA cm^{-2} step intervals from 20 mA cm^{-2} to 10 mA cm^{-2}, and 1 mA cm^{-2} step intervals from 10 mA cm^{-2} to 1 mA cm^{-2}) at 33°C. Both the overall cell potential (a) and the half cell potential (b) readings are shown.

While there is confidence in the overall cell potential readings (Figure 9.9a), there remains questions about the accuracy of the potential readings versus the reference electrode (Figure 9.9b). Firstly, the noise seen in the potential reading (Figure 9.9b) was due to gas bubbles forming on the reference electrodes. Secondly, in analysing these results it is noted that, based on the reference electrode potential readings, the overpotential was very low on the anode side prior to catalyst addition (0.59 V vs Hg/HgO, approximately 0.29 V overpotential) as compared to the cathode side (1.41 vs Hg/HgO, approximately 0.51 V overpotential). One explanation is that in this cell the nickel foam was highly active toward the OER. It is possible that the previous electrochemical testing had caused a highly active nickel oxide such as β-NiOOH to form. It is seen in Chapters 5 and 6 that slightly aged nickel performs significantly better than "fresh" nickel. There was concern, however, that this was an inaccurate half-cell potential reading.

It was hypothesized that an additional electrochemical reaction may be occuring causing the low potential on the anode side (e.g. anodic corrosion of the steel electrode contacts). For this reason, further studies were performed to investigate whether the gas output matched the expected output assuming all electrical current went toward the water electrolysis reaction. The gas flowrate

was calculated using the ideal gas law and Faraday's law. It was found that the gas flowrate was as expected, with all of the current going toward the water electrolysis reaction, with only a slight difference observed between the theoretical and actual flowrates (Figure 9.13). This was possibly due to a slight variation in temperature during the measurements.

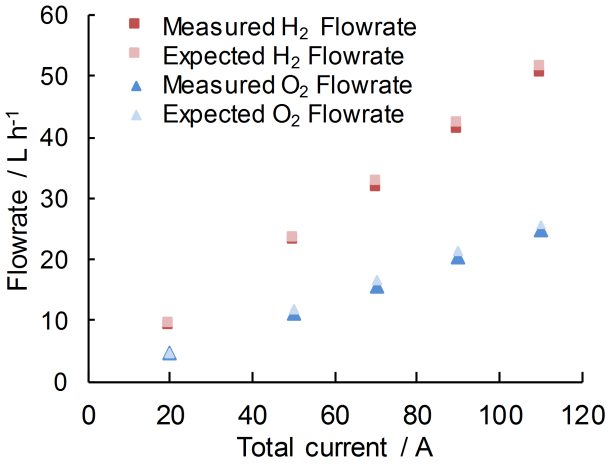

Figure 9.10: Expected gas flowrates (calculated using the current, Faraday's law and the ideal gas law) and measured gas flowrates in the full-scale cell.

After confirming the hydrogen and oxygen gas flowrates were as expected, the accuracy of the reference electrode measurements were questioned. Research shows that there can be inaccuracies in potential readings when the reference electrode is not correctly place [199, 200]. Electrode misplacements may lead to lower potential readings for the anodic reaction. As there are two reference electrodes in the system, it is possible to compare the readings between the two (Figure 9.11). It is clear that there is a difference in potential readings of the two reference electrodes, and the difference increases linearly with current. This can likely be attributed to the IR drop between the reference electrodes (2.3 mΩ or 2.3 Ω cm^2) rather that an indicator of inaccuracy in the reference potential readings.

9.3.3 Mid-Sized Cell

After unsuccessful attempts to improve the performance at full-scale, the decision was made to carry out testing on a smaller cell (5 cm x 4 cm electrodes) in a zero-gap formation. The cell is described in Section 9.2.3. Note that the cell can be altered to carry out tests in a gap configuration with a reference electrode should a researcher wish to measure the half cell potential. When adding this gap, there is an additional ion transfer resistance of 0.1 Ω based on impedance measurements. There are two differences between this cell and the large scale cell worth noting. Firstly there are no steel pins in this mid-sized cell to electrically connect the electrodes. Instead the electrodes are electrically connected by spot welded nickel wires. Secondly, rather than the back of the electrodes being pressed up against an acrylic plate there is an a gap to allow electrolyte to flow behind the electrodes.

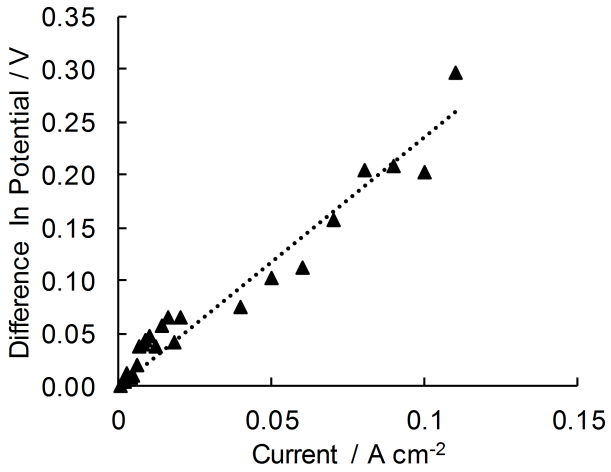

Figure 9.11: Difference in potential readings between the two reference electrodes in the full-scale cell.

A cobalt oxide coated anode, prepared by thermal decomposition, was tested in this mid-sized cell to investigate whether it was possible to obtain a performance improvement using a cobalt oxide coating in a zero-gap cell. There was a clear performance improvement for the cobalt oxide coated electrode seen at 25 mA cm^{-2} (Figure 9.12a), however it is noted that the performance improvement is not as great as that seen in the small-scale cell (Figure 9.7). A performance improvement was also seen over a range of currents in the linear sweep voltammogram (Figure 9.12b).

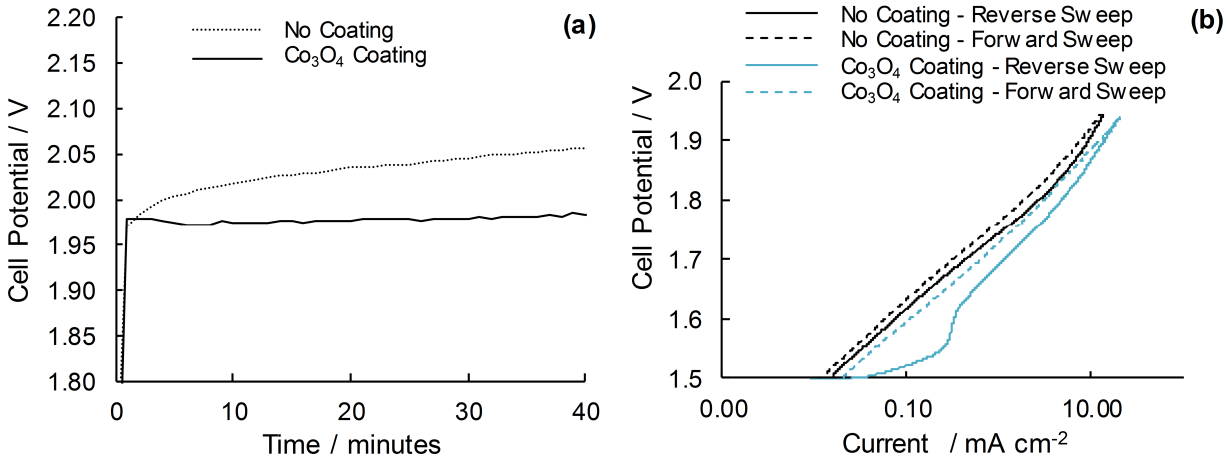

Figure 9.12: Cell potential during galvanostatic water electrolysis at 25 mA cm^{-2} (a) and a linear sweep in cell potential from 1.5-1.96 V and back (b) in a zero gap cell set-up.

One possible reason for the cobalt oxide coated electrode performing better than the uncoated electrode in this cell is due to the coating remaining on the electrode. Based on a visual inspection, the coating was more mechanically stable in the mid-sized cell than in the full-scale cell. This may have been due to the cell shape. The space behind the electrodes, may have allowed gas to escape more easily, preventing pressure building up and destabilizing the coating. More work would be

required to confirm this theory.

On comparison of the full-scale and the mid-sized cell, it is noted that the total cell potential is approximately 90 mV smaller in the large scale cell (at 10 mA cm^{-2}). There are a number of possible reasons for the differences. One possibility is that the steel rods in the full-scale cell are contributing to catalysis of the reaction and reducing the overpotentials. Electrodes containing iron have been investigated as possible electrocatalysts and have, in some cases, shown high activity [74, 51, 72, 52]. A second possible reason for the difference in cell potential is one discussed by Marini et al. [18] who found that in a zero-gap cell, the cell potential was above 2 V and unstable in the first weeks of operation at room temperature. They found that this was due to incomplete wetting of the separators. This same phenomenon may be occurring here, and is supported by the amount of gas blocking indicated by the potential instabilities during galvanostatic water electrolysis over 9 h (Figure 9.13). A third possible reason for the difference in cell potential is that in the full-scale cell, prior electrochemical testing had caused a highly active nickel oxide to form, such as β-NiOOH. A fresh nickel foam electrode had been used for mid-sized cell testing.

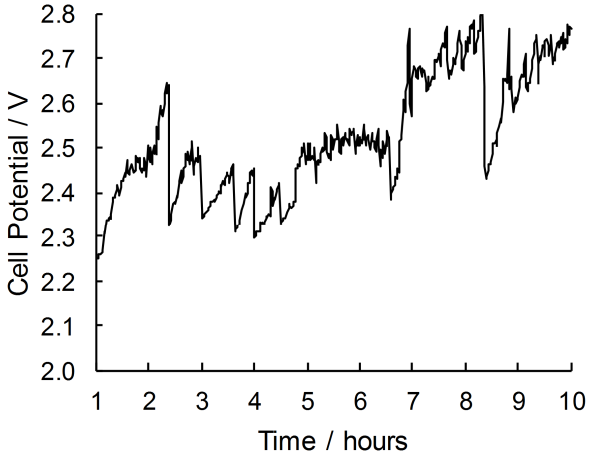

Figure 9.13: Gavlanostatic oxygen evolution at 25 mA cm^{-2} on an uncoated nickel foam electrode for 1-10 h.

9.3.4 Improvements and Redesign

It became clear throughout this investigation that significantly more work would be required to successfully scale up an electrocatalytic coating for the anode. It is suggested that more testing be done at the 5 cm x 4 cm scale before moving back to full-scale.

In order to carry out the recommended testing, a redesign of the testing cell is required. The first recommended change is to design the cell so that the electrolyte gap behind the anode and cathode can be removed to investigate what effect it has on coating mechanical stability, and therefore performance. Secondly, it is recommended that a pump is included to pump the electrolyte through the cell. This is to ensure that the gas bubbles continue to move thereby preventing excess gas blocking. A variable speed drive (VSD) is recommended for this pump system to allow trialling

a range of flowrates. The third recommendation for the cell design is to improve the electrical connection between the electrodes and the power source by increasing the number of connections. Pin-connectors are recommended to mimic the large scale cell. It is suggested that both nickel and steel pins are trialled to investigate the effect of iron in the system. A cell similar to the full-scale variant will allow more transferable results. As mechanical stability appears to be an issue, methods of improvement could be trialled in this cell without wasting materials while testing at large scale.

Results and observations from this study show that indeed further study related to the deposition process is required. Firstly, an investigation into the etching process should be carried out. The wire "crumbs" seen in the large scale cell indicate that over-etching is occurring. The amount of etching needs to be optimized to ensure the electrode remains intact, but that also the electrode surface is sufficiently cleaned to ensure effective deposition. Secondly it is recommended that an investigation into whether there is a difference in activity when thermal decomposition or electrodeposition is used to coat the foam electrodes. The work in Chapter 7 only compares the methods using nickel foil (not nickel foam). If there is no difference, thermal decomposition is the more efficient method to be used going forward. If the decision is made to continue to work with electrodeposition, furtherwork should be carried out to obtain an even coating through optimizing the mixing of the electrolyte during deposition. Bubble lift mixing generated by the argon sparger may be enough. Work related to the deposition cell geometry should also be carried out to minimize the amount of deposition fluid required to minimize waste. This will need to be done in parallel with the mixing work to prevent negative interactions. A third work stream would be to improve the mechanical stability of the cobalt oxide coating, as this appears to cause problems in this study. Finally, it appears that the full-scale cell would benefit from work being carried out on an electrocatalyst coating for the cathode to reduce the overpotential of the hydrogen evolution reaction.

9.4 Conclusions

In this chapter preliminary work on the scale-up of a cobalt oxide coated anode is carried out. It was successfully shown that a cobalt oxide coating improved the activity of the nickel foam electrode by reducing the overpotential by 150 mV at small-scale. However, scaling up to a 20 cm x 25 cm electrode for the Callaghan Innovation electrolyser did not produce the same results, with a slight decrease in performance observed on addition of a cobalt oxide catalyst. Possible reasons for this have been discussed and it is clear that further work is required at smaller scale (5 cm x 4 cm) in a cell similar to the full-scale version (e.g. zero gap with steel pin connections). Additionally, more work is required to optimize the deposition process, particularly in terms of the mechanical stability of the catalytic coating and ensuring the electrode is evenly coated.

Chapter 10

Conclusions and Recommendations

This work has demonstrated a number of electrocatalytic options for improving the efficiency of water electrolysis through the reduction of OER overpotentials. Initial work allowed the comparison of common, high performing electocatalysts utilising the same preparation procedure, similar catalyst loadings and identical testing conditions. On comparison of the perovskite ($La_{0.7}Sr_{0.3}CoO_3$), three spinel oxides ($CoFe_2O_4$, Co_3O_4, and $NiCo_2O_4$), IrO_2 and NiO_x, it was shown that the higher performing electrocatalysts at current densities above 20 mA cm^{-2} were Co_3O_4 and IrO_2. IrO_2 was clearly the higher performing electrocatalyst with potentials at least 48 mV lower at 50 mA cm^{-2} than the the other materials. Due to cost however, thick IrO_2 coatings are not the optimal solution. Co_3O_4 also had excellent performance, even with only a mid-range surface area compared to other electrocatalysts studied. Another key finding from this initial work was that the etched nickel substrate was a reasonably high performing electrocatalyst in itself, and should be investigated further for possible activity or stability improvements, as using a nickel electrocatalyst would remove the coating expense.

Due to this finding, work was carried out to increase understanding of surface structure and reactions on nickel in order to identify ways the performance and stability could be improved. Cyclic voltammograms indicated there were more than just the known α-γ and β-β reactions occurring. There was evidence to suggest that there are at least three surface reactions which can occur. Additionally, evidence suggested that it was neither α-$Ni(OH)_2$ nor β-$Ni(OH)_2$ which formed from metallic nickel at low potentials, but rather a third phase which is named $\alpha(II)_{compact}$. At higher potentials, in situ XAS measurements suggest that γ-NiOOH does not form further phases during oxygen evolution below 0.665 V. A major concern about nickel's performance of nickel toward the OER was its instability over time. It was found that during galvanostatic oxygen evolution, α/γ layers undergo a complex ageing pattern. There is an initial increase in performance (period I) which appears to be at least partially due to an increase in active surface area, followed by a stable potential for approximately 7 h (period II), before the performance begins to decrease (period III), followed by a more rapid performance decrease in the next period (period IV), at which point a change in the cyclic voltammogram is seen. It is suggested that this decrease in performance in

period IV is due to the formation of a phase which contains a large amount of Ni(IV). This is supported by the work of others.

Ageing can be prevented through a rejuvenation process. Holding the potential at 0.5 V vs HgHgO for 10 min for every 100 min of galvanostatic oxygen evolution was shown to rejuvenate the material and prevent the decrease in performance due to anode ageing. It is thought that this rejuvenation prevents an increase in the ratio of Ni(IV) to Ni(III). The effect of different rejuvenation potentials was also investigated, and it was found that the rejuvenation potential can be lower than 0.5 V vs HgHgO, but the nickel surface must not be allowed to reduce to Ni(II) (i.e., the rejuvenation potential must be above 0.36 V vs HgHgO). Through rejuvenating the nickel anode material at regular intervals, hydrogen can be produced with 8% less energy compared to an electrolyser running under continuous galvanostatic operation. Rejuvenation is a good option for maintaining a high electrocatalytic performance without the need for coating the nickel material with an oxide. It is recommended that should this method be utilised, more work is carried out to optimise rejuvenation in order to minimise the amount of time spent rejuvenating while still maintaining high performance. This should also be trialled on a larger zero-gap electrolyser.

If the goal is to improve the performance above that obtained by nickel, or to maintain performance stability without the need for rejuvenation, electrocatalytic coatings are still recommended. As the initial studies suggested that cobalt oxides were the optimal solution, of the six investigated further studies were carried out to optimise preparation procedures. The electrochemical behaviour of cobalt oxide layers prepared by thermal decomposition and electrochemical deposition are very similar, provided that the oxide layers have been annealed at a temperature of least 350°C. The decision was made to progress with electrodeposition, as this method can be more easily used for complex geometries such as nickel foam. The annealing temperature of the electrochemically deposited cobalt oxide strongly influences the performance of this coating. Higher annealing temperatures decrease the active surface area of the coating, as well as introducing additional resistances to the electrode due to a decrease in conductivity of the cobalt oxide layer and/or the formation of a nickel oxide layer between the coating and the nickel substrate. These resistances can account for non-linear Tafel behaviour without the "normal" change in rate-limiting step or reaction mechanism explanation. Due to these findings lower temperature (250-350°C) annealing was recommended, to maintain a high performance.

Iridium oxide had also been identified, in the preliminary work, as the most active electrocatalyst but due to its high cost, thinner coatings were required to progress with option. Spontaneous deposition can be utilized as a method for the production of thin iridium layers on nickel substrates. The optimum solution for spontaneous deposition was found to be a dilute H_2IrCl_6 solution, which is believed to form the active layer through both reduction and hydrolysis/localised precipitation. Cyclic voltammetry revealed evidence of the active iridium coating and also confirmed that this layer is porous enough to allow electrolyte penetration through the coating to the underlying nickel substrate. At 60°C, a deposition time of only 45 min is required to increase the activity of a nickel substrate towards the OER. When operating at low currents densities (below 45 mA cm^{-2}) this

method of producing an iridium catalyst is highly effective in increasing performance of the OER. At higher current densities however, a higher surface area iridium coating is recommended.

Based on the work carried out to this point, for current densities above 45 mA cm^{-2}, cobalt oxide deposited using electrodeposition with a heat treatment at 250-350°C was recommended for scale-up, and some preliminary scale-up work was carried out. At small-scale it was shown that a cobalt oxide coating improved the activity of the nickel foam electrode by reducing the overpotential by 150 mV compared to unetched nickel foam. However, scaling up to a 20 cm x 25 cm electrode and testing in the zero-gap Callaghan Innovation electrolyser did not produce the same results, and instead a slight decrease in performance was observed on addition of a cobalt oxide catalyst. Possible reasons for this were discussed. It was shown that in a smaller scale zero-gap cell (5 cm x 4 cm), cobalt oxide coated foam improved performance, thus the performance issue was unlikely to be related to the zero-gap configuration. It is recommended that further work is carried out at this smaller scale (5 cm x 4 cm) in a cell more similar to the full-scale version (e.g., zero gap with steel pin connections) to gain a better understanding of those performance issues. It is also recommended that further work is carried out to optimize the deposition process, particularly in terms of the mechanical stability of the catalytic coating and ensuring the electrode is evenly coated.

Bibliography

[1] K. Zeng and D. Zhang. Recent progress in alkaline water electrolysis for hydrogen production and applications. *Progress in Energy and Combustion Science*, 36(3):307–326, 2010.

[2] S. Rebouillat, M. Lyons, M. Brandon, and R. Doyle. Paving the Way to The Integration of Smart Nanostructures : Part II : Nanostructured Microdispersed Hydrated Metal Oxides for Electrochemical Energy Conversion and Storage Applications. *International Journal of Electrochemical Science*, 6(11):5830–5917, 2011.

[3] M. Momirlan and T. Veziroglu. Current status of hydrogen energy. *Renewable and Sustainable Energy Reviews*, 6:141–179, 2002.

[4] J. Turner. Sustainable Hydrogen Production. *Science*, 305(5686):972–974, 2004.

[5] M. Rosen and D. Scott. Comparative efficiency assessments for a range of hydrogen production processes. *International Journal of Hydrogen Energy*, 23(8):653–659, 1998.

[6] D. Trommer, F. Noembrini, M. Fasciana, D. Rodriguez, A. Morales, M. Romero, and A. Steinfeld. Hydrogen production by steam-gasification of petroleum coke using concentrated solar power–I. Thermodynamic and kinetic analyses. *International Journal of Hydrogen Energy*, 30(6):605–618, 2005.

[7] I. Godwin and M. Lyons. Enhanced oxygen evolution at hydrous nickel oxide electrodes via electrochemical ageing in alkaline solution. *Electrochemistry Communications*, 32:39–42, 2013.

[8] S. Mellsop, A. Gardiner, and A. Marshall. Electrocatalytic Oxygen Evolution on Electrochemically Deposited Cobalt Oxide Films: Comparison with Thermally Deposited Films and Effect of Thermal Treatment. *Electrocatalysis*, 5(4):445–455, 2014.

[9] S. Mellsop, A. Gardiner, B. Johannessen, and A. Marshall. Structure and transformation of oxy-hydroxide films on Ni anodes below and above the oxygen evolution potential in alkaline electrolytes. *Electrochimica Acta*, 168:356–364, 2015.

[10] S. Mellsop, A. Gardiner, and A. Marshall. Electrocatalytic oxygen evolution on nickel oxyhydroxide anodes: Improvement through rejuvenation. *Electrochimica Acta*, 180:501–506, 2015.

[11] S. Mellsop, A. Gardiner, and A. Marshall. Spontaneous Deposition of Iridium onto Nickel Substrates for the Oxygen Evolution Reaction. *Electrocatalysis*, 7(3):226–234, 2016.

[12] S. Mellsop, A. Marshall, and A. Gardiner. Development of Electrocatalysts for the Oxygen Evolution Reaction in Alkaline Solution. In *Chemeca2012*, 2012.

[13] D. Pletcher and X. Li. Prospects for alkaline zero gap water electrolysers for hydrogen production. *International Journal of Hydrogen Energy*, 36(23):15089–15104, 2011.

[14] M. Pourbaix. *Atlas of Electrochemical Equilibria in Aquesous Solutions*. Pergamon Press, New York, New York, United States of America, 1966.

[15] J. Ivy. Summary of Electrolytic Hydrogen Production Milestone Completion Report. Technical Report September, National Renewable Energy Laboratory (NREL), Golden, Colorado, United States of America, 2004.

[16] J. Genovese, K. Harg, M. Paster, and J. Turner. Current (2009) State-of-the-Art Hydrogen Production Cost Estimate Using Water Electrolysis Independent Review. Technical report, National Renewable Energy Laboratory, Golden, Colorado, 2009.

[17] L. Brossard and C. Messier. Effect of cobalt deposits on nickel substrates on the oxygen evolution reaction in KOH. *Journal of Applied Electrochemistry*, 23(4):379–386, 1993.

[18] S. Marini, P. Salvi, P. Nelli, R. Pesenti, M. Villa, M. Berrettoni, G. Zangari, and Y. Kiros. Advanced alkaline water electrolysis. *Electrochimica Acta*, 82:384–391, 2012.

[19] E. Laouini, M. Hamdani, M. Pereira, J. Douch, M. Mendonça, Y. Berghoute, R. Singh, and M. Mendonca. Preparation and electrochemical characterization of spinel type Fe-Co_3O_4 thin film electrodes in alkaline medium. *International Journal of Hydrogen Energy*, 33(19):4936–4944, 2008.

[20] M. Lyons and M. Brandon. The Oxygen Evolution Reaction on Passive Oxide Covered Transition Metal Electrodes in Alkaline Solution. Part II - Cobalt. *International Journal of Electrochemical Science*, 3(12):1425–1462, 2008.

[21] I. Man, H. Su, F. Calle-Vallejo, H. Hansen, J. Martinez, N. Inoglu, J. Kitchin, T. Jaramillo, J. Nørskov, and J. Rossmeisl. Universality in Oxygen Evolution Electrocatalysis on Oxide Surfaces. *ChemCatChem*, 3(7):1159–1165, 2011.

[22] S. Trasatti and G. Lodi. Oxygen and Chloride Evolution at Conductive Metallic Oxide Anodes. In S. Trasatti, editor, *Electrodes of Conductive Metallic Oxides: Part B*, chapter 10, pages 521–626. Elsevier, Amsterdam, 1981.

[23] E. Guerrini and S. Trasatti. Recent developments in understanding factors of electrocatalysis. *Russian Journal of Electrochemistry*, 42(10):1017–1025, 2006.

[24] R. Ramette. Outmoded Terminology: The Normal Hydrogen Electrode. *Journal of Chemical Education*, 64(10):885, 1987.

[25] C. Hamann, A. Hamnett, and W. Vielstich. *Electrochemistry*. WILEY-VCH Verlag GmbH & Co, Weinheim, Germany, 2007.

[26] R. Nickell, W. Zhu, R. Payne, D. Cahela, and B. Tatarchuk. Hg/HgO electrode and hydrogen evolution potentials in aqueous sodium hydroxide. *Journal of Power Sources*, 161(2):1217–1224, 2006.

[27] A. Bard and L. Faulkner. *Electrochemical Methods: Fundamentals and Applications*. John Wiley & Sons, Inc., New York, 2 edition, 2001.

[28] G. Spinolo, S. Ardizzone, and S. Trasatti. Surface characterization of Co_3O_4 electrodes prepared by the sol-gel method. *Journal of Electroanalytical Chemistry*, 423:49–57, 1997.

[29] S. Ardizzone, G. Fregonara, and S. Trasatti. Inner and outer active surface of RuO_2 electrodes. *Electrochimica Acta*, 35(1):263–267, 1990.

[30] H. Carapuca, M. da Silva Pereira, and F. da Costa. Effect of the preparation procedure on the surface properties of $NiCo_2O_4$ electrodes. *Materials Research Bulletin*, 25(9):1183–1192, 1990.

[31] C. de Pauli and S. Trasatti. Electrochemical surface characterization of IrO_2 + SnO_2 mixed oxide electrocatalysts. *Journal of Electroanalytical Chemistry*, 396:161–168, 1995.

[32] N. Krstajic and S. Trasatti. Cathodic Behavior of RuO_2-Doped Ni/Co_3O_4 Electrodes in Alkaline Solutions: Surface Characterization. *Journal of The Electrochemical Society*, 142(8):2675–2681, 1995.

[33] J. Hansen, G. Stoner, G. Cahen Jr., and L. Scribner. Selection and evaluation of materials for electrochemical energy conversion devices: Electrochemical evaluation of nickel whisker electrodes. In *Proceedings of the sixth annual Thermal and Chemical Storage Contractors' Review Meeting*, volume 1, pages 30–34, 1981.

[34] L. da Silva, L. de Faria, and J. Boodts. Determination of the morphology factor of oxide layers. *Electrochimica Acta*, 47(3):395–403, 2001.

[35] L. da Silva, J. Boodts, and L. DeFaria. In situ and ex situ characterization of the surface properties of the RuO_2 (x) + Co_3O_4 (1x) system. *Electrochimica Acta*, 45(17):2719–2727, 2000.

[36] R. Boggio, A. Carugati, and S. Trasatti. Electrochemical surface properties of Co_3O_4 electrodes. *Journal of Applied Electrochemistry*, 17(4):828–840, 1987.

[37] S. Levine and A. Smith. Theory of the differential capacity of the oxide/aqueous electrolyte interface. *Discussions of the Faraday Society*, 52:290–301, 1971.

[38] A. Tavares, M. Cartaxo, M. da Silva Pereira, and F. Costa. Effect of the partial replacement of Ni or Co by Cu on the electrocatalytic activity of the $NiCo_2O_4$ spinel oxide. *Journal of Electroanalytical Chemistry*, 464(2):187–197, 1999.

[39] E. Laouini, M. Hamdani, M. Pereira, Y. Berghoute, J. Douch, M. Mendonca, and R. Singh. Impedance Study of Spinel Type Fe-Co_3O_4 Oxide Thin Film Electrodes in Alkaline Medium. *International Journal of Electrochemical Science*, 4(8):1074–1084, 2009.

[40] I. Herraiz-Cardona, E. Ortega, J . Garcia Anton, and V. Perez-Herranz. Assessment of the roughness factor effect and the intrinsic catalytic activity for hydrogen evolution reaction on Ni-based electrodeposits. *International Journal of Hydrogen Energy*, 36(16):9428–9438, 2011.

[41] J. Randles. Kinetics of rapid electrode reactions. *Discussions of the Faraday Society*, 1:11–19, 1947.

[42] G. Silva, C. Fugivara, G. Tremiliosi Filho, P. Sumodjo, and A. Benedetti. Electrochemical behavior of cobalt oxide coatings on cold-rolled steel in alkaline sodium sulfate. *Electrochimica Acta*, 47(12):1875–1883, 2002.

[43] M. Lyons and M. Brandon. The significance of electrochemical impedance spectra recorded during active oxygen evolution for oxide covered Ni, Co and Fe electrodes in alkaline solution. *Journal of Electroanalytical Chemistry*, 631:62–70, 2009.

[44] E. Laouini, M. Hamdani, M. Pereira, J. Douch, M. Mendonça, Y. Berghoute, and R. Singh. Electrochemical impedance spectroscopy investigation of spinel type cobalt oxide thin film electrodes in alkaline medium. *Journal of Applied Electrochemistry*, 38(11):1485–1494, 2008.

[45] M. Lyons and M. Brandon. Redox switching and oxygen evolution electrocatalysis in polymeric iron oxyhydroxide films. *Physical Chemistry Chemical Physics*, 11(13):2203–2217, 2009.

[46] E. Rasten, G. Hagen, and R. Tunold. Electrocatalysis in water electrolysis with solid polymer electrolyte. *Electrochimica Acta*, 48(25-26):3945–3952, 2003.

[47] Y. Matsumoto and E. Sato. Electrocatalytic properties of transition metal oxides for oxygen evolution reaction. *Materials Chemistry and Physics*, 14(5):397–426, 1986.

[48] M. Lyons and M. Brandon. The Oxygen Evolution Reaction on Passive Oxide Covered Transition Metal Electrodes in Aqueous Alkaline Solution. Part I-Nickel. *International Journal of Electrochemical Science*, 3(12):1386–1424, 2008.

[49] B. Cui, H. Lin, J. Li, X. Li, J. Yang, and J. Tao. Core-Ring Structured $NiCo_2O_4$ Nanoplatelets: Synthesis, Characterization, and Electrocatalytic Applications. *Advanced Functional Materials*, 18(9):1440–1447, 2008.

[50] J. Kubisztal and A. Budniok. Study of the oxygen evolution reaction on nickel-based composite coatings in alkaline media. *International Journal of Hydrogen Energy*, 33(17):4488–4494, 2008.

[51] X. Li, F. Walsh, and D. Pletcher. Nickel based electrocatalysts for oxygen evolution in high current density, alkaline water electrolysers. *Physical Chemistry Chemical Physics*, 13(3):1162–1167, 2011.

[52] M. Lyons and M. Brandon. The Oxygen Evolution Reaction on Passive Oxide Covered Transition Metal Electrodes in Alkaline Solution . Part III Iron. *International Journal of Electrochemical Science*, 3(12):1463–1503, 2008.

[53] N. Singh, S. Tiwari, K. Anitha, and R. Singh. Electrocatalytic properties of spinel-type $Mn_xFe_{3-x}O_4$ synthesized below 100°C for oxygen evolution in KOH solutions. *Journal of the Chemical Society, Faraday Transactions*, 92(13):2397–2400, 1996.

[54] M. Dinamani and P. Vishnu Kamath. Electrocatalysis of oxygen evolution at stainless steel anodes by electrosynthesized cobalt hydroxide coatings. *Journal of Applied Electrochemistry*, 30(10):1157–1161, 2000.

[55] I. Nikolov, R. Darkaoui, E. Zhecheva, R. Stoyanova, N. Dimitrov, and T. Vitanov. Electrocatalytic activity of spinel related cobalties $M_xCo_{3-x}O_4$ (M = Li, Ni, Cu) in the oxygen evolution reaction. *Journal of Electroanalytical Chemistry*, 429:157–168, 1997.

[56] S. Singh, S. Samuel, S. Tiwari, and R. Singh. Preparation of thin Co_3O_4 films on Ni and their electrocatalytic surface properties towards oxygen evolution. *International Journal of Hydrogen Energy*, 21(3):171–178, 1996.

[57] J. Koza, Z. He, A. Miller, and J. Switzer. Electrodeposition of Crystalline Co_3O_4 - A Catalyst for the Oxygen Evolution Reaction. *Chemistry of Materials*, 24(18):3567–3573, 2012.

[58] M. Hamdani, M. Pereira, J. Douch, A. Ait Addi, Y. Berghoute, and M. Mendonça. Physicochemical and electrocatalytic properties of Li-Co_3O_4 anodes prepared by chemical spray pyrolysis for application in alkaline water electrolysis. *Electrochimica Acta*, 49(9-10):1555–1563, 2004.

[59] B. Lu, D. Cao, P. Wang, G. Wang, and Y. Gao. Oxygen evolution reaction on Ni-substituted Co_3O_4 nanowire array electrodes. *International Journal of Hydrogen Energy*, 36(1):72–78, 2011.

[60] J. Balej. Electrocatalysts for oxygen evolution in advanced water electrolysis. *International Journal of Hydrogen Energy*, 10(2):89–99, 1985.

[61] C. Bocca, G. Cerisola, E. Magnone, and A. Barbucci. Oxygen evolution on Co_3O_4 and Li-doped Co_3O_4 coated electrodes in an alkaline solution. *International Journal of Hydrogen Energy*, 24(8):699–707, 1999.

[62] E. Guerrini, H. Chen, and S. Trasatti. Oxygen evolution on aged IrO_x/Ti electrodes in alkaline solutions. *Journal of Solid State Electrochemistry*, 11(7):939–945, 2007.

[63] M. Lyons and S. Floquet. Mechanism of oxygen reactions at porous oxide electrodes. Part 2-Oxygen evolution at RuO_2, IrO_2 and $Ir_xRu_{1-x}O_2$ electrodes in aqueous acid and alkaline solution. *Physical Chemistry Chemical Physics*, 13(12):5314–5335, 2011.

[64] M. Morita, C. Iwakura, and H. Tamura. The anodic characteristics of manganese dioxide electrodes prepared by thermal decomposition of manganese nitrate. *Electrochimica Acta*, 22(4):325–328, 1977.

[65] M. Musiani, F. Furlanetto, and P. Guerriero. Electrochemical deposition and properties of PbO_2 + Co_3O_4 composites. *Journal of Electroanalytical Chemistry*, 440:131–138, 1997.

[66] A. Fundo and L. Abrantes. Electrocatalytic behavior of electroless Ni-P alloys for the oxygen evolution reaction. *Russian Journal of Electrochemistry*, 42(12):1291–1297, 2006.

[67] C. Bocca, A. Barbucci, M. Delucchi, and G. Cerisola. The influence of surface finishing on the electrocatalytic properties of nickel for the oxygen evolution reaction (OER) in alkaline solution. *International Journal of Hydrogen Energy*, 23(4):247–252, 1998.

[68] E. Castro, S. Real, and L. Pinheiro Dick. Electrochemical characterization of porous nickel-cobalt oxide electrodes. *International Journal of Hydrogen Energy*, 29(3):255–261, 2004.

[69] B. Chi, J. Li, Y. Han, and Y. Chen. Effect of temperature on the preparation and electrocatalytic properties of a spinel $NiCo_2O_4$/Ni electrode. *International Journal of Hydrogen Energy*, 29(6):605–610, 2004.

[70] B. Chi, H. Lin, J. Li, N. Wang, and J. Yang. Comparison of three preparation methods of $NiCo_2O_4$ electrodes. *International Journal of Hydrogen Energy*, 31(9):1210–1214, 2006.

[71] M. Musiani and P. Guerriero. Oxygen evolution reaction at composite anodes containing Co_3O_4 particles. Comparison of metal-matrix and oxide-matrix composites. *Electrochimica Acta*, 44(8-9):1499–1507, 1998.

[72] Anindita, A. Singh, and R. Singh. Effect of V substitution at B-site on the physicochemical and electrocatalytic properties of spinel-type $NiFe_2O_4$ towards O_2 evolution in alkaline solutions. *International Journal of Hydrogen Energy*, 35(8):3243–3248, 2010.

[73] M. Kumar, R. Awasthi, A. Sinha, and R. Singh. New ternary Fe, Co, and Mo mixed oxide electrocatalysts for oxygen evolution. *International Journal of Hydrogen Energy*, 36(15):8831–8838, 2011.

[74] M. Mendonca, M. Godinho, M. Catarino, M. da Silva Pereira, and F. Costa. Preparation and characterisation of spinel oxide ferrites suitable for oxygen evolution anodes. *Solid State Sciences*, 4(2):175–182, 2002.

[75] M. Godinho, M. Catarino, M. da Silva Pereira, M. Mendonca, and F. Costa. Effect of the partial replacement of Fe by Ni and/or Mn on the electrocatalytic activity for oxygen evolution of the $CoFe_2O_4$ spinel oxide electrode. *Electrochimica Acta*, 47(27):4307–4314, 2002.

[76] B. Chi, J. Li, X. Yang, H. Lin, and N. Wang. Electrophoretic deposition of $ZnCo_2O_4$ spinel and its electrocatalytic properties for oxygen evolution reaction. *Electrochimica Acta*, 50(10):2059–2064, 2005.

[77] S. Cattarin, I. Frateur, P. Guerriero, and M. Musiani. Electrodeposition of PbO_2+CoO_x composites by simultaneous oxidation of Pb^{2+} and Co^{2+} and their use as anodes for O_2 evolution. *Electrochimica Acta*, 45(14):2279–2288, 2000.

[78] S. Poznyak, V. Kharton, J. Frade, A.. Yaremchenko, E. Tsipis, S. Yakovlev, and I. Marozau. Behavior of (LaSr)CoO_3- and La_2NiO_4- based ceramic anodes in alkaline media: compositional and microstructural factors. *Journal of Solid State Electrochemistry*, 12(1):15–30, 2008.

[79] T. Otagawa and J. Bockris. Lanthanum Nickelate as Electrocatalyst: Oxygen Evolution. *Journal of The Electrochemical Society*, 129(10):2391–2392, 1982.

[80] J. Bockris and T. Otagawa. Mechanism of oxygen evolution on perovskites. *The Journal of Physical Chemistry*, 87(15):2960–2971, 1983.

[81] R. Singh, S. Tiwari, S. Singh, N. Singh, G. Poillerat, and P. Chartier. Synthesis of (La,Sr)CoO_3 perovskite films via a solgel route and their physicochemical and electrochemical surface characterization for anode application in alkaline water electrolysis. *Journal of the Chemical Society, Faraday Transactions*, 92(14):2593–2597, 1996.

[82] I. Arul Raj and K. Vasu. Transition metal oxides based oxygen electrodes in alkaline solution: electrocatalysis by some perovskite oxides based on manganese and cobalt. *Bulletin of Electrochemistry*, 9(11-12):560–563, 1993.

[83] O. Hammerich and H. Lund. *Organic Electrochemistry*. CRC Press, 4 edition, 2000.

[84] C. Bo, J. Li, Y Han, and J. Dai. Effect of precipitant on preparation of Ni-Co spinel oxide by coprecipitation method. *Materials Letters*, 58(9):1415–1418, 2004.

[85] C. Bocca, A. Barbucci, and G. Cerisoli. The influence of surface finishing on the electrocatalytic properties of nickel for the oxygen evolution reaction (OER) in alkaline solution. *International Journal of Hydrogen Energy*, 23(4):247–252, 1998.

[86] A. Vojvodic and J. Norskov. Optimizing Perovskites for the Water-Splitting Reaction. *Science*, 334(6061):1355–1356, 2011.

[87] J. Rossmeisl, Z. Qu, H. Zhu, G. Kroes, and J. Norskov. Electrolysis of water on oxide surfaces. *Journal of Electroanalytical Chemistry*, 607:83–89, 2007.

[88] C. Iwakura, K. Hirao, and H. Tamura. Preparation of ruthenium dioxide electrodes and their anodic polarization characteristics in acidic solutions. *Electrochimica Acta*, 22(4):335–340, 1977.

[89] H. Michishita, Y. Misumi, D. Haruta, T. Masaki, N. Yamamoto, H. Matsumoto, and T. Ishihara. Cathodic Performance of $La_{0.6}Sr_{0.4}CoO_3$ Perovskite Oxide for Platinum-Free Alkaline Water Electrolysis Cell. *Journal of The Electrochemical Society*, 155(9):B969–B971, 2008.

[90] D. Corrigan. The Catalysis of the Oxygen Evolution Reaction by Iron Impurities in Thin Film Nickel Oxide Electrodes. *Journal of The Electrochemical Society*, 134(2):377–384, 1987.

[91] J. Bockris and T. Otogawa. The Electrocatalysis of Oxygen Evolution on Perovskites. *Journal of The Electrochemical Society*, 131(2):290–302, 1984.

[92] L. Burke, O. Murphy, J. O'Neill, and S. Venkatesan. The oxygen electrode. Part 8.Oxygen evolution at Ruthenium Dioxide Anodes. *Journal of the Chemical Society, Faraday Transactions 1: Physical Chemistry in Condensed Phases*, 73:1659, 1977.

[93] G. Fiori and C. Mari. Electrocatalysis of oxygen evolution. *International Journal of Hydrogen Energy*, 7(6):489–493, 1982.

[94] P. Lu and S. Srinivasan. Electrochemical-Ellipsometric Studies of Oxide Film Formed on Nickel during Oxygen Evolution. *Journal of The Electrochemical Society*, 125(9):1416–1422, 1978.

[95] M. Gennero de Chialvo and A. Chialvo. Oxygen evolution reaction on thick hydrous nickel oxide electrodes. *Electrochimica Acta*, 33(6):825–830, 1988.

[96] A. Mohammad, M. Awad, M. El-Deab, T. Okajima, and T. Ohsaka. Electrocatalysis by nanoparticles: Optimization of the loading level and operating pH for the oxygen evolution at crystallographically oriented manganese oxide nanorods modified electrodes. *Electrochimica Acta*, 53(13):4351–4358, 2008.

[97] X. Qing, S. Liu, K. Huang, K. Lv, Y. Yang, Z. Lu, D. Fang, and X. Liang. Facile synthesis of Co_3O_4 nanoflowers grown on Ni foam with superior electrochemical performance. *Electrochimica Acta*, 56(14):4985–4991, 2011.

[98] F. Svegl, B. Orel, I. Grabec-Svegl, and V. Kaucic. Characterization of spinel Co_3O_4 and Li-doped Co_3O_4 thin film electrocatalysts prepared by the solgel route. *Electrochimica Acta*, 45(25-26):4359–4371, 2000.

[99] J. Brownson and C. Levy-Clement. Electrodeposition of α- and β-cobalt hydroxide thin films via dilute nitrate solution reduction. *Physica Status Solidi B*, 245(9):1785–1791, 2008.

[100] E. Castro, C. Gervasi, and J. Vilche. Oxygen Evolution on Electrodeposited Cobalt Oxides. *Journal of Applied Electrochemistry*, 28(8):835–841, 1998.

[101] C. Sequeira, D. Santos, E. Cameron, and P. Brito. Nickel coated electrodes for oxygen evolution in alkaline solution. *Materials Technology*, 23(3):142–144, 2008.

[102] C. Fan and D. Piron. Electrodeposition as a means of producing large-surface electrodes required in water electrolysis. *Surface and Coatings Technology*, 73:91–97, 1995.

[103] J. Brownson and C. Levy-Clement. Nanostructured α- and β-cobalt hydroxide thin films. *Electrochimica Acta*, 54(26):6637–6644, 2009.

[104] R. Qiu, D. Zhang, P. Wang, X. Zhang, and Y. Kang. Tunable electrochemical preparation of cobalt micro/nanostructures and their morphology-dependent wettability property. *Electrochimica Acta*, 58:699–706, 2011.

[105] S. Tiwari, P. Chartier, and R. Singh. Preparation of Perovskite-Type Oxides of Cobalt by the Malic Acid Aided Process and Their Electrocatalytic Surface Properties in Relation to Oxygen Evolution. *Journal of The Electrochemical Society*, 142(1):148–153, 1995.

[106] R. Singh, J. Singh, and A. Singh. Electrocatalytic properties of new spinel-type MMoO4 (M=Fe, Co and Ni) electrodes for oxygen evolution in alkaline solutions. *International Journal of Hydrogen Energy*, 33(16):4260–4264, 2008.

[107] C. Iwakura, A. Honji, and H. Tamura. The anodic evolution of oxygen on Co_3O_4 film electrodes in alkaline solutions. *Electrochimica Acta*, 26(9):1319–1326, 1981.

[108] S. Nakayama, M. Okazaki, Y. Lin, and M. Sakamoto. Preparations of perovskite-type oxides $LaCoO_3$ from three different methods and their evaluation by homogeneity, sinterability and conductivity. *Solid State Ionics*, 158:133–139, 2003.

[109] C. Wang, G. Gau, S. Gau, C. Tang, and J. Bi. Preparation and characterization of nanosized nickel oxide. *Catalysis Letters*, 101(3):241–247, 2005.

[110] E. Laouini, J. Douch, M. Hamdani, Y. Berghoute, M. Mendonça, M. Pereira, and R. Singh. Cathodic behaviour of CoFe2O4 spinel electrodes in alkaline medium. *Journal of Applied Electrochemistry*, 41(6):731–740, 2011.

[111] M. Cappadonia, J. Divisek, T. von der Heyden, and U. Stimming. Oxygen evolution at nickel anodes in concentrated alkaline solution. *Electrochimica Acta*, 39(11-12):1559–1564, 1994.

[112] M. Lyons and M. Brandon. A comparative study of the oxygen evolution reaction on oxidised nickel, cobalt and iron electrodes in base. *Journal of Electroanalytical Chemistry*, 641:119–130, 2010.

[113] B. Yeo and A. Bell. In Situ Raman Study of Nickel Oxide and Gold-Supported Nickel Oxide Catalysts for the Electrochemical Evolution of Oxygen. *The Journal of Physical Chemistry C*, 116(15):8394–8400, 2012.

[114] M. Lyons, R. Doyle, I. Godwin, M. O'Brien, and L. Russell. Hydrous Nickel Oxide: Redox Switching and the Oxygen Evolution Reaction in Aqueous Alkaline Solution. *Journal of the Electrochemical Society*, 159(12):H932–H944, 2012.

[115] P. Nkeng, J. Koenig, J. Gautier, P. Chartier, and G. Poillerat. Enhancement of surface areas of Co_3O_4 and $NiCo_2O_4$ electrocatalysts prepared by spray pyrolysis. *Journal of Electroanalytical Chemistry*, 402:81–89, 1996.

[116] S. Sunde, I. Lervik, M. Tsypkin, and L. Owe. Impedance analysis of nanostructured iridium oxide electrocatalysts. *Electrochimica Acta*, 55(26):7751–7760, 2010.

[117] I. Belova, T. Varlamova, B. Galyamov, Y. Roginskaya, R. Shifrina, S. Prutchenko, G. Kaplan, and M. Sevostyanov. The composition, structure and electronic properties of thermally prepared iridium dioxide films. *Materials Chemistry and Physics*, 20:39–64, 1988.

[118] E. Laouini, Y. Berghoute, J. Douch, M. Mendonca, M. Hamdani, and M. Pereira. Electrochemical behaviour of $Fe_xCo_{3x}O_4$ with (x = 0, 1, 2 and 3) oxides thin film electrodes in alkaline medium. *Journal of Applied Electrochemistry*, 39(12):2469–2479, 2009.

[119] M. Lyons, L. Russell, M. O'Brien, R. Doyle, I. Godwin, and M. Brandon. Redox Switching and Oxygen Evolution at Hydrous Oxyhydroxide Modified Nickel Electrodes in Aqueous Alkaline Solution : Effect of Hydrous Oxide Thickness and Base Concentration. *International Journal of Electrochemical Science*, 7(4):2710–2763, 2012.

[120] S. Trasatti and O. Petrii. Real surface area measurements in electrochemistry. *Pure and Applied Chemistry*, 63(5):711–734, 1991.

[121] R. Doyle and M. Lyons. An electrochemical impedance study of the oxygen evolution reaction at hydrous iron oxide in base. *Physical Chemistry Chemical Physics*, 15(14):5224–5237, 2013.

[122] S. Palmas, F. Ferrara, A. Vacca, M. Mascia, and A. Polcaro. Behavior of cobalt oxide electrodes during oxidative processes in alkaline medium. *Electrochimica Acta*, 53(2):400–406, 2007.

[123] C. Hsu and F. Mansfeld. Technical Note: Concerning the Conversion of the Constant Phase Element Parameter Y_0 into a Capacitance. *Corrosion*, 57(9):747–748, 2001.

[124] M. Battaglia, R. Inguanta, S. Piazza, and C. Sunseri. Fabrication and characterization of nanostructured NiIrO2 electrodes for water electrolysis. *International Journal of Hydrogen Energy*, 39(30):16797–16805, 2014.

[125] M. Gennero De Chialvo and A. Chialvo. Oxygen evolution reaction on $Ni_xCo_{3-x}O_4$ electrodes with spinel structure. *Electrochimica Acta*, 38(15):2247–2252, 1993.

[126] A. Marshall. *Electrocatalysts for the Oxygen Evolution Electrode in Water Electrolysers using Proton Exchange Membranes: Synthesis and Characterisation.* PhD thesis, Norwegian University of Science and Technology, 2005.

[127] I. Casella, M. Guascito, and M. Sannazzaro. Voltammetric and XPS investigations of nickel hydroxide electrochemically dispersed on gold surface electrodes. *Journal of Electroanalytical Chemistry*, 462(2):202–210, 1999.

[128] W. Visscher and E. Barendrecht. Anodic Oxide Films of Nickel in Alkaline Electrolytes. *Surface Science*, 135:436–452, 1983.

[129] N. Farley, S. Gurman, and A. Hillman. Simple cell for in situ X-ray absorption spectroelectrochemistry. *Electrochemistry Communications*, 1(10):449–452, 1999.

[130] L. de Souza, F. Kong, F. McLarnon, and R. Muller. Spectroscopic ellipsometry study of nickel oxidation in alkaline solution. *Electrochimica Acta*, 42(8):1253–1267, 1997.

[131] T. Capehart, D. Corrigan, R. Conell, K. Pandya, and R. Hoffman. In situ extended x-ray absorption fine structure spectroscopy of thin-film nickel hydroxide electrodes. *Applied Physics Letters*, 58(8):865–867, 1991.

[132] H. Bode, K. Dehmelt, and J. Witte. Zur kenntnis der nickelhydroxidelektrodeI. Uber das nickel (II)-hydroxidhydrat. *Electrochimica Acta*, 11(8):1079–1087, 1966.

[133] A. Delahaye-Vidal and M. Figlarz. Textural and structural studies on nickel hydroxide electrodes. II. Turbostratic nickel (II) hydroxide submitted to electrochemical redox cycling. *Journal of Applied Electrochemistry*, 17(3):589–599, 1987.

[134] L. Liu, Z. Zhou, and C. Peng. Sonochemical intercalation synthesis of nano γ-nickel oxyhydroxide: Structure and electrochemical properties. *Electrochimica Acta*, 54(2):434–441, 2008.

[135] T. Ohligschläger and G. Schwitzgebel. EQCM contributions to the reactions of the nickel oxide electrode. *Physical Chemistry Chemical Physics*, 3(23):5290–5296, 2001.

[136] W. Holstein and H. Rosenfeld. In-Situ X-ray Absorption Spectroscopy Study of Pt and Ru Chemistry during Methanol Electrooxidation. *The Journal of Physical Chemistry B*, 109(6):2176–2186, 2005.

[137] R. Barnard and C. Randell. Studies concerning charged nickel hydroxide electrodes. VI. Voltammetric behaviour for pre-cycled electrodes. *Journal of Applied Electrochemistry*, 12(1):27–38, 1982.

[138] V. Sethuraman, B. Lakshmanan, and J. Weidner. Quantifying desorption and rearrangement rates of carbon monoxide on a PEM fuel cell electrode. *Electrochimica Acta*, 54(23):5492–5499, 2009.

[139] R. Kostecki and F. McLarnon. Electrochemical and In Situ Raman Spectroscopic Characterization of Nickel Hydroxide Electrodes. *Journal of The Electrochemical Society*, 144(2):485–493, 1997.

[140] M. Bernard, P. Bernard, M. Keddam, S. Senyarich, and H. Takenouti. Characterisation of new nickel hydroxides during the transformation of α $Ni(OH)_2$ to β $Ni(OH)_2$ by ageing. *Electrochimica Acta*, 41(1):91–93, 1996.

[141] R. Barnard and C. Randell. Studies concerning charged nickel hydroxide electrodes. VII. Influence of alkali concentration on anodic peak positions. *Journal of Applied Electrochemistry*, 13(1):89–95, 1983.

[142] M. Alsabet, M. Grden, and G. Jerkiewicz. Electrochemical Growth of Surface Oxides on Nickel. Part 2: Formation of β-$Ni(OH)_2$ and NiO in Relation to the Polarization Potential, Polarization Time, and Temperature. *Electrocatalysis*, 5(2):136–147, 2014.

[143] K. Juodkazis, J. Juodkazyt, R. Vilkauskait, and V. Jasulaitien. Nickel surface anodic oxidation and electrocatalysis of oxygen evolution. *Journal of Solid State Electrochemistry*, 12(11):1469–1479, 2008.

[144] L. Burke and T. Twomey. Voltammetric behaviour of nickel in base with particular reference to thick oxide growth. *Journal of Electroanalytical Chemistry and Interfacial Electrochemistry*, 162:101–119, 1984.

[145] J. McBreen, W. O'Grady, G. Tourillon, E. Dartyge, A. Fontaine, and K. Pandya. In situ time-resolved x-ray absorption near edge structure study of the nickel oxide electrode. *The Journal of Physical Chemistry*, 93(17):6308–6311, 1989.

[146] Y. Hu, I. Bae, Y. Mo, D. Scherson, and M. Antonio. In situ X-ray absorption fine structure and optical reflectance studies of electrodeposited nickel hydrous oxide films in alkaline electrolytes. *Canadian Journal of Chemistry*, 75(11):1721–1729, 1997.

[147] J. McBreen, W. O'Grady, K. Pandya, R. Hoffman, and D. Sayers. EXAFS study of the nickel oxide electrode. *Langmuir*, 3(3):428–433, 1987.

[148] M. Balasubramanian, C. Melendres, and S. Mini. X-ray Absorption Spectroscopy Studies of the Local Atomic and Electronic Structure of Iron Incorporated into Electrodeposited Hydrous Nickel Oxide Films. *The Journal of Physical Chemistry B*, 104(18):4300–4306, 2000.

[149] W. O'Grady, K. Pandya, K. Swider, and D. Corrigan. In Situ X-Ray Absorption Near-Edge Structure Evidence for Quadrivalent Nickel in Nickel Battery Electrodes. *Journal of The Electrochemical Society*, 143(5):1613, 1996.

[150] M. Biesinger, B. Payne, L. Lau, A. Gerson, and R. Smart. X-ray photoelectron spectroscopic chemical state quantification of mixed nickel metal, oxide and hydroxide systems. *Surface and Interface Analysis*, 41(4):324–332, 2009.

[151] M. Vuković. Voltammetry and anodic stability of a hydrous oxide film on a nickel electrode in alkaline solution. *Journal of Applied Electrochemistry*, 24(9):878–882, 1994.

[152] Y. Huang, C. Lai, P. Wu, and L. Chen. Ni Inverse Opals for Water Electrolysis in an Alkaline Electrolyte. *Journal of The Electrochemical Society*, 157(3):P18–P22, 2010.

[153] T. Osaka and Y. Yatsuda. A study on time-dependence of the oxygen evolution reaction on nickel by FFT impedance measurement. *Electrochimica Acta*, 29(5):677–681, 1984.

[154] R. Barnard and C. Randell. Studies concerning charged nickel hydroxide electrodes. Part V. Voltammetric Behaviour of Electrodes Containing β-$Ni(OH)_2$. *Journal of Power Sources*, 9(2):185–204, 1983.

[155] M. Lyons, A. Cakara, P. O'Brien, I. Godwin, and R. Doyle. Redox, pH sensing and Electrolytic Water Splitting Properties of Electrochemically Generated Nickel Hydroxide Thin Films in Aqueous Alkaline Solution. *International Journal of Electrochemical Science*, 7(12):11768–11795, 2012.

[156] D. Hall, D. Lockwood, S. Poirier, C. Bock, and B. MacDougall. Raman and Infrared Spectroscopy of α and β Phases of Thin Nickel Hydroxide Films Electrochemically Formed on Nickel. *The Journal of Physical Chemistry A*, 116(25):6771–6784, 2012.

[157] S. Medway, C. Lucas, A. Kowal, R. Nichols, and D. Johnson. In situ studies of the oxidation of nickel electrodes in alkaline solution. *Journal of Electroanalytical Chemistry*, 587(1):172–181, 2006.

[158] G. Briggs and W. Wynne-Jones. The nickel oxide electrode. Part 3. *Transactions of the Faraday Society*, 52:1272–1281, 1956.

[159] E. Jones and W. Wynne-Jones. The nickel oxide electrode. Part 2. *Transactions of the Faraday Society*, 52:1260–1272, 1956.

[160] D. Davies and W. Barker. Influence of pH on Corrosion and Passivation of Nickel. *Corrosion*, 20:47t–53t, 1964.

[161] L. Vazquez-Gomez, S. Cattarin, P. Guerriero, and M. Musiani. Hydrogen evolution on porous Ni cathodes modified by spontaneous deposition of Ru or Ir. *Electrochimica Acta*, 53(28):8310–8318, 2008.

[162] E. Castro and C. Gervasi. Electrodeposited Ni-Co–oxide electrodes:characterization and kinetics of the oxygen evolution reaction. *International Journal of Hydrogen Energy*, 25(12):1163–1170, 2000.

[163] A. Esswein, M. McMurdo, P. Ross, A. Bell, and T. Tilley. Size-Dependent Activity of Co_3O_4 Nanoparticle Anodes for Alkaline Water Electrolysis. *The Journal of Physical Chemistry C*, 113(33):15068–15072, 2009.

[164] V. Gupta, S. Gupta, and N. Miura. Al-substituted α-cobalt hydroxide synthesized by potentiostatic deposition method as an electrode material for redox-supercapacitors. *Journal of Power Sources*, 177(2):685–689, 2008.

[165] F. Svegl, B. Orel, M. Hutchins, and K. Kalcher. Structural and Spectroelectrochemical Investigations of Sol-Gel Derived Electrochromic Spinel Co_3O_4 Films. *Journal of The Electrochemical Society*, 143(5):1532–1539, 1996.

[166] R. Gabr. Effect of thermal treatment on the surface characteristics and catalytic activity of pure and doped cobalt oxide. *Surface Technology*, 11(3):205–214, 1980.

[167] R. Garavaglia, C. Mari, S. Trasatti, and C. de Asmundis. Physicochemical characterization of Co3O4 prepared by thermal decomposition I: Phase composition and morphology. *Surface Technology*, 19(3):197–215, 1983.

[168] A. Manabe, M. Kashiwase, T. Hashimoto, T. Hayashida, A. Kato, K. Hirao, I. Shimomura, and I. Nagashima. Basic study of alkaline water electrolysis. *Electrochimica Acta*, 100:249–256, 2013.

[169] I. Belova, V. Shalaginov, B. Galyamov, Y. Roginskaya, and D. Shub. Defect Structure of Non-stoichiometric films of Co_3O_4. *Russian Journal of Inorganic Chemistry*, 23:161–163, 1978.

[170] A. Dukic, V. Alar, M. Firak, and S. Jakovljevic. A significant improvement in material of foam. *Journal of Alloys and Compounds*, 573:128–132, 2013.

[171] D. Harrington and P. van den Driessche. Mechanism and equivalent circuits in electrochemical impedance spectroscopy. *Electrochimica Acta*, 56(23):8005–8013, 2011.

[172] S. Kumari, M. Natarajan, V. Vaidyan, and P. Koshy. Surface oxidation of nickel thin films. *Journal of Materials Science Letters*, 11(11):761–762, 1992.

[173] M. Garcia-Mota, M. Bajdich, V. Viswanathan, A. Vojvodic, A. Bell, and J. Norskov. Importance of Correlation in Determining Electrocatalytic Oxygen Evolution Activity on Cobalt Oxides. *The Journal of Physical Chemistry C*, 116(39):21077–21082, 2012.

[174] S. Trasatti. Electrocatalysis in the anodic evolution of oxygen and chlorine. *Electrochimica Acta*, 29(11):1503–1512, 1984.

[175] H. Miao and D. Piron. Electrodeposition of Ni-transition alloys for the oxygen evolution reaction. *Journal of Applied Electrochemistry*, 21(1):55–59, 1991.

[176] H. Dumont, P. Los, A Lasia, H. Menard, and L. Brossard. Studies of the hydrogen evolution reaction on lanthanum phosphate-bonded composite nickelruthenium electrodes in 1 M alkaline solutions. *Journal of Applied Electrochemistry*, 23(7):684–692, 1993.

[177] I. Bianchi, E. Guerrini, and S. Trasatti. Electrocatalytic activation of Ni for H_2 evolution by spontaneous deposition of Ru. *Chemical Physics*, 319(1-3):192–199, 2005.

[178] E. Verlato, S. Cattarin, N. Comisso, A. Gambirasi, M. Musiani, and L. Vazquez-Gomez. Preparation of Pd-Modified Ni Foam Electrodes and Their Use as Anodes for the Oxidation of Alcohols in Basic Media. *Electrocatalysis*, 3(1):48–58, 2012.

[179] M. Duca, E. Guerrini, A. Colombo, and S. Trasatti. Activation of Nickel for Hydrogen Evolution by Spontaneous Deposition of Iridium. *Electrocatalysis*, 4(4):338–345, 2013.

[180] L. Vazquez-Gomez, S. Cattarin, R. Gerbasi, P. Guerriero, and M. Musiani. Activation of porous Ni cathodes towards hydrogen evolution by electrodeposition of Ir nuclei. *Journal of Applied Electrochemistry*, 39(11):2165–2172, 2009.

[181] H. Nong, H. Oh, T. Reier, E. Willinger, M. Willinger, V. Petkov, D. Teschner, and P. Strasser. Oxide-Supported $IrNiO_x$ Core-Shell Particles as Efficient, Cost-Effective, and Stable Catalysts for Electrochemical Water Splitting. *Angewandte Chemie International Edition*, 54(10):2975–2979, 2015.

[182] H. Nong, L. Gan, E. Willinger, D. Teschner, and P. Strasser. IrO_x core-shell nanocatalysts for cost- and energy-efficient electrochemical water splitting. *Chemical Science*, 5(8):2955, 2014.

[183] I. Poulsen and C. Garner. A Thermodynamic and Kinetic Study of Hexachloro and Aquopentachloro Complexes of Iridium(III) in Aqueous Solutions. *Journal of the American Chemical Society*, 84(11):2032–2037, 1962.

[184] J. Chang and C. Garner. Kinetics of Aquation of Aquopentachloroiridate(III) and Chloride Anation of Diaquotetrachloroiridate(III) Anions. *Inorganic Chemistry*, 4(2):209–215, 1965.

[185] Y. Roginskaya and O. Morozova. The role of hydrated oxides in formation and structure of DSA-type oxide electrocatalysts. *Electrochimica Acta*, 40(7):817–822, 1995.

[186] Y. Roginskaya, O. Morozova, E. Loubnin, A. Popov, Y. Ulitina, V. Zhurov, S. Ivanov, and S. Trasatti. X-ray diffraction, transmission electron microscopy and X-ray photoelectron spectroscopic characterization of IrO_2 + Ta_2O_5 films. *Journal of the Chemical Society, Faraday Transactions*, 89(11):1707–1715, 1993.

[187] Y. Zhao, E. Hernandez-Pagan, N. Vargas-Barbosa, J. Dysart, and T. Mallouk. A High Yield Synthesis of Ligand-Free Iridium Oxide Nanoparticles with High Electrocatalytic Activity. *The Journal of Physical Chemistry Letters*, 2(5):402–406, 2011.

[188] M. Schnippering, P. Unwin, J. Hult, T. Laurila, C. Kaminski, J. Langridge, R. Jones, M. Mazurenka, and S. Mackenzie. Evanescent wave broadband cavity enhanced absorption spectroscopy using supercontinuum radiation: A new probe of electrochemical processes. *Electrochemistry Communications*, 10(12):1827–1830, 2008.

[189] D. Xu, P. Diao, T. Jin, Q. Wu, X. Liu, X. Guo, H. Gong, F. Li, M. Xiang, and Y. Ronghai. Iridium Oxide Nanoparticles and Iridium/Iridium Oxide Nanocomposites: Photochemical Fabrication and Application in Catalytic Reduction of 4-Nitrophenol. *ACS Applied Materials & Interfaces*, 7(30):16738–16749, 2015.

[190] W. Chrzanowski and A. Wieckowski. Ultrathin Films of Ruthenium on Low Index Platinum Single Crystal Surfaces: An Electrochemical Study. *Langmuir*, 13(22):5974–5978, 1997.

[191] W. Liu, A. Migdisov, and A. Williams-Jones. The stability of aqueous nickel(II) chloride complexes in hydrothermal solutions: Results of UVVisible spectroscopic experiments. *Geochimica et Cosmochimica Acta*, 94:276–290, 2012.

[192] M. Yagi, E. Tomita, and T. Kuwabara. Remarkably high activity of electrodeposited IrO_2 film for electrocatalytic water oxidation. *Journal of Electroanalytical Chemistry*, 579(1):83–88, 2005.

[193] Y. Chen, P. Taylor, and D. Scherson. Electrochemical and In Situ Optical Studies of Supported Iridium Oxide Films in Aqueous Solutions. *Journal of The Electrochemical Society*, 156(1):F14–F21, 2009.

[194] J. Baur and T. Spaine. Electrochemical deposition of iridium (IV) oxide from alkaline solutions of iridium(III) oxide. *Journal of Electroanalytical Chemistry*, 443(2):208–216, 1998.

[195] M. Petit and V. Plichon. Anodic electrodeposition of iridium oxide films. *Journal of Electroanalytical Chemistry*, 444(2):247–252, 1998.

[196] Y. Mo, I. Stefan, W. Cai, J. Dong, P. Carey, and D. Scherson. In Situ Iridium L III -Edge X-ray Absorption and Surface Enhanced Raman Spectroscopy of Electrodeposited Iridium Oxide Films in Aqueous Electrolytes. *The Journal of Physical Chemistry B*, 106(14):3681–3686, 2002.

[197] A. Marshall and L. Vaisson-Bethune. Avoid the quasi-equilibrium assumption when evaluating the electrocatalytic oxygen evolution reaction mechanism by Tafel slope analysis. *Electrochemistry Communications*, 61:23–26, 2015.

[198] T. Douglas, A. Cruden, and D. Infield. Development of an ambient temperature alkaline electrolyser for dynamic operation with renewable energy sources. *International Journal of Hydrogen Energy*, 38(2):723–739, 2013.

[199] S. Adler. Reference Electrode Placement in Thin Solid Electrolytes. *Journal of The Electrochemical Society*, 149(5):E166–E172, 2002.

[200] R. Halseid. *Ammonia as Hydrogen Carrier: Effects of Ammonia on Polymer Electrolyte Membrane Fuel Cells*. PhD thesis, Norwegian University of Science and Technology, 2004.